FILM COOLING ANALYSIS OF INJECTION CONFIGURATIONS FOR AFTERBURNER AERO-ENGINE APPLICATIONS

A Thesis

Submitted in partial fulfilment of the requirements
For the Degree of

DOCTOR OF PHILOSOPHY

By

Ashutosh Kumar Singh

DEPARTMENT OF MECHANICAL ENGINEERING
INDIAN INSTITUTE OF TECHNOLOGY GUWAHATI
GUWAHATI – 781039, ASSAM, INDIA
MAY-2023

Dedicated to my parents

Jagannath Singh, and Ramki Devi

Whose endless faith and blessings always inspired me to move forward.

Declarations

I certify that the work compiled in this thesis results from research work performed by myself under the supervision of **Prof. Niranjan Sahoo and Dr. Dushyant Singh**.

Any part of this work has not been submitted for the award of any degree, diploma, fellowship, or equivalent to any institution or university.

Ashutosh Kumar Singh

Ashutosh Kumar Singh

Registration No. 186103109

Department of Mechanical Engineering

Indian Institute of Technology Guwahati.

Certificate

This is to certify that the thesis entitled "**Film Cooling Analysis of Injection Configurations For Afterburner Aero-Engine Applications"** being submitted to the Department of Mechanical Engineering, Indian Institute of Technology Guwahati, India by **Ashutosh Kumar Singh (Registration No. 186103109)** for the award of Doctor of Philosophy, has carried out his research work under my supervision and the results embodied in the thesis has not been submitted to any other University or Institute for the award of any degree.

Dushyant Singh

Dr. Dushyant Singh

(Co-Supervisor)
Associate Professor
Department of Mechanical Engineering
National Institute of Technology Manipur.
Imphal-795004, Manipur, India
Date: 10/05/2023

Prof. Niranjan Sahoo

(Supervisor)
Professor
Department of Mechanical Engineering
Indian Institute of Technology Guwahati.
Guwahati-781039, Assam, India
Date:10/05/2023

Acknowledgment

First of all, I would like to express thanks to **Almighty God**, **my parents,** and my **teachers** for their benevolent shower of grace. I would like to express my deep and sincere gratitude to my research Supervisor, **Prof. Niranjan Sahoo**, Department of Mechanical Engineering, IIT Guwahati, and Co-Supervisor **Dr. Dushyant Singh**, Department of Mechanical Engineering, NIT Manipur for giving me the opportunity to do the project and providing the best possible guidance. Their dynamism, vision, sincerity, and motivation have deeply inspired me. It was a great privilege and honour to work under their guidance.

I would like to express my sincere thanks to the doctoral committee members, **Prof. Dipankar Narayan Basu, Prof. Amaresh Dalal**, and **Prof. Raghvendra Gupta**, IIT Guwahati. I am also thankful to **Dr**. **Kuldeep Singh**, Senior CFD Research Fellow, University of Nottingham, United Kingdom, for his valuable, discussion and suggestions on film cooling.

My sincere acknowledgment goes to the former Head of the Mechanical Engineering Department, IIT Guwahati, **Prof. Santosha K. Dwivedy** for his support during the initial days of MTech-PhD. I am also thankful to the faculty and staff of the Mechanical Engineering Department, for their enthusiastic support in day-to-day activities and official works at IIT Guwahati.

I am also grateful to the Ministry of Education, Government of India for providing me the opportunity to pursue a Ph.D. under the **“MHRD Trainee Teacher Scheme.”**

I would like to also thank my friends and colleagues from IIT Guwahati, friends, **Shashikant Roy**, **Arshad Khan**, and **Abhishek Punia** for their immense support throughout. I am also grateful to the research scholars of the thermal fluid experimentation lab of NIT Manipur, **Mr. Chankyraj Khangembam, Raj Gaurav, Ashutosh Narayan Singh, Ghulam Rabbani, Sumit Kumar, Hitesh Sharma, and W. Maniketan** for their contributions. I would also like to thank all of my friends **Krivi Singh**, including my brother **Ayush Kumar Singh** for their great support. Without this outcome would not have been possible.

Ashutosh Kumar Singh
Indian Institute of Technology Guwahati, Assam
May 2023

Abstract

There is a significant need for thrust augmentation in aircraft for several specific operations, such as combat or take-off from short runways. The additional thrust requirement is achieved by burning extra fuel in the afterburner, which further raises the temperature to 2200K. In order to increase thermal efficiency and power output, the turbine entry temperature of modern gas turbine engines has to be increased considerably. Furthermore, the exposed components in the pathway of the exhaust stream experience a very high temperature. Therefore, to maintain the permissible metal temperature for safe operation, the component under such high thermal loads requires a sophisticated cooling technique. “Film cooling” is one of the most adopted to protect the component that is subjected to hot flue gases. In the last few decades, this technique has been used for protecting critical components such as the afterburner of aero engines, gas turbine blades, and vanes from the hot flue gases.

The main objective of the present work is to design an efficient film cooling configuration for aero-engine afterburner applications, with a primary focus on corrugated surfaces. Corrugated surfaces are the most adopted surface configuration for afterburners of aero-engine liners, due to its effectiveness in terms of coolant attachment, high stiffness, and structural rigidity. The scope of the work involves the following: (a) film cooling assessment of cylindrical and laidback fan-shaped holes with reverse injection; (b) study of effect of various injection locations on film cooling performance of a corrugated surface; (c) study of the effect of double-row slot injection locations on film cooling performance of a corrugated surface; (d) study of the effect of reverse injection on film cooling and thermal stress of a corrugated surface. The methodological approach involves experimental study as well as numerical. A due focus has been given to the design of components of the experimental test facility along with calibration techniques. Experiments were mainly performed for corrugated surfaces with different injection locations and cooling hole configurations. Experimental investigations have been carried out for a limited temperature range and used to validate the numerical models. However, a sophisticated numerical model is employed for the reverse injection study on flat surfaces.

To develop an effective injection configuration, as an initial step the numerical studies on a flat plate are conducted using forward and reverse configurations. In the case of reverse/backward injection, the secondary flow is injected in such a way that its axial velocity component is in the direction opposite to the mainstream flow. The study is carried out for a blowing ratio ($M = 1$), density ratio ($DR = 2.42$), and injection angle ($\alpha = 35^{o}$). The formation of a counter-rotating vortex pair (CRVP) is one of the major issues in film cooling. This study revealed that the CRVP found in the case of the forward cylindrical hole which promotes coolant jet "lift-off" is completely mitigated in the case of the reverse-shaped hole. The coolant coverage for reverse cylindrical and reverse-shaped holes is uniform and higher. The reverse-shaped hole shows promising results among investigated configurations. The lateral averaged film cooling effectiveness of the reverse-shaped hole is 1.16–1.42 times higher as compared to the forward-shaped holes. The improvement in the lateral averaged film cooling effectiveness of reverse cylindrical hole (RCH) injection over forward cylindrical hole (FCH) injection is 1.33–2 times. After developing the numerical model for flat plates using reverse configurations, the focus has been given to the corrugated surface. The numerical studies have been to identify the suitable injection locations and amplitude to wavelength ratio for film cooling performance on corrugation. First of all, the effort has been done by using single injection locations, on a corrugated liner to identify suitable injection locations. The effects of various operating parameters such as blowing ratio, density ratio, and operating pressure on film cooling effectiveness are reported. Experimental studies are conducted on the corrugated surface to validate the computational methodology. The present study reveals that the film cooling on the corrugated surface is strongly influenced by the secondary stream injection locations and corrugation amplitude to wave-length ratio. This study also shows that the film cooling behaviour on a corrugated surface is inherently different from that of a flat surface; the effectiveness plots show improvements even at a higher blowing ratio. Thereafter, focus has been given to double-row secondary injection locations on a corrugated surface. Various double-row injection location combinations have been used. Based on the parametric studies 15 to 19% improvements have been reported in film cooling performance. Moreover, the increase of amplitude to wavelength ratio is reported to be a detrimental effect and decreases the film cooling effectiveness. After identifying the suitable injection location, experimental and numerical studies have been conducted using forward and reverse injection configurations on a corrugated surface. This study includes three rows of cylindrical holes per wavelength at 45^{o}, and the outcome of the parametric study demonstrates that reverse holes are more effective as compared to the forward hole. Apart from that coolant coverage is also uniform for reverse injection, as compared to forward injection. Moreover, thermal stress is also reduced in the case of reverse injection. A maximum improvement of 21% in maximum Von-mises stress has been reported for reverse injection case.

Table of Content

List of Figures

List of Tables

Nomenclature

A_{ij}	strain rate, s^{-1}
A_c	the cross-sectional area of the coolant hole, m^2
C_p	specific heat, J/kg-K
D	diameter of the cylindrical hole, m
D_{ms}	characteristic length of the mainstream inlet, m
DR	density ratio, $(\rho)_{sec} / (\rho)_{ms}$
i,j,k	unit vectors in X, Y, and Z directions respectively.
K_p	thermal conductivity of nickel superalloy (IN738LC), W/m-K
K_{th}	thermal conductivity of air, W/m-K
Ks	thermal conductivity of solid, W/m-K
k	turbulent kinetic energy, m2 /s2
L	length of hole, m
L_0, L_{25}, L_{50}, and L_{75}	various slot injection locations
L_{ref}	reference length, m
M	blowing ratio, $(\rho U)_{sec} / (\rho U)_{ms}$
M_a	Mach number
$m_{theoretical}$	theoretical mass flow rate through coolant hole, kg/s
P	pressure, N/m^2
P_a	ambient pressure, N/m^2
P_{rt}	turbulent Prandtl number
P_r	Prandtl number
P_{ra}	pressure ratio, P/P_a
R	gas constant, J/kg-K
R_1, R_2, R_3	rows of cooling holes
Re_{ms}	mainstream Reynolds number for flat surface, $\frac{\rho U D_{ms}}{\mu}$
Re_λ	mainstream Reynolds number for corrugated surface, $\frac{\rho_{ms} U_{ms} \lambda}{\mu}$
T	local temperature, K
T_{ad}	adiabatic wall temperature, K
T_{wx}	wall temperature, K
T_{sec}	coolant/secondary stream temperature, K
u	mean flow velocity, m/s
u_τ	friction/shear velocity, $\sqrt{\tau/\rho}$
U	velocity magnitude, m/s
VR	velocity ratio, (U_{sec}/U_{ms})

w	width of the slot, m
X	streamwise/ along mainstream flow direction, m
Y	direction normal to teat plate, m
ΔX^+, ΔY^+, ΔZ^+	non-dimensional grid spacing ($\frac{\Delta x u_\tau}{\upsilon}$,$\frac{\Delta x u_\tau}{\upsilon}$ and $\frac{\Delta x u_\tau}{\upsilon}$respectively)
Z	spanwise/lateral direction of test plate,m
Greek Symbols	
α	angle of inclination with mainstream,
β	angle of expansion in stream wise
γ	angle of expansion in span wise
δ_{ij}	kronecker delta
Δ	cut-off width, m
ε	dissipation rate of turbulent kinetic energy, m^2/s^3
λ	wavelength of corrugated plate, m
η	effectiveness, $\eta = \frac{T_{ms}-T_w}{T_{ms}-T_{sec}}$
λ	wavelength of corrugated plate, m
ρ	density of air, kg/m^3
θ	non-dimensional temperature, theta $\theta = \frac{T_{ms}-T}{T_{ms}-T_{Sec}}$
μ	dynamic viscosity, Pa-s
ω	specific dissipation rate of turbulence, m^2/s^3
Subscripts	
ad	adiabatic
ms	mainstream
min	minimum
max	maximum
sec.	secondary
SGS	subgrid scale
abm.	ambient
ref	reference
w_x	corrugated wall

Acronyms	
CFD	computational fluid dynamics
CFL	Courant–Friedrichs–Lewy number
CRVP	counter-rotating vortex pair.
FCH	forward cylindrical hole
FSH	forward shaped hole
LES	large eddy simulations
PIV	particle image velocimetry
RANS	Reynolds averaged Navier Stokes equations
RCH	reverse cylindrical hole
RSH	reverse shaped hole
SGS	subgrid scale
FR	forward injection
RE	reverse injection

CHAPTER1: INTRODUCTION

1.1 Background and Motivation

Over the past few decades, the aviation and power generation industry has endeavoured to improve the performance of gas turbines. The modern gas turbine engine's turbine entry temperature (TET) has significantly increased over the years to improve thermal efficiency and power output. The components of gas turbine aero-engine in the pathways of hot gases are exposed to very high temperatures. Apart from that, the requirement of additional thrust for specific situations like combat or take-off from small runways is fulfilled by burning additional fuel in the after-burner section. Afterburner is an additional component in the fighter planes situated downstream of the turbine exit. The hot flue gases enter this section after expending in the turbine. Because of the burning of additional fuel inside the afterburner chamber, the temperature of this section increases further to 2200K. Despite the advancement in material science, no material can withstand such a high temperature to date. Therefore, to maintain the permissible metal temperature for safe operation, the component under such high thermal loads requires a sophisticated cooling technique. “Film cooling” is one of the most adopted to protect the component which is subjected to hot flue gases. In the last few decades, this technique has been used for protecting critical components such as the afterburner of aero engines, gas turbine blades, and vanes from the hot flue gases.

1.2 Cooling Techniques

The gas turbine blades, afterburner, and combustor liners are essential components of modern aero engines and are placed in the exhaust stream of hot flue gases. Therefore, the heat transfer to the components also increases with an increase in turbine inlet temperature. The increase in thermal load leads to excessive thermal stress and causes the failure of the components. Thus, the cooling of such components is essential for safe operation

The “film cooling” technique has been used for the last 70 years for protecting critical components such as the afterburner of aero engines, gas turbine blades, and vanes from the hot flue gases [1]. For the cooling of such critical parts, a secondary stream of coolant relatively at a lower temperature is injected from the slot/hole made over the surface of the component that must be cooled, which forms a thin film over the surface as shown in Fig. 1.1. Figure 1.1, it is evident that coolant is allowed to pass through the slot/hole to the externally exposed surface. Since the secondary stream is at a lower temperature than hot flue gas, it acts as a blanket and thus heat transfer into the component reduces [2,3]. The efficient applications of film cooling can reduce the temperature of the blade up to 1000 K, which is under the permissible temperature limit for safe operations. As the compressed air is extracted from the compressor is ejected through the hole for cooling so for better power output film cooling effectiveness needs to be optimized. Although film cooling technology has been used over the decades it needs advancement. The application of film cooling is justified when the proximate fluid (hot flue gas) temperature is very high or it chemically reacts with the material of the component.

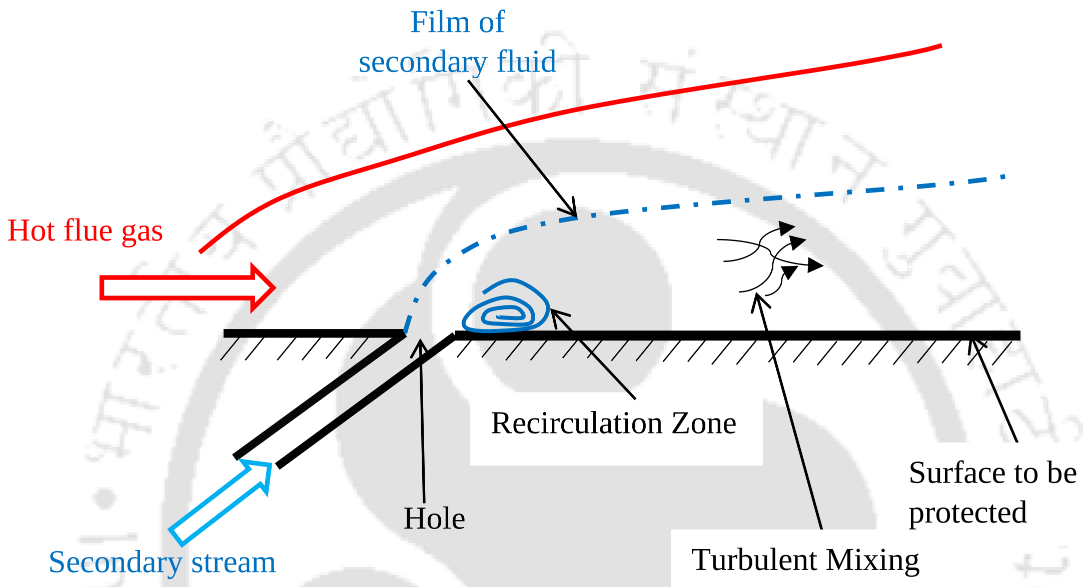

Fig.1.1: Schematics of film cooling over the flat surface.

1.3 Applications of Film Cooling

Film cooling is one of the most used techniques, to protect the components from overheating and excessive thermal stresses. This technique is effectively used in many applications such as gas turbine blades, afterburner afterburners, aero-engine liners, and rocket nozzles. Figure 1.2 shows the cooling of gas turbine blades, where the secondary stream cold air is discharged through discrete holes in the inner and outer end walls (platforms) of blade passage [4]. After leaving the surface holes, the coolant air forms a protective layer between the hot mainstream gas and the surface that is to be protected.

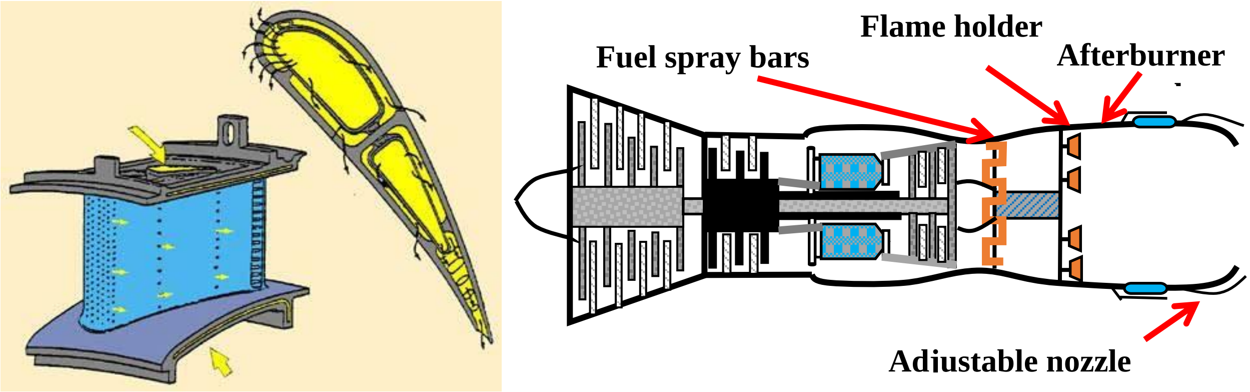

(a) (b)

Fi.1.2: Film cooling of (a) gas Turbine blade [4]; (b) afterburner.

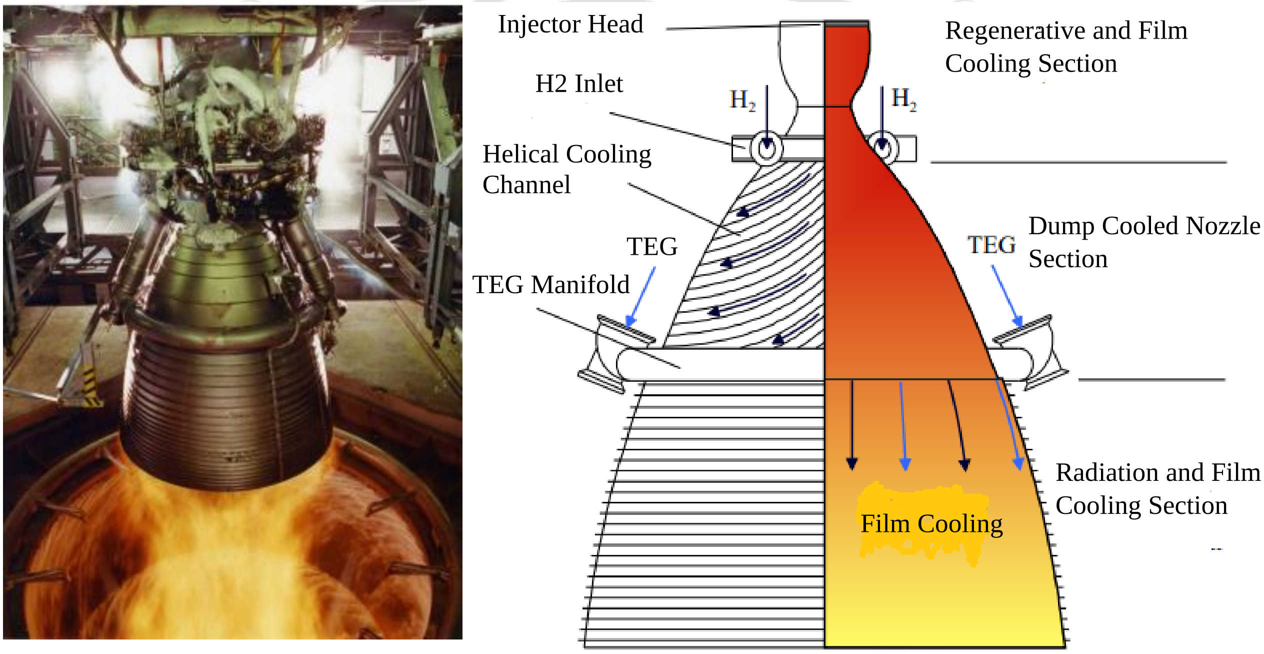

Fig.1.3: Cooling design of combustion chamber and rocket nozzle; (a) exhaust flow from vulcain engine; (b) coolant flow configuration, [5].

The enormous temperature difference between the hot combustion gases and the chamber walls leads to excessive heat flux and thermal load in the combustion chamber and rocket nozzles. The most common cooling methods for rocket nozzle and combustion liner are regenerative cooling, radiation cooling, and film cooling, Suslov et al. [5].

In scramjet combustors and rocket nozzles, the mainstream flow, and often the film coolant stream cooling itself, are supersonic [6,7]. Because of its simple design and ability to lower skin friction, supersonic film cooling in scramjet combustors is considered one of the most effective supplementary cooling techniques for regenerative cooling [8,9]. However, for hypersonic scramjet engines, the air's total temperature is too high to be used as the coolant, so the fuel becomes the only available coolant source. For the thermal protection of such components in the way of supersonic high enthalpy gases, film cooling is generally used in association with radiation or regenerative cooling techniques, as shown in Fig.1.3. The Liquid film cooling is accomplished by interposing a thin layer of liquid film between the surface to be protected and the hot gas. The liquid is introduced directly into the thrust chamber through slots or surface holes and directed along the walls (Fig. 1.3). The coolant liquid fuel forms thin layers and mix-up and fires with hot combustion gases.

1.4 Recent Trends in Film Cooling

Air Film cooling is a mature technology for the cooling of turbine blades**.** Before 1950 uncooled turbine blades were used. With the increase in the demand for high specific thrust and highly efficient gas turbine blades, (Fig. 1.4) the convection cooling technique was replaced by air film cooling in the decades of 1960, [1]. Many researchers such as Goldstein et al. [10]; Bogard and Thole [11] Sen [12] have given their significant contribution both experimentally and numerically to explore the film cooling technique. At the initial stage of film cooling development, the focus was the geometry of the slot and cylindrical hole. The development of shape holes viz. fan shape laidback fan-shape and branch holes was one of the major developments. The film cooling study with the slot hole reveals that the flow can be modeled analytically. Due to the lack of computational facilities in the 1960s most of the work was focused on slot holes. Although slot holes were found to be less effective for cooling because of the reduction in mechanical strength of gas turbine vanes in the trailing edge. Because of decreases in mechanical strength, cylindrical holes were investigated as the alternative to the slot hole. They investigated the cylindrical hole for injection angle, and blowing ratio for the film cooling performance. The cylindrical hole is an example of a cross-flow jet hence the flow physics of the cross-flow will be utilized to explain the kidney vortices. The counter-rotating vortex pair (CRVP) well known as the kidney vortex is the most common phenomenon of mixing in the cross-flow region. Immediately after entering the cross-flow region the sides of the jet experience intense lateral shear stress directed towards the outer region. In the case of flow with a low-velocity ratio (example: film cooling) the potential core of the jet experiences the combined effect of pressure and shear stress that changes the shape of the circular jet into a counter-rotating vortex (CRVP). The phenomenon of counter-rotating vortex pair tries to uplift the jet by mutual induction which reduces the jet spreading in the lateral directions. The computational fluid dynamics (CFD) approaches are latest and extensively used approach to predict the flow mechanism. In case of film cooling the flow is identified as cross flow and turbulent. The governing equations of flow, heat transfer based on boundary conditions and discretization and modeling of eddies. These are Direct Numerical Simulation (DNS), Large Eddy Simulations (LES) and Reynolds Average Navier Stokes (RANS) turbulent models. The choice of a particular modeling approach depends on the flow pattern, accuracy required and availability of resources.

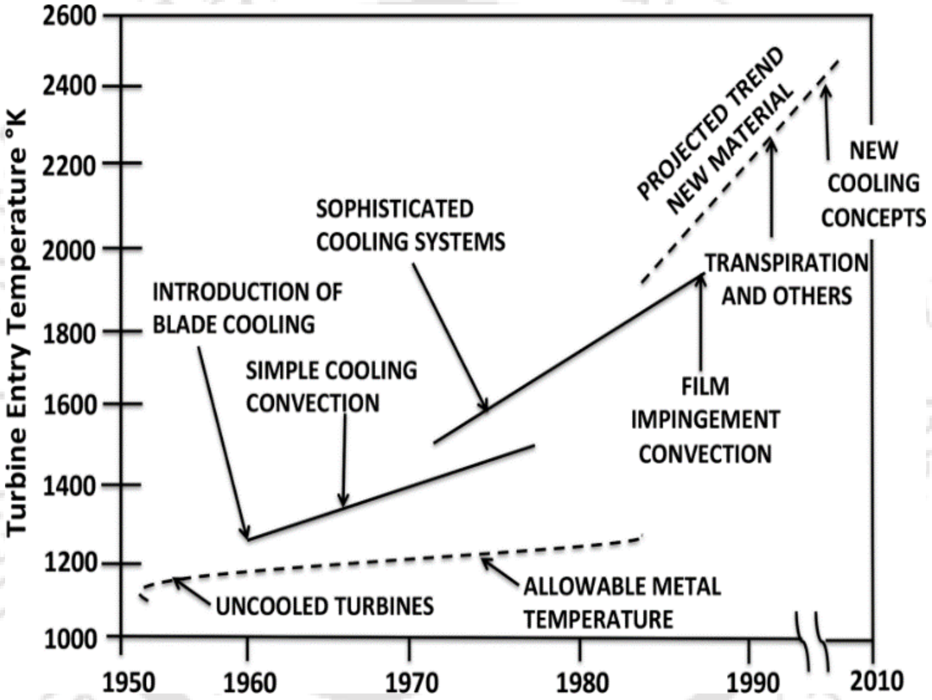

Fig.1.4: Advancement in turbine inlet temperature in recent years, [1].

1.5 Background Definitions

Film cooling is an essential technique to protect the competent from excessive temperature and thermal stresses by injecting a secondary jet of coolant over the surface. The heat flux (q_o) for a surface directly exposed to hot flue gases can be expressed as:

$$q_o = h_o(T_{ms} - T_w) \tag{1.1}$$

where h_o is the heat transfer coefficient, T_{ms} is the hot mainstream temperature, T_w is the wall temperature in the absence of film cooling. Apart from that heat flux (q_f) for the surface protected from the thin layer film cooling can be expressed as:

$$q_f = h_f(T_{ad} - T_w) \tag{1.2}$$

where, h_f is the heat transfer coefficient with film cooling, T_{ad} is the adiabatic wall temperature (wall temperature when there is no heat transfer from the wall).

The ultimate aim of using film cooling is to reduce thermal stress and improve the life span of components. Thus, the heat flux with the application of film cooling is expected to be lower than without film cooling. Hence the heat flux ratio of the two heat fluxes with and without film cooling should be lower than 1.

The film cooling phenomena deal with three different temperature fields such as mainstream temperatures (T_{ms}), Secondary stream temperature (T_{sec}), and T_w is wall temperature. This three-temperature field phenomenon can be well understood with single non-dimensional temperature (θ) which can be expressed as:

$$\theta_w = \frac{T_{ms}-T_w}{T_{ms}-T_{\sec}} \tag{1.3}$$

The continuous mixing of the coolant jet in the downstream direction of the flow increases the temperature of the coolant jet and simultaneously the cooling of the surface reduces. Thus, the perfectly insulated surface performance of film cooling is expressed in terms of adiabatic film cooling effectiveness (η_{ad}) as:

$$\eta_{ad} = \frac{T_{ms}-T_{ad}}{T_{ms}-T_{\sec}} \tag{1.4}$$

The adiabatic effectiveness is a quantitative measure of film cooling performance and the higher the value of film cooling effectiveness better the film cooling. It can be understood well understood as the limiting case of non-dimensional temperature (θ_w) when the surface is perfectly insulated.

The ratio of two heat fluxes with and without film cooling can be expressed in terms of the non-dimensional temperature and adiabatic effectiveness as:

$$\frac{q_f}{q_o} = \frac{h_f(T_{ad}-T_w)}{h_o(T_{ms}-T_w)} = \frac{h_f}{h_o}(1 - \frac{T_{ms}-T_{ad}}{T_{ms}-T_w}) = \frac{h_f}{h_o}(1 - \frac{\eta_{ad}}{\theta_w}) \tag{1.5}$$

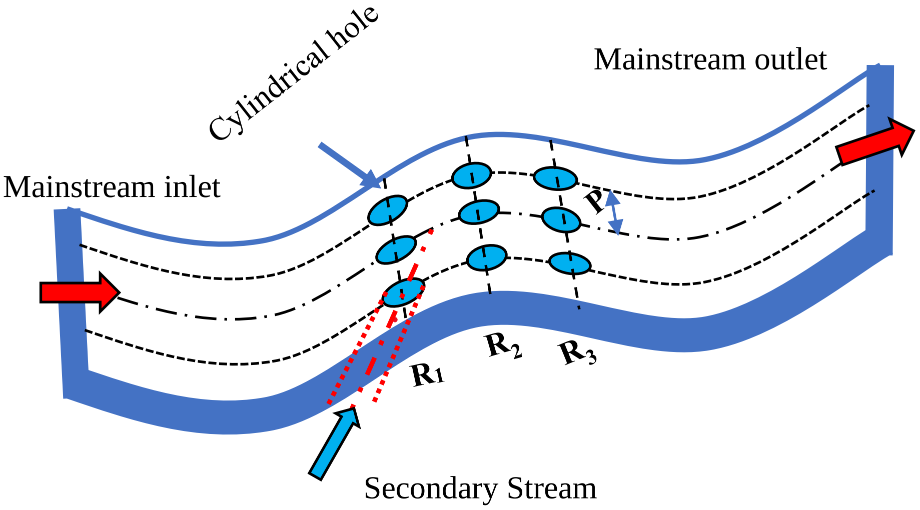

Fig.1.5: Schematic diagram of film cooling over the corrugated surface.

1.6 Factors Affecting the Performance of Film Cooling

Although film cooling is a complex phenomenon however certain parameters are identified that mainly govern the film cooling characteristics. Those parameters are broadly classified as:

(I). Factor related to the geometry of the cooling hole:

1) The shape of the injection hole.
2) Injection angle of the hole.
3) Length to diameter ratio of cooling hole (L/D).
4) The angle of the orientation of the hole.

(II). Factor related to operating parameters:

1) Blowing ratio (M),$\frac{\rho_{\mathrm{sec}}U_{\mathrm{sec}}}{\rho_{ms}U_{ms}}$.
2) Density ratio (DR), $\frac{\rho_{\mathrm{sec}}}{\rho_{ms}}$.
3) Turbulence intensity (I).
4) Reynolds number based on the mainstream ($\mathrm{Re}_{ms} = \frac{\rho U D_{ms}}{\mu}$).

(III). Factor related to Surface Configurations:

1) Flat surface.
2) Curved and Aerofoils surfaces.
3) Corrugated surface.

Film cooling has been investigated both experimentally and numerically since 1950 for various geometric and operating parameters. In the 1960s of film cooling development, film cooling was mainly investigated for the flow attachment and stability under the influence of highly turbulent hot gas flow. All such initial investigations of film cooling asserted that stable film depends on hole geometry, velocity, and density of the secondary stream. There is abundant literature is available on the film hole geometry, angle of injection, and other operating parameters. The expansion of the hole exit is found to decrease the momentum flux ratio and hence decrease the penetration of the secondary fluid into the mainstream. Because of this, jet lift-off and formation of kidney vortices are controlled up to some extent. Moreover, anti-kidney vortices are formed in the expanded holes which minimizes the effect of kidney vortices. However, manufacturing shaped holes in the very thin liners of the combustion chamber or afterburner section is not a feasible solution. The present study is organized in the order of hole geometry, and surface configuration operating parameters.

1.7 Literature Review

1.7.1 Injection Through Slot

The Wieghardt was considered the pioneer to start slot for injection in 1946 for the De-icing of aircraft [13]. In this work, the secondary jet of heated air is injected tangentially into the aircraft wings.

A similar study on the tangential slot was carried out by Seban et al. [14]. Fig.1.6 (a) shows the injection configuration where the slot height is varied from 0.063 inches to 0.25 inches and the results suggest that the effectiveness shows power law dependence over the ratio of distance to the slot height.

The experimental investigations of Hartnett et al. [15] are focused on the slot injection configuration shown in Fig.1.6(b). This study provides a clear picture of velocity and temperature profiles for tangential injection through a single slot.

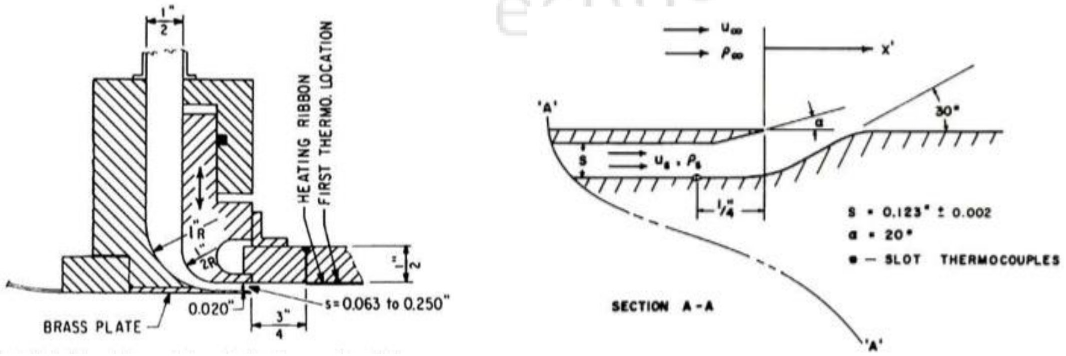

(a) (b)

Fig.1.6: Slot injection film cooling (a) tangential slot, Seban et al.[14]; (b) tangential injection, Hartnett et al. [15].

Papell [16] experimentally investigated the slot jet for various injection angles viz. 45^{o} and 90^{o}.The results show that an increase in angle injection angle promotes the mixing with mainstream and hence a significant drop in the effectiveness can be observed.

Burns and Stollery [17] experimentally studied foreign gas or fuel injection through the tangential slot, as shown in Fig. 1.7. The study heightened the influence of density in the range of (0.14 to 4.17). The authors concluded that at a low-density ratio (DR<1) foreign gas injection has more significance over the effectiveness.

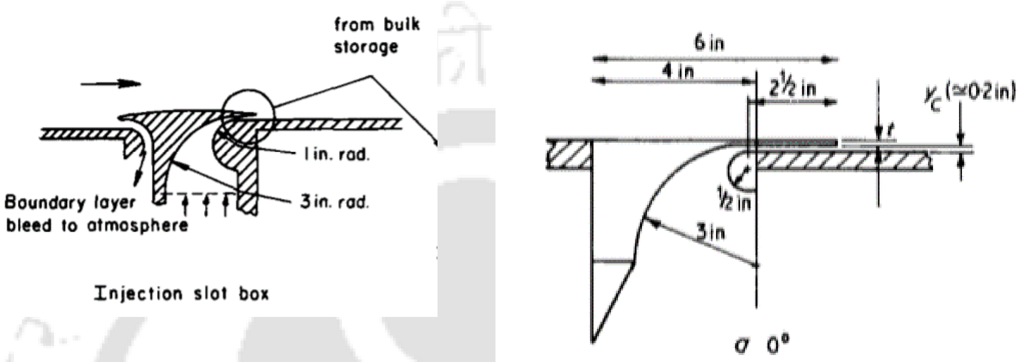

(a) (b)

Fig.1.7: Slot injection configurations (a) Burns and Stollery [17]; (b) Sivasegaram and Whitelaw [18].

Sivasegaram and Whitelaw [18] carried out an experimental study in order to find out the influence of geometrical parameters on the effectiveness. The experiments are performed for the various non-dimensional slot heights (25, 50, and 100) injection angle viz. 0^{o}, 30^{o}, 60^{o} and 90^{o}.They reported that the increases in the flow rate improve the effectiveness. However, an increase in injection angle and slot height reduces the film cooling effectiveness.

The theoretical model of Fitt et al. [19] clearly shows the flow physics of slot jets into the cross-flow region. The proposed model suggested that the slot jet injected into free incompressible flow detached at the rare end of the slot, which further reattached in the downstream (as shown in Fig.1.8), and due to the instability in shear layers in the downstream, the flow became turbulent.

The previous study by Fitt et al. [19] reveals that the increase in the mass flow requires a significant increase in slot size, however, Fitt and Wilmott [20] model overcomes such limitations. In this model, the slot stepped and additional micro rump is provided.

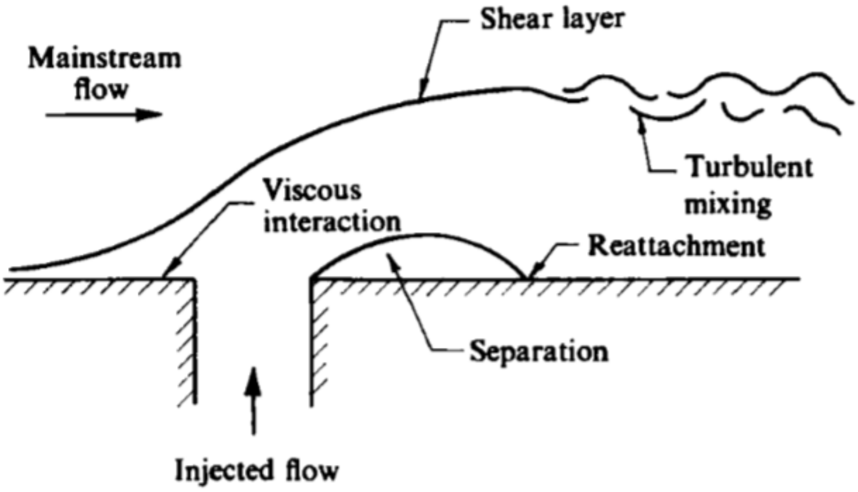

Fig.1.8: Schematic diagram of slot jet interactions in cross flow, Fitt et al. [19].

Hyams and Leylek [21] carried out a numerical assessment of the effect of slot shape. For the closure of the momentum equation, the typical k-ε, turbulence model with generalized wall functions was employed. Four different slot geometries an inclined slot, an inclined slot with inlet shaping, an inclined slot with exit shaping, and an inclined slot with inlet and exit shaping were studied. Additionally, they noted the significant influence of entrance and exit shaping on film cooling. The exit shaping shows better performances compared to the inlet for reducing the turbulence effects.

Jia et al. [22] Conducted an experimental and numerical investigation on the film cooling performance of slot injection. The numerical study is carried out with three different turbulence models Three viz. SST- k-ω, Reynolds stress transport model (RSTM), and v2-f model, for a fixed density ratio of 1.26, blowing ratios ranging from 0.5 to 9.22, and injection 16° to 90°. The study reveals that the SST- k-ω model accurately predicts the results, however, the other two models show similar trends.

Table.1.1: Summary of literature related to injection through slot.

Sr. No.	**Author(s)**	**Year**	**Exp./Num.**	**Slot height**	**Injection Angle**	**Secondary Fluid**	**Operating Parameters**
1.	Wieghardt [13]	1946	Exp.	0.123 inches	Tangential	Air	----------
2.	Seban [14]	1960	Exp.	0.063 to 0.25 inches	Tangential	Air	M = 0.6 - 0.9; DR = 1.14.
3.	Hartnett et al. [15]	1961	Exp.	0.123 inches	Tangential	Air	M = 0-0.28
4.	Papell [16]	2009	Exp.	0.25 inches	45^o,80, 90^o	Air	VR= 0.49-21.83, Ma = 0.2-0.7
5.	Burns and Stollery [17]	1969	Exp.	.0625 inches	Tangential	Helium, Arcton-12 with Air	DR= 0.14 to 4.17, VR = 0.53-4
6.	Sivasegaram and Whitelaw [18]	1969	Exp.	0.074, 0.132, 0.25 and 0.50 inches	30^o,60^o, 90^o	Air	DR =1, M = 2.5,5
7.	Hyams and Leylek [21]	1996	Num.	Slot length to width, 3 to 4.5	35^o	Air	DR =1.5-2, M = 1-2
8.	Jia et al. [22]	2005	Exp./Num.	4mm	16^o, to 90^o	Air	DR =1.26, M = 0.5,9.22

1.7.2 Injection Through Cylindrical Hole

Although injection through slot is an effective arrangement for many applications viz. film cooling, combustion chamber, and afterburner, however, the applications of the slot are limited due to significant reduction in the mechanical strength of the component.

Goldstein et al. [10] the study is considered the first organized study of shape holes. The experiment is conducted for the flat plate film cooling and secondary steam is injected from the circular hole, as shown in Fig. 1.9, at the angle of 35^o and 90^o from the mainstream flow. The result is analyzed for various blowing ratios from 0.5 to 2. There are two important parameters in this experimental study, one is the blowing ratio (M), and the other one is the velocity of the mainstream and secondary streams. As the secondary stream enters the mainstream flow region through the cylindrical hole it retards the mainstream in the upstream location. The retardation of flow leads to the pressure difference which transfers the circular jet in two counter-rotating flows.

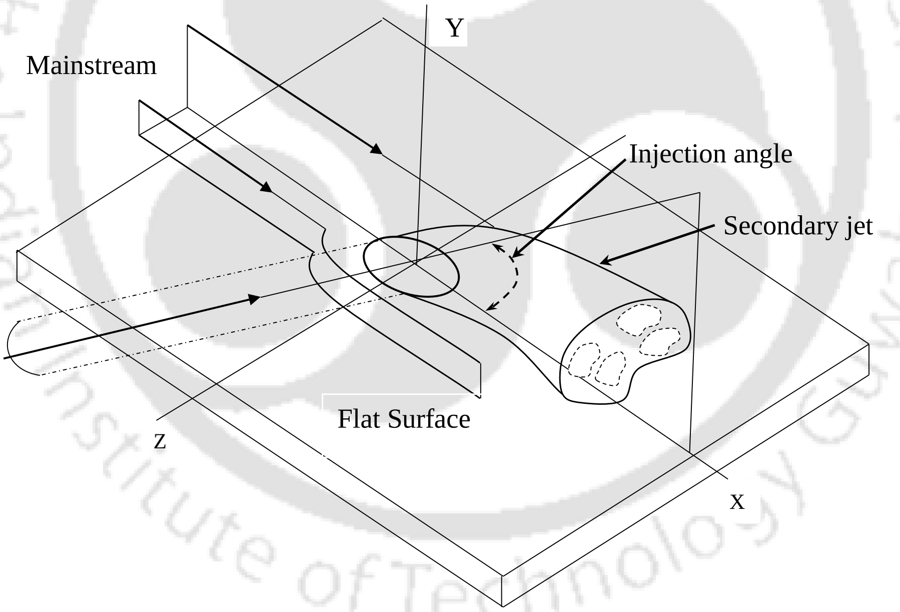

Fig.1.9: Interaction of secondary fluid with mainstream flow, [10].

The jet in a cross-flow is very significant for the practical engineering applications of film cooling, hence some studies have been done [23,24]. The mainstream and secondary interactions in film cooling are analogous to the jet in cross-flow.

Keffer and Baines [25] experimentally concluded that at a low-velocity ratio, the defection of the potential core is obvious however, the secondary flow maintains natural symmetry, and static pressure variations are very small. Due to this the width of the jet increases continuously downstream.

The brief study of Fric and Roshko et al. [26] over the vertical structure for the cross, flow is presented through a schematic diagram in Fig.1.10. They reported four types of vortices near the flow field (i) Jet shear-layer vortices; (ii) Horseshoe vortices; (iii) Counter-rotating vortex pair; and (iv) Wake vortices. The first two of these, the shear-layer vortices and the wake vortices, are unsteady; the other two, i.e., the horseshoe vortices and the vortex pair, are steady. The jet shear-layer vortices were found to be in the initial portion of the jet as instability of the annular shear layer which is separating from the edge of the orifice. The horseshoe vortices are wrapped in the wall near the jet base. The third and most important vortices are counter-rotating vortex pair which is the result of the combined effect of shear and pressure difference. The wake vortices are formed downstream in the wake region.

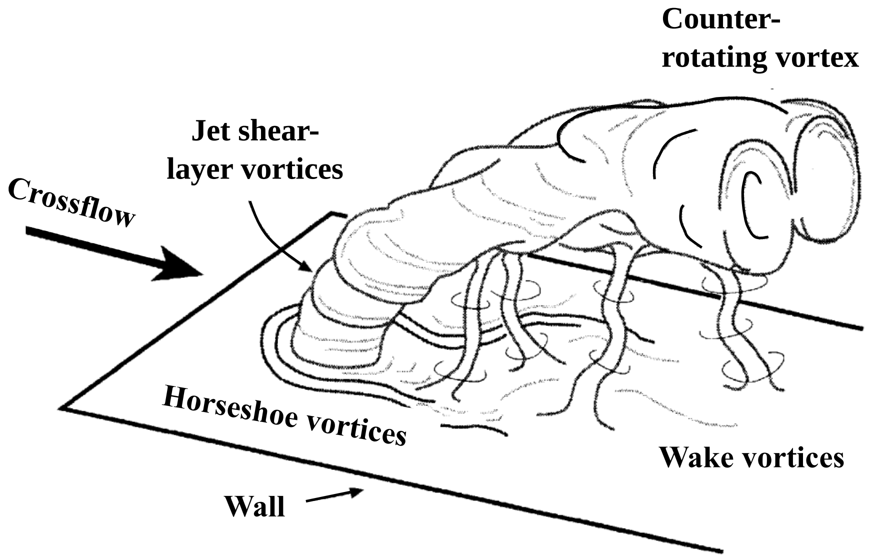

Fig.1.10: Schematic diagram of vortex field in cross flow [26].

The experimental study of Androploish [27] is illustrated in Fig.1.11 (a) and (b). Figure 1.11 clearly shows the flow characterizes of the jet in cross-flow. The cross-flow interactions and developments are reported for low and high-velocity ratios, VR (0.5 and 2). The flow development for the low-velocity ratio is completely different from the high-velocity ratio. The figure shows that at a low-velocity ratio, the tube flow completely bends near the exit, however, in the case of a high-velocity ratio the tube flow is weakly affected near the exit, and penetrates the flow before bending. The wake region the downstream of exit is a complex region where the revere flow can be observed. The reverse flow moves in upstream and is lift-off by the jet fluid and travels downstream.

Kelso et al. [28] conducted an experimental investigation over the jet in cross-flow in order to study the vortex topology. The study is carried out for jet to free-stream velocity ratios, VR (2.0 to 6.0), and Reynolds numbers based on the jet diameter and free-stream velocity, Re_{ms} (440 to 6200). Figure 1.11 (a) and (b) observed that the vortex rolling characteristic in the wake region is strongly influenced by the velocity ratio. Apart from that the unsteady vortex evolution mechanism in the wake region changes with the Reynolds number.

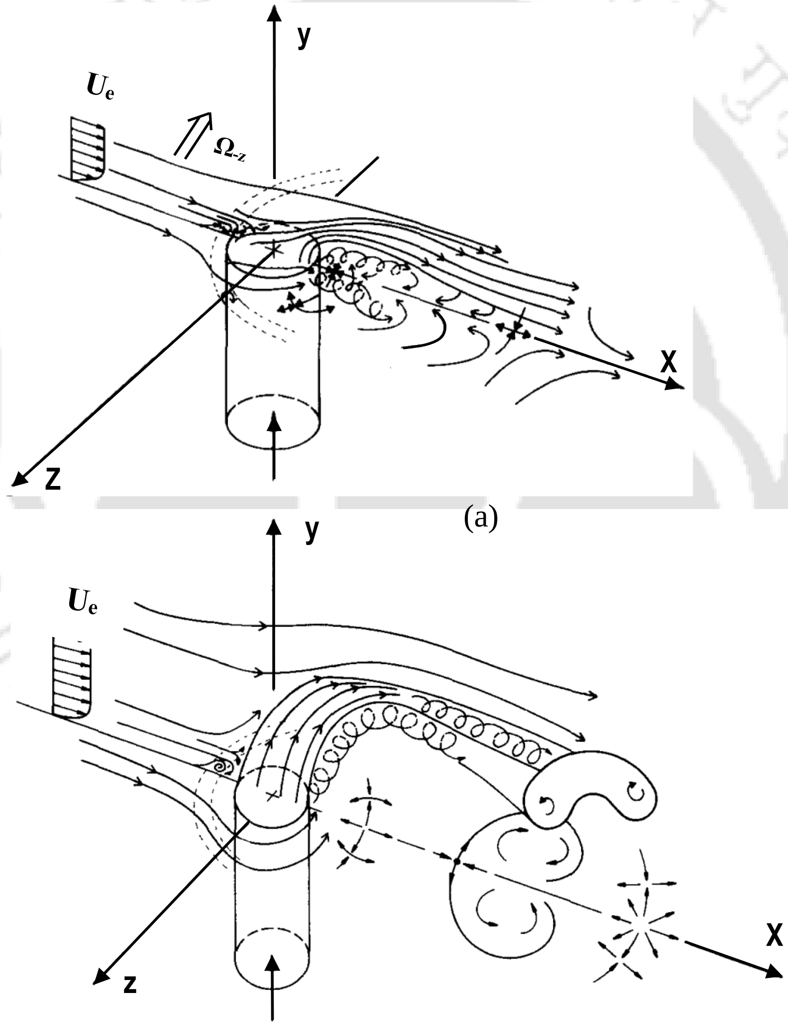

(a)

(b)

Fig.1.11: Schematic diagram of secondary jet interactions in cross flow (a) low Reynolds Number; (b) high Reynolds number [27].

The majority of the cross-flow studies motivated for the film cooling are found to be focused on the experimental and numerous visualization techniques. The recent advancement in computational trends of DNS (Direct Numerical Simulations) and LES (Large Eddy Simulations) are capable to resolve coherent structures, Acharya et al. [29].

Tyagi and Acharya [30] performed a large eddy simulation to quantify the vortex field for the cylindrical holes. The parametric study was carried out for blowing ratio, M (0.5 and 1), and mainstream Reynolds number, Re_{ms} (11100 and 22200). They concluded that the coherent structures evolved in the flow field are dominated by hairpin vortices, and it influences the unsteady wall heat transfer, as shown in Fig. 1.12. Hairpin packets are generally formed in a cluster and small clusters are surrounded by large hairpin. Hairpin vortices evolve and move in further downstream to the wake region. Such vortical structures control the mixing mechanism in the wake region and lead to a temperature hot spot over the cooling surface.

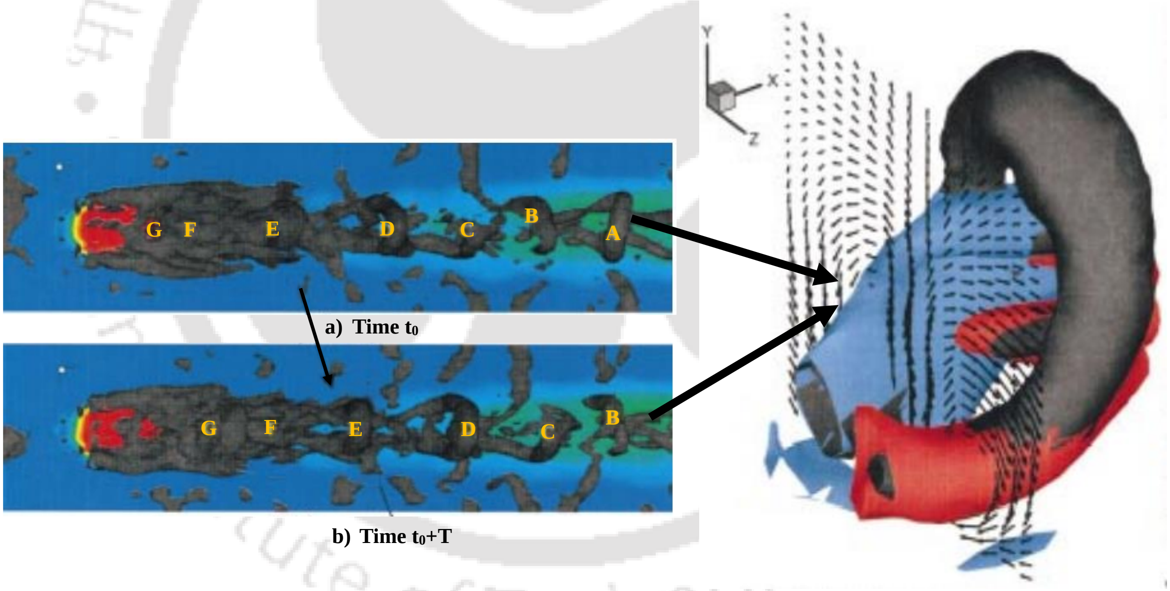

a) Time t_0

b) Time t_0+T

Fig.1.12: Harpin vortices formation in the wake region of film cooling flow [30].

Table. 1.2: Summery of literature related to injection through cylindrical hole.

Sr. No.	Author(s)	Year	Exp./Num.	Hole Arrangement	Injection Angle	Secondary Fluid	Operating Parameters
1.	Goldstien et al. [10]	1968	Exp.	Cylindrical	30^o , 90^o	Air	M = 0.5 to 2
2.	Keffer and Baines al. [25]	1963	Exp.	Cylindrical	90^o	Air	VR = 4, 6 and 8.
3.	Faric and Roshko [26]	1994	Exp.	Cylindrical	90^o	Air	VR = 2, and 10. Re =3800 to 11400
4.	Andropolish [27]	1985	Exp.	Cylindrical	90^o	Air	VR= 0.5, 1and 2
5.	Kelso et al. [28]	1995	Exp.	Cylindrical	----	Air	VR = 2, and 6. Re = 440 to 6200
6.	Tyagi and Acharya [30]	2003	Exp.	Cylindrical	30^o,60^o,90^o		Re =11000 to 22200 , M = 0.5 to 1

1.7.3 Injection Through Shaped Hole

Goldstein et al. [31] are among the first to suggest the use of shaped holes for improved film cooling performance. They reported that the use of an initially round cross-section which diffused/widened to 10^{o} on each side significantly improves the film cooling downstream of the hole. Apart from that the coolant spread in the lateral direction also improved.

The coolant injection through a cylindrical hole forms a pair of vortices downstream of the hole. These vortices have a specific sense of rotation and are often referred to as kidney vortices that promote jet lift-off and thus the film cooling effectiveness degraded; Haven et al. [6]. Haven et al. [32] carried out an experimental investigation in order to examine the impact of hole geometry on the near-field flow characteristics. The cylindrical, rectangular, elliptical, and square shapes of the same cross-sectional area are considered. Figure 1.13 reveals that the formation of kidney, anti-kidney, and jet lift-off is strongly influenced by hole shape. For the low aspect ratio holes, with reduced separation between the end wall vortices jet lift-off tendency is higher while it is lower for high aspect ratio holes. However, in the rectangular and elliptical holes, the kidney vortices are accompanied by an upper deck having an opposite sense of rotation called anti-kidney pairs which counters the resultant effect of kidney vortices.

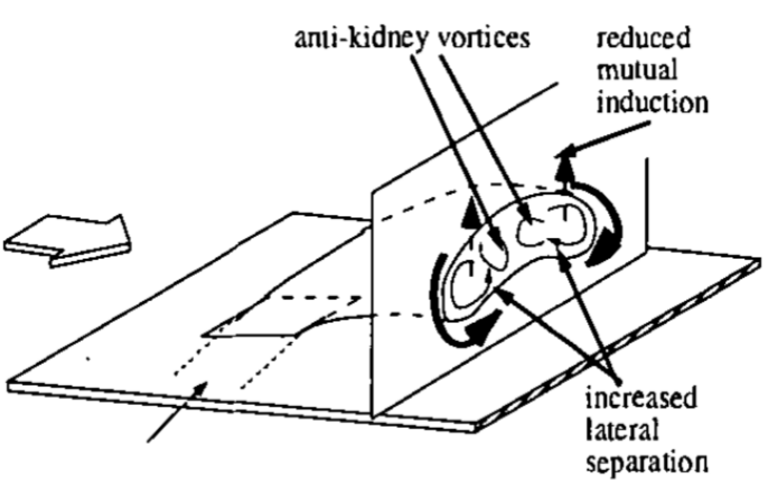

Fig.1.13: Schematic diagram of rectangular slot jet interactions in cross flow, [32].

The experimental study of Thole et al. [33] is focused on the flow measurement for shaped holes. Three-hole shapes include the round, laterally expanded (Fan shaped), and forward-lateral expanded hole (Laidback fan-shaped), as shown in Fig.1.14. The study reveals that the flow field of both the expanded holes is similar in terms of velocity gradient, however, the jet penetration and velocity are lower as compared to round holes. The reduced jet penetration and velocity gradient at exit improve the film cooling performance.

Grisch et al. [34] experimentally investigated the heat transfer coefficient downstream of three different hole configurations including standard cylindrical, two-shaped holes with expanded exits (i.e., Fan-shaped and Laidback fan-shaped). The test is conducted for blowing ratio, M (0.25 to 1.75), density ratio, DR (1.85), and Mack number, M_a (0.6). They highlighted that most of the previous studies on film cooling assumed that convection heat transfer coefficients remain unchanged by coolant injection, however, this fact is valid in the region downstream of the injection hole. The results show that the heat transfer coefficient for shaped holes is lower as compared to cylindrical holes.

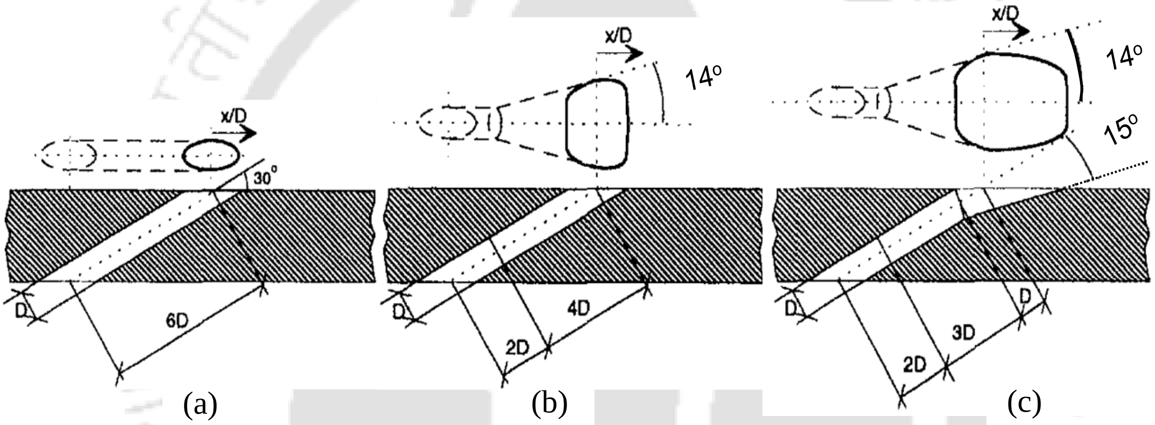

(a) (b) (c)

Fig.1.14: Schematic diagram of slot jet interactions in cross flow (a) cylindrical; (b) fan-shaped; (c) laidback fan-shaped, [33].

Saumweber et al. [35] Numerically investigated the impact of turbulence intensity on film cooling performance. This study was conducted for the three-hole configurations cylindrical, fan shape (expanded in spanwise) and laidback fan shape (expanded in both spanwise and streamwise) as shown in Fig.1.14, at density ratio 0.59, blowing ratio (0.5-2.5) and turbulence intensity (3.6-11%). The results reveal that at the lower blowing ratio, an increase in turbulence intensity results in a significant change in the film cooling effectiveness. The film cooling effectiveness is maximum for shape holes and minimum for cylindrical holes. For the shape hole due to an increase in the turbulence intensity, the mixing of the secondary jet intensified however it not result in an adverse effect in the streamwise direction even at a high blowing ratio.

Several numerical studies over the shaped holes revealed that coolant flow inside the shaped holes is very complex and highly sensitive to the flow supply of the hole; Gilbert et al. [36] and Kohli and Bogard [37].

The experimental study of Gritsch et al. [38] is focused on the discharge coefficient measurement for the expanded exits shaped holes. The results demonstrate that the discharge coefficient strongly depends on the flow configurations (both inside and outside the hole), Mach number, and pressure ratio. For similar flow conditions, the discharge coefficients of expanded exit-shaped holes are higher than the cylindrical holes.

Shaped holes and compound angle holes were studied by Bell et al. [39]. Five-hole geometries were considered viz.(i) cylindrical round simple angle holes; (ii) laterally diffused simple angle holes; (iii) forward diffused compound angle holes; (iv) forward diffused compound angle holes (iv) laterally diffused compound angle holes. For simple hole geometry, the holes are simply inclined with flow direction, however, compound angle holes were given some inclination in the lateral direction also. In comparison to cylindrical holes, all shapes of holes are found to distribute cooling film more effectively. Laterally diffused compound angle holes and forward diffused compound angles are reported to have the best performance for film cooling.

Another remarkable advancement in hole shaping is slot converging slot or console [40]. The experimental and numerical study of Liu et al. [41] is focused on converging slot holes, the converging slot holes show remarkable improvements in coolant coverage over the conventional cylindrical holes. The console holes are generally used for the combustor liner to protect from hot combustion gases. The experimental and numerical study of Sarigosan et al. [42] is focused on the aerodynamic performance of console holes. The performance of the console hole is compared with the typical cylindrical and fan-shaped holes. The comparative study shows that with the promising performance of the console hole, there is a significant improvement in thermal performance over the other holes.

Table.1.3: Summery of literature related to injection through shaped hole.

Sr. No.	**Author(s)**	**Year**	**Exp./Num.**	**Hole Arrangement**	**Injection Angle**	**Secondary Fluid**	**Operating Parameters**
1.	Goldstein et al. [31]	1974	Exp.	Cylindrical 10^o expanded on exit	35^o	Air	M = 0.53-2.02
2.	Haven et al. [32]	1997	Exp.	Cylindrical, Fan-shaped and Laidback fan-shaped	30^o	Air	DR =1.1, Re = 1×10^5
3.	Thole et al. [33]	1961	Exp.	Cylindrical, Fan-shaped and Laidback fan-shaped	30^o	Air	M =1, DR =1, Re = 0.52×10^5
4.	Gristch et al. [34]	2003	Exp.	Cylindrical, Fan-shaped and Laidback fan-shaped	30^o	Air	M = 0.25-1.75 DR= 1.85, Tu = 2% , Re = 2.5×10^5
5.	Saumweber et al. [35]	2003	Exp.	Cylindrical, Fan-shaped and Laidback fan-shaped	30^o	Air	M =0.5-2, DR =0.59 and Tu= 3.6-11%
6.	Gilbert et al. [36]	1997	Exp./ Num.	Cylindrical, Fan-shaped and Laidback fan-shaped	30^o	Air	1< DR <2, Ma = (0-6)
7.	Liu et al. [41]	2015	Num.	Laidback fan-shaped	30^o	Air	M = 0.5,1,1.5 and 2 Tu = 0.9-13%
8.	Sargison et al. [42]	2002	Exp.	Console, Cylindrical, and Fan-shaped	35^o	Air	DR=1, I =1.1

1.7.4 Effect of Injection Angle

Eriksen and Goldstein [43] studied the flat plate film cooling characteristics of a single cylindrical hole at an injection angle of 35°and 90°. They observed that the heat transfer coefficient downstream for normal injection is higher as compared to the 35° injection. The large difference in heat transfer coefficient between 90° and 35°. The injection is mainly due to the different flow patterns and jet interactions. For the normal injection, the streamwise velocity component is zero, and the jet injection is at 35°, there is one stream-wise velocity. Therefore, the normal interactions result in a higher turbulence level downstream and hence a higher transfer coefficient compared to 35° injection.

Forster and Lampard [44] study is mainly focused on the injection angle, boundary layer, and hole spacing. The study is carried out for 35°, 55°, and 90° injection angles at blowing ratios 0.5 and 1.4. It is observed that at a low blowing ratio, the small injection angles result in higher lateral average effectiveness injection angles. However, at a high blowing ratio the boundary layer thickness in the upstream increases with injection angles which offers greater trajectory to the flow and results in higher lateral average effectiveness.

Kohli and Bogard [45] carried out an experimental study in order to compare the film cooling characteristics of a row of discrete holes at injection, 55°, and single round holes at 35°. This study reveals that at a low momentum flux ratio, the reduction in film cooling effectiveness with the injection is relatively lower, as compared to high momentum flux.

Yuen and Martinez-Botas [46] experimentally studied the impact of the angle of inclination of the cylindrical hole on flat plate film cooling for different angles of inclination 30°, 60°, and 90°. The Reynolds number based on the hole diameter is taken as 8563, and the blowing ratio varies from (0.33 to 2). They reported the maximum film cooling effectiveness for blowing ratio, and injection angle 30°, which is approximately 20% more than the other angle of inclination.

Yuen and Martinez-Botas [47] Further extending their study for single and multiple row of holes with similar parameters and techniques as previously [46]. They claimed that the best injection angle for a single row of holes is 30°, for optimum performance.

Singh et al. [48] numerically investigated the 2D flat plate film cooling for the cylindrical hole. The angle of inclination varies from 15° to 90°, for the wide range of operating parameters like density ratio (1.1 to 5), mainstream Reynolds no (8104 and 15100), and three-blowing ratios (1 to 3). The results of the numerical study show that the maximum value of film cooling effectiveness was found at a lower injection angle which lies between (15° to 45°). That maximum value is obtained at the combination of other operating parameters.

Table.1.4: Summary of literature related to the effect of inclination angle.

Sr. No.	Author(s)	Year	Exp./Num.	Hole Arrangement	Injection Angle	Secondary Fluid	Operating Parameters
1.	Ericsion et al. [43]	1997	Exp.	Cylindrical		Air	-----------
2.	Forster and Lampard [44]	1980	Exp.	Cylindrical	35^{o},55^{o} and 90^{o}	Freon-12	M = 0.5 – 2.5; DR =2
3.	Kohli and Bogard [45]	1997	Exp.	Cylindrical	35^{o}, and 55^{o}	Air (cryogenic cooled)	M = 0.35 – 1; DR =1.6
4.	Yuen and Martinez-Botas [46]	2003	Exp.	Cylindrical	30^{o},$60^{o}$and 90^{o}	Air	M = 0.33 – 2; Re =8563
5.	Yuen and Martinez-Botas [47]	2005	Exp.	Multiple Rows Cylindrical	30^{o},$60^{o}$and 90^{o}	Air	M = 0.33 – 2; Re =8563
6.	Singh et al. [48]	2015	Exp.	Cylindrical	15^{o}-90^{o}	Air	DR = 1.1-5, M = 1-3, Re = 8104-150000

1.7.5 Reverse Injection Film Cooling

In reverse injection, the configuration is an emerging trend of film cooling in which the secondary fluid is injected in such a way that the axial velocity component is in the direction opposite to mainstream flow, as shown in Fig.1.15.

Shetty et al. [49] numerically investigated the backward injection film cooling on a simplified aerofoil turbine model. The numerical simulations are carried out for blowing ratio, density ratio, and injection angle of 1, 2.42, and 35°. They concluded that film cooling lateral effectiveness for backward injection was significantly higher than for forward injection. It was also reported that film cooling effectiveness obtained from backward injection decreases with an increase in blowing ratio on the pressure side of the vane.

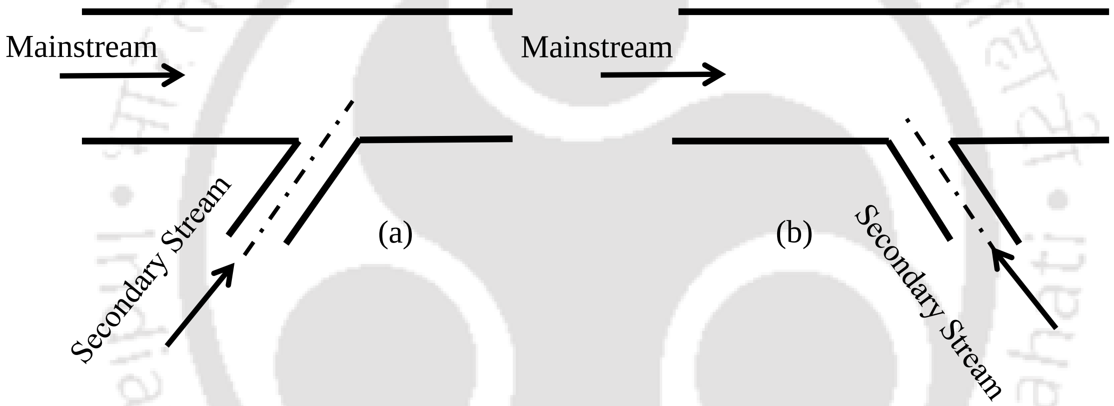

Fig.1.15: Cooling hole arrangement (a) forward injection; (b) reverse injection.

Chen et al. [50] numerically studied the backward injection for three-hole configuration viz. simple cylindrical, fan-shaped, and compound hole for the flat surface. The study was conducted for the blowing ratio (0.3 to 3), turbulence intensity (0.5 to 6%), and density ratio (1 to 2). They reported improved laterally averaged effectiveness for the backward injection of simple cylindrical and compound holes; however, reverse fan-shaped holes gave lower film cooling effectiveness.

Singh et al. [51] experimentally and numerically investigated forward and reverse hole film cooling over the flat plate. The blowing ratio was varied from 0.25 to 5 and the density ratio was kept fixed at 0.91 for all angles of injection (30° to 60°). They found a remarkable increase in film cooling effectiveness at all the blowing ratios. They also concluded that the kidney vortices observed in the case of the forward cooling hole were eliminated with the use of the reverse hole and eventually significant gain in film cooling effectiveness was observed.

Li et al. [52] carried out an experimental and numerical study of the film cooling performance of backward/reverse injection configuration. The study is focused on flat and curved surfaces at an injection angle of 30^o in both forward and reverse injection. The numerical simulations are done with RANS turbulence modeling at the laboratory and the actual operating conditions of the gas turbine. The laboratory condition investigates blowing ratio 1.33, and density ratio 1.33, however, for the actual operating conditions the parameters extended to blowing ratio 2, and density ratio 2.43. The backward injection shows improved performance for flat surfaces at both laboratory and actual operating conditions of gas turbine. The backward injection for aerofoil is effective on the pressure side to some extent.

Park et al. [53] experimentally investigated the backward injection film cooling. The study is performed on a flat surface with two rows of cylindrical holes at an angle of 30^o in both forward and reverse injection. The results are compared for the blowing ratio in the range of 0.5-2 and fixed density ratio 1. The results indicated that the film cooling effectiveness improved with reverse injection. It can also be observed that lateral coolant spreading is much more uniform and better for the reverse injection.

Table.1.5: Summary of literature related to reverse injection.

Sr. No.	**Author(s)**	**Year**	**Exp./Num.**	**Hole Arrangement**	**Injection Angle**	**Secondary Fluid**	**Operating Parameters**
1.	Shetty et al. [49]	2012	Num.	Cylindrical	35^o (Both Forward and Reverse)	Air	M = 0.5, 0.75 and 1 (Pressure side) and M = 1, 1.5 and 2 (Suction side), DR= 2.46
2.	Chen et al. [50]	2014	Exp.	Cylindrical, Fan Shaped and Compound angle	30^o, (Both Forward and Reverse)	Air mixed with N_2, CO_2	M = 0.3-2; DR = 1-2.
3.	Singh et al. [51]	2016	Exp., Num.	Cylindrical	30^o-60, (Both Forward and Reverse)	Air	DR = 0.25-3, DR=0.91 and Re = 3.75×10^5
4.	Li et al. [52]	2011	Exp./Num.	Cylindrical	30^o, (Both Forward and Reverse)	Air	DR = 2.43, M = 2 and 1.3
5.	Park et al. [53]	2016	Exp.	Cylindrical	35^o, (Both Forward and Reverse)	Air	DR= 0.5-2, DR = 1.

1.7.6 Effect of Density Ratio

The density ratio is one of the important operating parameters that govern the flow field, jet interactions in cross-flow regions, and its associated heat transfer.

Goldstein and Eckert [31] presented the first open literature on the effect of density ratio on film cooling. The study was carried out for cylindrical holes inclined at 35^o to the mainstream, and a mass transfer analogy was used for data recording. The experimental study highlighted the mass transfer analogy in order to study the effect of density changes on film cooling performance. The density ratio variations in the range of 0.75 to 4.17, are achieved by mixing a suitable concentration of refrigerants or helium with air. They reported that film cooling effectiveness through cylindrical holes strongly depends on the density ratio, however, the effect is insignificant for porous strips.

The experimental study of Ekkad et al. [54] investigates the effect of variable density ratio on the leading edge of a cylindrical model. This study uses liquid crystal thermography to measure film cooling effectiveness and Nusselt number distribution. The study reveals that higher-density coolant (CO_2) provides lower Nusselt numbers than lower-density coolant (air), at all blowing ratios.

Ammari et al. [55] carried out an experimental study on the effect of density ratio on cylindrical hole film cooling. The study is performed for density ratio (1, 1.38, and 1.52), and blowing ratio (0.5-2). The high-density ratio is obtained by using foreign gas injection. They heightened that normal injection penetrates deeper in the mainstream before turning parallel to the wall, which results from quick mixing with the mainstream. Therefore, 90^o injection results in higher heat transfer coefficients just downstream of the hole, and 35^o injection results far from the hole downstream. For the same blowing ratio, the 35^o injection is highly sensitive to changes in the density ratio, and the increase in density ratio reduces the heat transfer coefficient.

The experimental study of Sinha et al. [56] is focused on the effect of density ratio on film cooling performance. The variations in the density are obtained by injecting cryogenically cooled air. The density ratio independently varied from 1.2 to 2 and adiabatic effectiveness is reported for the bowing ratio and momentum flux. They concluded that at a low blowing ratio coolant jet remains attached to the surface, and the increase in density ratio at fixed ratio momentum flux will increase the blowing ratio and hence increase centreline effectiveness. Apart from that decrease in density ratio and an increase in momentum flux reduces the lateral spreading of the cooling jet, therefore the lateral average effectiveness reduces.

Hass and Rodi [57] carried out an experimental and analytical investigation in order to accurately predict the effect of density differences on film cooling. They extended the two-dimensional boundary layer model of Souchang and Rodi [58] , and the model consists of two components, the injection model to predict the boundary layer and the dispersion model to predict the three-dimensional effectiveness. It is observed that the model accurately predicts the experimental results of the flat plate with an insignificant deviation near the hole, whereas the for the aerofoil a small deviation can be observed.

The velocity and temperature fields of cold jets injected into a hot cross flow were experimentally studied by Rydholm [59]. A flat plate with 30° angle inclination angle holes has been used. The study has been carried out for two density ratios, DR = 1.2 and 1.8. They reported that at the low-density ratio, greater vortices have been found, which further causes inbound velocities. They also reported that high-density jet has high viscosity which causes high-velocity diffusion as well as high-temperature diffusion.

Recently, Eberly and Thole [60] conducted an experimental study in order to study the time-resolved characteristics of film cooling flows. The experiments are conducted for high and density ratios of 1.6 and 1.2 respectively, with cylindrical holes. The coolant Reynolds number for the flow field study varied from 2500 to 7000. The vortex generation and flow fields are recorded with PIV and the results show that low and high density strongly influence the time average and unsteady vortex characteristics. Additionally, the adiabatic effectiveness results reveal that when the jet remains attached to the surface, its spreading increases for the same mass flux ratio at the high-density ratio.

Table.1.6: Summary of literature related to effect of density ratio.

Sr. No.	**Author(s)**	**Year**	**Exp./Num.**	**Hole Shape**	**Injection Angle**	**Secondary Fluid**	**Operating Parameters**
1.	Pedersen et al. [31]	1974	Exp.	Cylindrical (10^o widen at exit)	35^o	Air, and R-12	M = 0.53-2.02
2.	Ekkad et al. [54]	1998	Exp.	Cylindrical	30^o, and 90^o	Air, and CO_2	M = 0.4, 0.8, 1.2, DR = 1, 1.5, Tu = 1, 4.1 and 7.1.
3.	Ammari et al. [55]	1989	Exp.	Cylindrical	35^o, and 90^o	Air, Argon, CO2	DR= 1.38, 1.52; Rems = 3.8×10^3, M = 0.5-2.
4.	Sinha et al. [56]	1991	Exp.	Cylindrical	35^o	Air (cryogenic cooled)	DR= 1.2-2, M = 0.25-1, VR = 0.208-0.625
5.	Hass and Rodi [57]	1992	Exp., Num.	Cylindrical	35^o	Air, Freon	DR =2
6.	Rydholm [59]	1998	Exp.	Cylindrical	30^o	Air	M=0.94-1.34, Tu =1%
6.	Eberly and Thole [60]	2014	Exp.	Cylindrical	30^o, and 35^o	Air (cryogenic cooled)	DR=1.2,1.6, M = 0.25-2, Rems = 2500-7000

1.7.7 Effect of Surface Curvature

Surface curvature is a critical parameter in the design of turbine blades and vanes with convex and concave profiles on the suction and discharge sides, respectively [61]. The effect of curvature on film cooling has been widely discussed by many authors.

The experimental study of Winka et al. [61] demonstrates the surface curvature effects on the film cooling performance of a vane model, as shown in Fig.1.16. The setup was designed to investigate the scaling effect of surface curvature effects using the 2r/d parameters, where r and d indicate the radius of curvature and the hole diameter, respectively.

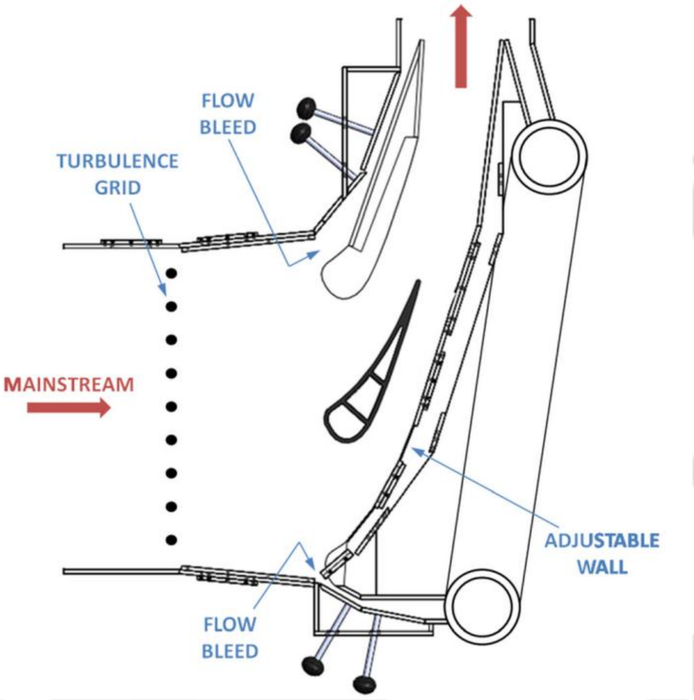

Fig.1.16: Film cooling study on vanes, [61].

The first set of the study was performed with a single row of the hole, placed at different locations on the suction side. However, the second set of experiments was performed using double rows of holes placed at high and other curvature locations respectively. The turbulence intensity of 20% was generated with the help of rods in the upstream direction to the vane, the generator consists of 12 vertical rods of each 18 mm. The exit Reynolds number of mainstream based on chord length was reported as 7×10^5 at a fixed density ratio of 1.2. The outcome of different cases indicates that film cooling and flow attachment are strongly influenced by the surface curvature, particularly in the immediate downstream.

The experimental study of Mayle et al. [62] is focused on the effect of streamline curvature on film cooling effectiveness. The experiments are performed for flat, concave, and convex surfaces. The influence of different curvature profiles on film cooling efficiency is summarized.

The experimental study of Schwarz et al. [63] is focused on the effect of curvature strength on film cooling. The effect of curvature strength and blowing ratio on film cooling performance of a convex surface. The different curvature strength was obtained by changing the ratio of the radius of curvature to the hole diameter. The study was performed for, three different relative strengths of curvatures, density ratios (0.95 and 2.0), and a wide range of blowing ratios (0.3 to 2.7). They reported that at low blowing ratio, the convex surfaces were more effective than flat and concave surfaces, however at high blowing ratios coolant lift-off leads to decreased performance.

A numerical study by Berhe and Patankar [64] addresses the effect of surface curvature on film cooling. Three different surface profiles were used in the study viz. flat, convex, and concave. The numerical study was carried out for the blowing ratios of 0.5, 1.0, and 1.5, injection angle of 35^o at a density ratio of 2.0 and a detailed comparison of the results shows that the cooling effectiveness is greatly influenced by the aerodynamic curvature. For low blowing coefficients, the effectiveness of the convex surface dominates over the flat and concave surfaces. The flow structure in these three planes also has significant differences The flow structure resulted in the formation of strong vortices on the concave surfaces and increased mixing instead, in the presence of convex surfaces, counter-vortices are damped.

Moore et al. [65] experimentally investigated the effect of surface curvature on shaped hole performance. The study was performed for two rows of shaped holes, placed on the suction side of the scaled-up turbine blade. At higher blowing ratios, the low curvature row shows decreased performance. However, at lower blowing ratios, the low curvature row shows a similar performance to the flat plate.

Table.1.7: Summary of literature related to effect of the curve surfaces.

Sr. No.	Author(s)	Year	Exp./Num.	Surface curvature	Injection Angle	Secondary Fluid	Operating Parameters
1.	Winka et al. [61]	2014	Exp.	Convex	45^o	Air	M = 0.3-1.8, DR = 1.2
2.	Mayle et al. [62]	1977	Exp.	Flat, Concave and Convex	----	Air	Ums = 21m/s, Tms=30°C
3.	Schwarz et al. [63]	1990	Exp.	Cylindrical	35^o	Freon-12	M = 0.3-2.7, DR =0.95 and 2,
4.	Berhe and Patankar [64]	1999	Num.	Flat, Concave and Convex	35^o	----	M = 0.5,1 and 1.5, DR=2.0
5.	Morre et al. [65]	2020	Exp.	Cylindrical	30^o	Air	Ums=6.4m/s, Tms=303K

1.7.8 Film Cooling on Wavy/Corrugated Surfaces

Singh et al. [66] numerically investigated the film cooling and heating characteristics of the corrugated surfaces through slot injection. The numerical study carried a wide range of density ratio, (0.2-5), bowing ratio (1-3), injection angle (30^o-90^o), and Reynolds number, (1.5×10^5). They concluded that film cooling effectiveness gradually increases with an increase in the blowing ratio, which is inherently different from flat plate film cooling. Apart from that it also observed that the film cooling and film heating effectiveness are comparable at a density ratio close to unity, however, the difference in the effectiveness became more significant at a higher density ratio. Therefore, film heating can't be considered analogous to film cooling at a high-density ratio.

The experimental and numerical investigation of Singh et al. [67] is focused on designing a suitable injection configurations for corrugated surface film cooling. The detailed numerical study includes a wide range of parameters, Reynolds number (1×103-1.5×10^5), blowing ratio (0.3-8), and density ratio (1.5-5). The four rows of holes are located at L0, L30, L62, and L80, as shown in Fig.1.17, and the effect of injection angle is also considered by varying the injection angle (45-90^o). The study reveals that film cooling effectiveness increases with an increase in the blowing ratio, even at a high blowing ratio. It is also reported that film cooling drastically decreases with an increase in injection angle from 45^o to 90^o.

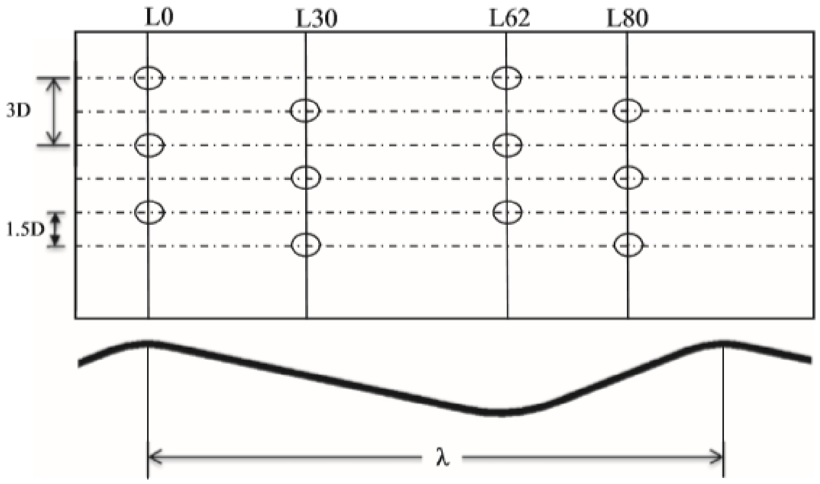

Fig.1.17: Cooling hole arrangements on the corrugated surface, [67].

Funazaki et al. [68] performed an experimental study on the corrugated surface in order to study the film cooling and flow configurations of the corrugated surface. The experimental results show that the jet core decays much faster downstream of the hole, which is mainly due to the strong turbulence and mixing in the valley of the corrugation. Hence a more uniform coolant distribution is observed in the lateral directions.

Singh et al. [69] numerically investigated the effect of gas radiation and thermal barrier coatings (TBC) on the film cooling performance of the corrugated surfaces. The mainstream Mach number is kept at 0.6 and the secondary stream varies from 0.3 to 0.58. They reported that the use of thermal barrier coatings improves the film cooling effectiveness by 50%. It is also observed that the film cooling effectiveness reduces on consideration of the effect of gas radiation.

Lihong et al. [70] numerically investigated the effect of blowing ratio on film cooling effectiveness and heat transfer coefficient of transverse corrugated surfaces. The blowing ratio is varied in the range of 1 to 2.5 for a fixed density ratio (i.e., DR = 2.44). The study reveals that the surface corrugations produce a more non-uniform distribution of coolant relative to the flat surface. Moreover, surface corrugation has also a significant influence on the heat transfer coefficient.

Yong et al. [71] experimentally studied the film cooling on corrugated liners of afterburners with discreet cylindrical holes. The carried out for sinusoidal corrugation and the study suggests that the film cooling effectiveness for the corrugated surface is 10 % as compared to the flat surface, at a blowing ratio of 0.5.

Table.1.8: Summary of literature related to effect of the wavy/corrugated surface.

Sr. No.	**Author(s)**	**Year**	**Exp./Num.**	**Hole Arrangement**	**Injection Angle**	**Secondary Fluid**	**Operating Parameters**
1.	Singh et al. [66]	2016	Num.	Single slot	30^o-90^o	Air	DR= 0.2-5, M = 1-3, Re = 1.5×10^5
2.	Singh et al. [67]	2016	Exp. and Num.	Multiple rows, Cylindrical	45^o-90^o	Air	M = 0.8-3, DR= 1.8-5 and Re = 0.1×10^5-1.5×10^5
3.	Funazaki et al. [68]	2009	Exp. and Num.	Multiple rows, Cylindrical	45^o,90^o	Air	Re = 1.6×10^5, M = 2 and Tu = 4%
4.	Singh et al. [69]	2017	Num.	Multiple rows, Cylindrical	-----	Air	Ma (Mainstream) = 0.6, Ma (Secondary stream) = 0.3-.58, DR = 4.
5.	Lihong et al. [70]	2017	Num.	Discrete cylindrical holes	------	Air	M = 1-2.5, DR= 2.44
6.	Yong et al. [71]	2017	Exp.	Discrete cylindrical holes	-----	Air	Re = 3.4×104,Tms = 700 K, T_{sec} =293.3, M= 0.5-2.5.

1.7.9 LES Studies on Film Cooling

Tyagi and Acharya [30], and Acharya et al. [29] reported that turbulence modeling using RANS is inaccurate, especially in the wake region where the RANS model under-predicts important turbulent flow features and flow spreading in the lateral direction and over-predicts the flow penetration into the vertical direction. Therefore, RANS modeling over-predicts the centreline film cooling and under-predicts the lateral spread of secondary fluid. The size of kidney vortices is also not predicted accurately using RANS modeling.

Guo et al. [72] carried out large eddy simulations study in order to study the effect of blowing ratio and angle of inclination. For the same blowing ratio, it was reported that the counter-rotating vortex shifted to the downstream direction for 30° injection as compared to 90°.

Ke and Wang [73] carried out large eddy simulations over the film cooling characteristics of the cylindrical and fan-shaped hole in order to understand the vortex structure in the cross-flow region. The simulations are performed for two different blowing ratios $M = 0.5$ and $M = 1$ and the results suggest that plenty of hairpin vortices are formed in the case of the fan-shaped hole as compared to the cylindrical hole. Apart from that, time-frequency analysis shows that periodicity in the case of the fan-shaped hole is weaker than the cylindrical hole.

Schiender et al. [74] conducted a numerical study on high-pressure turbine blade trailing edge. The study is carried out by imposing the laminar and turbulent flow conditions in the coolant channel for two different blowing ratios $M = 0.5$ and 1.1. They reported that at a low blowing ratio turbulent coolant flow shows improved film cooling performance over laminar flow, whereas at a high blowing ratio opposite phenomena can be observed.

Shinn and Vanka [75] carried out an LES study on the flat plate film cooling with the micro-ramp vortex generator. The micro ramp vortex generator was found to create a vortex pair having the opposite sense to the main counter-rotating vortex and thus diminishes the effect of jet lift-off. Eventually, film cooling was found to be better than the configuration without the micro ramp.

Renze et al. [76] investigated jets in crossflow using LES. The investigated operating parameters were: density ratio ($DR = 1.53$), blowing ratio ($M = 1$), and free stream Reynolds number ($Re = 4\times10^5$). They simulated the effect of density ratio by using a high-density coolant stream of CO_2 and found that flow attachment and recirculation are more sensitive to the velocity ratio as compared to the density ratio.

Table.1.9: Summary of Literature related LES studies.

Sr. No.	Author	Year	Hole Shape	Injection angles	Surface	Operating parameter's
1.	Tyagi et al. [30]	2003	Cylindrical	$\alpha = 35^0$	flat	M =0.5 and 1 Re_{ms} = 11000
2.	Acharya et al. [29]	2006	Cylindrical	$\alpha = 35^0$	flat	M =0.5 to 2 DR = 2
3.	Gauo et al. [72]	2006	Cylindrical	$\alpha = 30^0$and 90^0	flat	--
4.	Wang et al. [73]	2016	Fan-shaped and Cylindrical	$\alpha = 35^0$	flat	M = 0.5 and 2
5.	Schiender et al. [74]	2010	Slot	$\alpha = 10^0$	aerofoil cut back	M = 0.5 and
6.	Shinn and Vanka [75]	2017	Cylindrical	$\alpha = 20^0$	flat	VR= 1.414
7.	Renge et al. [76]	2008	Cylindrical	$\alpha = 30^0$	flat	VR= 0.1 and 0.28 and $Re_{ms} = 4\times10^5$

1.8 Gaps of Literature

Based on the study of film cooling-related literature it can be concluded that most of the film cooling work is done either for flat surface or aerofoil shape or and impact of different operating parameters viz. blowing ratio, density ratio mainstream Reynolds number and turbulence intensity is evaluated. The most emphasis is given over the hole shape. By changing hole shapes, the film cooling can be improved but there are practical limitations also. Many of the suggested hole shapes are giving good results but are difficult to manufacture. However, some gap from the above study is identified which are as follows:

- Most of the researchers have suggested different types of hole shapes and angles of inclination for operating conditions. The recent study on film cooling through reverse cylindrical holes has shown promising results to mitigate kidney vortices. However, this is at the infantry stage which needs further exploration to understand the flow mechanism and film cooling characteristics.
- From the literature survey, it can be concluded that most of the research on film cooling is carried out for flat surfaces and aerofoils, however, the film cooling study on the corrugated surface is very limited in the literature. The corrugated surfaces are practically used in the afterburner of aero engines because of their high structural rigidity. Hence the film cooling study on the corrugated surface needs further exploration.
- The most of available literature on film cooling is carried out without considering the effect of gas radiation. However, in modern fighter aircraft, the temperature of hot flue gas in the afterburner is typically in the range of 2200K. At such a high temperature the contribution of gas radiation is significant hence a thorough investigation is required over the gas radiation.
- The available literature on film cooling is mainly focused on the film cooling performance parameters such as effectiveness and heat transfer coefficient, however

thermal stresses developed due to uneven cooling is also one of the critical inputs for the designer of afterburner sections which is not given due attention in the literature.

1.9 Objective of the Present Work

The main objective of the present work is to design an efficient film cooling configuration for the afterburner of the aero engine. The experimental study will be conducted on the corrugated surface in order to validate the numerical results. The scope of work includes the following:

- The numerical study (Large Eddy Simulations) for film cooling assessment of cylindrical and laidback fan-shaped holes with reverse injection.
- Experimental and numerical analysis of film cooling performance of a corrugated surface.
- Experimental and numerical study of the effect of double-row slot injection locations on film cooling performance of a corrugated surface.
- Experimental and numerical study of the effect of forward and reverse injection on film cooling and thermal stress distribution on a corrugated surface.

1.10 Layout of the Thesis

This thesis contains seven chapters, the ***First Chapter*** presents the backgrounds, applications, and literature related to film cooling. ***Chapter 2*** provides the design of the experimental setup and methodology. The components of the experimental test facility have been presented exhaustively along with calibration techniques. This chapter also discussed the design and fabrication of components such as corrugated test plate, test section, various accessories, and their mountings. Moreover, the computational methodology to investigate film cooling with various injection configurations has been presented in this chapter. The governing equations of mass, momentum, and energy along with the conjugate heat transfer and their solution methods are depicted. ***Chapter 3*** focuses on forward and reverse injection configurations using cylindrical and shaped holes. LES is performed to access the film cooling performance of cylindrical and shaped holes for forward and reverse injection configurations. ***Chapter 4*** includes the effect of injection locations on the film cooling performance of a corrugated surface. The experimental results are used to validate the computational model. The suitable two-equation model for accurate prediction of corrugated surface film cooling flow and heat is also reported. ***Chapter 5*** focuses on finding the suitable injection configuration using double-row slot injections on sinusoidal corrugated surface. After developing the numerical model, flow field, and film cooling fundamentals of single injection locations, the study has been extended for double rows slot injection on sinusoidal corrugated surface. ***Chapter 6*** dwells the forward and reverse injection on a corrugated surface. The previous studies on reverse injection (*Chapter 3*) show encouraging performance. Therefore, the due focus has been given to the merits of reverse injection on the sinusoidal surface Finally, the concluding remarks for the present experimental and numerical studies are added in ***Chapter 7***. It also incorporates future work suggestions for film cooling designers.

CHAPTER2: METHODLGY

CHAPTER2

2.1 Introduction

The experimental setup designed for the present investigations of film cooling is used to validate the numerical work for the limited range of variations in temperature ratio. The film cooling investigations are carried out on both flat and corrugated surfaces. The mainstream is heated whereas the secondary stream is maintained at ambient conditions. The mainstream is heated by passing through various stages of electrical heaters and flow velocity is maintained by a centrifugal blower while the secondary stream is drawn from the compressor tank and passes through the air filter, pressure regulator, and mass flow controller. In the test section, the secondary is supplied by passing through the plenum chamber. The temperature measurement over the test plate is done by infrared thermography. The operating parameters and the geometrical dimensions are selected such that the actual conditions of the phenomenon cooling phenomenon after the burner of the aero engine can be replicated.

2.2 Experimental Test Facility

The experimental setup consists of a centrifugal blower, open circuit subsonic wind tunnel, reciprocating compressor, storage tank, mainstream heating arrangement, and test section mounted with various measuring instruments such as infrared camera, thermocouples, pitot tube, etc. The detailed schematic layout of the experimental setup is shown in Fig.2.1. Figure 2.1 shows the detailed description of various heaters, wind tunnel accessories, and other components used in the present study. Wind tunnel is completely insulated with glass wool and styrofoam as shown in Fig.2.2. The wind tunnel suction type is where one end is connected with a centrifugal blower of capacity 1400 litter per second while the other end is open to the ambient for suction of air. The wind tunnel flow velocity is derived by a variable speed motor of capacity 5Hp.

The stream of coolant air is drawn from a tank that is connected to a double-stage reciprocating compressor. The compressed air is stored in the compressor tank and before passing through the pressure regulator the air is filtered and dehumidified. The pressure regulator and air filter are mounted just upstream of the mass flow regulator. The pressure regulator can be operated in the pressure range of (0-10 bar). The compressed air is then passed through the mass flow controller. The mass flow rate of secondary air is controlled by a mass flow controller (Make: Alicat, Model: MCR-3000SLPM-D-PAR).

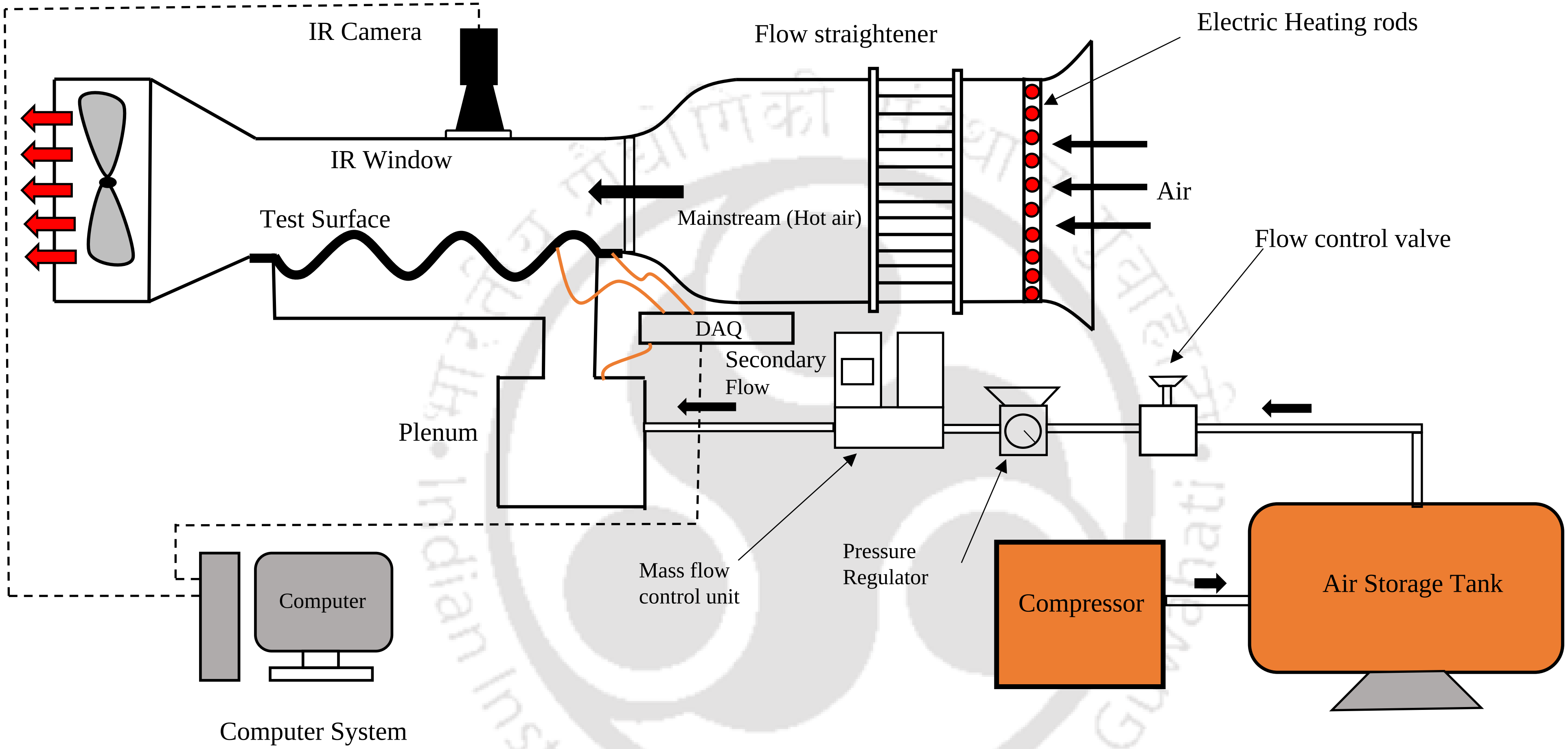

Fig. 2.1: The schematic layout of the experimental setup used in present study.

Figure 2.3 shows the details of the mounting of the pressure regulator, air filter, and mass flow controller. The mass flow controller flow rate range is 0-3000 SLPM with the rated accuracy of mass flow, mass flow controller ± 0.8 %, and the actual response time of 0.1 s.

Fig.2.2: Wind tunnel experimental test facility.

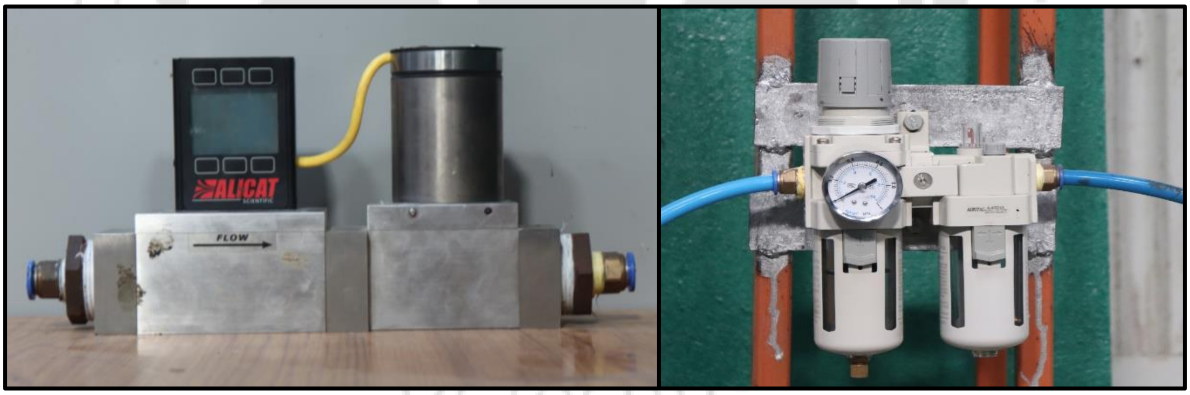

(a) (b)

Fig.2.3: (a) Mass flow controller; (b) air filter and dehumidifier system.

2.2.1 Test Section Design for the Present Study

In the present experimental study, the replaceable test section made up of acrylic is used. It has a cross-section of 0.2× 0.2 m^2 and a length of 1.6 m. The total length of the test section is divided into four replaceable sections of 0.4 m each (as shown in Fig.2.4) and there is provision to mount the test plate of different thicknesses. The test section also is sufficiently long to mount the digital pitot tube and manometer downstream of the test plate. There is a provision for mounting the Infrared camera (i.e., IR Camera) on the top of the test section for the temperature measurement. As the mainstream is heated air and to avoid thermal losses all sides of the test section after mounting the measuring instruments are covered with glass wool packing (as discussed in section 2.2, Fig.2.2).

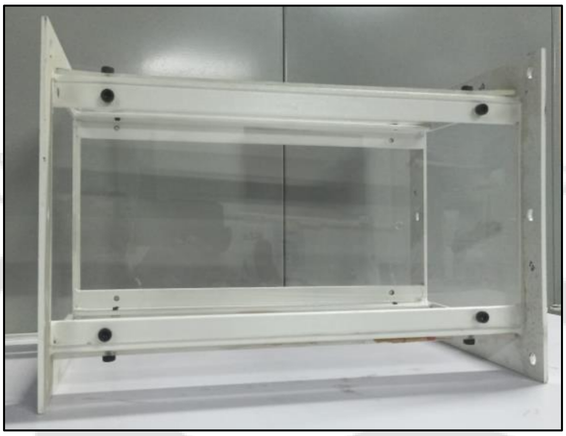

Fig.2.4: Design of the replaceable test section.

2.2.2 Plenum Design for the Present Study

In the present study, the plenum chamber is used to supply the secondary stream of cold air. The plenum used in this study is made up of acrylic and mounted on a test plate to supply the coolant through the cooling hole. Figure 2.5 shows the schematic layout of the plenum chamber shown in this study.

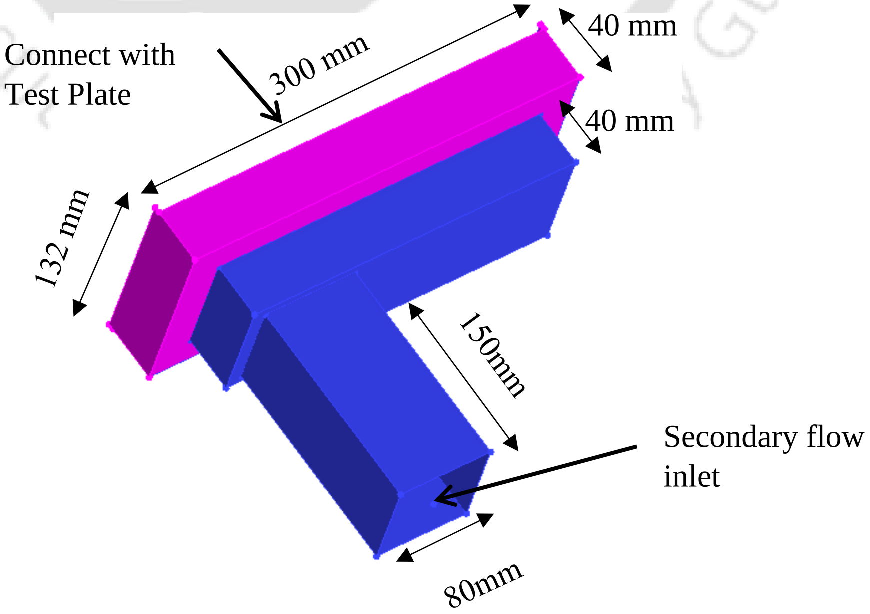

Fig.2.5: Schematic layout of the plenum chamber.

2.3 Test Plates Layout for Experimental Studies

2.3.1 Corrugated Test Plate (Single Injection)-Dimensions and Cooling Slot Arrangements

Figure 2.6 shows the layout of the corrugated plate along with the specific slot positions. The corrugated plate used in this study is the sinusoidal profile of amplitude to wavelength ratio ($a/\lambda = 0.05$), wavelength (λ), and length 3λ. The sinusoidal profile of the corrugated surface is generated by mathematical equations given by Maass and Suchusman [77]. The corrugated plate is smooth 3D printed and mounted on the bottom of the test section.

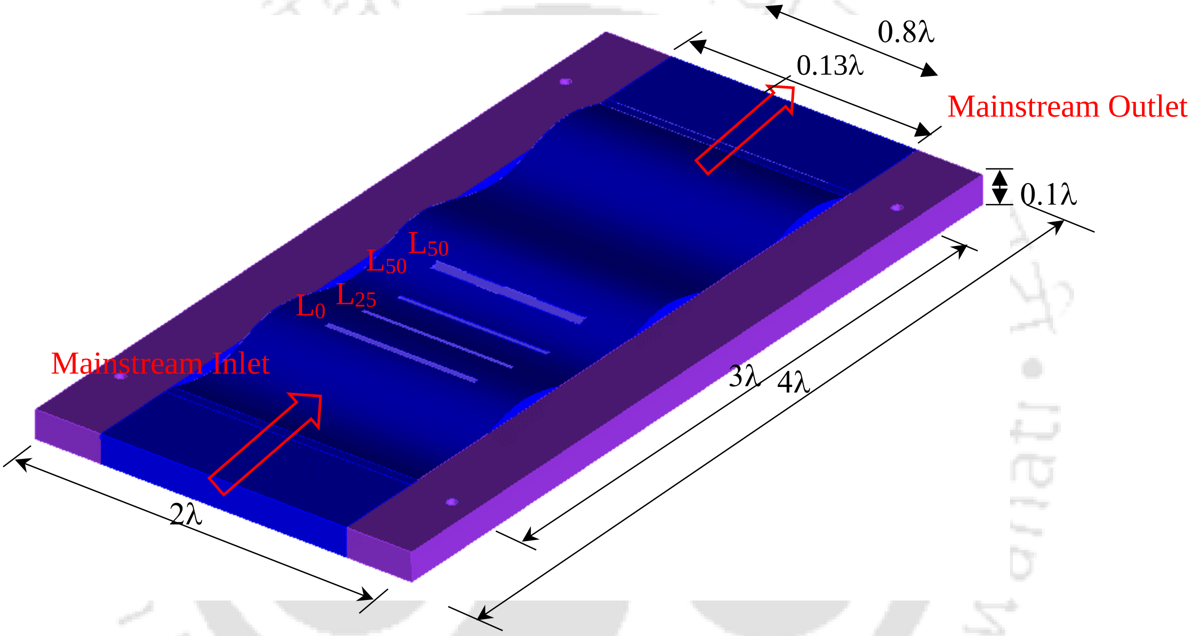

Fig. 2.6: Schematic layout of the corrugated test plate and various single-injection locations.

The corrugated surface is exposed to the mainstream of heated air in the test section, and the secondary stream of cooled air is injected over it through the slot of width ($w/\lambda = 0.02$). The slot configurations are designed by following the previous experimental work of Buns and Stollery [17]. Figure 2.6 shows the detailed layout of the corrugated plate and various slot locations viz. L_0, L_{25}, L_{50}, and L_{75}. Various slot locations are measured with reference to the peak of the first corrugation in the direction of mainstream flow, and labels with slot locations indicate the distance from the first corrugation. To supply the secondary stream of coolant air the bottom of the corrugated plate is attached to the plenum chamber. The mainstream and secondary stream temperatures are measured with thermocouples, whereas the corrugated surface is measured with infrared thermography techniques.

2.3.2 Corrugated Test Plate (Double Injection)-Dimensions and Cooling Slot Arrangements

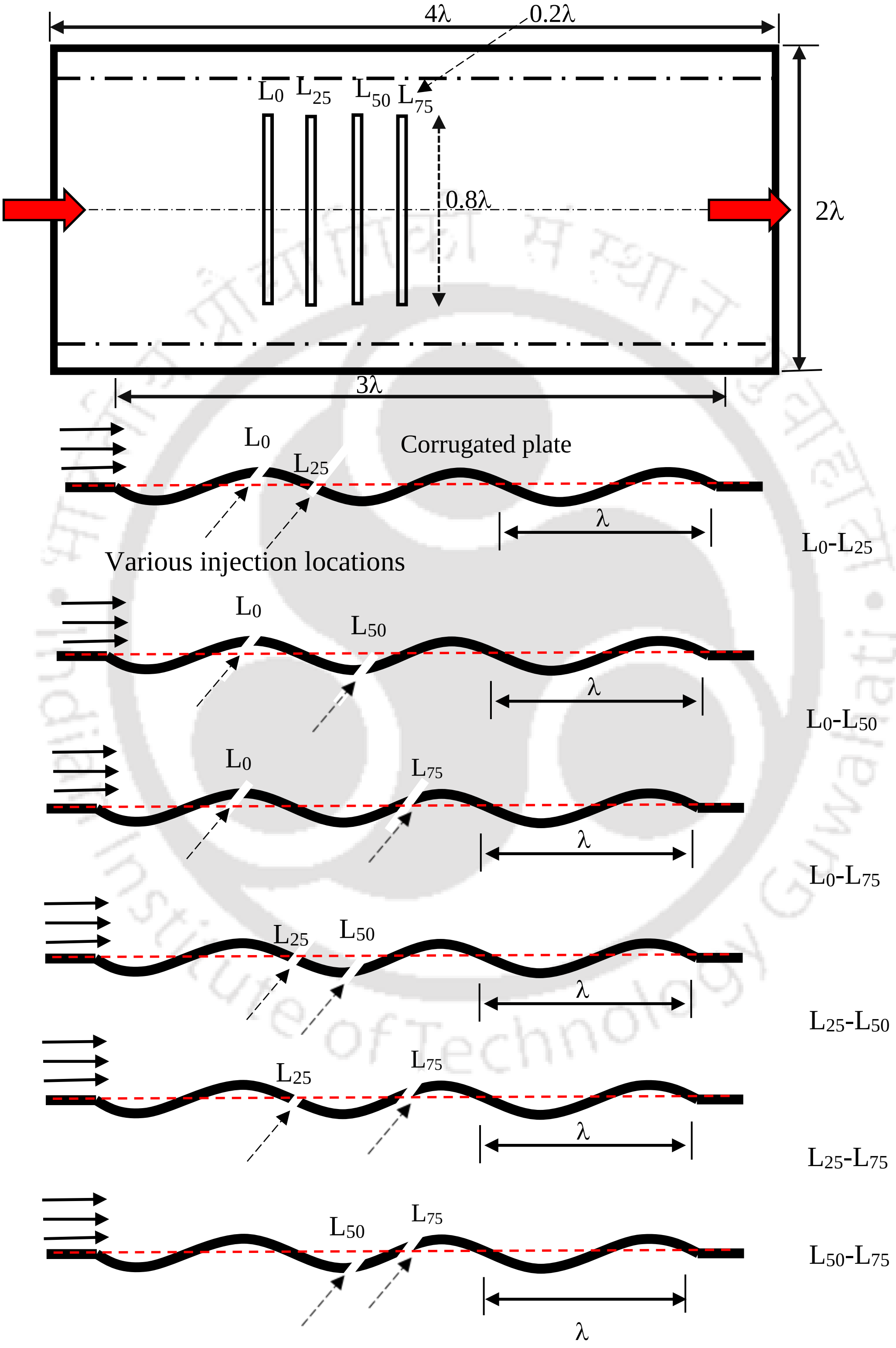

Fig.2.7: Schematic layout of the corrugated test plate and various double-injection.

The present double-row slot study uses a corrugated test plate of a sinusoidal profile, and the profile is generated by the expression given by Maass and Suchusman [77]. The corrugated plate used in this study is the sinusoidal profile of amplitude to wavelength ratio ($a/\lambda = 0.05$), wavelength (λ), and length 3λ (Fig.2.7). The corrugated plate is smooth 3D printed and mounted on the bottom of the test section. The corrugated surface is exposed to the mainstream of heated air in the test section, and the secondary stream of cooled air is injected over it through the slot of width ($w/\lambda = 0.02$). The slot configurations are designed by following the previous experimental work of [17]. The present study considers double slot injection locations in one wavelength. Figure 2.7 shows the detailed layout of the corrugated plate and various slot locations viz. L_0, L_{25}, L_{50}, and L_{75}.Various slot locations on the test plate, were measured with reference to the peak of the first corrugation in the direction of mainstream flow. The level with the slot indicates the distance from the first peak of the first corrugation. The various double slot-row injection considered in this study are, (L_0-L_{25}), (L_0-L_{50}), (L_0-L_{75}), (L_{25}-L_{50}), (L_{25}-L_{75}), and (L_{50}-L_{75}). In the present case, all the measurements are performed downstream to the first hole (i.e., from L_0 for L_0-L_{25}).

2.3.3 Corrugated Test Plate (Reverse Injection)-Dimensions and Cooling Hole Arrangements

Figure 2.8 shows the detailed layout of the cooling hole and test plate arrangement for forward and reverse injection with cylindrical holes. The test plate is corrugated profile, followed by the mathematical expression of Maass and Suchusman [77]. The corrugated plate used in the present study is the sinusoidal profile of amplitude to wavelength ratio ($a/\lambda = 0.05$), wavelength (λ), and length 3λ, as shown. The corrugated plate is smooth 3D printed and made of low thermally conductive material PA12 (Nylon 12). The positions of rows are measured from the peak of the first corrugation in the mainstream flow direction. Three rows of holes (R_1, R_2, and R_3) are placed at 0.45λ, 0.75λ, and 0.125λ from the peak of the first corrugation respectively. The holes are placed at a constant pitch of 3D in the lateral direction and holes are inclined at 45^o with the mainstream flow direction. In the case of forward injection, the axial component of the secondary is along the mainstream. However, reverse injection is the axial component of secondary stream velocity opposite to mainstream flow.

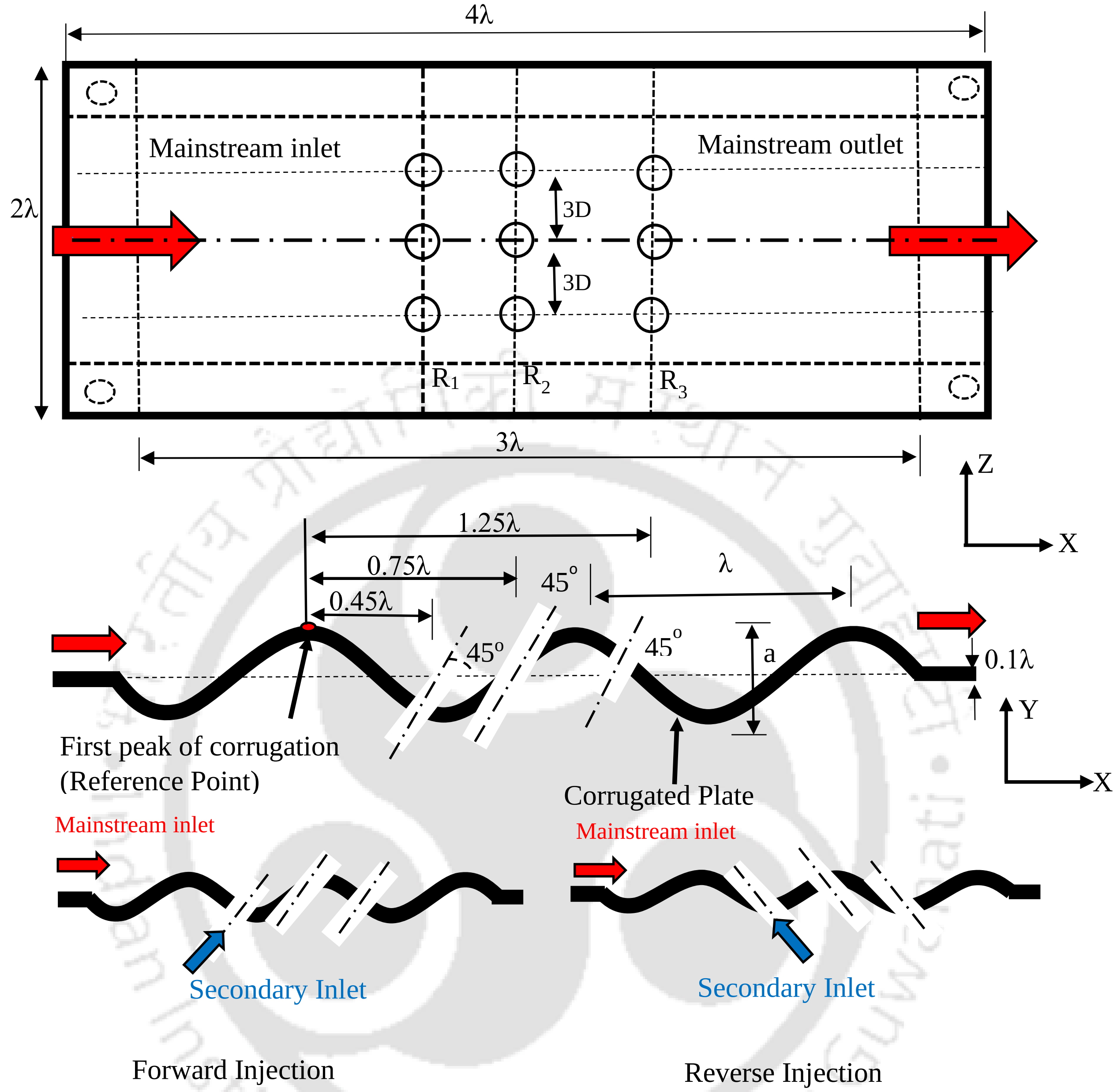

Fig.2.8: Schematic layout of the corrugated plate for forward and reverse injection locations.

2.4 Measurement Techniques

The velocity of the mainstream is measured with a pitot static tube. The accuracy of the pitot tube is ± 0.3%. The mainstream is heated air while the secondary is coolant and both temperatures are measured with the T-type thermocouples (Maker: OMEGA). The thermocouples used in the present measurement are calibrated with boiling water with an uncertainty of ± 0.5°C. The FLAIR IR Camera A325 with a temperature range of -20 to 350°C (Pitch 25μm) is used for surface temperature measurements. The resolution of the camera is 320×240 pixels, the frame range is 60 Hz, and the dictator pitch is 25μm. The accuracy of the camera is ± 2°C or ± 2% of the reading. It uses the uncooled Microbolometer and spectral range of 7.5 – 13.0 μm to detect the infrared radiations. The research IR Software is integrated with the system which provides this facility for video recording. The detailed instrumental uncertainty is summarized in Table.2.1.

2.4.1 Calibration of IR Camera

An Infrared camera is an image-capturing device that images infrared radiation emitted from an object. The cameras show contour images based on their surface emissivity and temperature. Emissivity is one of the most important parameters that need to be specified for any measurement. The surface emissivity is maintained with the help of a black painted cubical box of cooper sheet of size 150×150×150mm^3(Fig.2.9 (b)).

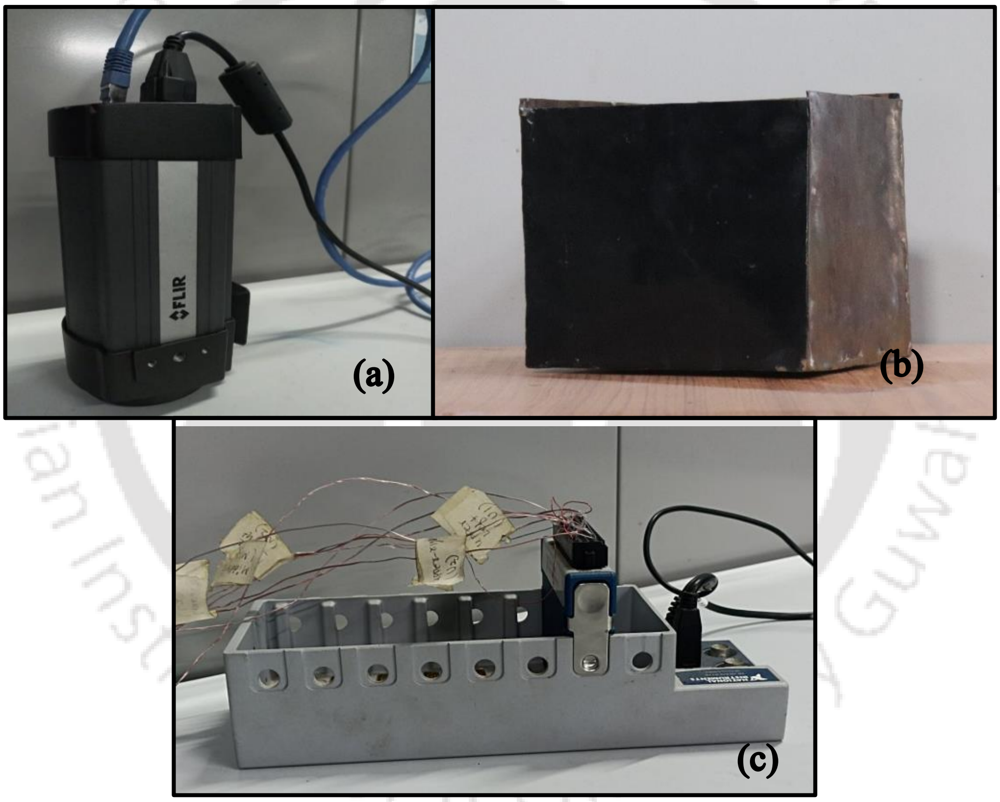

Fig. 2.9: (a) infrared camera (IR Camera); (b) calibration tank of copper; (c) data acquisition system (DAQ).

This tank is fitted with a resistance heater of 1500W capacity. One side of the cubical box is painted with matt finish black paint while the other sides remain unpainted. The tank is filled with water, and heated upto the boiling point long enough and then the heater is switched off and the boiled water is allowed to cool to the room.

The surface temperature is measured by "T" type thermocouple and the emissivity is adjusted till the thermocouple and IR camera readings are equalized. The average value of the emissivity is observed to be 0.95. Figure 2.10 shows the details of the calibration plot for both the infrared camera and the thermocouple. Figure 2.10 shows that both IR camera and thermocouple readings are nearly the same during the initial cooling periods of 1000 sec however a small deviation can be observed after 2000sec which is less than 1^oC. The test plate of the test section whose temperature is to be measured using the infrared camera was also with the same black paint coating so that its emissivity is the same as that of the calibrated surface, hence the same emissivity can it can be further used for the temperature measurement.

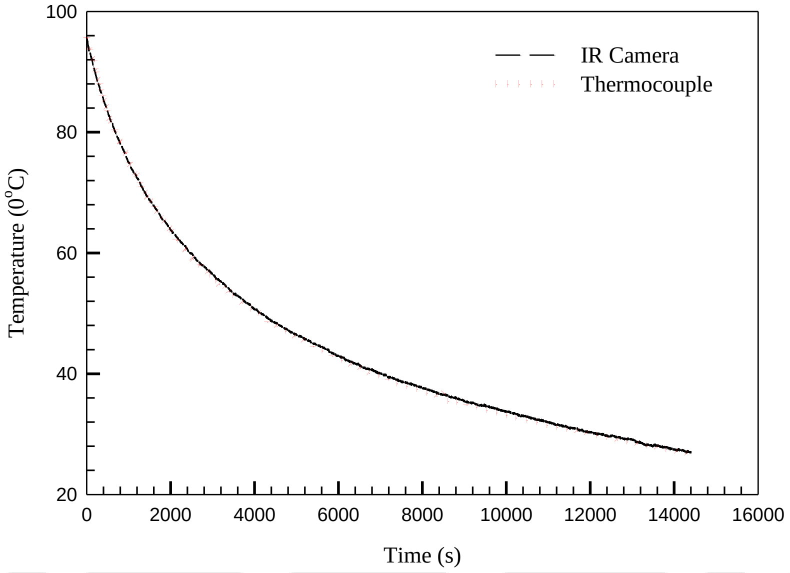

Fig.2.10: Calibration of infrared camera with the thermocouple.

Table 2.1: Uncertainty data of various instruments.

SN.	**Measured quantity**	**Uncertainty**
1.	Temperature measurement with IR Camera	± 1^oC
2.	Temperature measurement with Thermocouple	± 0.5^oC
3.	Pitot Tube	± 0.3%
4.	Mass flow controller	± 0.8%

2.5 Measurement Procedure

The mainstream flow is switched on with various heaters to reach the desired temperature limit and thereafter, the secondary stream is injected into the test section through the plenum chamber. The mainstream and secondary stream temperature is measured using both thermocouples and the surface temperature is measured with IR camera. The thermocouples are arranged on all sides of the test section for mainstream the upstream of the injection hole. The secondary stream thermocouple is located just below the test plate near the secondary stream injection location. The data acquisition system is connected with a thermocouple and switched on well before the mainstream flow and data collection. In the present experimental study, the steady state is reached after a certain time and thereafter the data collection is performed for the parameters. The steady state is referred as the condition where statistical differences in the measured quantities are negligible with respect to time.

2.6 Uncertainty Analysis

In the present study, the uncertainty analysis is done in order to assess the confidence level in the experiment followed by Moffat [78].

2.6.1 Uncertainty Analysis of Film Cooling Effectiveness

In the present study test plate is made up of acrylic and the face exposed to the ambient is covered with glass wool and styrofoam. The thermal conductivity of plate material is very less as well as covered with insulating materials and it can be treated as an adiabatic wall. The expression for calculating the film cooling effectiveness is given as:

$$\eta = \frac{T_{ms} - T_w}{T_{ms} - T_{\mathrm{sec}}} \tag{2.1}$$

where, T_{ms} is the temperature of heated mainstream, T_{sec} is secondary stream temperatures and T_w is the wall temperature. The uncertainty in film cooling effectiveness can be calculated in terms of temperature as given in the equation below:

$$\eta = \sqrt{\left(\frac{\partial \eta}{\partial T_{\mathrm{sec}}} \Delta T_{\mathrm{sec}}\right)^2 + \left(\frac{\partial \eta}{\partial T_{ms}} \Delta T_{ms}\right)^2 + \left(\frac{\partial \eta}{\partial T_{\mathrm{w}}} \Delta T_{\mathrm{w}}\right)^2} \tag{2.2}$$

The Eq. (2.2) can be further written as:

$$\frac{\Delta \eta}{\eta} = \sqrt{\left(\frac{\Delta T_{\mathrm{sec}}}{T_{\mathrm{sec}}}\right)^2 + \left(\frac{\Delta T_{\mathrm{sec}}}{T_{\mathrm{sec}}}\right)^2 + \left(\frac{\Delta T_{\mathrm{w}}}{T_{\mathrm{w}}}\right)^2} \tag{2.3}$$

A total of 30 sets of data are recorded for this analysis, and the temperature of the secondary fluid and mainstream fluid was measured at a point whereas the surface temperature of the test plate was recorded using an IR camera up to a downstream distance of X/D = 10. For a sample case of mainstream temperatures (59.4°C) and secondary stream temperature (29.6°C) for 30 sample data, at 95 percent confidence level the overall uncertainty for effectiveness is reported as ±12%.

Uncertainty Analysis of Blowing Ratio

The blowing ratio (M) can be defined as:

$$M = \frac{(\rho U)_{\mathrm{sec}}}{(\rho U)_{ms}} \tag{2.4}$$

where, $(\rho U)_{\mathrm{sec}}$ and $(\rho U)_{\mathrm{ms}}$ are mass fluxes of mainstream and secondary streams respectively. The mass flux of secondary steam can be expressed in terms of mass flow rate ($\dot{m}$) and hole cross-sectional area (A_c) as:

$$(\rho U)_{\mathrm{sec}} = \frac{\dot{m}}{\Sigma A_c} \tag{2.5}$$

The mainstream flow density ρ_{ms} can be calculated as:

$$\rho_{ms} = \frac{P}{RT_{ms}} \tag{2.6}$$

where, P is atmospheric pressure, R is gas constant for air, R= 8.314 J/ (mol K). The velocity of mainstream air is calculated from the measurement of differential pressure using Eq. (2.7):

$$U_{ms} = K_{av}\sqrt{\frac{2g\rho_w H}{\rho_{ms}\times 1000}} \tag{2.7}$$

Where, K_{av} is the average probe constant, K_{av} =0.9926, g is the acceleration due to gravity, g = 9.81 m/s^2, ρ_{w} indicates the density of water, and H indicates pressure differential measured by Pitot-static probe.

The uncertainty in the blowing ratio can be calculated as:

$$\Delta M = \sqrt{\left(\frac{\partial M}{\partial \dot{m}}\Delta \dot{m}\right)^2 + \left(\frac{\partial M}{\partial A_c}\Delta A_c\right)^2 + \frac{1}{2}\left(\frac{\partial M}{\partial H}\Delta H\right)^2 + \frac{1}{2}\left(\frac{\partial M}{\partial T_{ms}}\Delta T_{ms}\right)^2} \tag{2.8}$$

For 95% confidence level and 30 data (with a coverage factor of 2.04) the overall uncertainty in the blowing ratio is observed as 3.1%.

2.7 Comparison of Measurement Techniques

To compare the experimental setup and methodology the results are compared with Sinha et al. [56]. Infrared thermography is used for temperature measurement on test plates however for measurements pre-calibrated thermocouples are also used.

2.7.1 Comparison of Infrared Thermography Measurement with Thermocouple

The experiments are conducted on a flat plate made up of acrylic. The experiments are conducted for blowing ratio (M= 0.5, 1) and without heated mainstream. The coolant hole diameter (D = 12.7mm), and five thermocouple positions are mounted as given in the Table 2.2. Figure 2.11 (a) shows the experimental results without heated mainstream, and the results clearly show that both an infrared camera and thermocouple measurement show and close agreement with a maximum deviation of 1^{o} C.

Table.2.2 Thermocouple positions on a flat plate.

S.N.	Thermocouple	Position (Downstream of Hole in mm)
1.	A	5
2.	B	15
3.	C	27
4.	D	42
5.	E	57

Figure 2.11(b) demonstrates the blowing ratio (M=0.5), and it can be observed that both an infrared camera and thermocouple measurement show close agreement close to the hole, and further downstream a maximum deviation of 2^{o}C can be observed. Similarly moving to the higher blowing ratio (M= 1) a maximum deviation of 2.1^{o}C can be seen from the thermocouple, (Fig.2.11(c)).

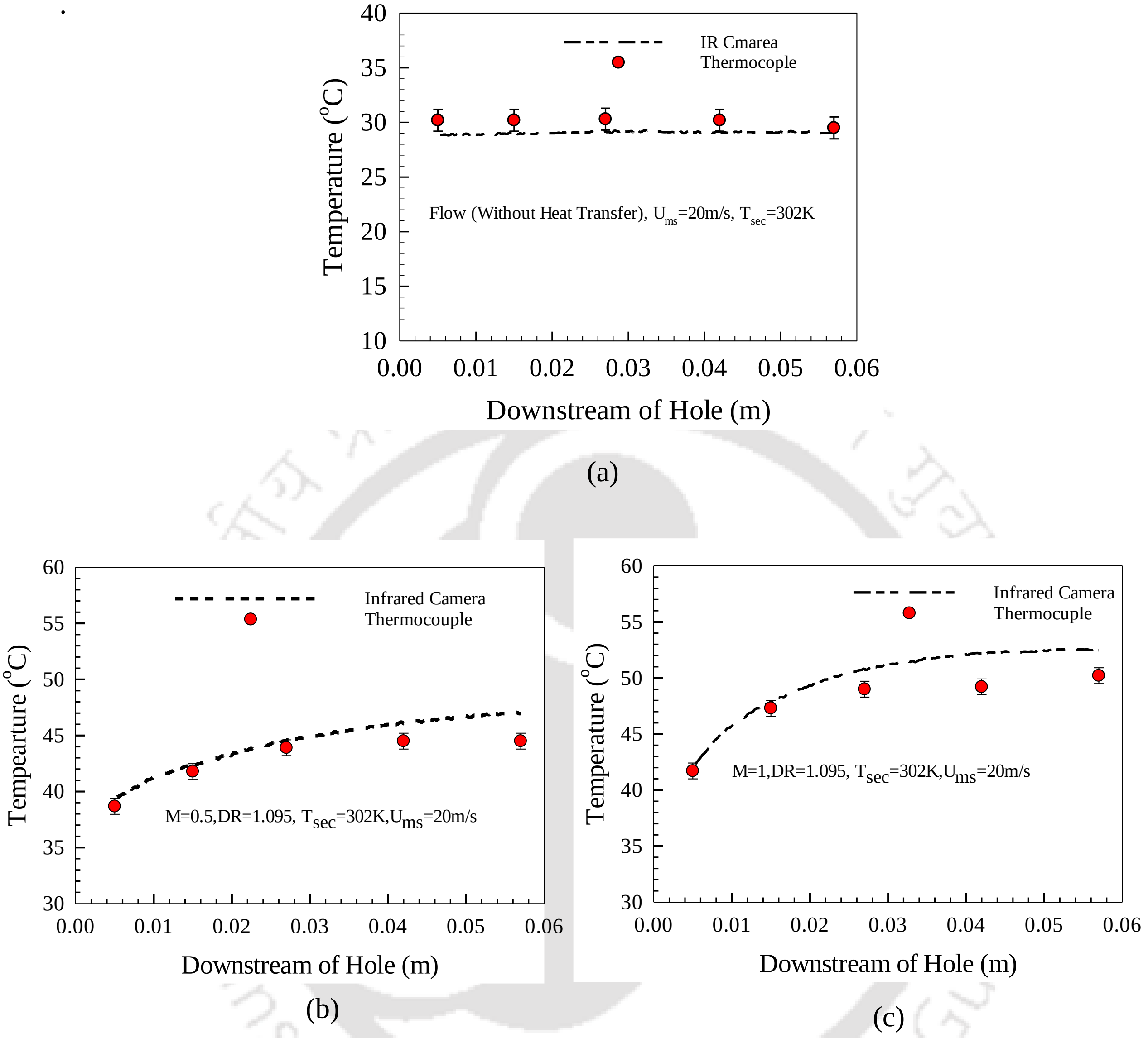

Fig.2.11: Comparison of infrared camera measurement with thermocouple (a) blowing ratio (M= 1) flow only; (b) blowing ratio (M =0.5); (c) blowing ratio (M =1).

2.7.2 Comparison of Present Study with Previous Experiments

Figure 2.12 shows the centreline effectiveness plot for the blowing ratios 0.25 and 1, and it can be observed that the present experimental results show close agreement with the experimental reference (as discussed in Table.2.3). Moreover, the local lateral effectiveness at M=0.5 also follow the trends of Sinha et al. [56], as shown in Fig.2.12(c). Hence it can be concluded the present experimental methods can be adopted for further investigations.

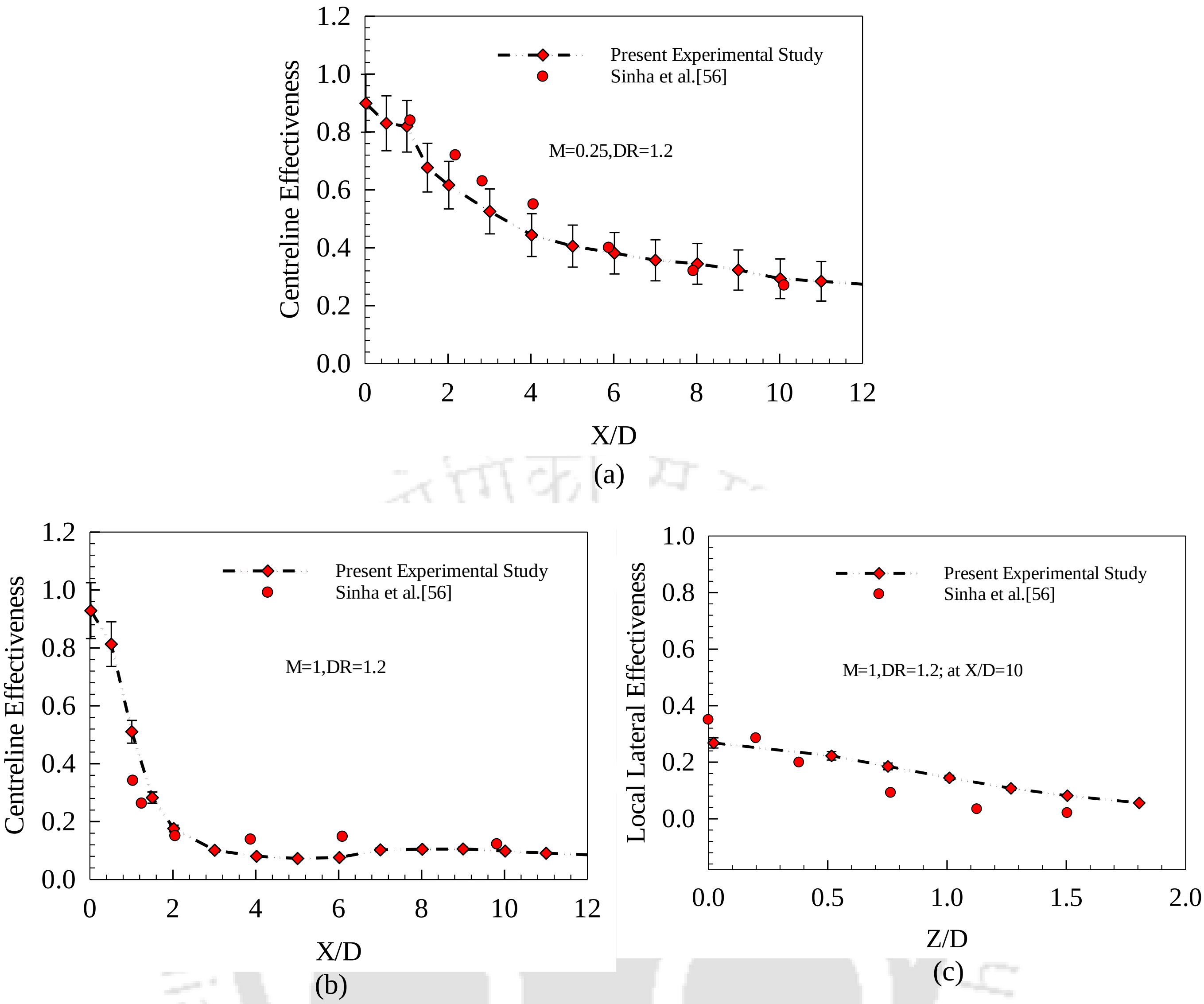

Fig.2.12: Comparison of present experiments for (a) centreline effectiveness (M=0.25); (b) centreline effectiveness (M= 1); (c) local lateral effectiveness at (M=0.5).

Table.2.3: Parameters considered for comparison with the experimental reference [56].

Parameters	**Present Experimental**	**Sinha et al. [56]**
D(mm)	12.7	12.7
L/D	1.75	1.75
Injection Angle	35°	35°
Density Ratio	1.09	1.19
Vms (m/s)	20	20
Blowing Ratio, M	0.25, 05, 1.0	0.25, 0.5, 1.0

2.8 Backgrounds of Numerical Methods

The main objective of numerical investigations is to carry out the parametric study, and optimization of film cooling design variables. In case of afterburner and turbine blades the exhaust, stream temperature is as high as 2000K, and to ensure the film cooling of such components a secondary stream relatively at a lower temperature is injected. It is hard to obtain such a high temperature along with the flow in a laboratory experimental condition. Therefore, the experimental studies are conducted for a limited temperature range and used to validate the numerical models. The numerical operating conditions are close to the actual operating conditions of the afterburners of aero-engines. For the further parametric study, it is extended for a wide range of operating parameters. The selection of a suitable turbulence model for simulation is a critical task. The selection of a suitable turbulence model is based on the flow features and accuracy required. The previous numerical studies exhaustively discussed turbulence models. Various injection configurations are modeled using, Reynolds Average Navier Stokes (RANS) and Large Eddy Simulations (LES) turbulence models. This section also discusses the governing equations, grid topology, and solution procedure. The numerical results obtained from the simulation are presented for comparison. The film cooling studies with reverse configuration are the recent trend in film cooling, which shows promising results to mitigate kidney vortices. However, it is missing in previous literature for shaped holes. Therefore, the first the Large Eddy Simulations (LES) studies on film cooling of forward and reverse configuration on a flat plate is presented. Thereafter, the numerical studies on the corrugated surface are presented.

2.9 Computational Domain

The computational domains are critical components of the numerical formulation. The present study is on film cooling. It provides a mathematical representation of geometry as well as the physical understanding of the problem. The present study investigates various injection configurations with a wide range of operating parameters. The numerical results are presented to highlight the effect of various operating parameters such as blowing ratio, density ratio, and operating pressure. Apart from that the effect of injection configuration such as injection location and reverse injection are also incorporated.

2.9.1 Forward and Reverse Injection with Shaped Hole

In order to understand the film cooling characteristics with forward and reverse hole, a numerical investigation has been carried out for cylindrical and shaped holes. The behaviour of film cooling and vortex formation in the flow field has been evaluated by using an LES study. Figure 2.13, and 2.14 shows the systematic layout of the computational domains addressed in the present study.

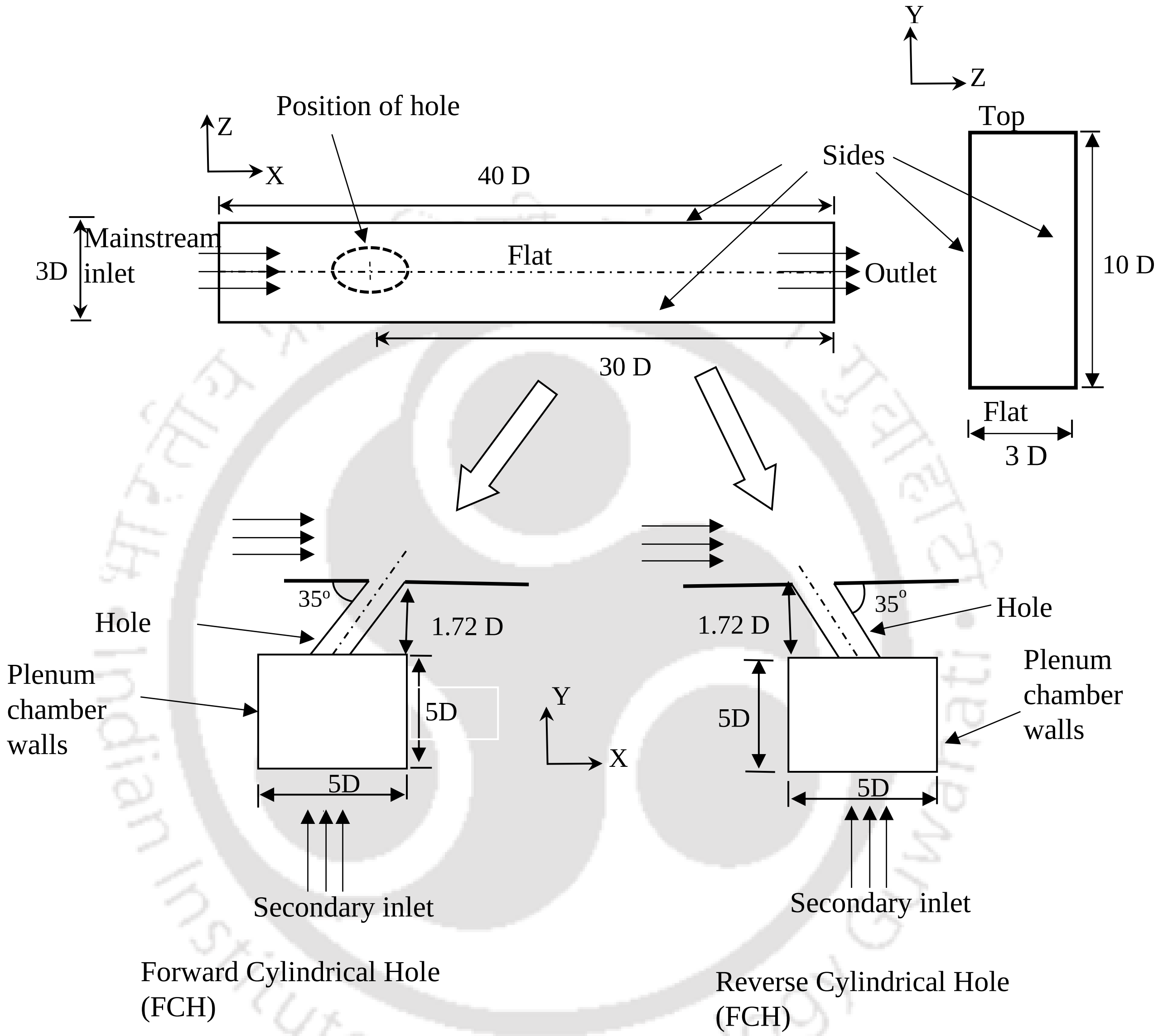

Fig.2.13: Three-dimensional domain of film cooling over the flat surface along with boundary conditions: Forward and reverse cylindrical hole.

In order to protect the surface from the detrimental effect of hot mainstream flow conditions, a secondary stream relatively at a lower temperature is injected at 35° with different hole configurations viz: (i) Forward cylindrical hole (FCH); (ii) Reverse cylindrical hole (RCH); (iii) Forward shaped hole (FSH); (iv) Reverse shaped hole (RSH). The secondary stream of air is supplied to the hole via the plenum chamber of dimensions 5D×5D×5D. The film cooling performance is evaluated over the flat surface for the length of 30D where D is the diameter of the hole, considered as 1 mm [31]. The hole position is fixed at a distance of 10D from mainstream inlet, for both forward and reverse injection configurations. However, reverse injection configuration is positioned in such a way that the axial component of secondary stream flow is opposite to mainstream flow. The design parameters for shaped hole is taken from previous works of Saumweber et al.[35].

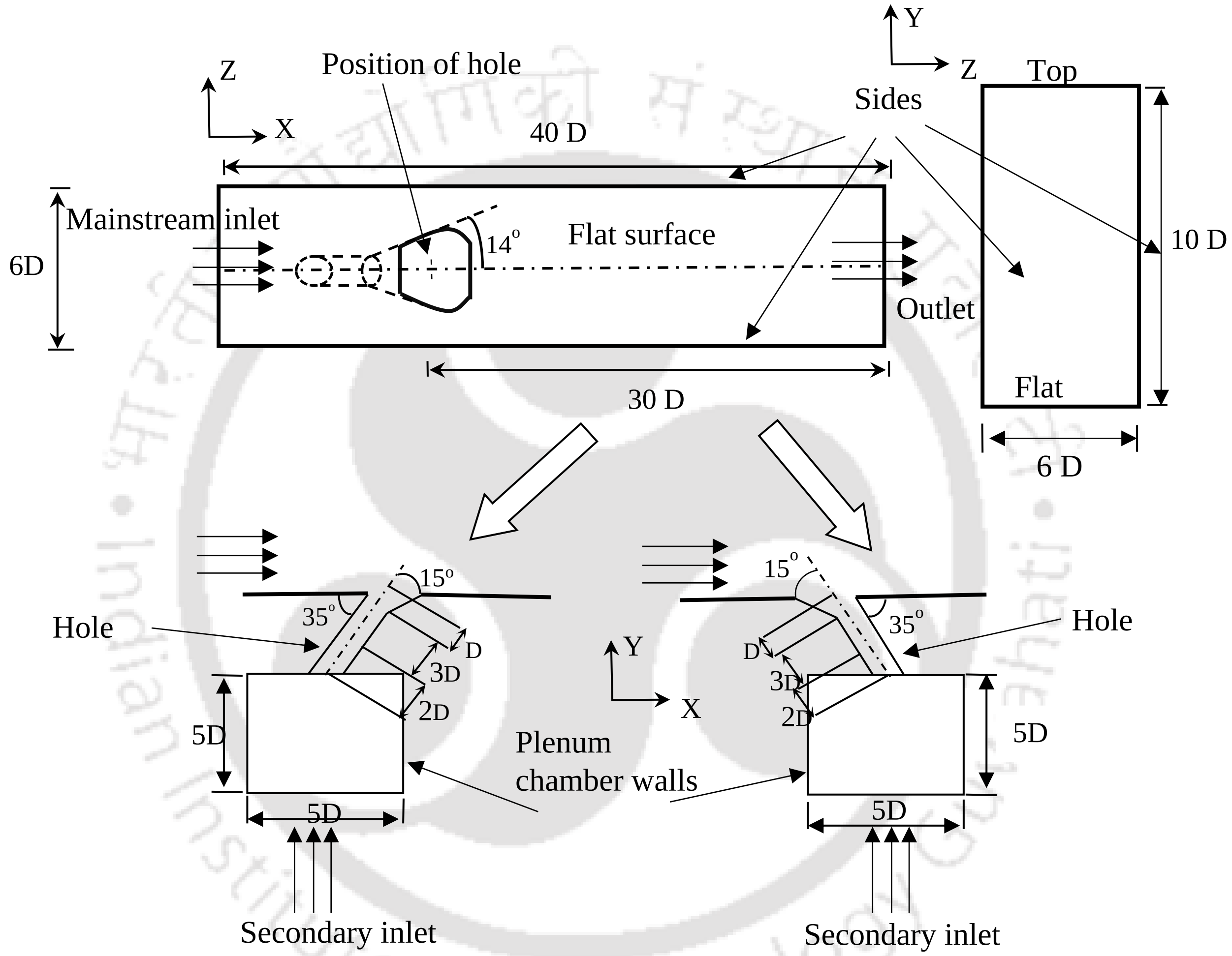

Forward shaped hole (FSH) Reverse shaped hole (RSH)

Fig.2.14: Three-dimensional domain of film cooling over the flat surface along with boundary conditions: Forward and reverse cylindrical hole.

2.9.2 Single Slot Injection Locations Study on the Corrugated Surface

The computational domain addressed in the present study is two-dimensional as shown in Fig.2.15. The length and height of the computational domain are 4λ and 2λ respectively, where λ is the wavelength of the corrugated surface. The mainstream of heated air and secondary stream of coolant air enters through the mainstream and secondary stream inlet.

The secondary stream of air is supplied via the plenum chamber, as shown in Fig. 2.15. The secondary air is well mixed in the plenum chamber before the slot injection. To study the flow characteristics and their effect on film cooling and thermal loading, the slot locations were also varied. The present study considers three amplitude-to-wavelength ratios ($a/\lambda = 0.05$, 0.075, 0.1), and four different slot locations (L_0, L_{25}, L_{50}, and L_{75}), as shown in Fig. 2.15.

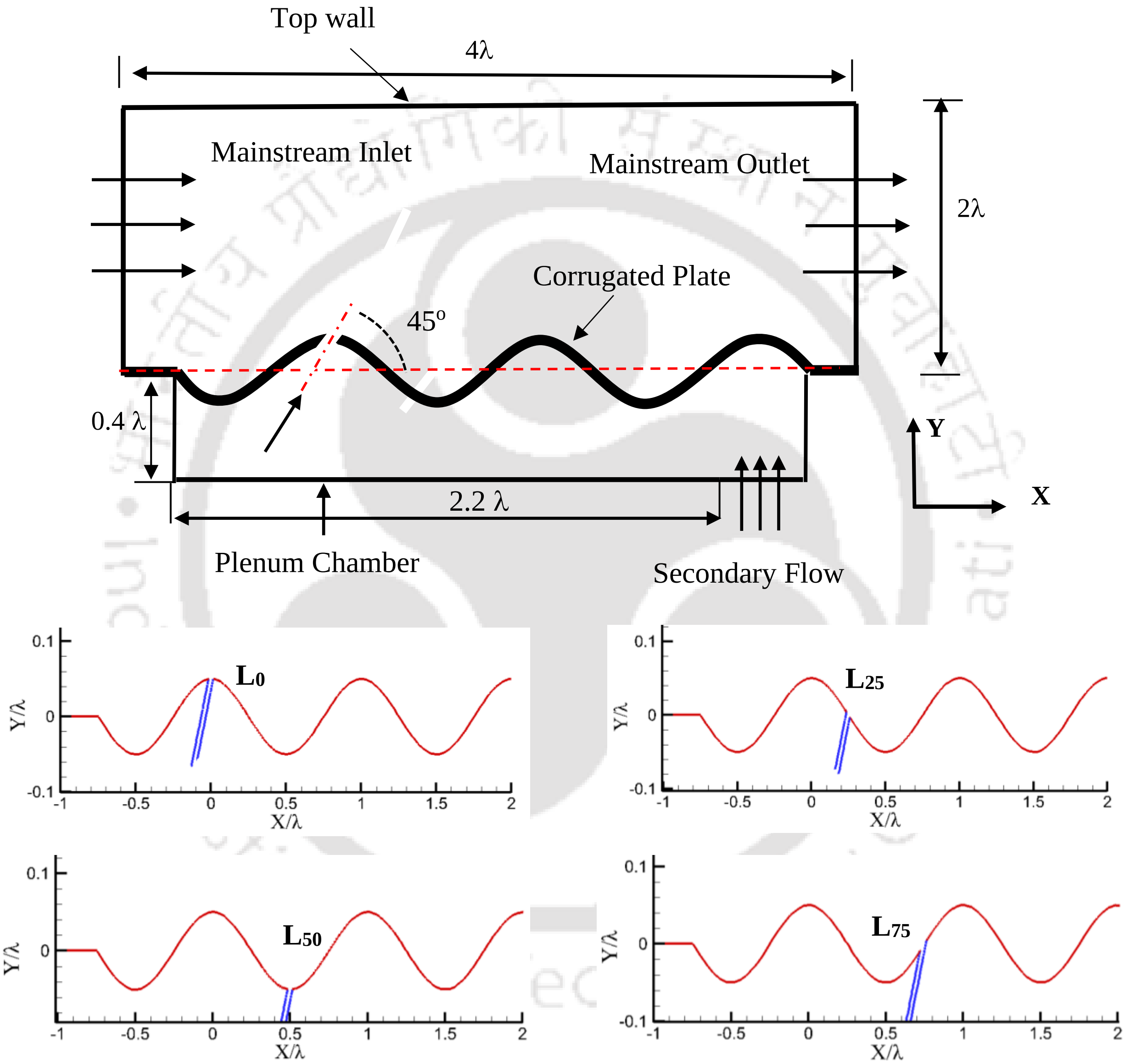

Fig.2.15: Schematic layout of the computational domain and various single slot injection locations.

2.9.3 Double-Row Slot Locations Study on the Corrugated Surface

Fig.2.16 shows the schematic of the computational domain used in the present numerical study. The computational domain is a two-dimensional domain that consists of a mainstream inlet, secondary stream inlet, pressure outlet, plenum chamber, and corrugated wall. The length and height of the domain are 4λ and 2λ, where λ indicates the wavelength of the corrugated surface.

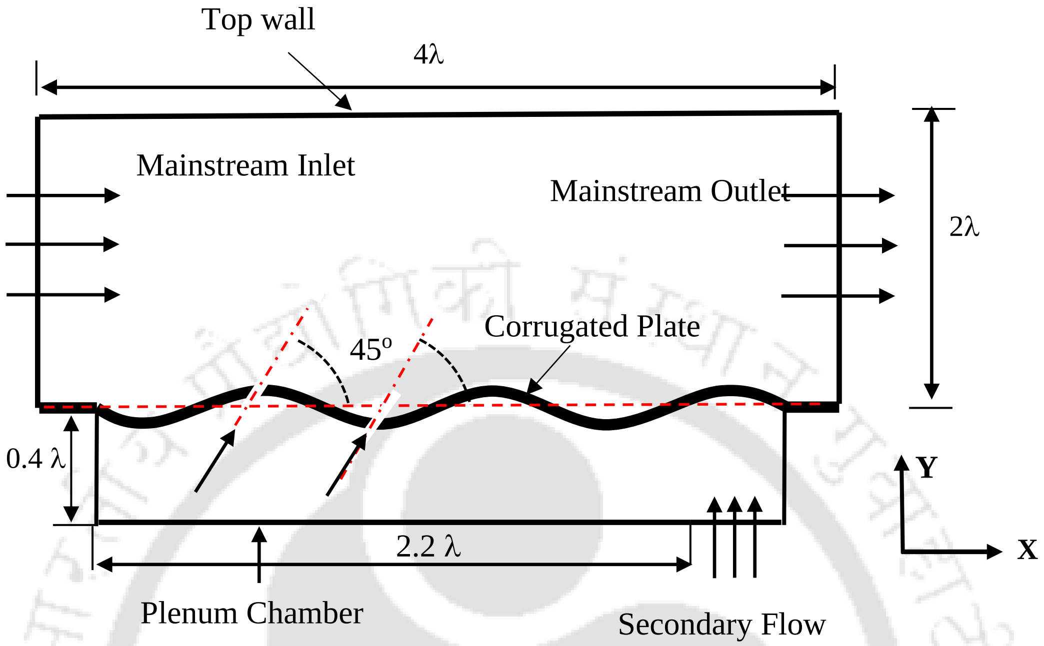

Fig.2.16: Schematic layout of the computational domain used in double slot injection study.

The mainstream is a heated stream of air whereas the secondary stream is a relatively cold stream of air. The secondary steam of air is mixed uniformly in the plenum chamber before being supplied to the corrugated wall. In order to investigate the effect of various injection locations of double slot, various double injection combinations viz., (L_0-L_{25}), (L_0-L_{50}), (L_0-L_{75}), (L_{25}-L_{50}), (L_{25}-L_{75}), and (L_{50}-L_{75}) were considered.

2.9.4 Forward and Reverse Injection Study on the Corrugated Surface

A three-dimensional domain is used for present numerical investigations, as shown in Fig.2.17. It consists of various inlets and outlet boundaries, side walls, plenum walls, and corrugated wall. The length, width, and height of the domain are 4λ, 2λ and 2λ where λ indicates the wavelength of the corrugation profile. The mainstream is heated air injected passing over sinusoidal corrugated surface, and two protect it coolants are injected through three rows (R_1, R_2, and R_3) holes. The holes are placed at the uniform lateral pitch of 3D, where D is the cylindrical hole diameter. Figure 2.17 clearly shows the specific positions of holes measured from the peak of the first corrugation in the direction of mainstream flow. The coolant holes are cylindrical and inclined at 45° with the mainstream flow direction. In case of reverse injection, the axial component of secondary stream velocity is opposite to mainstream flow.

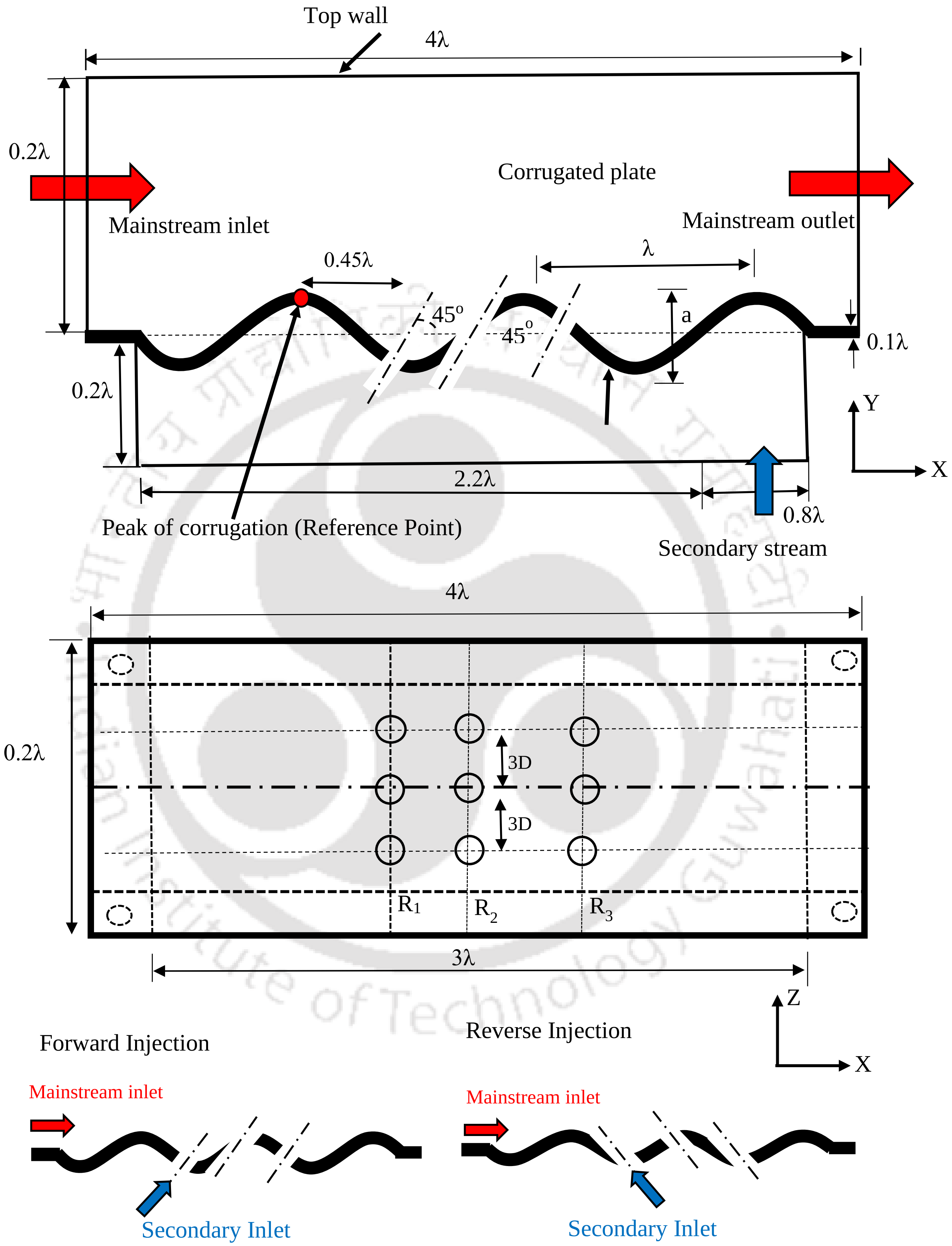

Fig.2.17: Schematic layout of the computational domain used in forward and reverse injection.

2.10 Governing Equation and Numerical Modeling

The steady-state form of Reynolds-averaged conservation equations of mass momentum and energy for two-dimensional turbulent flows are given as:

$$\frac{\partial(\rho u_i)}{\partial X_i} = 0 \tag{2.9}$$

$$\left(\frac{\partial(\rho u_i u_j)}{\partial X_j}\right) = -\frac{\partial p}{\partial X_j} + \frac{\partial}{\partial X_j}\left[\mu\left(\frac{\partial(u_i)}{\partial X_i} + \frac{\partial(u_j)}{\partial X_i}\right) - \rho\overline{u'_\iota u'_J}\right] \tag{2.10}$$

$$\frac{\partial \rho u_j T}{\partial X_j} = \frac{\partial}{\partial X_j}\left(\frac{\mu}{Pr}\frac{\partial T}{\partial X_j} - C_p\overline{u'_J T'}\right) \tag{2.11}$$

where, u and u' denotes the mean and fluctuating velocity components, p is pressure, ρ is density, T is temperature, μ is the dynamic fluid viscosity, X is coordinate, and the subscripts i and j denote the directions used in the cartesian coordinates system. The $\rho\overline{u_\iota u'_J}$ is known as the Reynolds stress tensor. The Boussinesq approximation is assumed to calculate the Reynolds stress term as:

$$-\rho\overline{u_i' u_j'} = \mu_t\left(\frac{\partial u_i}{\partial X_j} + \frac{\partial u_j}{\partial X_i}\right) - \frac{2}{3}\rho k\delta_{ij} \tag{2.12}$$

The term $C_p\overline{u'_J T'}$ represents the specific turbulence heat fluxes. the specific turbulence heat fluxes flux term is computed using the eddy diffusivity model as:

$$\rho\overline{T' u_j'} = -\frac{\mu_t}{\mathrm{Pr}_t}\frac{\partial T}{\partial X_j} \tag{2.13}$$

where, Pr_t is a turbulent Prandtl number. In order to calculate the turbulent viscosity, the turbulent quantities such as k- ε and k-ω are used to get velocity and length scale, $\sqrt{k}$ is used as a velocity scale in both k-ε and k-ω models, while $\frac{k^{3/2}}{\varepsilon}$ and $\frac{k^{1/2}}{\omega}$ are used to represent the turbulent length scales in k-ε and k-ω models respectively, using the mixing length hypothesis to determine the eddy viscosity.

The heat condition in the solid domain is calculated by solving the following equation for the corrugated plate, which is considered solid [79].

$$\frac{\partial}{\partial X_j}\left(k_s\frac{\partial T}{\partial X_j}\right) = 0 \tag{2.14}$$

2.10.1 Standard k– ε Model

The standard k-ε model, is a semi-empirical model that assumes that the flow is completely turbulent and that the impacts of molecular viscosity are minimal. The conventional k-ε gives the turbulent viscosity calculated as:

$$\mu_t = \frac{\rho C_\mu k^2}{\varepsilon} \tag{2.15}$$

where the term C_μ is a constant and ε represents turbulent diffusivity.

The transport equation for k, Eqn. (2.16) is derived from the exact equation using the Boussinesq hypothesis whereas the transportation equation for ε, Eqn. (2.17) is obtained using the physical understanding:

$$\frac{\partial}{\partial X_i}(\rho u_i k) = \frac{\partial}{\partial x_j}\left[\left(\mu + \frac{\mu_t}{\sigma_k}\right)\frac{\partial k}{\partial X_j}\right] + G_k - \rho\varepsilon \tag{2.16}$$

$$\frac{\partial}{\partial X_i}(\rho u_i \varepsilon) = \frac{\partial}{\partial X_j}\left[\left(\mu + \frac{\mu_t}{\sigma_\varepsilon}\right)\frac{\partial \varepsilon}{\partial X_j}\right] + C_{1\varepsilon} G_k \frac{\varepsilon}{k} - C_{2\varepsilon}\rho\frac{\varepsilon^2}{k} \tag{2.17}$$

where, the terms σ_k and σ_ε represents the Prandtl number for turbulent kinetic energy and dissipation rate respectively, whereas G_k represents the turbulence kinetic energy generation. The various model constants of the equations are $C_{1\varepsilon}$ =1.44, $C_{2\varepsilon}$ =1.92, C_μ=0.09, σ_k=1.0, σ_ε=1.3.

2.10.2 RNG k–ε Model

A rigorous statistical method, commonly known as renormalization group theory was used to determine the RNG model [80]. The approach is similar to the Standard k– ε model for the k transport equations, however the transport equation for ε is refined for high speed and swirl flow. Additionally, the RNG model solves an equation of turbulent Prandtl numbers, while the standard k– ε turbulence model uses user-defined, constant values. The transport equation for ε is expressed as:

$$\frac{\partial}{\partial X_i}(\rho u_i \varepsilon) = \frac{\partial}{\partial X_j}\left[\alpha_\varepsilon \mu_{eff}\frac{\partial \varepsilon}{\partial X_j}\right] + C_{1\varepsilon}\frac{\varepsilon}{k}G_k - C_{2\varepsilon}^{*}\rho\frac{\varepsilon^2}{k} \tag{2.18}$$

Where, the term G_k represents the turbulence kinetic generation due to the mean velocity gradients, quantities α_k, and α_ε are the inverse effective Prandtl numbers for k and ε, respectively. $C_{2\varepsilon}$the term has $C_{2\varepsilon}$* term of standard k-ε model and additional term which varies with the strain rate. renormalization group theory models the turbulent viscosity term for low-speed flow as:

$$d\left(\frac{\rho^2 k}{\sqrt{\varepsilon u}}\right) = 1.72\frac{\hat{v}}{\sqrt{\hat{v}^3 - 1 + C_v}}d\hat{v} \tag{2.19}$$

where, $\hat{v} = \frac{\mu_{eff}}{\mu}$

The model constants are $C_{1\varepsilon}$ =1.42, $C_{2\varepsilon}$=1.68, C_{μ}=0.0845, $C_{v} \approx 10$.

2.10.3 Realizable k–ε Model

The recent advancement in k–ε Model is known as the realizable k–ε Model, Shih et al.[81], it is a relatively new development in which an additional equation is incorporated for turbulence dissipation modeling. It also presents a new formulation for turbulent viscosity. In standard k–ε, RNG k–ε Models C_{μ} is treated as constant which yields negative shear strain, particularly at higher strain flow. Apart from that Schwarz inequality was also violated. To ensure a reliable solution and positive shear strain the C_{μ} is modeled in terms of dissipation rate, kinetic energy and strain rate, and angular velocity of the system. These model modifications enable to capture of flows involving rotation, pressure gradients, separation, and recirculation of boundary layers under strong adverse. The transport equations for modeling the k and ε are:

$$\frac{\partial}{\partial X_j}\left(\rho u_j \varepsilon\right) = \frac{\partial}{\partial X_j}\left[\left(\mu + \frac{\mu_t}{\sigma_\varepsilon}\right)\frac{\partial \varepsilon}{\partial X_j}\right] + \rho C_1 S \varepsilon - \rho C_2 \frac{\varepsilon^2}{k + \sqrt{v\varepsilon}} \tag{2.20}$$

$$\text{where,} C_1 = max\left[0.43, \frac{\eta}{\eta+5}\right], \eta = S\frac{k}{\varepsilon}, S = \sqrt{2S_{ij}S_{ij}} \tag{2.21}$$

The model constants used in this model are $C_2 = 1.9$, $\sigma_k = 1.0$, $\sigma\varepsilon = 1.2$.

2.10.4 Standard k–ω Model

The standard k-ω model is based on the Wilcox k-ω model [82], which incorporates modifications for low-Reynolds-number, compressibility, and shear flow spreading effects.

Turbulent viscosity, μ_t in the standard k–ω model is expressed as:

$$\mu_t = \alpha^* \frac{\rho k}{\omega} \tag{2.22}$$

Like k–ε models the k–ω model is also a two equations turbulence model. The transport equations for k and ω are given as:

$$\frac{\partial}{\partial X_i}\left(\rho u_i k\right) = \frac{\partial}{\partial X_j}\left[\left(\mu + \frac{\mu_t}{\sigma_k}\right)\frac{\partial k}{\partial X_j}\right] + G_k \tag{2.23}$$

$$\frac{\partial}{\partial X_i}\left(\rho u_i \omega\right) = \frac{\partial}{\partial X_j}\left[\left(\mu + \frac{\mu_t}{\sigma_\omega}\right)\frac{\partial \omega}{\partial X_j}\right] + G_\omega \tag{2.24}$$

where G_k and G_ω indicate turbulent kinetic and specific dissipation generation respectively.

2.10.5 Shear Stress Transport (SST) k–ω Model

The shear-stress transport (SST) k–ω model was developed by Menter [83], to improve an accurate formulation of the k–ω model. It uses the advantage of both k–ε and k–ω models. Near the wall region, it acts like the k–ω model, and further away from the wall, it switches to the k–ε model. Transport equations for the SST k–ω model are given below:

$$\frac{\partial}{\partial X_i}(\rho u_i k) = \frac{\partial}{\partial X_j}\left[\left(\mu + \frac{\mu_t}{\sigma_k}\right)\frac{\partial k}{\partial X_j}\right] + \tilde{G}_k \tag{2.25}$$

$$\frac{\partial}{\partial X_i}(\rho u_i \omega) = \frac{\partial}{\partial X_j}\left[\left(\mu + \frac{\mu_t}{\sigma_\omega}\right)\frac{\partial \omega}{\partial X_j}\right] + G_\omega + D_\omega \tag{2.26}$$

where G_k indicates turbulent kinetic energy generation due to mean velocity gradients, D_ω are cross diffusion term and G_ω is the generation of ω.

2.10.6 Large Eddy Simulations (LES) Modeling

In the case of the Large Eddy Simulations (LES), the governing equations are obtained by following filtering operations:

$$\bar{\varphi}(X_i', t) = \int_{\Delta} \varphi(X_i', t) G(|X_i - X_i'|) dX_i' \tag{2.27}$$

where the term $\bar{\varphi}(X_i', t)$and G represent arbitrary resolved quantity and the filter function respectively. In the present study, the top-hat filter is considered a filtering function. The 3D non-uniform grids are used and the filter width Δ is taken as the cube root of cell volume as follows [84]:

$$\Delta = (\Delta X \Delta Y \Delta Z)^{1/3} \tag{2.28}$$

To account for the variations in the density with the temperature changes, the Favre Averaging is used as follows:

$$\tilde{\varphi}(X_i', t) = \frac{\overline{\rho\varphi(X_i', t)}}{\rho} \tag{2.29}$$

The instantaneous variable $\varphi(X_i', t)$ can be written in terms of resolved and unresolved

$$\varphi(X_i', t) = \tilde{\varphi}(X_i', t) + \varphi''(X_i', t) \tag{2.30}$$

where the term $\tilde{\varphi}(X_i', t)$, and $\varphi''(X_i', t)$ represents the resolved (filtered) and un-resolved (sub-grid scale) components respectively.

Flow is assumed to be turbulent and Large eddy simulations (LES) are used for modeling. The filtered governing equations, viz. continuity, momentum, and energy equations for the flow are given in Eqns.(2.31-2.33), as referred in literature [85].

$$\frac{\partial\bar{\rho}}{\partial t}+\frac{\partial\bar{\rho}\tilde{u}_i}{\partial X_i}=0 \tag{2.31}$$

$$\frac{\partial\bar{\rho}\tilde{u}_i}{\partial t}+\frac{\partial(\bar{\rho}\tilde{u}_i\tilde{u}_j)}{\partial X_i}=\frac{\partial\bar{p}}{\partial X_i}+\frac{\partial}{\partial X_i}[\mu(\frac{\partial\tilde{u}_i}{\partial X_j}+\frac{\partial\tilde{u}_j}{\partial X_i})-\frac{2}{3}\mu\frac{\partial\tilde{u}_k}{\partial X_k}\delta_{ij}]+\frac{\partial\bar{A}_{u_iu_j}}{\partial X_i} \tag{2.32}$$

$$\bar{\rho}C_p\frac{\partial\tilde{T}}{\partial t}+\bar{\rho}C_p\tilde{u}_i\frac{\partial\tilde{T}}{\partial X_i}=\frac{\partial}{\partial X_i}(\frac{\mu C_p}{Pr}\frac{\partial\tilde{T}}{\partial X_i})+\frac{\partial\bar{A}_{u_jT}}{\partial X_i} \tag{2.33}$$

Here, the term u, p, T, and A indicates velocity, pressure, temperature, and stress tensor respectively where bar terms, $\bar{u}$ indicates the resolved (filtered) velocity, and the tilde over the term, $\tilde{u}$ indicates Favre averaged quantity. The Favre averaging is used to account for the variations in the density with temperature changes. The density of air is calculated by using the ideal gas equations. The unknown terms like sub-grid stress tensor ($\bar{A}_{u_iu_j}$) and sub-grid scale heat flux ($\bar{A}_{u_iT}$) in Eqns. (2.32) and (2.33) respectively, are computed by, the sub-grid scale (SGS) model.

The SGS viscosity using the eddy viscosity hypothesis can be expressed as:

$$\bar{A}_{u_iu_j}=-2\mu_{SGS}\tilde{S}_{ij}+\frac{2}{3}k_{SGS}\delta_{ij} \tag{2.34}$$

where, $\tilde{S}_{ij}$ is called filtered strain rate tensor which is expressed as follows:

$$\tilde{S}_{ij}=\frac{1}{2}\left[\frac{\partial\tilde{u}_i}{\partial X_j}+\frac{\partial\tilde{u}_j}{\partial X_i}\right] \tag{2.35}$$

The eddy viscosity term in Eqn. (2.34) can be calculated by using the one equation eddy-viscosity model “as follows [86]:

$$\mu_{SGS}=C_k(k_{SGS})^{1/2}\Delta \tag{2.36}$$

where the turbulent kinetic energy (k_{SGS}) can be expressed as [87]:

$$k_{SGS}=\frac{1}{2}(\overline{u_ju_j}-\bar{u}_j\bar{u}_j) \tag{2.37}$$

The comprehensive LES study suggested that one equation eddy-viscosity model shows a better prediction near the wall hence it is considered for the present study [88].To compute

k_{SGS}, the present approach (one equation eddy-viscosity model) solves an additional transport equation:

$$\frac{\partial k_{SGS}}{\partial t} + \frac{\partial \tilde{u}_j k_{SGS}}{\partial X_j} = \frac{\partial}{\partial X_j}\left(\frac{\mu_t}{\sigma_k}\frac{\partial k_{SGS}}{\partial X_j}\right) - A_{u_i u_j}\frac{\partial \tilde{u}_i}{\partial X_j} - C_{\varepsilon}\frac{(k_{SGS})^{3/2}}{\Delta} \qquad (2.38)$$

The model constants $C_k = 0.094$, $C\varepsilon = 0.916$, and $\sigma_k = 1.048$ are taken from reference [89]. The SGS heat flux, $\bar{A}_{U_iT}$ in equation (2.33) is calculated based on the simple gradient diffusion hypothesis.

$$\bar{A}_{U_iT} = \frac{-\mu_{SGS}}{\mathrm{Pr}_t}\frac{\partial \tilde{T}}{\partial X_j} \qquad (2.39)$$

2.11 Material Properties

2.11.1 Fluid Properties

Air is used as a working fluid for both the mainstream and the secondary stream. The temperature difference in the region is very large so the variation in the physical properties of air with temperature is considered in the present study. Air is assumed to be incompressible which means that the density of air depends on the local fluid temperature and operating pressure in the physical domain. A fourth-order polynomial as suggested in reference [48], is used for the thermal conductivity, specific heat, and dynamic viscosity. All the properties are valid in the temperature range of 100 K - 2300 K. The temperature-dependent properties are given in Eqns. (2.40-2.42) as:

Specific heat, (C_p) J/kg.K

$$C_p = (9.0813 \times 10^{-11})T^4 - (4.8066 \times 10^{-7})T^3 + (8.073 \times 10^{-4})T^2 - 0.32136T + 1.0450 \times 10^3 \qquad (2.40)$$

Dynamic viscosity (μ), Pa.s

$$\mu = (1.7020 \times 10^{-14})T^3 - (4.0405 \times 10^{-11})T^2 + 6.8539 \times 10^{-8}T + 1.0616 \times 10^{-6} \qquad (2.41)$$

Thermal conductivity (K_{th}), W/m.K

$$k_{th} = (7.9957 \times\times 10^{-12})T^3 - (2.4013 \times 10^{-8})T^2 + (8.3047 \times 10^{-5})T + (2.8822 \times 10^{-3}) \qquad (2.42)$$

2.11.2 Nickle Superalloy Properties (IN738LC)

Nickel-based alloy (IN738LC) is a commonly used material for manufacturing turbine blades, the liner of afterburners, and combustion chambers. It can bear excessive temperature as well as high creep-rupture strength and hot corrosion resistance. Therefore, in the present study, IN738 (density 8110kg/m3) is considered as test plate material. The variation of specific heat and thermal conductivity with temperature are considered by feeding fourth-order polynomials for the data given by Kermanpur et al. [90], which is valid in the temperature range 298–1773 K.

Thermal conductivity (k_p), W/m.K

$$k_p = (1.345 \times 10^{-11})\mathrm{T}^4 + (-4.844 \times 10^{-8})\mathrm{T}^3 + (6.578 \times 10^{-5})\mathrm{T}^2 + (2.63710^{-2})\mathrm{T}^1 + (1.363 \times 10^{-1}) \tag{2.43}$$

Specific heat, (C_p) J/kg.K

$$C_p = (-2.994 \times 10^{-10})\mathrm{T}^4 + (8.038 \times 10^{-7})\mathrm{T}^3 + (-3.934 \times 10^{-4}) + (-1.281 \times 10^{-2})\mathrm{T}^1 + (4.712 \times 10^{-2}) \tag{2.44}$$

2.12 Boundary Conditions

In the present numerical study, the computational domain consists of various boundaries, the mainstream and secondary stream inlet, are assigned velocity inlets where flow velocity, turbulence intensity, and temperature are specified. The numerical values of velocity and temperature correspond to the parameter sets of the various cases being computed (i.e., density ratio, blowing ratio, and Reynolds number). The outlet is assigned as a pressure outlet boundary with zero-gauge pressure. The values of velocity and temperature at mainstream and secondary stream inlets correspond to the parameter sets of the cases being computed, i.e., density ratio, Reynolds number, blowing ratio, etc. The corrugated test plate wall is assumed to be conjugate.

However, for the LES study on a flat surface, the inlet of the mainstream and plenum is assigned to be a time-invariant turbulent velocity profile obtained from the RANS study of channel flow. The outlet of the domain is assumed to be the pressure exit with zero-gauge pressure. The side walls in the lateral direction of the mainstream flow of the flow field are considered as the periodic boundary. All other walls in the domain are assigned as the no-slip adiabatic condition. The plenum chamber is provided to obtain the actual experimental conditions of the coolant supply [91].

2.13 Numerical Schemes

For numerical studies on corrugated walls, use a Finite Volume solver, ANSYS FLUENT v20.0 [92] to solve governing equations of mass, momentum, and energy. The conservation equations terms are discretized with second-order accurate schemes, and the SIMPLE algorithm [93] is used for coupling of pressure and velocity. The convergence criteria for mass and momentum energy are defined as $10^{-6,}$ and 10^{-8} respectively.

In the case of large eddy simulations, the study is carried out and the filtered equations of continuity, momentum, and energy are solved by finite volume method-based CFD source codes (OpenFOAM 5.0 and Greenshields [94]). The convective and diffusive fluxes are calculated by a second-order accurate central differencing scheme. The temporal term in governing equations discretized by the backward scheme is second-order accurate. The solution is considered to be converged when the residuals of continuity, velocity, turbulence quantities, and energy fall below 10^{-6}. In order to accurately capture the cross-flow physics, the time step is selected based on the Courant–Friedrichs–Lewy (CFL) number, CFL = 0.8 according to the guidelines of Acharya and Leedom [95]. The PIMPLE algorithm is used for pressure and velocity coupling.

2.14 Grid Independence Study

The mesh pattern is the foundation of the numerical discretization of governing equations. The computational accuracy is significantly affected by mesh size and mesh quality [96]. This section presents the grid topology design and selection of optimum grid size for numerical studies. a non-uniform structured grid is designed using ANSYS FLUENT ICEM.

2.14.1 Grid Topology for Forward and Reverse Injection on the Flat Surface

To ensure the computational accuracy in LES, all the computational domains were discretized by structural hexahedral cells as shown in Fig.2.18 (a)-(d). The grid used for the numerical study of all four domains shows nearly similar topology, the only number of grid points is slightly different from each other. As the turbulent length scale is highly mesh-sensitive for LES-based computation [97,98], a careful design of the computational grid is a prerequisite. The grid is highly refined near the wall regions and secondary flow exits.

Table.2.4: LES grid refinement comparison with previous studies.

S No.	**Authors**	**Non-dimensional grid refinement parameters**	**Non-dimensional grid refinement parameters (Present LES study)**
1	Jiang et al. [99]	$\Delta X^+ < 90$; $\Delta Y^+ = 0.24$; $\Delta Z^+ = 161.8$	$\Delta X^+ < 60$; $\Delta Y^+ < 1$; $\Delta Z^+ < 60$ where ΔX^+, ΔY^+ and ΔZ^+ represent the non-dimensional grid spacing near the wall in the direction tangent to the wall, normal to the wall, and spanwise respectively.
2	Georgiadis et al. [100]	$50 \leq \Delta Z^+ \leq 150$; $\Delta Y^+ < 1$; $15 \leq \Delta Z^+ \leq 40$	
3	Johnson and Shyam et al. [101]	$\Delta X^+ \sim 35$; $\Delta Y^+ < 1$; $\Delta Z^+ \sim 16$	
4	Pachpute and Premachandran [102]	$\Delta X^+ < 100$; $\Delta Y^+ < 2$; $\Delta Z^+ < 30$	
5	Babu and Sarkar [103]	$\Delta X^+ \approx 50$; $\Delta Y^+ \approx 1$; $\Delta Z^+ \approx 20$	

The minimum size of the grid for all computational domains in the direction normal to the wall is 5×10^{-6} (normalized by $L_{ref} = 40D$, where $D = 10^{-3}$ m). For the present LES study, the grid topology is carefully designed to ensure computational accuracy.

The recent LES study of Georgiadis et al. [100] recommends the wall-resolved LES rather than the grid convergence study due to the basic nature of LES. However, in our present study, the basic criteria for grid selection are the total number of cells as well as the non-dimensional grid refinement parameters, followed by the previous LES studies which are shown in Table. 2.4. The mesh is well-refined near the walls and critical zones. Therefore, the grid density in the domain is characterized by: $\Delta X^+ < 60$, $\Delta Y^+ < 1$, and $\Delta Z^+ < 60$ where ΔX^+, ΔY^+ and ΔZ^+ represent the non-dimensional grid spacing near the wall in the direction tangent to the wall, normal to the wall, and spanwise respectively, followed by previous LES literature [100–105]. The grid resolution near the wall surface for different holes viz: FC, RC, FS, and RS can be described in terms of non-dimensional ratios, $\Delta X/L_{ref} < 0.0017$ and $\Delta Y/L_{ref} < 0.0065$.

2.14.2 Grid Topology for Single-Slot Injection Location on the Corrugated Surface

In the present study, the governing equations are discretized using non-uniform structure grids. Fig.2.19 shows the typical layout of the meshing technique used in this study. The figure shows that the grids are well-refined near the walls and cross-flow mixing regions. The wall regions are well refined to capture the boundary layer physics accurately and for that, the non-dimensional grid spacing (ΔY^+) is maintained below 1 whereas (ΔX^+) is maintained below 34. The grid refinement factor is maintained greater than 1.3, followed by [106]. To obtain the numerically grid-independent solution, the three different grids (i.e., 75132 nodes (Grid-1),125828 nodes (Grid-2), and 192108 nodes (Grid-3) are selected and the centreline effectiveness is compared. Figure 2.20 shows the comparison of centreline effectiveness for injection location, L_0 at blowing ratio (M= 1 and density ratio (DR= 1.095). From Fig.2.19, it can be observed that all three grids (Grid-1, Grid-2, and Grid-3) show close agreement near the injection locations upto $X/\lambda= 0.12$; after that, the deviations can be observed between Grid-1 and Grid-2. Moreover, the predictions of Grid-2 and Grid-3 are in consensus. The maximum variation in the predictions of Grid-2 and Grid-3 is ± 1.95% (between $X/\lambda= 0$ to1). Finally, the optimum grid size (Grid-2) is selected for further investigations considering a balanced approach between accuracy and computational resources.

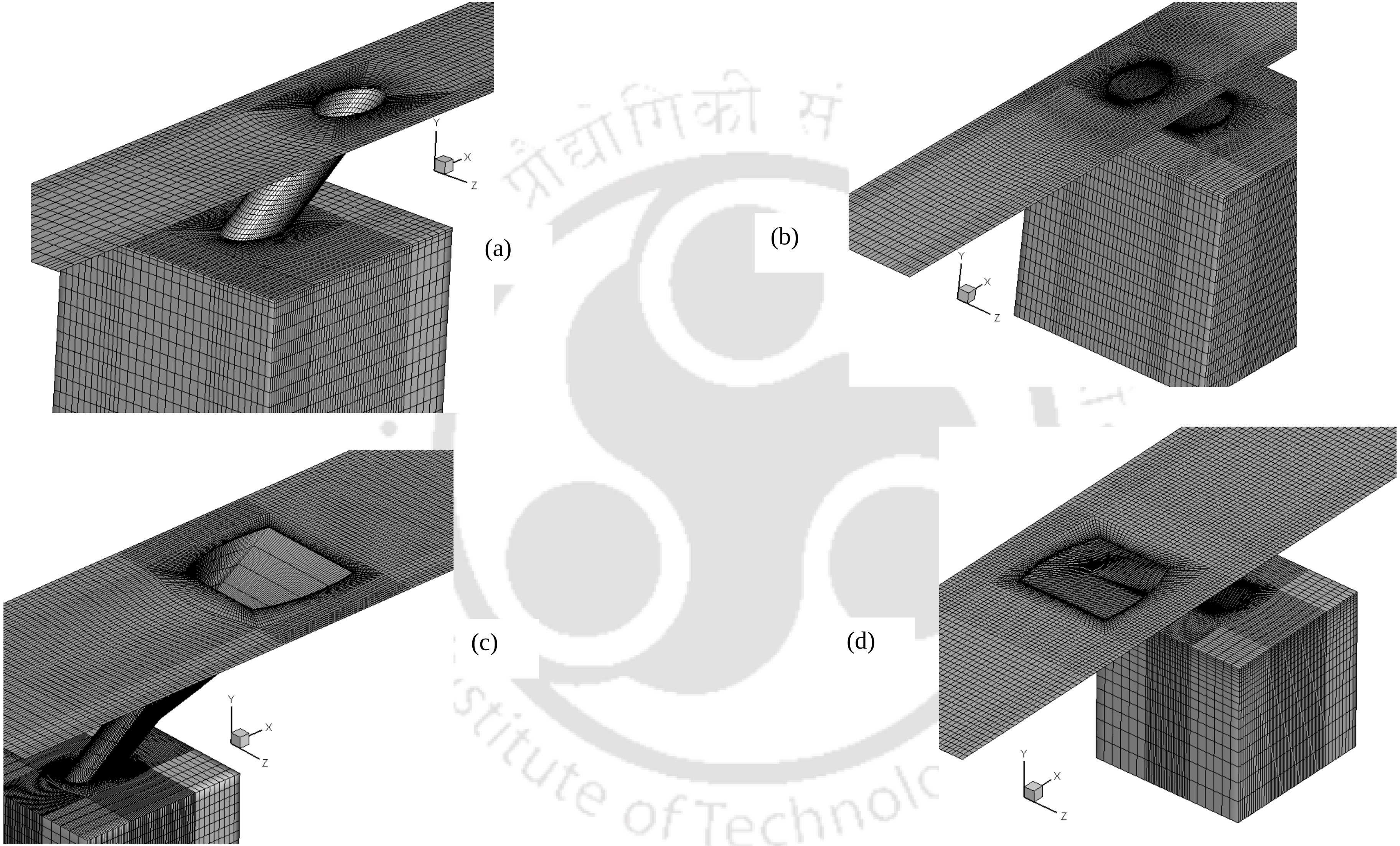

Fig.2.18: Typical mesh for 3D computational domain: (a) forward cylindrical hole (FCH); (b) reverse hole (RCH); (c) forward shaped hole (FSH); (d) reverse shaped hole (RCH).

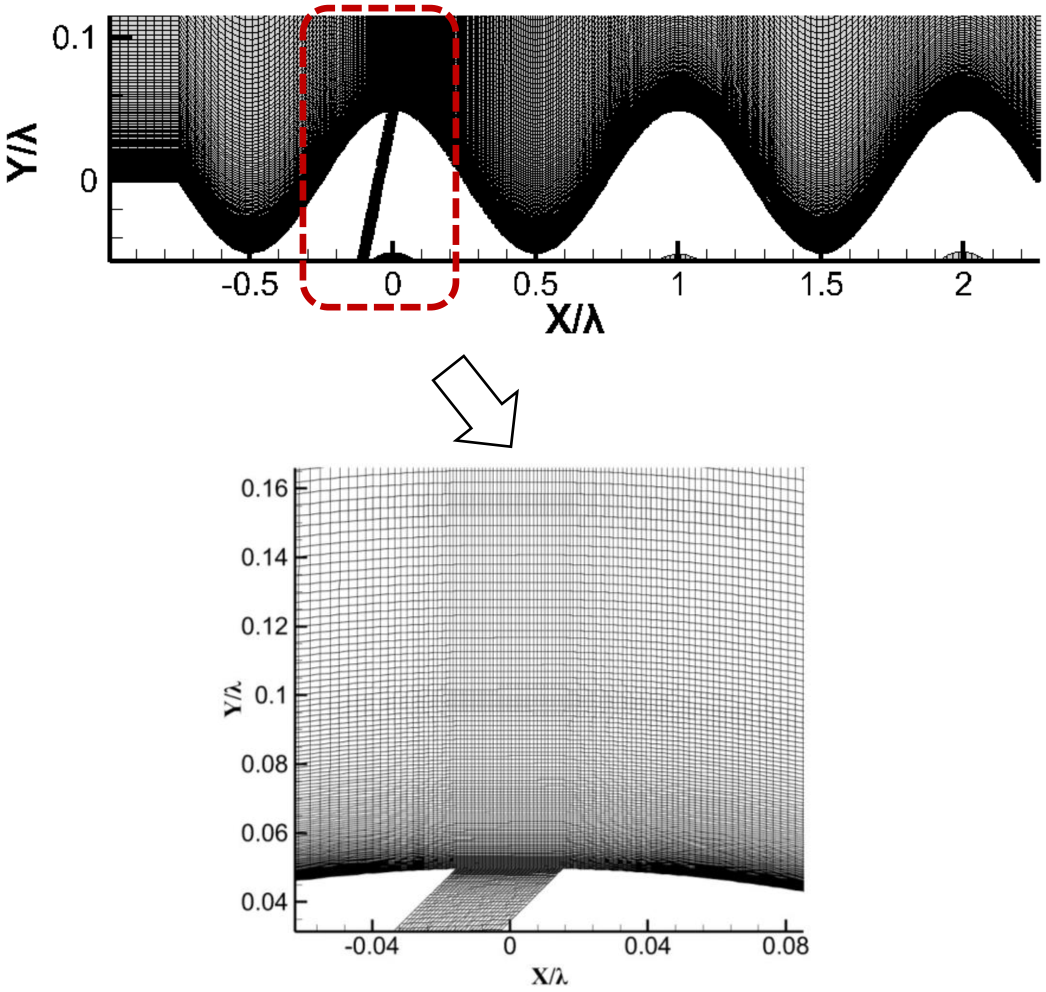

Fig.2.19: Typical mesh for single slot injection

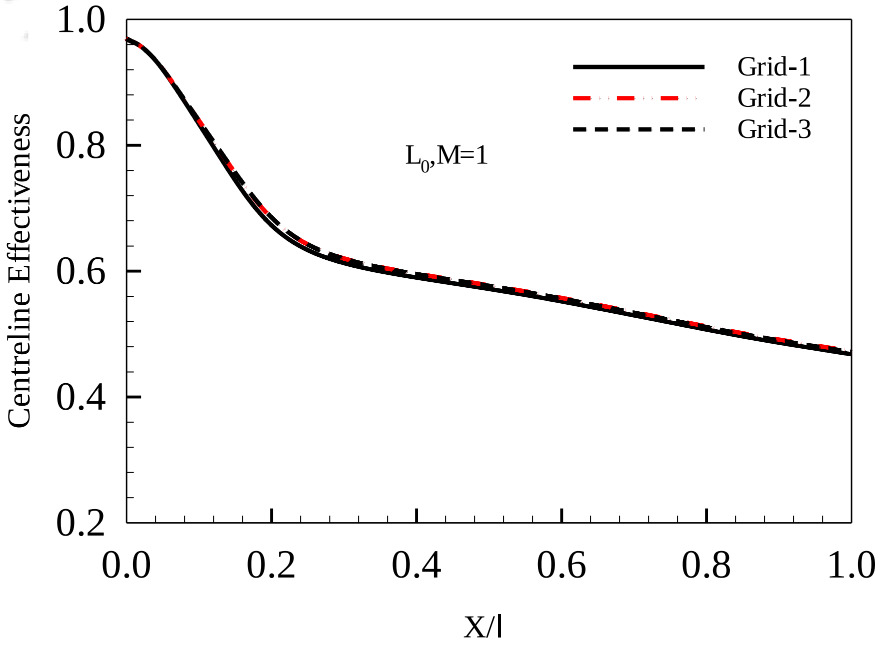

Fig.2.20: Grid independence study for 2D computational domain with single slot injection.

2.14.3 Grid Topology for Double-Slot Injection Location on the Corrugated Surface

To resolve the boundary layer physics, the grids are highly refined near the solid walls, as shown in Fig.2.21. Moreover, the grids are also refined in the region where both mainstream and secondary streams cross flow. The grid resolution near the regions of the solid wall is specially built to keep the non-dimensional wall coordinate (ΔY^+) less than unity. Three different grids (i.e., 147902 nodes (Grid-1), 205401 nodes (Grid-2), and 261941 nodes (Grid-3)) are chosen to conduct the grid sensitivity test.

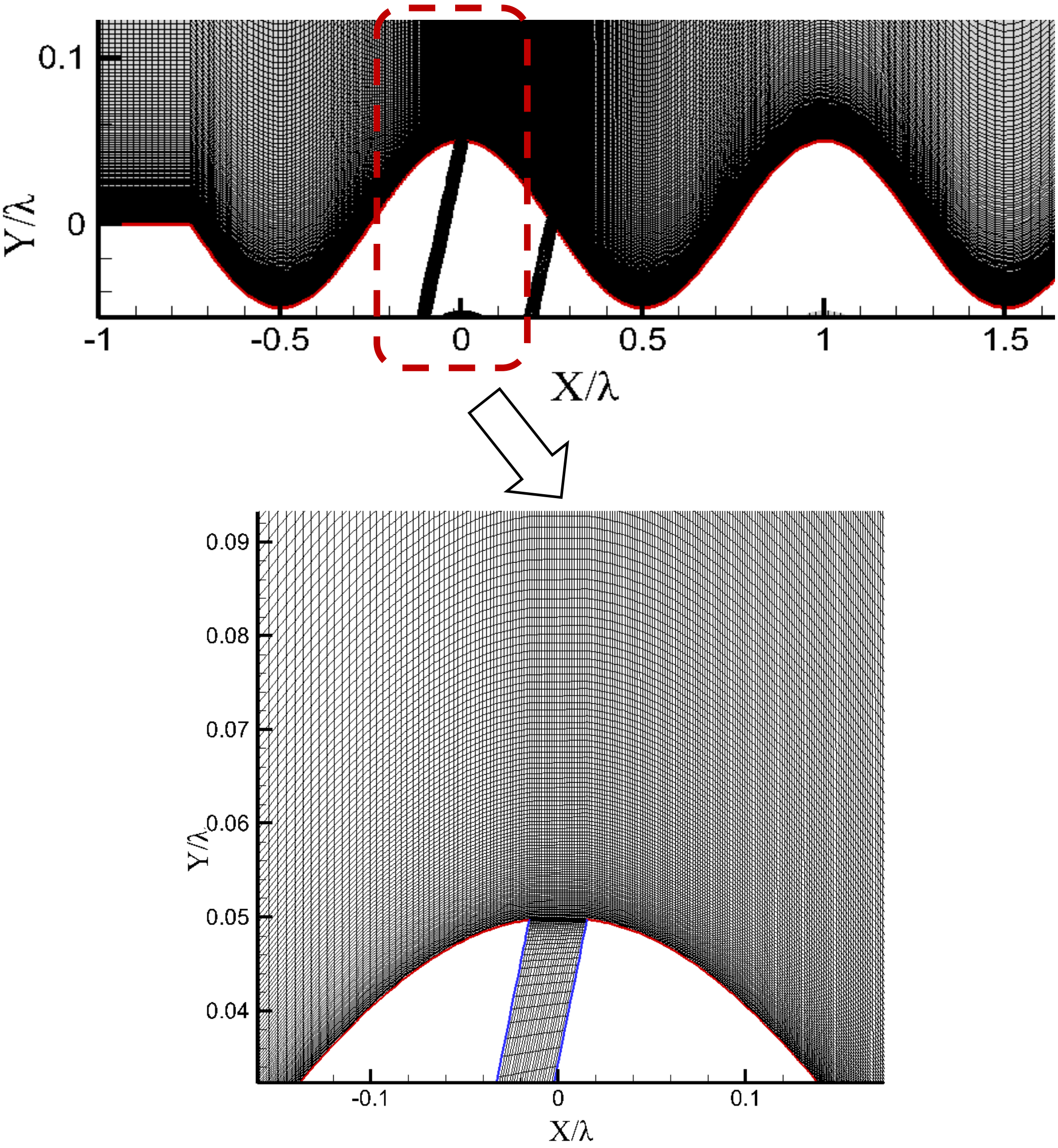

Fig.2.21: Typical mesh for double slot single location.

The mesh refinement factor is 1.4. The slot film cooling effectiveness downstream of holes is analysed for selected grids. Figure 2.22 shows the comparison of slot effectiveness for injection location L_0-L_{25} at blowing ratio (M=1), and density ratio (1.095). Figure 2.22 clearly shows that all three selected grids show close agreement for the slot effectiveness, and Grid-2 and Grid-3 show concurrency with a maximum deviation of 0.25%. Therefore, the grid setup of Grid-2 was finally adopted for further study by comprehensively considering the computational cost and accuracy.

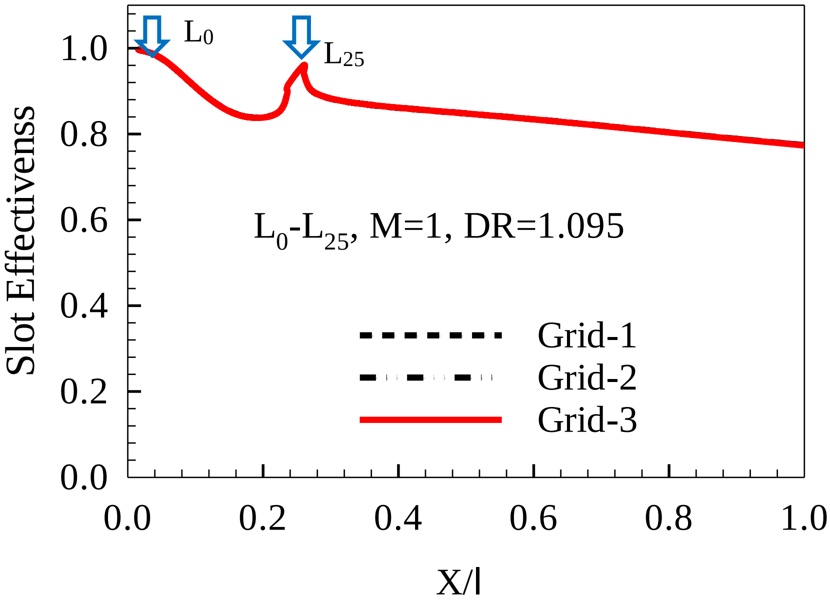

Fig.2.22: Grid dependence test for double slot single location.

2.14.4 Grid Topology for Forward and Reverse Injection on the Corrugated Surface

The computational study is highly sensitive to the grid topology; therefore, the grids are carefully designed, and focus is given while refining grids in critical areas. This study uses non- non-uniform structured hexahedral grid, as shown in Fig.2.23. In the near-wall region and cross-flow region, the mesh is highly refined to accurately capture important parameters such as the steep gradients of pressure, velocity, and temperature. The dimensionless distance ΔY^+ is maintained below unity. In order to obtain grid-independent results, a mesh sensitivity analysis is conducted for the forward case using the Realizable k-ε turbulence model. Three different grids with 1368480 nodes (Grid1), 1785264 nodes (Grid2), and 2567035 nodes (Grid3) are employed for the grid sensitivity study. The grids are increased by increasing nodes in all three directions, i.e., X, Y, and Z. Fig.2.24 compares the film cooling effectiveness along the centreline, all three grids show close agreements. Therefore, the grid setup of 1785264 nodes is finally adopted by comprehensively focusing on the computational cost and precision.

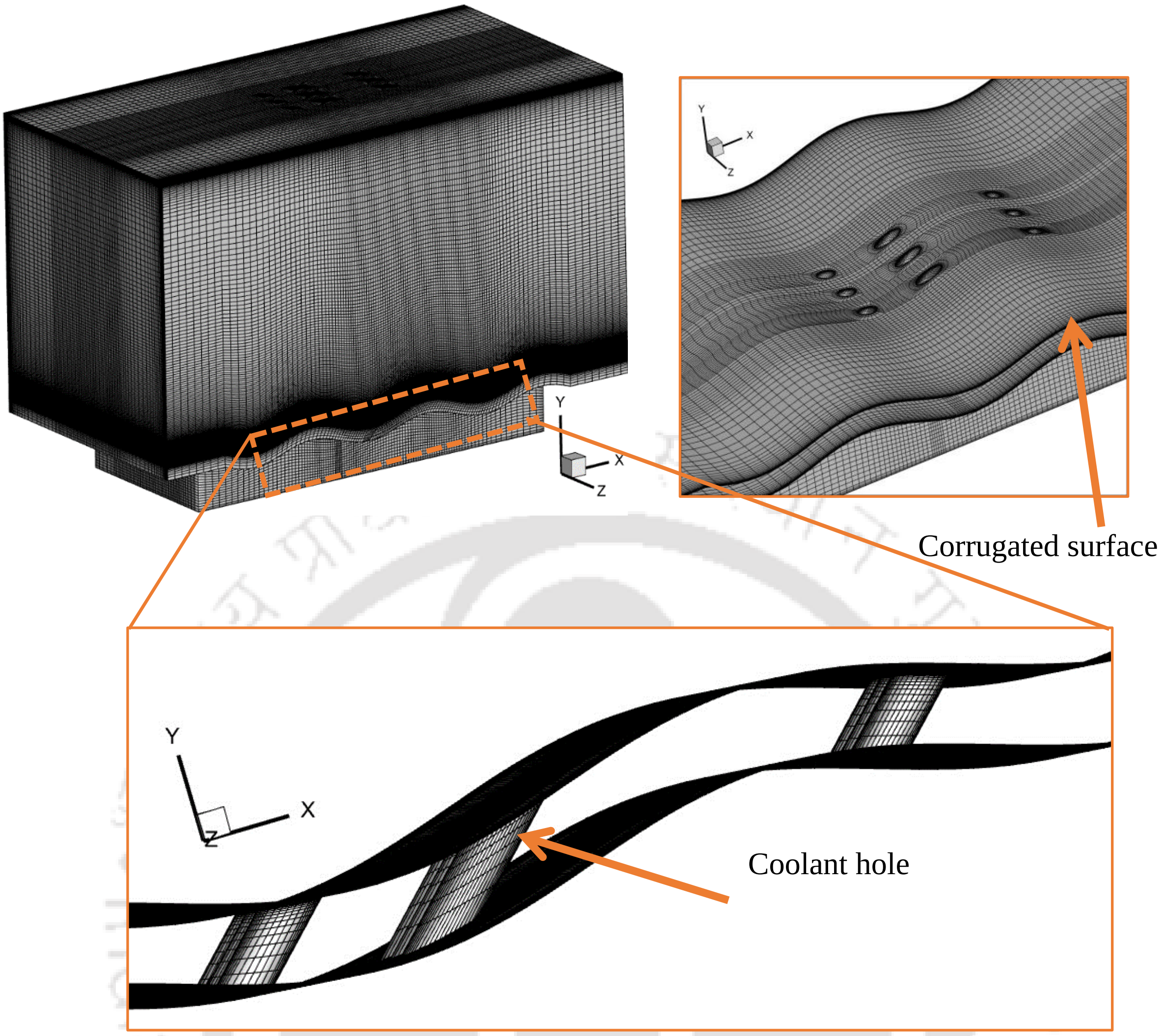

Fig. 2.23: Typical mesh for reverse injection study on corrugated surface.

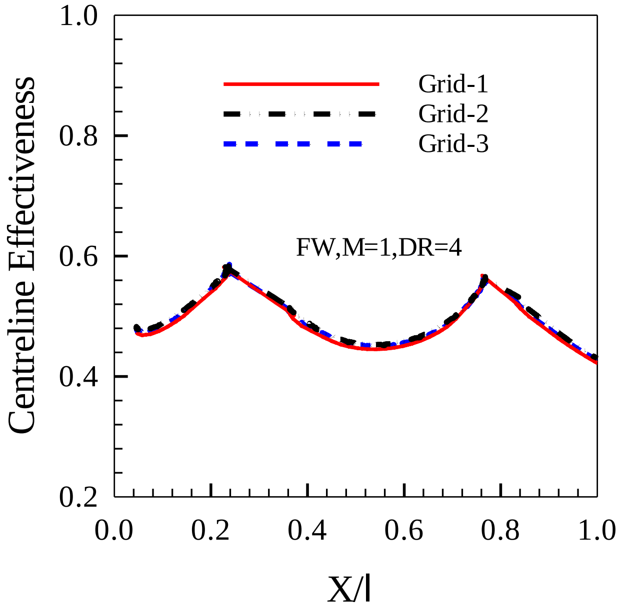

Fig. 2.24: Grid independence test for reverse injection study on corrugated surface.

2.15 Conclusion

In this chapter, both the experimental and numerical methodology of the present work is discussed. The measurement techniques, calibration methodology, and uncertainty calculations are discussed in detail. The results obtained through the present experimental procedure are also compared with the available experimental data, and the results show good agreement. Therefore, the present experimental procedure and calibration techniques can be adopted for further experimental studies. This chapter also presents detailed descriptions of all the computational domains along with the governing equations and turbulence modeling. Finally, the grid topology for different computational domains is summarized.

CHAPTER 3: LARGE EDDY SIMULATIONS FOR FILM COOLING ASSESSMENT OF CYLINDRICAL AND LAIDBACK FAN-SHAPED HOLES WITH REVERSE INJECTION

3.1 Introduction

In this chapter, the results obtained from three-dimensional numerical study have been presented for both forward and reverse injection using cylindrical and shaped holes. The formation of counter-rotating vortex pair (CRVP) is one of the major issues in film cooling. The CRVP promotes coolant jet lift-off from the surface which further causes a significant reduction in coolant coverage over the surface. The previous works on reverse injection film cooling holes show promising design to mitigate the problem of kidney vortices. However, the flow structure related to the reverse cylindrical and shaped holes is not well-understood in available experimental works. Motivated by the above challenges of film cooling flow, a due focus has been given on cylindrical and shaped holes. Shaped holes show promising performance over conventional cylindrical holes in forward configuration.

For the numerical simulations of film cooling flow, the selection of a suitable turbulence model is vital. The selection of a suitable turbulence model is a reasonable compromise between desired accuracy and computational resources. The previous studies on flat plate film cooling comprehensively discussed the various two-equation models turbulence models [48]. Moreover, it is well documented in the literature that RANS is not suitable for predicting the instantaneous flow feature of a film cooling flow[29]. Therefore, in the present study, large eddy simulation is carried out to investigate the film cooling performance and flow characteristics of the forward-cylindrical hole (FCH) and reverse cylindrical hole (RCH), forward-shaped hole (FSH), and reverse-shaped hole (RSH). The numerical model is validated with available experimental data [51], and further parametric study is extended for the actual operating conditions of gas turbines. The study is carried out for a blowing ratio; M =1, density ratio; DR = 2.42, and injection angle; $\alpha = 35^o$ and Reynolds number based on secondary flow, and hole diameter (0.9×10^3). The film cooling performance of both cylindrical shaped holes are compared for centreline, lateral average, and local lateral effectiveness, in both forward and reverse configuration. Apart from that the three-dimensional vortices are also presented for different flow configurations.

3.2 Numerical Study

3.2.1 Computational Domain

In the case of the present LES study, the computational domain is three-dimensional. A detailed description of the domain is given in the previous chapter 2 (section 2.9.1, and 2.9.2). To protect the surface from the detrimental effect of hot mainstream flow, a secondary stream relatively at a lower temperature is injected at 35^o with different hole configurations viz: (i) Forward cylindrical hole (FCH); (ii) Reverse cylindrical hole (RCH); (iii) Forward shaped hole (FSH); (iv) Reverse shaped hole (RSH). The secondary stream of air is supplied to the hole via the plenum chamber of dimensions 5D×5D×5D. The film cooling performance is evaluated over the flat surface for the length of 30D where D is the diameter of the hole, considered as 1 mm [31].

3.2.2 Numerical Schemes and Solutional Methodology

In the present numerical study, the large eddy simulations are carried out and the filtered equations of continuity, momentum, and energy are solved by finite volume method-based CFD source codes (OpenFOAM 5.0 and Greenshields [94]). The grids are carefully designed and well-refined near important regions (as discussed in chapter 2, section 2.14.1). The details of the LES governing equations are given in the previous chapter 2 (section 2.10.6). The convective and diffusive fluxes are calculated by second-order accurate central differencing scheme. The temporal term in governing equations discretized by the backward scheme is second-order accurate. The solution is considered to be converged when the residuals of continuity, velocity, turbulence quantities, and energy fall below 10^{-6}. In order to accurately capture the cross-flow physics, the time step is selected based on the Courant–Friedrichs–Lewy (CFL) number, CFL = 0.8 according to the guidelines of Acharya and Leedom [95] . The PIMPLE algorithm is used for pressure and velocity coupling.

The present numerical simulations are transient by nature, but the quasi-static state is reached after 15,000-time steps. So, the time averaging is performed for the parameters such as pressure, temperature, and velocity. The quasi-static state is referred as the condition where statistical differences in the time-averaged quantities are negligible (generally lie in the range of 2-4%). The time averaging is performed over a period after quasi-static conditions until the statistical differences in the average quantities fall below the acceptable range of (2%), which further requires 10-15 flow overtime. The flow over time is the time taken by the mainstream to reach the outlet.

3.2.3 Boundary Conditions and Operating Parameters

For both the mainstream and the secondary stream, the air is used as the working fluid. Since there is a significant temperature difference. Therefore, temperature-dependent thermophysical properties are used. The temperature-dependent thermophysical properties are expressed in the previous chapter 2 (section 2.11.1). The inlet of the mainstream and plenum is assigned to be a time-invariant turbulent velocity profile obtained from the RANS study of channel flow. The outlet of the domain is assumed to be pressure exit with zero-gauge pressure. All the input parameters for the different geometrical configurations are given in Table.3.1. The side walls in the lateral direction of the mainstream flow of the flow field are considered as the periodic boundary. All other walls in the domain are assigned as the no-slip adiabatic condition.

Table.3.1: Operating parameters considered in the present numerical study.

Parameters	**Forward-cylindrical (FCH)**	**Reverse cylindrical (RCH)**	**Forward shape (FSH)**	**Reverse shape (RCH)**
$Re_{sec.}$	0.9×10^3	0.9×10^3	0.9×10^3	0.9×10^3
Blowing ratio (M)	1	1	1	1
Density ratio (DR)	2.42	2.42	2.42	2.42
T_{ms} (K)	1561	1561	1561	1561
$T_{sec.}$ (K)	644	644	644	644

All simulations use mainstream conditions of 128 m/s at 1561 K with the inlet temperature in the plenum specified as 644 K at a density ratio (DR) of 2.46. The plenum inlet boundary condition is fixed for blowing ratio (M = 1) and secondary flow Reynolds number of 0.9×10^3 in coolant pipe. The Large Eddy Simulations are highly sensitive to grid topology. Therefore, to ensure computational accuracy in LES, all the computational domains were discretized by structural hexahedral cells as shown in the previous chapter 2 (section 2.14.1).

3.2.4 Fluid Flow and Heat Transfer Validations

The computational results were validated with the experimental results from the literature [51]. For effectiveness validations the operating parameters viz. M = 1 and DR = 0.91 are considered which is the same as experimental conditions of reference [51]. For this validation, one might expect film heating instead of film cooling because DR < 1. For flat plate film cooling, it has been shown that at low-density ratio film heating is analogous to film cooling [48].

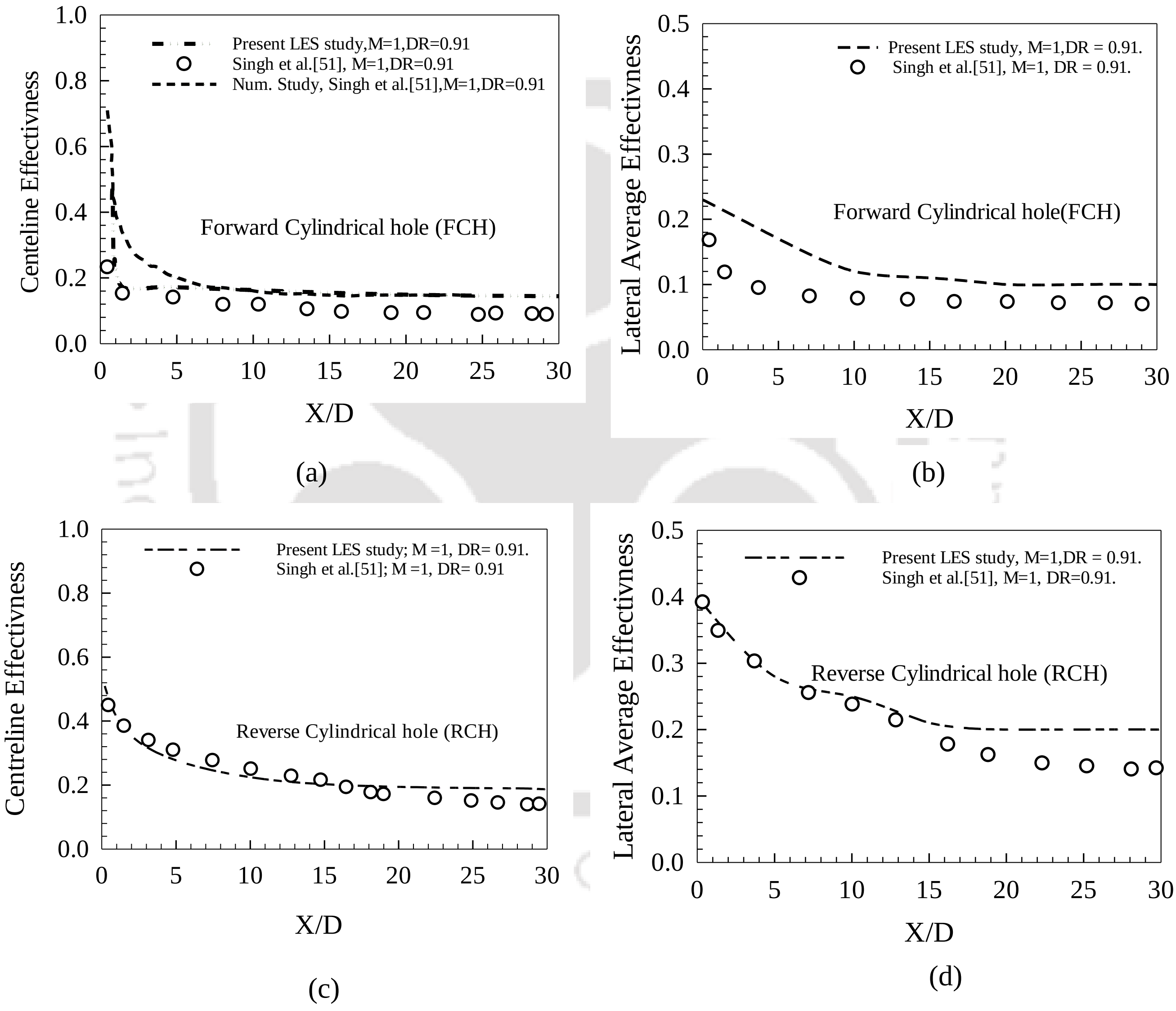

(a) (b)

(c) (d)

Fig.3.1: Comparison of the present numerical result of effectiveness with the experimental results of Singh et al. [51].

The centreline and lateral average effectiveness of forward and reverse hole are compared with reference data. Figure 3.1 (a) shows that the centreline effectiveness of the forward cylindrical hole is in close agreement with the experimental data. The predictions of the present LES model is more accurate as compared to two-equation model (Realizable k-ε). From Fig. 3.1 (b), it can be seen that the lateral average film cooling effectiveness has small deviations near the downstream of the coolant hole. The center line effectiveness and lateral average effectiveness of reverse hole given in Figs. 3.1 (c-d) showed excellent agreement near the hole. However, a small deviation can be observed downstream of the hole. The present computational model follows the nature of variations shown in the experimental data; however, the film cooling effectiveness is slightly over-predicted.

3.3 Results and Discussions

3.3.1 Film Cooling Effectiveness: Centreline and Lateral Average

In order to compare the centreline film cooling effectiveness for various hole configurations, the effectiveness is plotted along the centreline (Z/D = 0) over the flat surface as shown in Fig. 3.2 (a). It can be observed from Fig. 3.2(a) that the centreline effectiveness of FCH and FSH are much higher than that of RCH and RSH along the downstream (i.e., X/D). It can also be inferred that FCH is more effective along the centreline than FSH for a short distance downstream of the hole, i.e., X/D = 8. From X/D = 8 to 30, FSH effectiveness is maximum among all hole configurations. The centreline effectiveness of FCH is relatively higher at a very short distance downstream of the hole due to more coolant skewness toward the narrow central part of the surface. Lateral average film cooling effectiveness would be a better representation for the performance assessment of these cooling holes. Figure 3.2 (b) and (c) shows the variations of lateral average effectiveness of various hole configurations for both cylindrical and shaped holes. The lateral average is obtained from the downstream edge of the hole (where no-hole footprints are present). It may be emphasized that the width of the shaped hole is 6D due to its lateral expansion (more than 3D in the lateral direction). As the domain width is different for both cylindrical and shaped holes, the lateral average effectiveness is compared separately in Fig. 3.2 (b) and Fig. 3.2 (c). For the FCH and RCH lateral averaging is taken over lateral distance, Z/D = -1.5 to 1.5. In the case of shaped holes, FSH, and RSH the lateral averaging is taken over the Z/D = -3 to 3. It is considered to be the most important effectiveness parameter in film cooling which represents the spread of the coolant stream at each lateral location, downstream of the injection holes. Figure 3.2 (b) clearly shows that the lateral average effectiveness of RCH is higher than FCH, for all locations along with the flow. The effectiveness of RCH is 2 times the FCH near the hole at X/D = 1. However, in Fig. 3.2 (c), RSH shows better lateral average effectiveness as compared to FSH near the hole from X/D = 2 to 10, and in the near the hole region (X/D = 1), the effectiveness is 1.42 times the FSH. The effectiveness contours in Figs. 3.3 (a)-(d), reflects that the coolant coverage is better in the case of reverse holes than the forward hole, which essentially means better lateral average effectiveness. Apart from these observations, Figure 3.2 (c), reveals that the RSH is 1.42 to 1.16 times more effective than FSH at X/D =2 and X/D = 30 respectively.

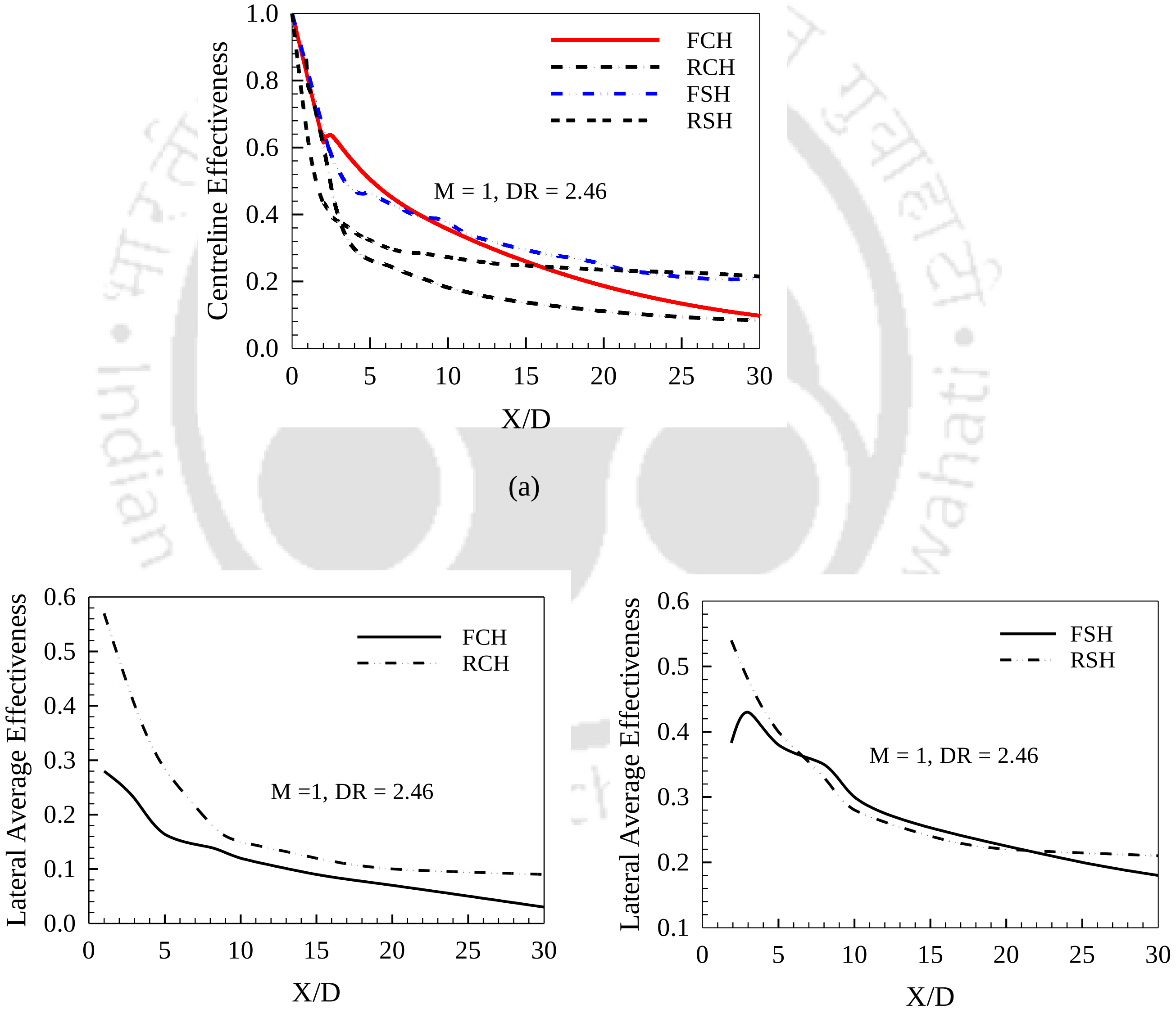

(a)

(b)

(c)

Fig.3.2: Effectiveness plot for various hole configurations: (a) centreline effectiveness; (b) lateral average effectiveness (cylindrical holes); (c) lateral average effectiveness (shaped holes).

Figures 3.4-3.7 show the streamlines contours of non-dimensional temperature, theta (θ). The formation of vortex pair in the case of film cooling flows plays a vital role in the mixing of coolant with the mainstream and coolant jet lift-off that finally governs the film cooling performance. It has been seen that as coolant/secondary jet exit from the simple cylindrical hole into the cross-flow region and split into counter-rotating pairs (CRVP) which is of similar evidence from literature [51]. In this study, four different planes are considered for the systematic understating of the formation of CRVP. Figure 3.4 (a) shows the flow streamlines for the FCH, in the X-Z plane at Y/D = 0. The streamlines near the flat surface at Y/D = 0, is presented by taking a plane one node above the surface. The streamlines for the FCH appear to be symmetric and skewed towards the centreline. As a result of this fact, most of the cooling effects can be seen along a narrow part of the central region. At X/D = 1, the formation of kidney vortices in the plane Y-Z i.e., normal to the flow leads to "coolant stream lift-off" through mutual induction as shown in Fig. 3.4 (b). As the flow moves in the downstream direction (Fig. 3.4-c) at X/D = 3 in the Y-Z plane, the strength of CRVP increases which leads to coolant lift-off. In Fig. 3.4 (d) at Y/D = 0.5 in the X-Z plane, some cooling effect can be observed that represents that coolant is not trapped below this plane and hence the coolant coverage over the surface is lower. The present observation of counter-rotating vortex pairs for FCH shows close consistency with the previous studies [26].

Figure 3.5 (a) illustrates the three-dimensional vortex pair formation for the RCH. This figure distinctly shows a vortex pair in the plane parallel to mainstream flow which promotes the coolant spread in the lateral direction. The vortex pair shown in Fig 3.5(a) is distinctly different from the commonly observed CRVP. Referring to the coordinate sign convention in the present study, CRVP appears in the Y-Z plane downstream of hole whereas vortices formed in the case of the reverse hole are predominately in the X-Z plane. The other difference between these two vortices is: CRVP has a sense of upward movement which enhances mixing with the mainstream whereas vortices observed in the case of reverse holes direct fluid in the lateral direction. This results in the uniform spreading of the coolant onto the hot surface which eventually will diminish thermal stresses. Figure 3.5 (b) shows the formation vortex pair for the RCH in the plane of a flat surface (X-Z plane) at Y/D = 0. It can be observed from this figure that the vortices in the X-Z plane are extended to X/D = 4 downstream of the hole for the investigated flow conditions. The temperature of the coolant suggests that coolant is not mixed with the mainstream up to X/D = 4 and hence higher area-weighted average film cooling effectiveness is observed. Since the vortices observed in Fig. 3.5(a) are three-dimensional, the analysis on the Y-Z plane can shed some light on the propagation of these vortices. Figure 3.5 (c-d) shows the vortices in the Y-Z plane at X/D = 1 and X/D = 3, respectively. It can be observed from Fig. 3.5 (c) that the coolant penetrates into mainstream up to Y/D = 0.4 at X/D = 1, just after the injection. Despite the vortices, coolant remains confined to Y/D = 0.4 as downstream distance increases to X/D = 3, depicted in Fig. 3.5 (d). This also indicates that the vortices observed in the case of reverse holes do not have any sense of upward movement. Figure 3.5 (e) shows streamlines plot X-Z plane parallel to the flat surface at Y/D = 0.5. The plane reveals that the streamlines are more uniform and the coolant effect can be observed. This confirms that coolant is not mixed with the mainstream and provides an adequate blanket to the heated surface eventually enhancing the cooling effectiveness.

In the case of shaped holes, the observations are different from the conventional cylindrical holes. Figure 3.6 (a) represents streamlines for the FSH at Y/D = 0 in the X-Z plane, which shows a uniform pattern of flow streamlines without any skewness. However, a counter-rotating pair can be seen at X/D = 2 in the Y-Z plane, as shown in Fig. 3.6 (b) which further transforms into a kidney vortex accompanied by anti-kidney pair at X/D = 5 as shown in Fig. 3.6 (c). As a result of the strong anti-kidney pair in Fig. 3.6 (b), the tendency of coolant jet lift-off dominates. Thus, a better coolant coverage is observed in Fig. 3.6 (a)-(c) for FSH as compared to FCH. The present observations of FSH show consistency with previous experimental results from reference [107]. Despite the presence of anti-kidney vortices which are suppressing the upward movement of the coolant, Fig. 3.6 (d) shows that there is only a small amount of coolant at Y/D = 0.5. Similar to the reverse cylindrical hole, a three-dimensional vortex predominately in the X-Z plane is observed as depicted in Fig. 3.7 (a) and the formation vortex pair for the RSH in the plane of a flat surface (Z-X plane) at Y/D = 0, is shown in Fig. 3.7 (b). It can be observed that the penetration of the coolant into the mainstream at the location of injection is up to Y/D = 0.6 which is not significantly increased as downstream distance increases (Fig. 3.7-d). Rather, the lateral spread of the coolant increases with the increase in downstream distance. These vortices show similarity with the vortex pair discussed for the RCH in the previous section (Figs. 3.5a – b). It is also observed from Fig. 3.7 (b)-(c) as the jet moves downstream from X/D = 2 to 5, the strength of the counter-rotating vortex reduces and hence the jet lift-off also diminishes. Figure 3.7 (e) shows a plane parallel to the plane shown in Fig. 3.7 (a), where a more regular streamline with uniform coolant spread can be observed.

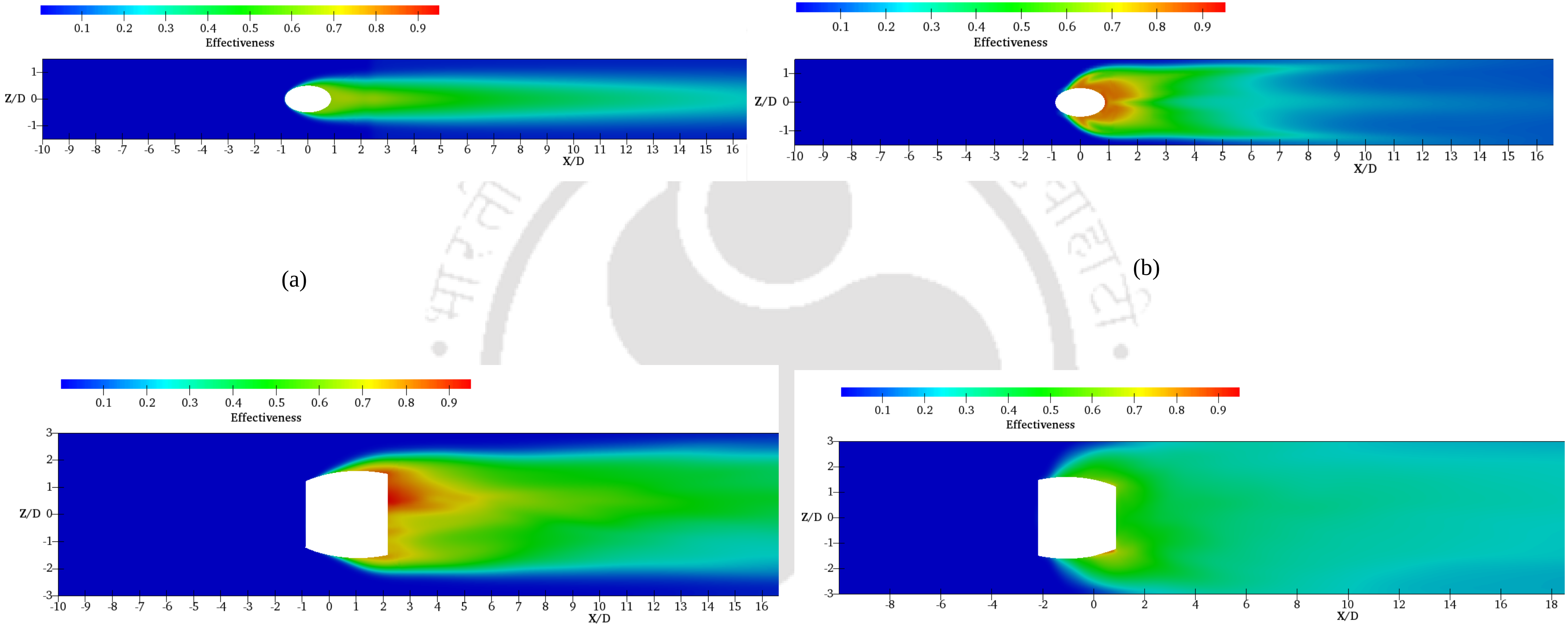

(a)

(b)

(c)

(d)

Fig.3.3: Effectiveness contours of various hole configurations: (a) effectiveness contour (FCH); (b) effectiveness contour (RCH); (c) effectiveness contour (FSH); (d) effectiveness contour (RSH).

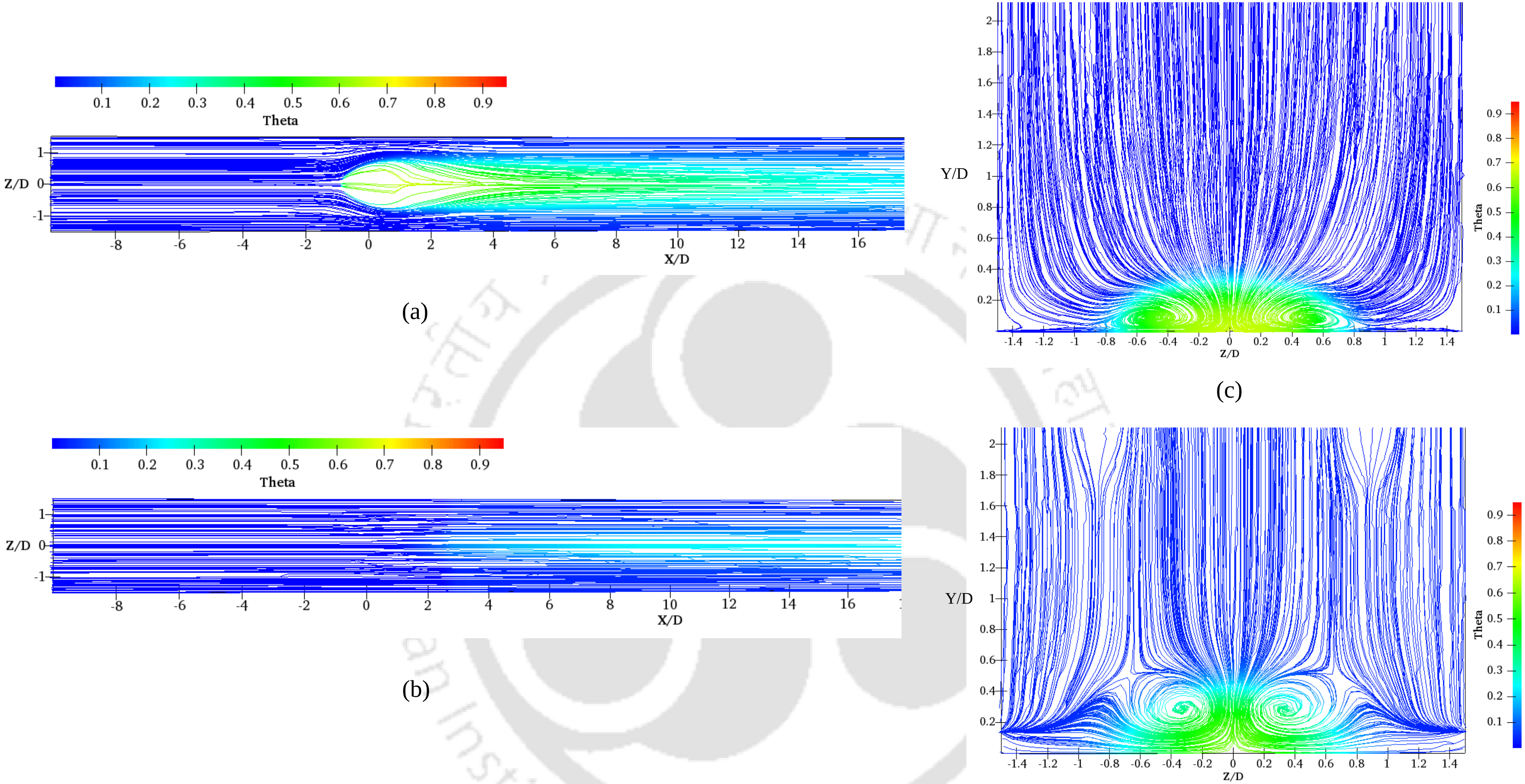

(a)

(b)

(c)

(d)

Fig.3.4: Streamline contours of non-dimensional temperature (θ) for FCH: (a) Y/D = 0, (X-Z plane); (b) X/D = 1, (Y-Z plane); (c) X/D = 3, (Y-Z plane); (d) Y/D = 0.5, (X-Z plane).

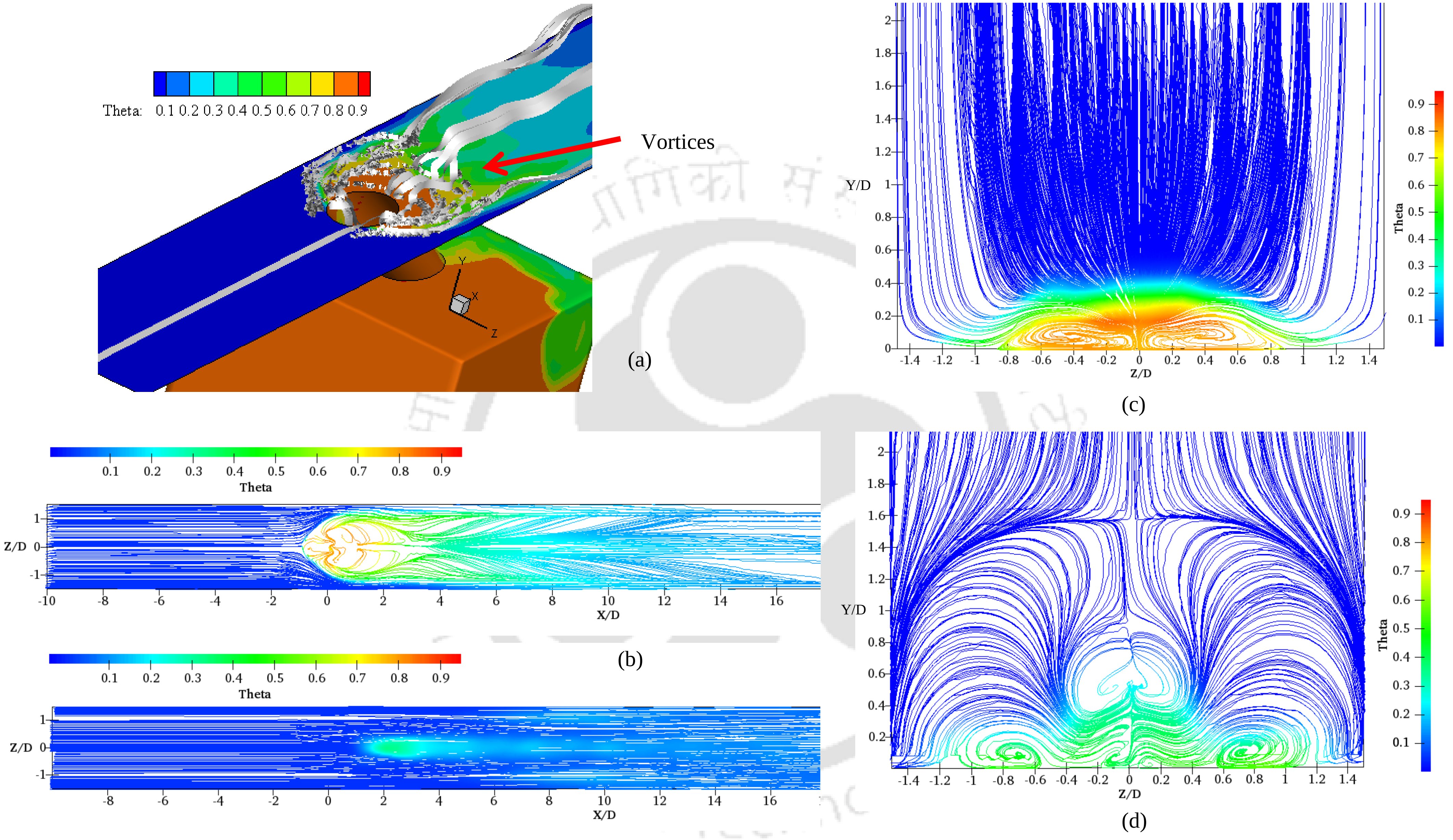

(a)

(c)

(b)

(d)

(e)

Fig.3.5: Streamline contours of non-dimensional temperature (θ) for FCH: (a) Three dimensional vortices; (b) Y/D = 0, (X-Z plane); (c) X/D = 1, (Y-Z plane); (d) X/D = 3, (Y-Z plane); (e) Y/D = 0.5, (X-Z plane).

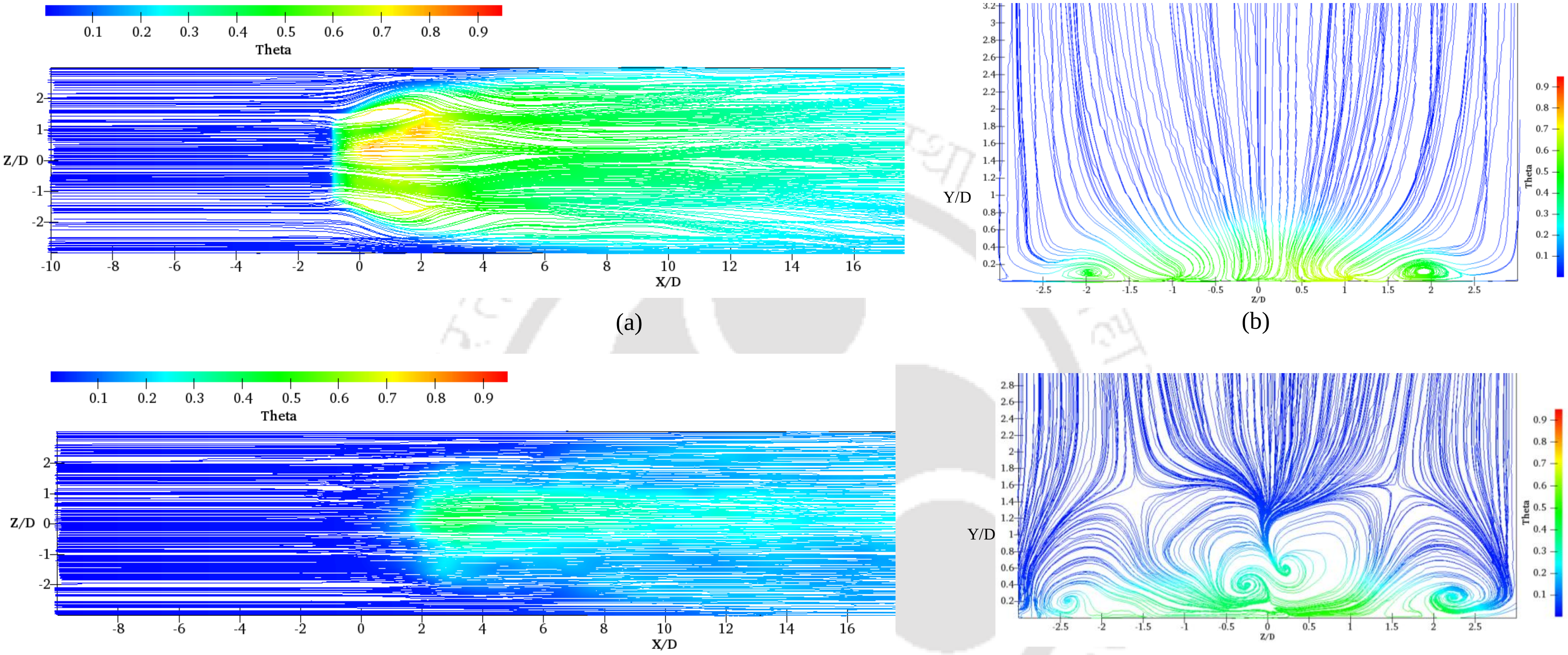

(a) (b)

(c) (d)

Fig.3.6: Streamline contours of non-dimensional temperature (θ) for FSH: (a) Y/D = 0, (X-Z plane); (b) X/D = 2, (Y-Z plane); (c) X/D = 5, (Y-Z plane); (d) Y/D = 0.5, (X-Z plane).

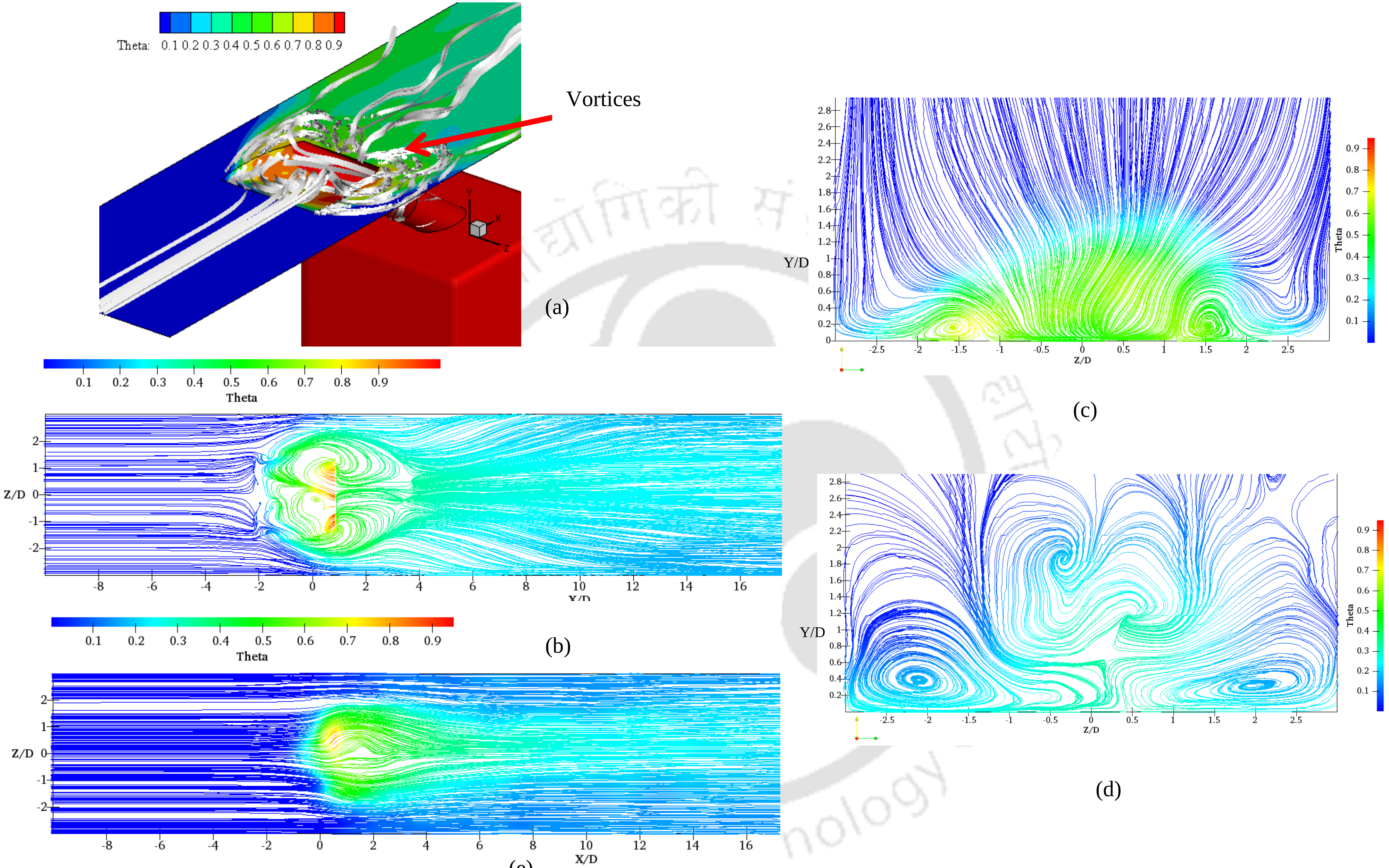

(a)

(b)

(c)

(d)

(e)

Fig.3.7: Streamline contours of non-dimensional temperature (θ) for RSH and FCH: (a) Three-dimensional vortices; (b) Y/D = 0, (X-Z plane); (c) X/D = 2, (Y-Z plane); (d) X/D = 5, (Y-Z plane); (e) Y/D = 0.5, (X-Z plane).

3.3.2 Local Lateral Effectiveness

The variations in local lateral film cooling effectiveness for various hole configurations are shown in Fig. 3.8. The different holes are compared for stream-wise distance X/D = 5 and 10. From Fig. 3.8 (a)-(b), it can be observed that for the FCH, the local effectiveness is relatively higher in the central region as compared to RCH. This is because of the more skewed flow of coolant along the central line. Apart from this fact, FCH coolant spread in the lateral direction is poor which results in a lower effectiveness and hence increased temperature (Figs. 3.3 (a) and (b)). However, the coolant coverage for RCH is much better than that of FCH, which leads to uniform effectiveness throughout the lateral directions of Z/D from -1.5 to 1.5 as shown in Fig.3.8 (a)-(b).

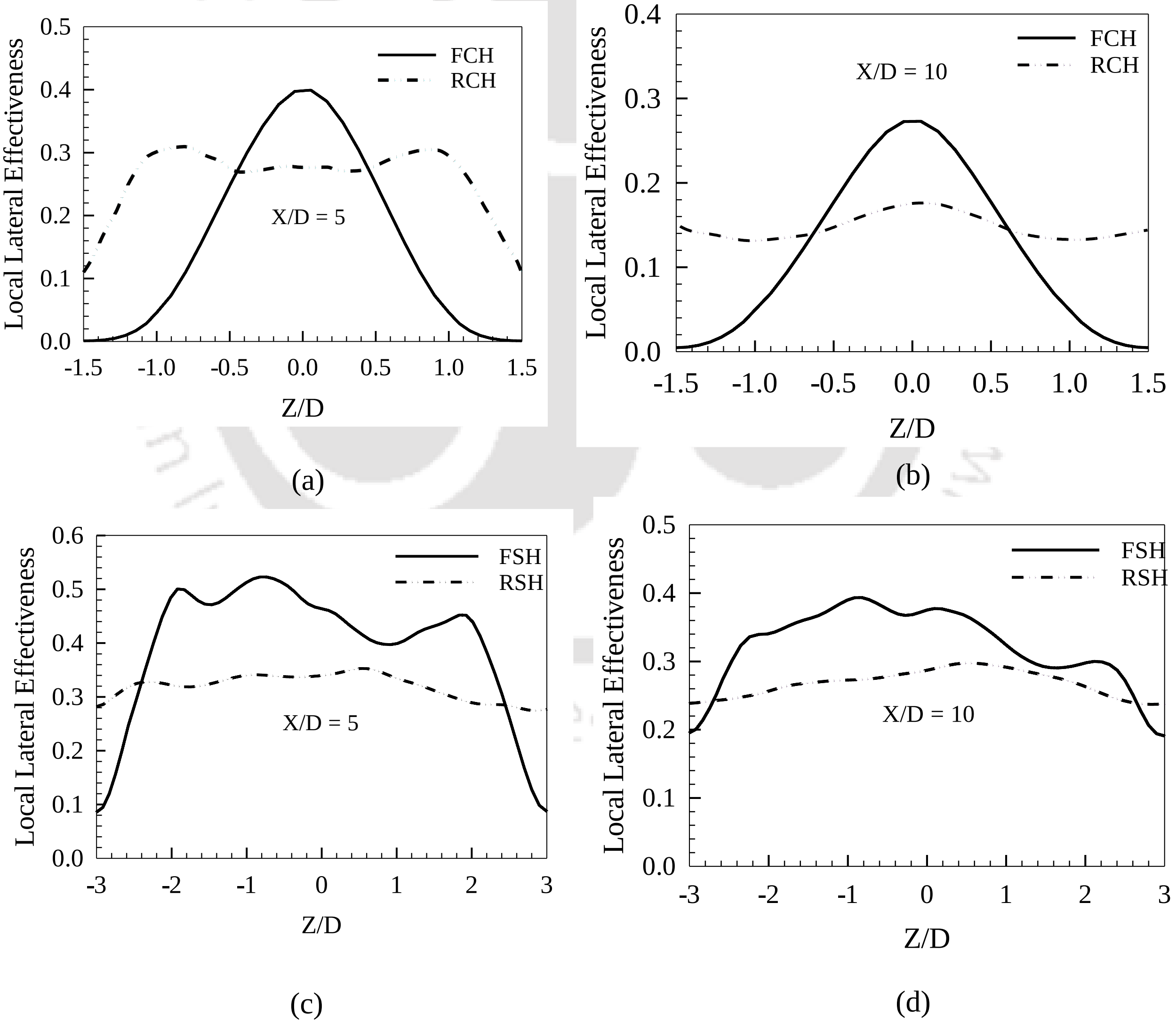

(a)

(b)

(c)

(d)

Fig.3.8: Local lateral effectiveness contours: (a) FCH and RCH at X/D = 5; (b) FCH and RCH at X/D = 10; (c) FSH and RSH at X/D = 5; (d) FSH and RSH at X/D = 10.

A similar observation is reported with FSH in Fig.3.8 (c)-(d), where the coolant coverage is much limited to the width of the hole in the central region at Z/D = 0, which leads lower effectiveness in the lateral directions of Z/D from -3 to 3, for X/D = 5 and 10. Most of the coolant spread in the lateral direction is limited to Z/D = -1 to 1 and beyond this region, the coolant spread is poor which results in a faster decay of lateral effectiveness for FSH. As compared to FSH the lateral effectiveness of RSH is much higher and coolant spread is almost uniform in the lateral directions of Z/D from -2 to 2. This phenomenon is seen from the contour results for FSH and RSH in Fig. 3.3 (c) and (d). The FSH coolant spread in the lateral direction is limited to the width of injection holes whereas, in the case of RSH, coolant spreading is almost double the width of the injection hole.

3.3.3 Flow Velocity Profiles

The flow characteristics near the secondary flow exit are shown in Fig.3.9. The present results for non-dimensional velocity magnitude compared with the experimental measurement [76] using particle image velocimetry (PIV). The available experimental data of PIV at VR = 0.28, M = 0.5, and DR = 1.53 are compared with the present numerical model at VR = 0.46, M = 1, and DR = 2.46 for quantitative comparison. Figure 3.9 shows the non-dimensional mean velocity magnitude for different hole configurations such as FCH, RCH, FSH, and RSH. The velocity profiles are plotted along Y/D for centreline locations at X/D = 0, 1, 1.5, and 2. All the velocity profiles look nearly similar outside the shear layer. However, the differences can be seen in the inner part of the shear layer i.e., vicinity of the cooling surface. The velocity gradients of FCH and FSH are steeper as compared to RCH and RSH for the investigated streamwise locations (i.e., X/D = 0 to 2). The steeper velocity profile for RCH and RSH shows higher turbulence due to its opposite flow to the mainstream. It may be inferred that the discharge coefficient is strongly influenced by injection configuration. The discharge coefficient is inversely proportional to the pressure drop in the coolant hole. The pressure losses are higher in reverse injection configurations resulting reduction in discharge coefficient as shown in Fig.3.10. Also, it will have a more aerodynamic loss on the mainstream flow. The results show that the qualitative trend of non-dimensional velocity follows the trend predicted by the experimental findings [76].

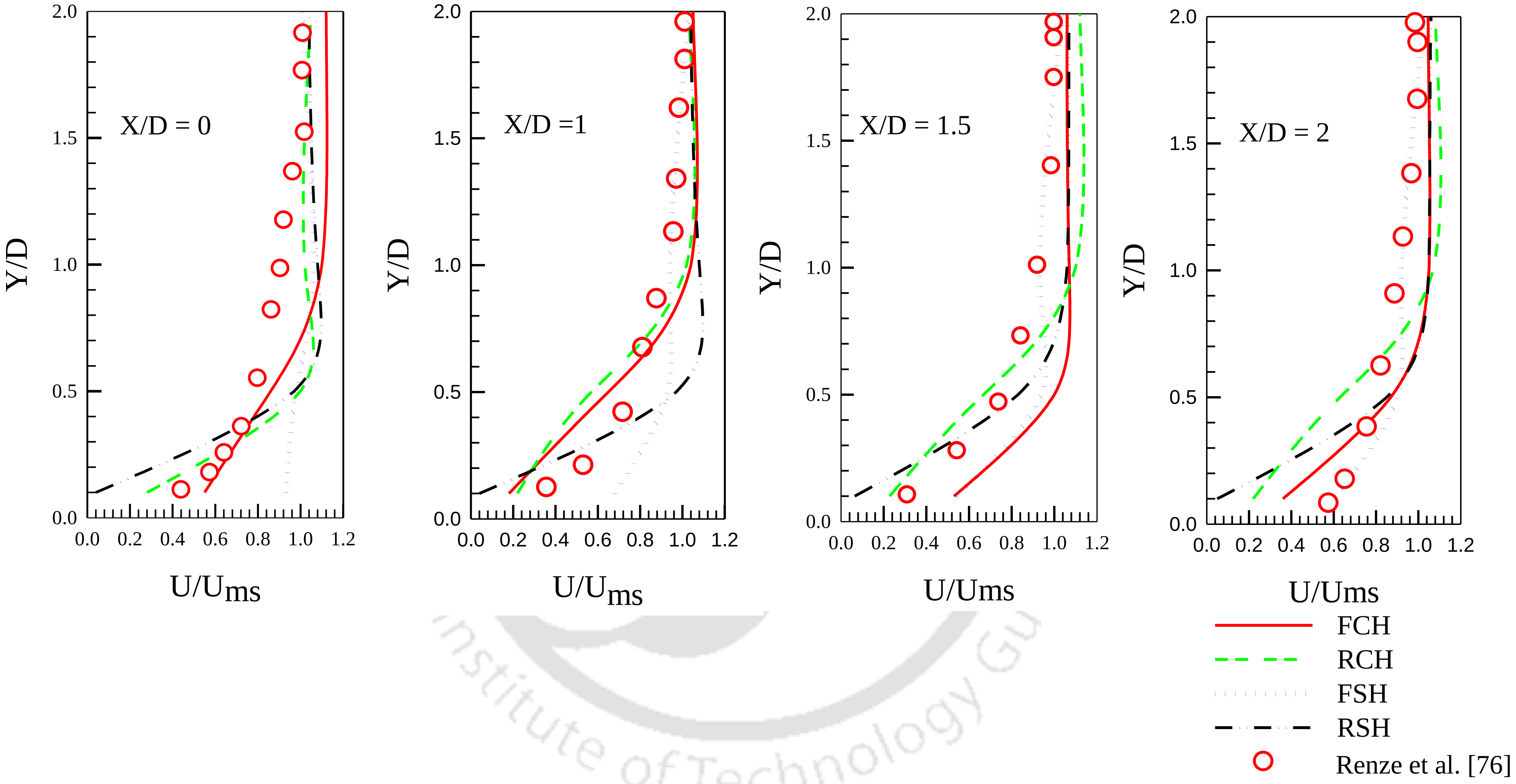

Fig.3.9: Comparison of non-dimensional velocity profiles of various hole configuration at centreline along the Y/D direction at various stream wise locations (X/D = 0, 1, 1.5, 2) with PIV results from reference [76].

3.3.4 Discharge Coefficient

The discharge Coefficient (C_d) is an important parameter to express the pressure losses through coolant injection holes. In the previous sections, it has been seen that the RCH and RSH, film cooling performance was found to be better than FCH and RCH (Fig. 3-b). However, one might expect higher pressure losses in the case of reverse injection holes since the flow of coolant is opposite to the mainstream. In this section, the discharge coefficient is plotted for all four-hole configurations viz. FCH, RCH, FSH, and RSH for comparison of the pressure losses. The discharge coefficient (C_d) is defined as the ratio of the actual mass flow rate to the theoretical mass flow rate in the coolant holes. The theoretical mass flow rate is calculated by using Eqn. (3.1), assuming one directional isentropic expansion from coolant total pressure (P_{tc}) at the inlet to the cooling hole to the mainstream static pressure (P_{ms}) as followed in reference [51].

$$m_{theoretical} = A_c p_{tc} \left(\frac{p_{ms}}{p_{tc}}\right)^{\gamma+1/_{2\gamma}} \sqrt{\frac{2\gamma}{(\gamma-1)RT_{tc}}\left[\left(\frac{p_{tc}}{p_{ms}}\right)^{\gamma-1/_{\gamma}} - 1\right]} \quad (3.1)$$

Here, γ is the ratio of specific heats, R is gas constant, T_{tc} is the coolant total temperature and A_c is the cross-sectional area of the cooling hole. For the FCH and RCH, the cross-sectional area remains the same throughout however for shaped holes viz. FSH and RSH, it changes from cylindrical inlet to expanded exit. In order to calculate the theoretical mass flow rate for shaped holes with expanded exits, it was suggested to consider the cross-section of the inlet of injection holes [108]. Thus, the discharge coefficient of shaped holes can be directly compared with the cylindrical holes. This is a slight deviation from the actual calculation however it makes contouring of shaped holes more convenient. The total pressure from reference [109], is taken at the inlet of the hole near the plenum, and mainstream static pressure is taken at X/D = - 5 (means upstream of injection holes).

Figure 3.10 shows the systematic comparison of the coefficient of discharge for different hole configurations. The coefficient of discharge of FCH at 35° injection angle is compared with forward cylindrical hole results from the literature [51], at 30° for blowing ratio (M) =1. The experimental reference is presented for quantitative comparison with present results. It was found to be 18.1% higher than the present results. This deviation may be attributed to the difference in density ratio (DR) and mainstream Reynolds number (Re) and length-to-diameter ratio (L/D). However, the coefficient of discharge for RCH at 35° injection angle and blowing ratio (M) =1 shows excellent agreement with reverse cylindrical hole, from literature findings

[20]. The FSH discharge coefficient at 35^o injection angle and blowing ratio (M) = 1, also shows good agreement with the results of Liu et al. [110] at 30^o injection angle and blowing ratio (M) = 1. Figure 3.10 also illustrates that the discharge coefficients of FCH are 10% more compared to RCH. The discharge coefficient of the FSH hole is 3.7 % more than that of RSH. It is also important to observe from the figure that the discharge coefficient of FSH is 9.6 % more than the FCH and the discharge coefficient of RSH is 16.67% more than RCH. The discharge coefficient is inversely related to pressure loss.

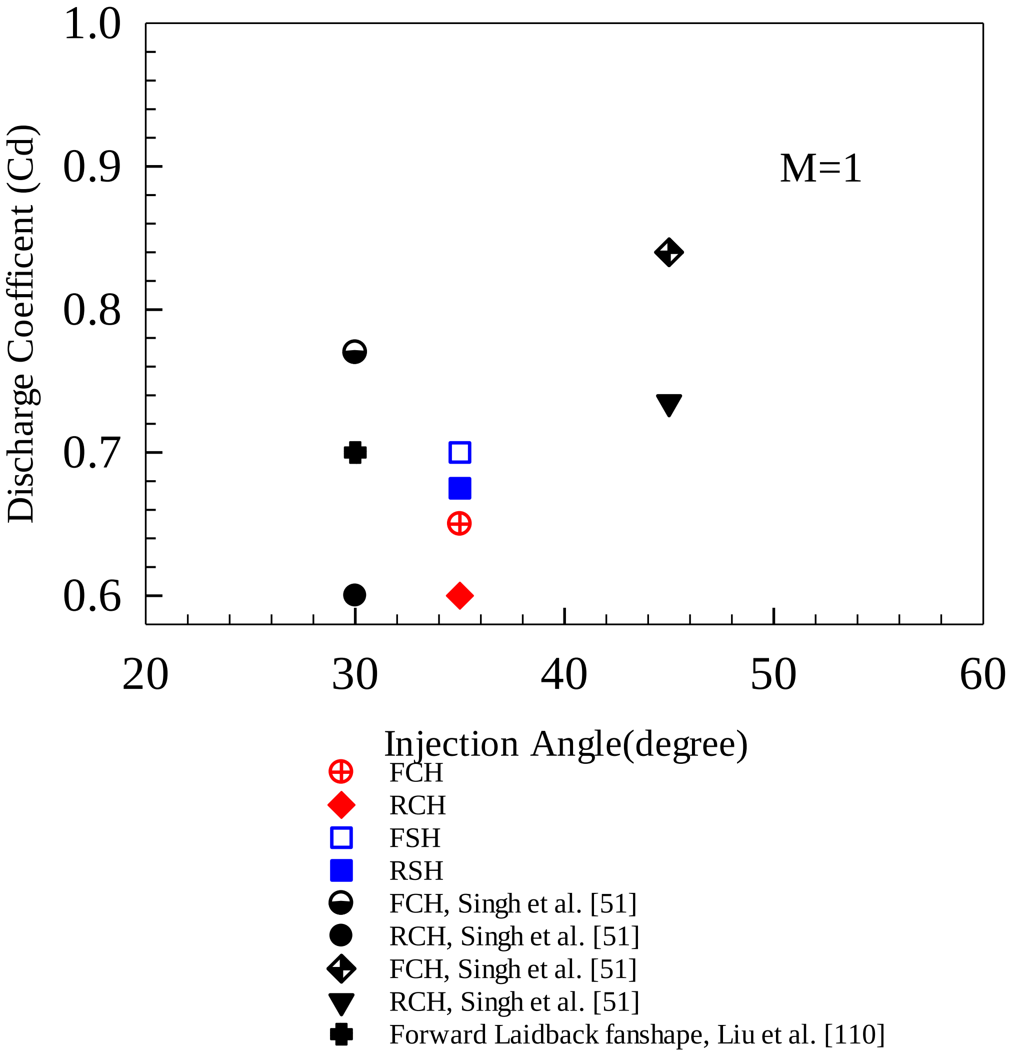

Fig.3.10: Comparison of discharge coefficients for various injection configurations.

It is interesting to note that the use of reverse-shaped holes increases film cooling effectiveness by 70 to 300 % (from the coolant injection hole to the rear end of the target surface) at the 4% additional pumping power as compared to the forward-shaped holes. The improved spread of coolant and increased effectiveness can further decrease the total mass of coolant required to meet the targeted temperature. Hence, the overall pumping power required may decrease in actual operation where many cooling holes are made on the surface. From Fig. 3.10, it can also be observed that the discharge coefficient is strongly influenced by injection configuration. In the case of reverse holes, the discharge coefficient is lower as compared to forward holes. The discharge coefficient is inversely proportional to the pressure drop in the coolant hole. Hence, it can be observed that pressure losses are higher in reverse injection configurations.

Figure 3.11 shows the contours of velocity magnitude non-dimensional at the exit of the coolant hole for all four injection configurations. The non-dimensional velocity (U/Ums), the contour is plotted by taking a plane one node below the flat surface. Figure 3.11 shows the shifting of the velocity profile towards the trailing edge in the case of the reverse hole. It can be observed from Fig. 3.11 that the RCH and RSH velocity magnitude near the leading edge is much lower as compared to the trailing edge. The coolant flow is in the opposite direction to the mainstream; hence the hole is partially blocked in the upstream (leading side). The opposite flow of the coolant stream also results in greater momentum loss. The partial blockage adds resistance to the flow and thus it requires more pumping power. Apart from the forward injection cases such as FCH and FSH, the velocity distribution was found to be nearly uniform throughout the hole. Similar, results were also reported from reference [51].

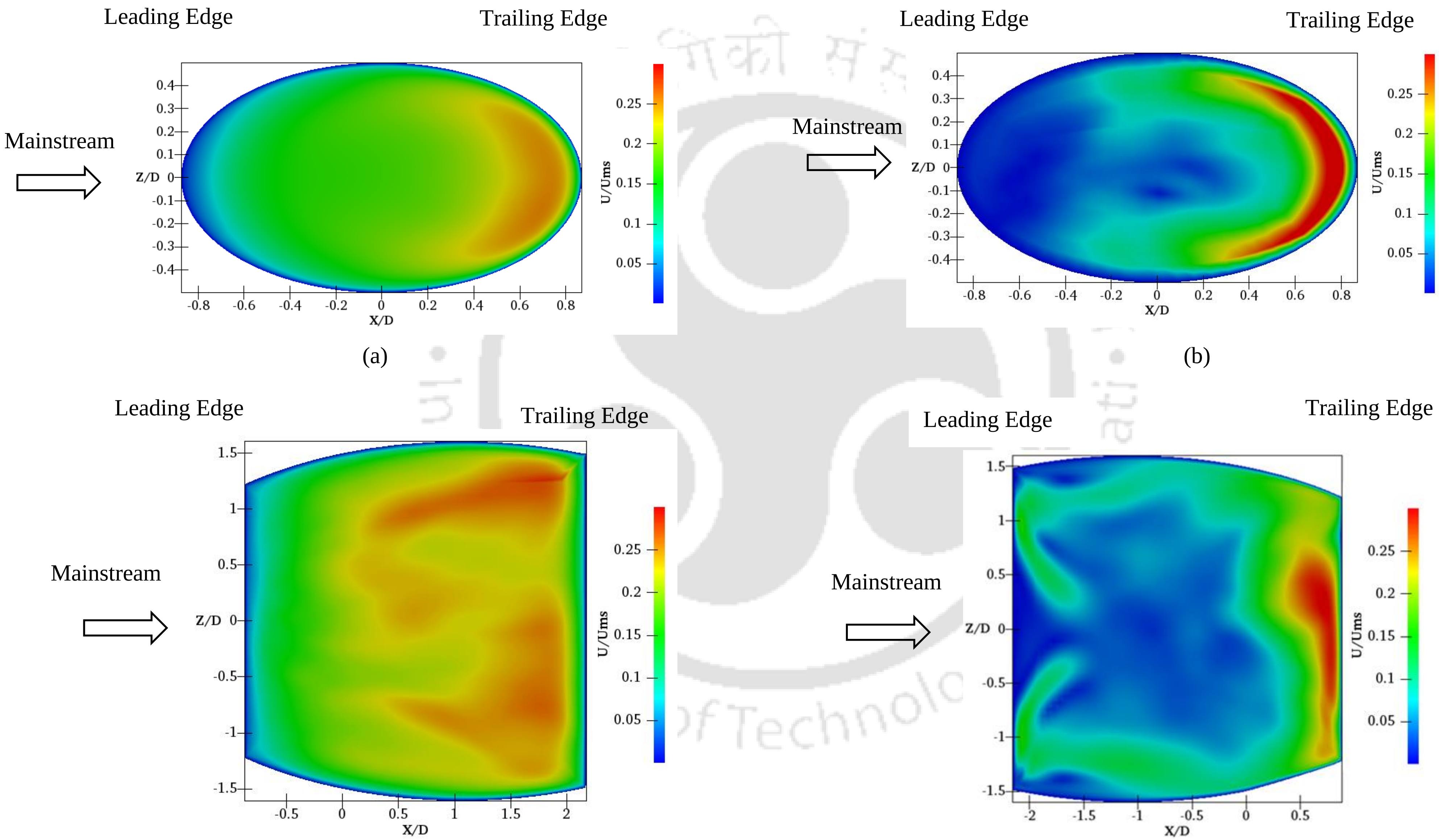

(a)

(b)

(c)

(d)

Fig.3.11: Non-dimensional velocity contours at flow exit from hole for various hole configurations: (a) FCH; (b) RCH; (c) FSH; (d) RSH.

3.4 Conclusion

Large eddy simulation is conducted in order to study the effect of cylindrical and shaped hole configuration over the forward and reverse injection film cooling performance. This study is carried out for a flat surface for the different hole configurations. The other operating parameters are, blowing ratio (M) =1, DR = 2.42, and 35^o injection angle. Based on the present study following inferences can be drawn: -

1. The vortices observed in the case of reverse cylindrical and reverse shaped are predominately in the plane of the plate and mitigate the problem of the formation of kidney vortices.
2. The reverse cylindrical hole (RCH) shows better laterally average effectiveness over the forward cylindrical hole (FCH). The maximum improvement in lateral average effectiveness lies in the range of 33-100%, from downstream to hole exit. The coolant coverage in the case of reverse injection is nearly uniform throughout the surface.
3. The coolant coverage of reverse-shaped (RSH) is much better and covers more area as compared to the forward-shaped (FSH). Improvement in lateral average effectiveness of RSH is maximum near the hole which is 42% more compared to the FSH hole. Apart from this fact, the coolant coverage for RSH is more uniform as compared to FSH.
4. The pressure drop is maximum for RCH and minimum for FCH. Moreover, the pressure drop in the case of RSH is comparable to that of FSH.

CHAPTER 4: EXPERIMENTAL AND NUMERICAL STUDY OF FILM COOLING PERFORMANCE OF A CORRUGATED SURFACE

CHAPTER4

4.1 Introduction

The sinusoidal corrugated surfaces are widely used in combustor liners and afterburners of aero engines in order to improve structural rigidity and stiffness. However, the literature related to corrugated surfaces is very limited. The cross-section of the afterburner liner and combustion chamber are usually thin, and hence hole shaping, branching and trenches are not feasible for these sections. Therefore, slot injection over the corrugated surfaces is practically used in combustor liners and afterburners of aero engines. Thus, the present study is focused on the effect of slot locations on the film cooling performance of sinusoidal corrugated surfaces.

In this chapter, numerical validation of experimental results is presented for film cooling study on the sinusoidal corrugated surfaces. After the validation and turbulence model selection, the detailed numerical procedure is given. The present study proposes a suitable injection configuration and operating parameters for the film cooling of an aero-engine afterburner, based on experimental and numerical studies. The experimental investigations are carried out for different injection locations for blowing ratios 0.5 and 1, fixed injection angle (45^o), and density ratio (1.095). The numerical study is extended for various injection locations with a wide range of operating parameters such as blowing ratios from (0.25-3), density ratios (1.095, 2.5, and 4), and different pressure ratios from 1 to 15, representing the operating conditions of an actual aero-engine afterburner. In order to access the effect of the effect of various injection locations on the film cooling performance of a corrugated surface, numerically obtained effectiveness is compared at different blowing ratios and density ratios. Additionally, the non-dimensional contour plots are also plotted for various injection locations to demonstrate the effect of vortices on film cooling characteristics.

4.2 Test Plate Configuration

The corrugated plate used in the present study is the sinusoidal profile of amplitude to wavelength ratio ($a/\lambda = 0.05$), wavelength (λ), and length 3λ, as discussed in previous chapter 2 (section 2.2.3). Chapter 2 also discusses the experimental methods and uncertainty calculation procedure. The sinusoidal profile of the corrugated surface is generated by mathematical equations given by Maass and Suchusman [77]. The corrugated plate is smooth 3D printed and mounted on the bottom of the test section. The corrugated surface is exposed to the mainstream of heated air in the test section, and the secondary stream of cooled air is injected over it through the slot of width ($w/\lambda = 0.02$). The slot configurations are designed by following the previous experimental work of Burns and Stollery [17]. The shows the detailed layout of the corrugated plate and various slot locations viz. L_0, L_{25}, L_{50}, and L_{75}. The label with slot locations indicates the distance from the first corrugation.

4.3 Numerical Study

4.3.1 Computational Domain

The computational domain addressed in the present study is two-dimensional. The length and height of the computational domain are 4λ and 2λ respectively, where λ is the wavelength of the corrugated surface. The detailed description of computational domains is addressed in chapter 2 (section 2.9.2).

4.3.2 Boundary Conditions, and Solution Methodology

The mainstream and secondary stream inlet is considered a velocity inlet where all the velocity components, temperature, and turbulence intensity are specified. The mainstream outlet is considered a pressure outlet, the corrugated wall is specified as no-slip (solid with thermal conductivity 0.16 W/mk), and other walls are specified as no-slip adiabatic conditions. The present study is carried out for various injection locations (i.e., L_0, L_{25}, L_{50}, and L_{75}) and amplitude to the wavelength ratio ($a/\lambda = 0.05$, 0.075, and 0.1). The detailed descriptions of various cases and operating parameters are systematically given in Table.4.1.

Table.4.1: Details of operating parameters used in the present numerical study.

S.N.	Parameters	Value
1.	Blowing ratio (M)	0.25, 0.5,1,2,3.
2.	Density ratio (DR)	1.095,2.5 and 4
3.	Pressure ratio (P_r)	1,5,10 and 15
4.	Mainstream Reynolds Number (Re_λ)	0.95×10^5

The conservation equations of mass, momentum, and energy are solved by the finite volume solver ANSYS Fluent 20.1 [92]. A detailed description of governing equations and turbulence modeling approach is given in chapter 2. The grids are highly refined near walls and cross-flow regions (as discussed in chapter 2, section 4.7.2). A detailed grid independence study is presented in chapter 2. The second-order accurate upwind schemes are used to discretize the conservation equations and the pressure and velocity are coupled with the SIMPLE algorithm [93]. The numerical solution is assumed to converge when the residual of mass momentum falls below $10^{-6,}$ whereas energy is 10^{-8}.

4.4 Results and Discussions

4.4.1 Selection of Turbulence Model for Numerical Studies

The numerical predictions in any turbulent flow study significantly depend on the turbulence modeling approach. Hence, selecting suitable turbulence models for corrugated surface film cooling is essential. To access the capabilities of two-equation models in predicting the film cooling performance of corrugated, three different turbulence models, viz. k-ε (RNG), k-ε (Realizable), k-ω (SST) were employed. The numerical results of various turbulence models are compared with the experimental case of L_{25} at blowing ratio (M = 1) and fixed density ratio (DR=1.095), as shown in Fig. 4.1. Figure 4.1 shows that RNG and Realizable models more closely follow the experimental variations compared to the SST model within the uncertainty limits. The RNG model shows a maximum over predictions of 21% in the range of X/λ = 0.25 to 1.25 (at X/λ = 0.26).

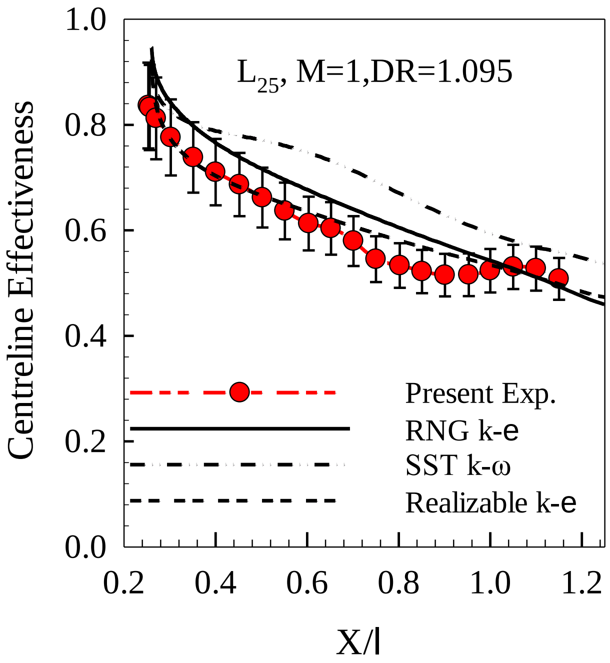

Fig.4.1: Centreline effectiveness comparison with various turbulence models.

The predictions of the k-ε (Realizable) model in more accurate as compared to the other two models, it follows the experimental trends accurately in the range of X/λ = 0.25 to 0.55 and the maximum over predictions of 8.5% in the range of X/λ = 0.55 to 1.25. Hence the Realizable, k-ε model is considered for further studies.

4.4.2 Validation of Numerical Results

To compare the accuracy of the present numerical model, experimental investigations have been carried out on the corrugated surface.

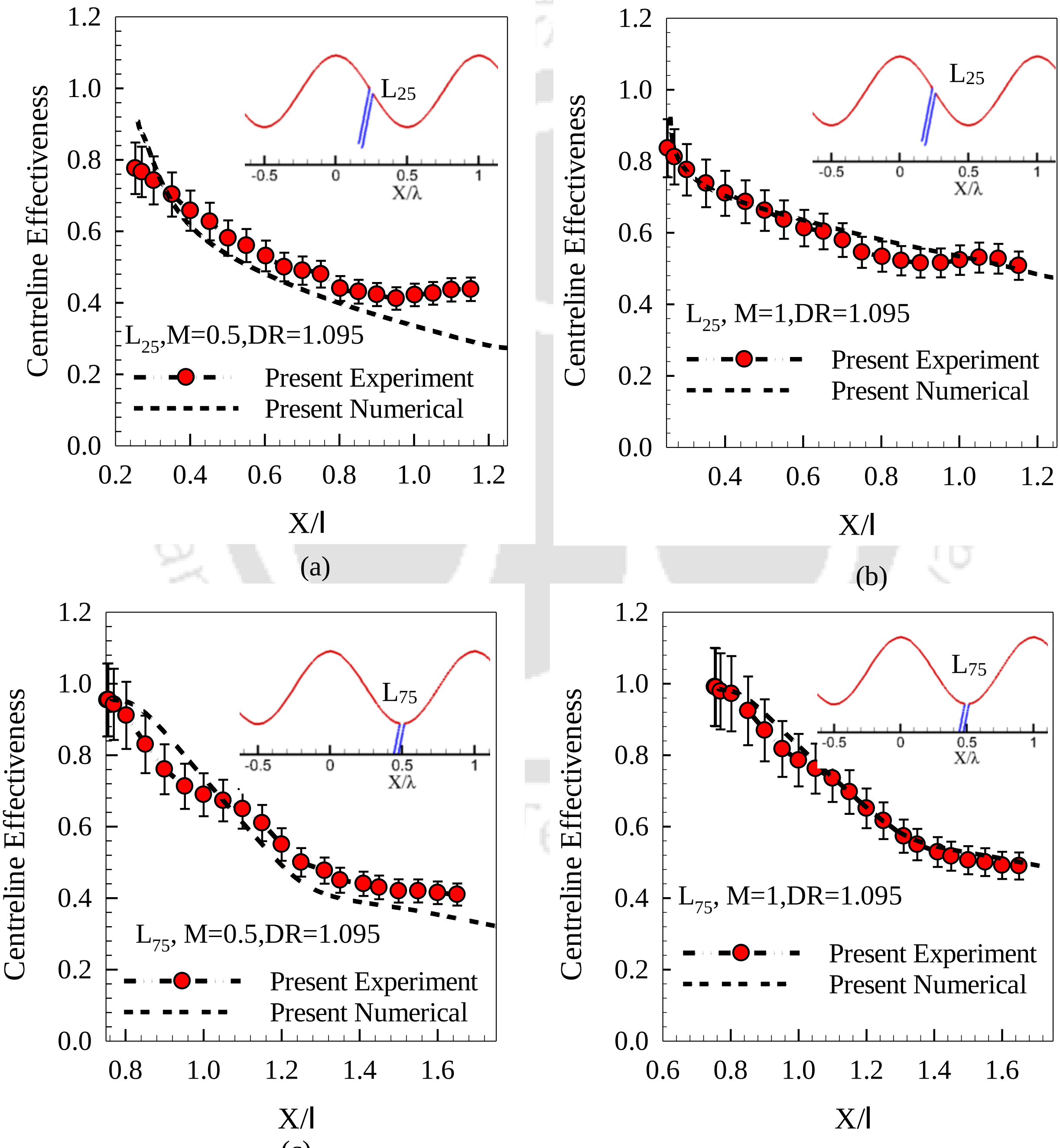

(a)

(b)

(c)

(d)

Fig.4.2: Comparison of experimental and numerical results for (a) L_{25}; (M=0.5) (b) L_{25} (M= 1); (c) L_{75} (M=0.5); (d) L_{75} (M= 1).

The present experiment considers injection slot locations i.e., L_{25} and L_{75}. In the present experimental study, the mainstream is heated air, whereas the secondary stream is at a relatively lower temperature to maintain a constant density ratio (i.e.; DR=1.095). The experiments are performed for M = 0.5 and 1 at fixed DR= 1.095 at an injection angle of 45^o, and the centreline effectiveness is plotted for comparisons. The experimental results are plotted with an error bar in the range of $X/\lambda = 0$ to 0.925. The numerical model is two-dimensional, and all the dimensions, injection locations, and operating parameters for comparison are considered as identical to the experimental case. Figure 4.2 (a) shows the comparison of numerical trends of variations with the present experimental case. The numerical results follow the experimental trends of variation within the error limits; however, a slight deviation can be observed after $X/\lambda = 0.9$. For the M= 0.5, the numerical model shows mixed prediction trends, i.e., near the injection location and far from the injection location. The further increase of the blowing ratio to M = 1 shows inherently different trends of variations, as shown in Fig. 4.2(b). From Fig. 4.2(b), it can be observed that the numerical results show a peak close to $X/\lambda= 0.25$ with a maximum overprediction of 10.8%, and accurately predict the further downstream from $X/\lambda = 0.275$ to 0.5. For the further downstream locations of $X/\lambda = 0.5$ to 1.25, a small over-prediction of 8.9% (at $X/\lambda = 0.85$) deviation can be observed. Interestingly, numerical prediction is entirely different for M = 0.5, as shown in Fig. 4.2(b).

The comparison of centreline effectiveness with the present experiment for the injection location, L_{75}, is shown in Fig. 4.2(c)-(d) at the blowing ratio of 0.5 and 1, respectively. For M = 0.5 numerical model shows both over-predictions and under-predictions in the range of $X/\lambda = 0.75$ to 0.167. From Fig.4.2(c), it can be observed that numerical results show a maximum overprediction of 10.5% in the range of $X/\lambda = 0.75$ to 0.105, whereas maximum underpredictions of 19% in the range of $X/\lambda = 0.105$ to 0.167. The numerical result follows the trends of experimental variations within the limit of experimental uncertainty. However, small deviations can be observed downstream after $X/\lambda=1.4$. Interestingly, numerical prediction is entirely different when the blowing ratio increases to M=1, and the numerical model shows accurate predictions in the range of $X/\lambda = 1.1$ to 1.35 and small over predictions for the rest of the locations. From Fig.4.2 (d), it can be observed that numerical results show a maximum overprediction of 6.4 % and 3.7% in the range of $X/\lambda = 0.75$ to 1.1 and $X/\lambda = 1.35$ to 1.67, respectively. The numerical results follow the trends of experimental variations within the limit of experimental uncertainty.

4.4.3 Effect of Injection Locations

Four injection locations are considered to study the effect of slot injection locations on the film cooling performance of corrugated surfaces, i.e., L_0, L_{25}, L_{50}, and L_{75}, for the amplitude to wavelength ratio ($a/\lambda = 0.05$). As the holes are located at different positions, the centreline effectiveness is plotted in one wavelength downstream, i.e., in the range of $X/\lambda = 0$ to 1, irrespective of their actual coordinate. The variations of centreline effectiveness for the above injection locations are shown in Fig.4.3 (a)-(c). Figure 4.3 (a) shows the effectiveness plot for $M= 0.25$, and from it can be observed that L_{50} and L_{75} locations exhibit similar trends of variations. The effectiveness of L_{50} and L_{75} locations is higher than the L_0 and L_{25} locations, in the range of $X/\lambda = 0$ to 1. The performance of the L_0 location is higher as compared to L_{25} near the hole up to $X/\lambda = 0$ to 0.16 and comparable further downstream. Due to changes in corrugation profile in the immediate downstream of L_0 and L_{25} injection location form diverging region whereas L_{50} and L_{75}, converging region. The secondary stream of coolant shows better attachment with the corrugated surface in the converging area, and hence centreline effectiveness improves. The performance of the L_{50} location is best among all locations in the range of $X/\lambda = 0$ to 0.64. The further increase in blowing ratio ($M=0.5$) exhibits different trends of variations, as shown in Fig. 4.3 (b). Moreover, the L_{75} injection location dominates all injection locations, except in the range of $X/\lambda = 0.42$ to 0.6, where the L_{50} area dominates. The L_0 location shows better performance than L_{25} close to the slot location in the range of $X/\lambda = 0$ to 0.15, and further downstream, the L_{25} location is better. Similarly, the further increase of the blowing ratio exhibits similar trends as $M = 1$ (Fig.4.3(c)); however, the L_0 location dominates L_{25} throughout downstream. The L_{75} injection location dominates just downstream of the slot in the range $X/\lambda = 0$ to 0.25, and further downstream, L_{50} dominates among all selected injection locations.

The flow attachments and effectiveness mechanism can be observed with the contour's plots shown in Fig. 4.4 (a)-(d). The contours plot clearly shows that for the case of L_0 and L_{25} injection locations, the secondary flow diminishes after a very short distance downstream. For the L_0 and L_{25} locations effect of the secondary stream is visible in the range of $X/\lambda = 0$ to 0.3 and $X/\lambda = 0.25$ to 0.35 respectively. However, for the L_{50} and L_{75} injection locations, the secondary stream can be seen relatively long downstream. For the L_{50} and L_{75} locations effect of secondary stream is visible in the range of $X/\lambda = 1.5$ to 1 and $X/\lambda = 0.75$ to 1.35 respectively.

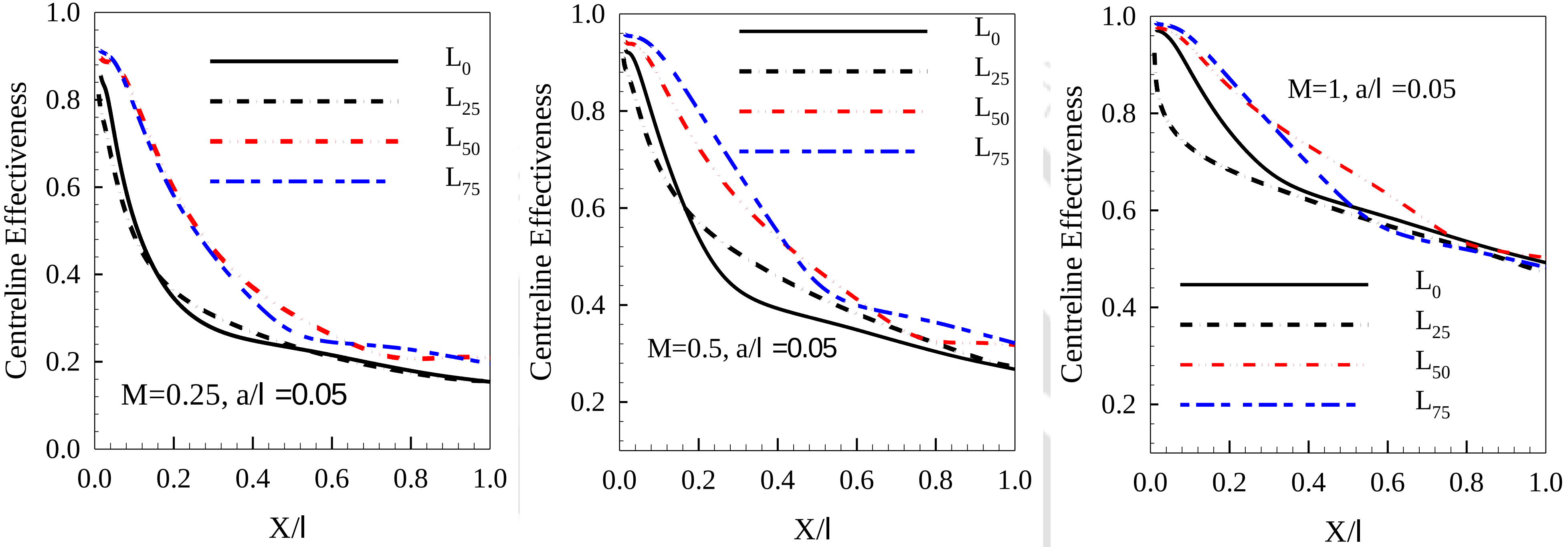

(a)

(b)

(c)

Fig.4.3: Effect of various injection locations on centreline film cooling effectiveness at (a) M=0.25; (b) M=0.5; (c) M=1.

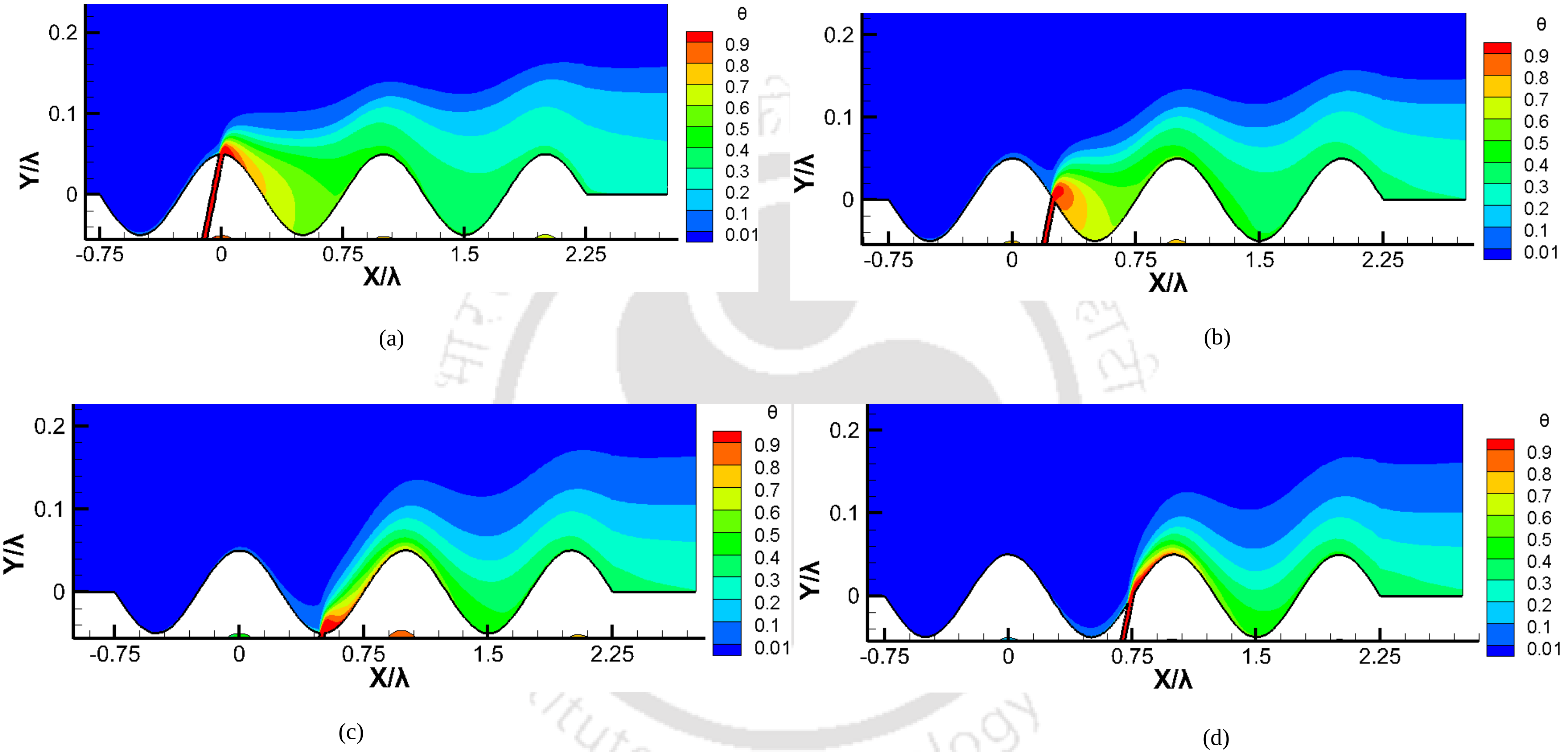

(a)

(b)

(c)

(d)

Fig.4.4: Non-dimensional temperature contours of various injection locations at M =1, (a) L_0; (b) L_{25}; (c) L_{50}; (d) L_{75}.

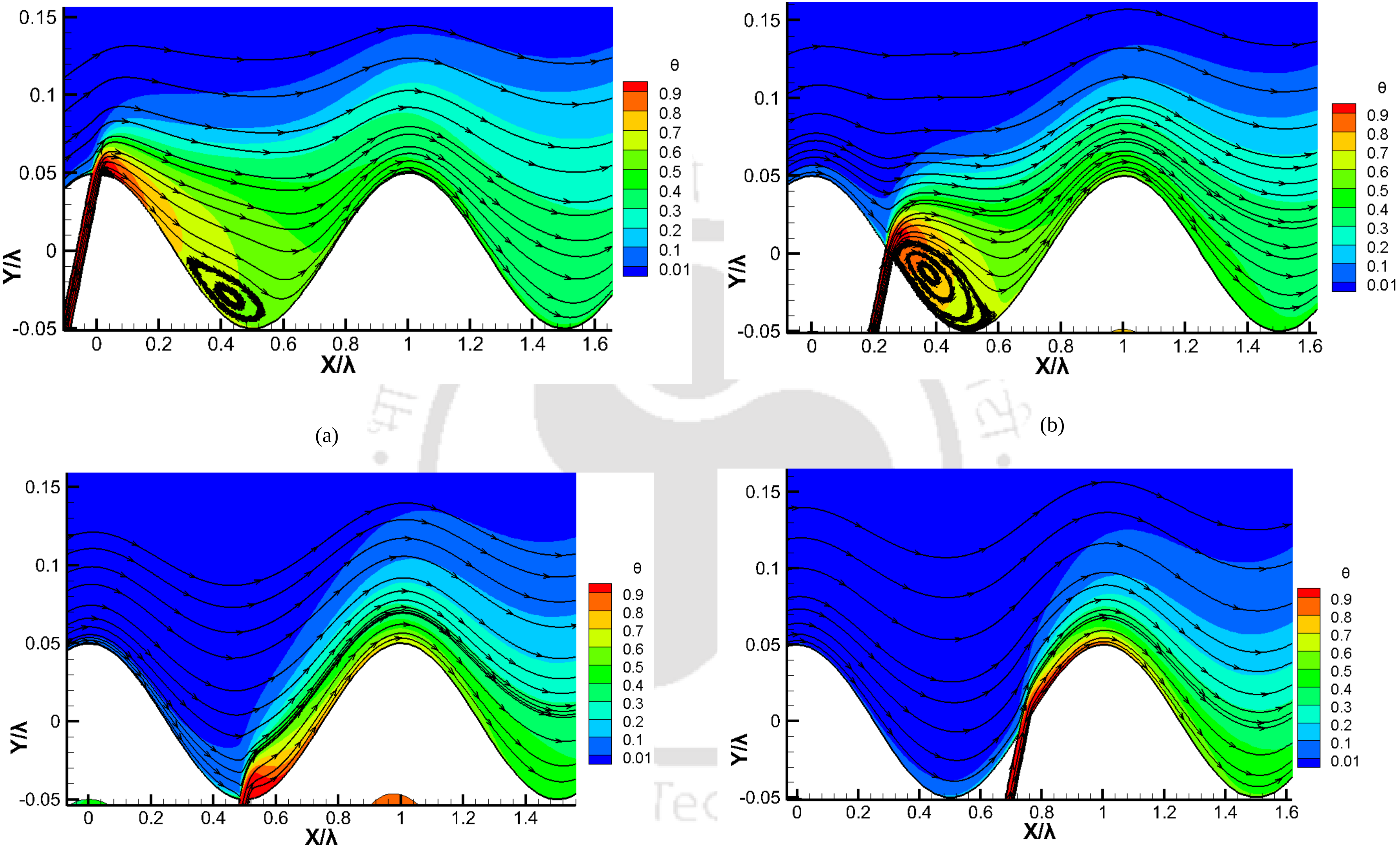

(a)

(b)

(c)

(d)

Fig.4.5: Streamline contours of non-dimensional temperature (θ) various injection locations at M =1, (a) L_0; (b) L_{25}; (c) L_{50}; (d) L_{75}.

To understand the effect of vortices and mixing mechanism on corrugated surfaces' film cooling characteristics, the streamline contour plots are plotted in Fig.4.5. Figure 4.5 shows the streamline traces for different injection locations at M=1, DR=1.095, and a/λ =0.05. Figure 4.5 (a) shows the streamline traces for L_0 injection location, the streamline forms a small recirculation zone for X/λ = 0.3 to 0.6. Similarly, Fig. 4.5 (b) shows small recirculation zone for L_{25} injection locations for X/λ = 0.25 to 0.6. The recirculation zone is trapped in the corrugation wind width. Moreover, the recirculation for the L_{25} injection location is higher as compared to L_0 injection location. Apart from that, the streamline contours exhibit inherently different trance trends for the L_{50} and L_{75} injection locations, as shown in Fig. 4.5 (c)-(d). The L_{50} and L_{75} secondary flow show more streamlined flow with a corrugated surface and the recirculation zone is absent. The formation of the recirculation zone in the corrugation valley improves the coolant mixing with the mainstream flow. Hence, the L_{50} and L_{75} injections show better effectiveness as compared to the L_0 and L_{25} injection locations.

4.4.4 Effect of Amplitude to Wavelength Ratio

In order to assess the effect of corrugation geometry on film cooling characteristics, three different amplitude-to-wavelength ratios (a/λ), i.e., 0.05, 0.075, and 0.1, are considered. The numerical simulations are carried out for various injection locations, viz. L_0, L_{25}, L_{50}, and L_{75}, at M=1, DR = 1.095 and injection angle 45°. Figure 4.6 (a)-(d) presents the variations of centreline effectiveness for one wavelength from the respective injection locations. The amplitude-to-wavelength ratio has a relatively significant influence on effectiveness. Fig. 4.6(a) presents the comparison of centreline effectiveness for L_0 injection location. Fig. 4.6(a) clearly shows that the increase of a/λ from 0.05 to 0.1 causes a sudden drop of effectiveness in downstream of L_0. The increase in the corrugation amplitude to wavelength ratio increases the depth of the wavy valley, which improves the flow accumulation and restricts the coolant spread further downstream. Thus, the coolant flow is restricted to the narrow region, and film cooling effectiveness is reduced. Moreover, the amplitude-to-wavelength ratio increases from 0.05 to 0.075 and 0.05 to 0.1 reduces the centreline average effectiveness by 24% and 31.3%, respectively. Similar variations are observed in Fig. 4.6(b) at the L_{25} injection location; for the increase of a/λ= 0.05 to 0.1, the centreline effectiveness drops. The increase of, a/λ= 0.05 to 0.075 and a/λ= 0.05 to 0.1 reduces the centreline average effectiveness by 10% and 12%, respectively. Contrary to the L_0 and L_{25} injection locations, the centreline effectiveness for L_{50} shows an inherently different profile, as shown in Fig.4.6 (c).

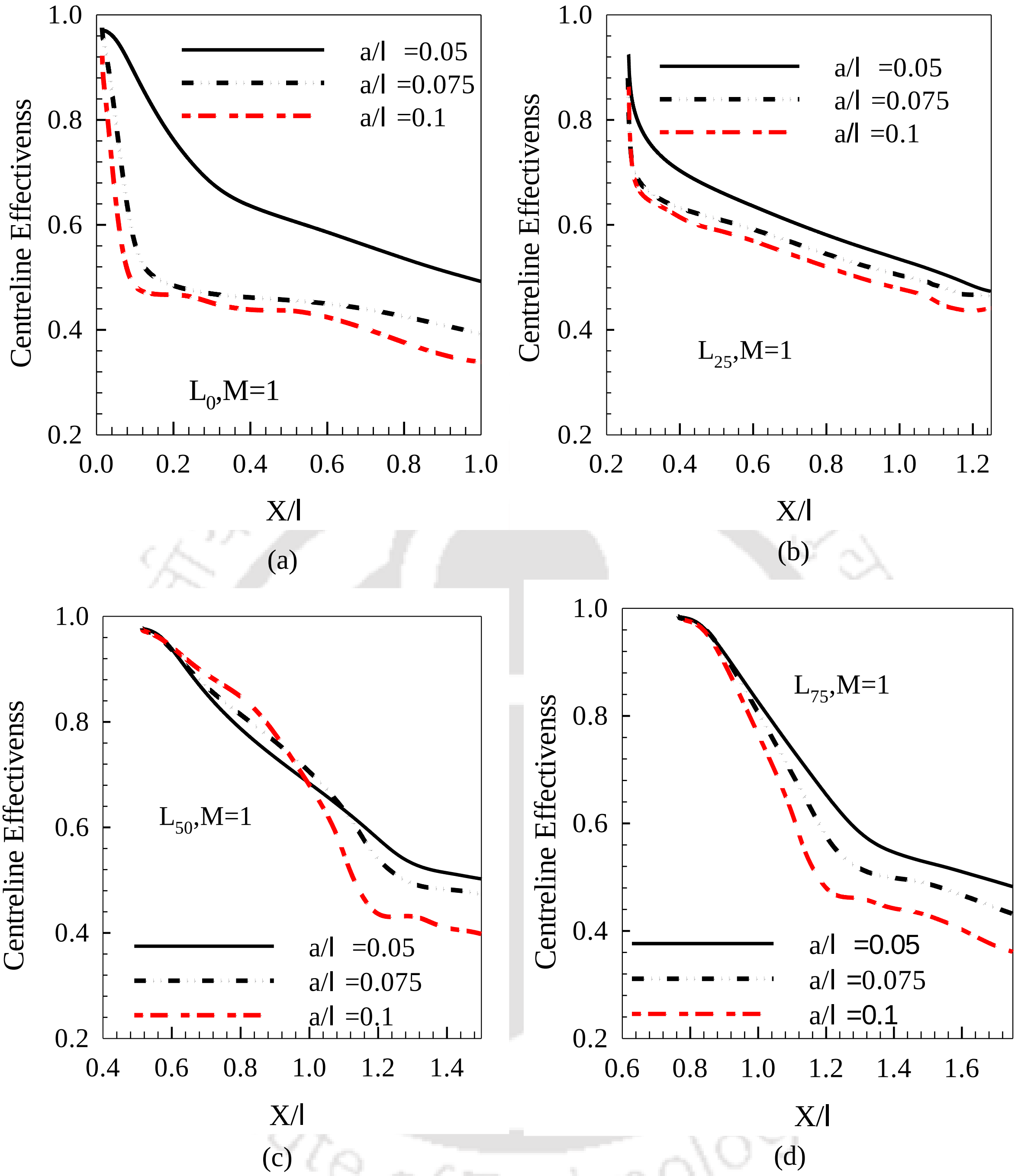

Fig.4.6: Comparison of centreline effectiveness for various amplitude to wavelength ratios at (a) L_0; (b) L_{25}; (c) L_{50}; (d) L_{75}.

For the L_{50} location the increase of a/λ= 0.05 to 0.1 results increase of effectiveness for X/λ = 0.5 to 1 and reduces in further downstream from X/λ = 1 to 1.5. Figure 4.6(d) presents the centerline effectiveness comparisons for L_{75} injection location. From Fig. 4.6(d), it can be observed that the increase of a/λ= 0.05 to 0.1 results in a significant drop in effectiveness for the X/λ = 0.9 to 1.75, however close to the slot the effects are insignificant. The increase of a/λ= 0.05 to 0.075 and a/λ= 0.05 to 0.1 reduces the centreline average effectiveness by 10% and 13.6%, respectively.

4.4.5 Effect of Operating Pressure

The numerical studies on the effect of amplitude to wavelength ratio in section 4.4.4 revealed that the increase of a/λ ratios reduces the film cooling effectiveness. For the present investigation, three different operating pressure ratios (P_{ra}), viz. 5, 10, and 15, are considered.

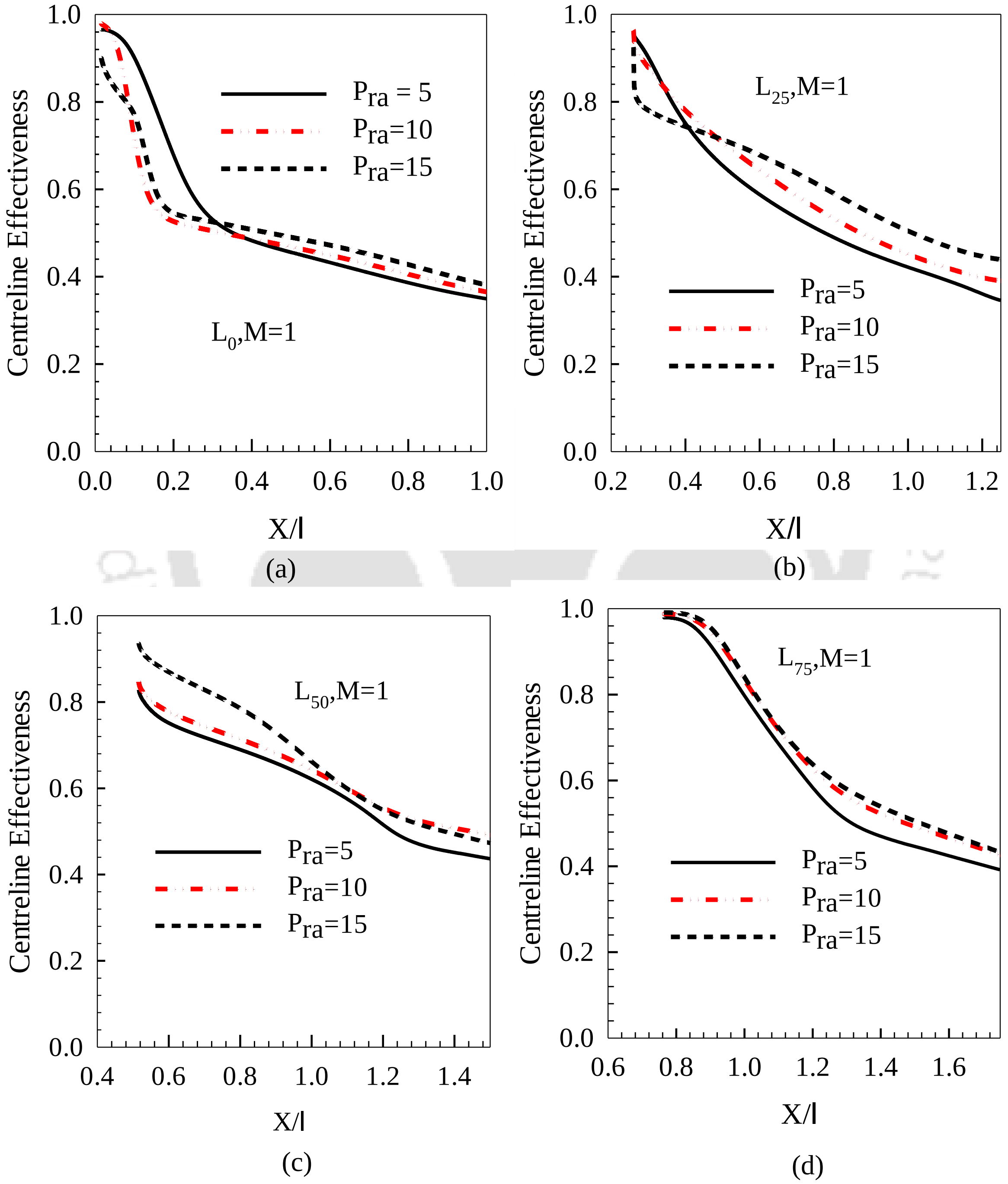

(a) (b) (c) (d)

Fig.4.7: The comparison of effect of pressure ratio (P_{ra}) at (a) L_0; (b) L_{25}; (c) L_{50}; (d) L_{75}.

Four locations are selected, and centreline effectiveness is compared, as shown in Fig.4.7. From Fig.4.7 (a) it can be observed that the increase of operating pressure ratio from P_{ra} = 5 to 15, improves the film cooling performance from X/λ = 0 to 0.3 and decreases in for further downstream. For the fixed mainstream and secondary stream temperature the increase of operating pressure results in a significant change in the local density, which further improves the local Reynolds number, and hence a significant improvement in effectiveness is obtained. Figure 4.7 (b) shows the centerline effectiveness plots for L_{25} injection location, it can be observed that the increase of P_{ra} = 5 to 15 results in significant improvement in centreline effectiveness. However, a small drop in centreline effectiveness can be noted for X/λ = 0 to 0.25. The effectiveness plots shown in Fig. 4.7 (c)-(d) for L_{50} and L_{75} injection locations revels inherently different trends as compared to the L_0 and L_{25} locations. From Fig.4.7 (c) it can be observed that the increase of P_{ra} = 5 to 15 results in the increase in effectiveness throughout the downstream locations from X/λ = 0 to 1. Similar trends can be seen for the L_{75} injection location as shown in Fig. 4.7(d).

4.4.6 Effect of Density Ratio

To study the effect of density ratio on film cooling performance on various injection locations (L_0, L_{25}, L_{50}, and L_{75}), the centreline effectiveness is plotted as a function of density ratio, as shown in Fig.4.8. The present study is carried out for three different density ratios viz., 1.095, 2.5 and 4. Fig.4.8 (a) presents the effect of density ratio for L_0 injection location. From Fig. 4.8(a), it can be observed that the centreline effectiveness increases with an increase in density ratio from DR = 1.095 to 2.5. The increase in density ratio results in a lower velocity ratio, which reduces the secondary flow penetration into the mainstream flow, and hence higher effectiveness is obtained. With the increase in density ratio, the monotonic increase in centreline effectiveness is expected, however, the further increase of DR = 2.5 to 4 reduces the film cooling performance in comparison to DR= 2.5. The same phenomenon can be well understood with the non-dimensional temperature contours, shown in Fig.4.9. Figure 4.9 clearly shows that with the increase of density ratio from DR = 1.095 to 2.5, the secondary flow penetration into the mainstream reduces, and the tendency of secondary flow attachment improves. The further increase of density ratio from DR = 2.5 to 4 also reduces the velocity ratio; however, due to the dominating effect of conjugate cooling of the corrugated plate through secondary flow, a small drop in centreline effectiveness is obtained. However, the centreline effectiveness plot at DR= 4 shows better performance than DR= 1.095 case. A similar trend of variations can be observed for L_{25} injection locations throughout the downstream location except in the region close to the injection from X/λ = 0.25 to 0.48, as shown in Fig.4.8 (b). The centreline film cooling effectiveness increases with the increase of density ratio from DR = 1.095 to 2.5 and thereafter the further increase of density ratio to DR = 4, the centreline effectiveness reduces.

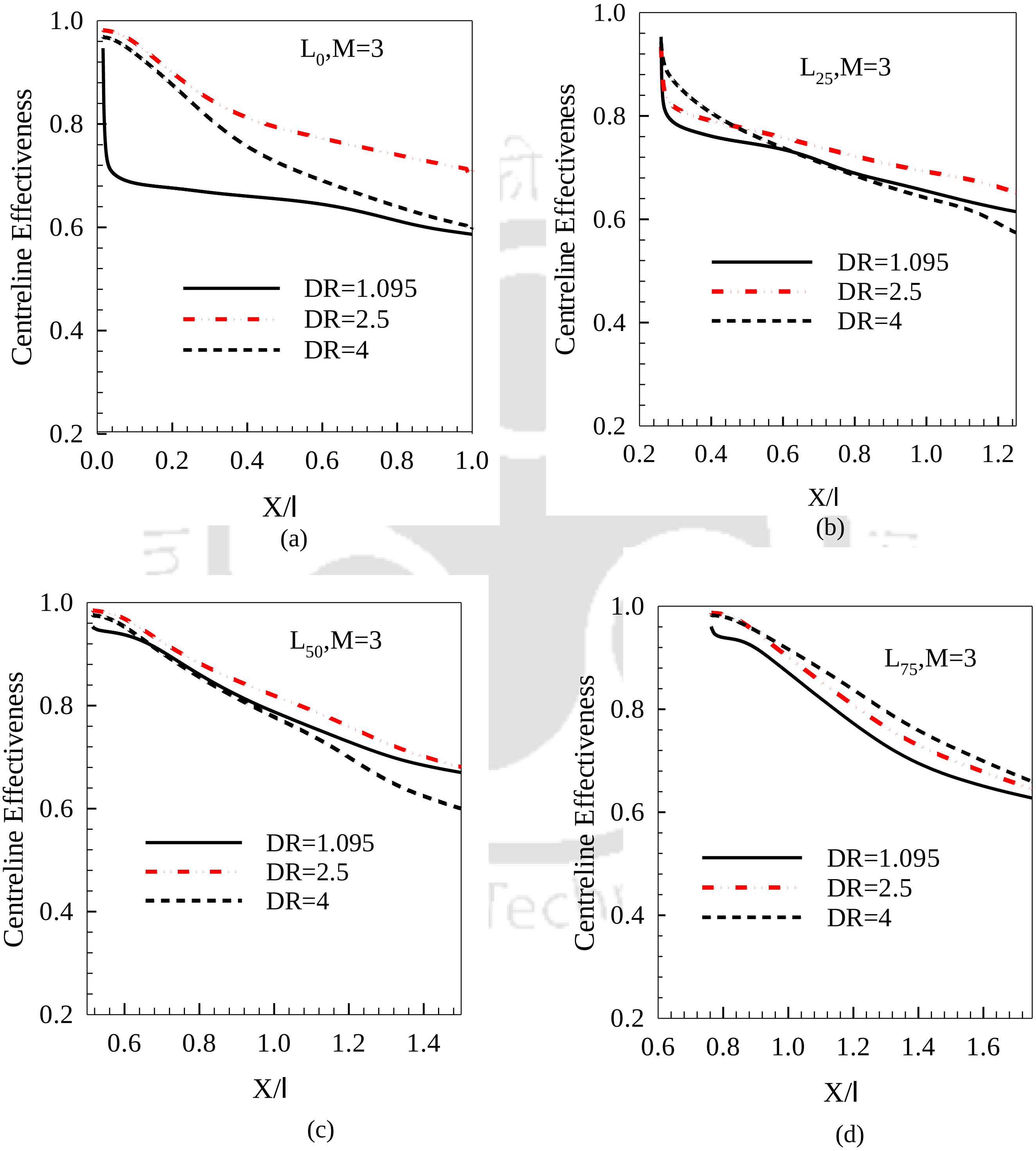

(a)

(b)

(c)

(d)

Fig.4.8: Effect of density ratio on centreline film cooling effectiveness (a) L_0; (b) L_{25}; (c) L_{50}; (b) L_{75}.

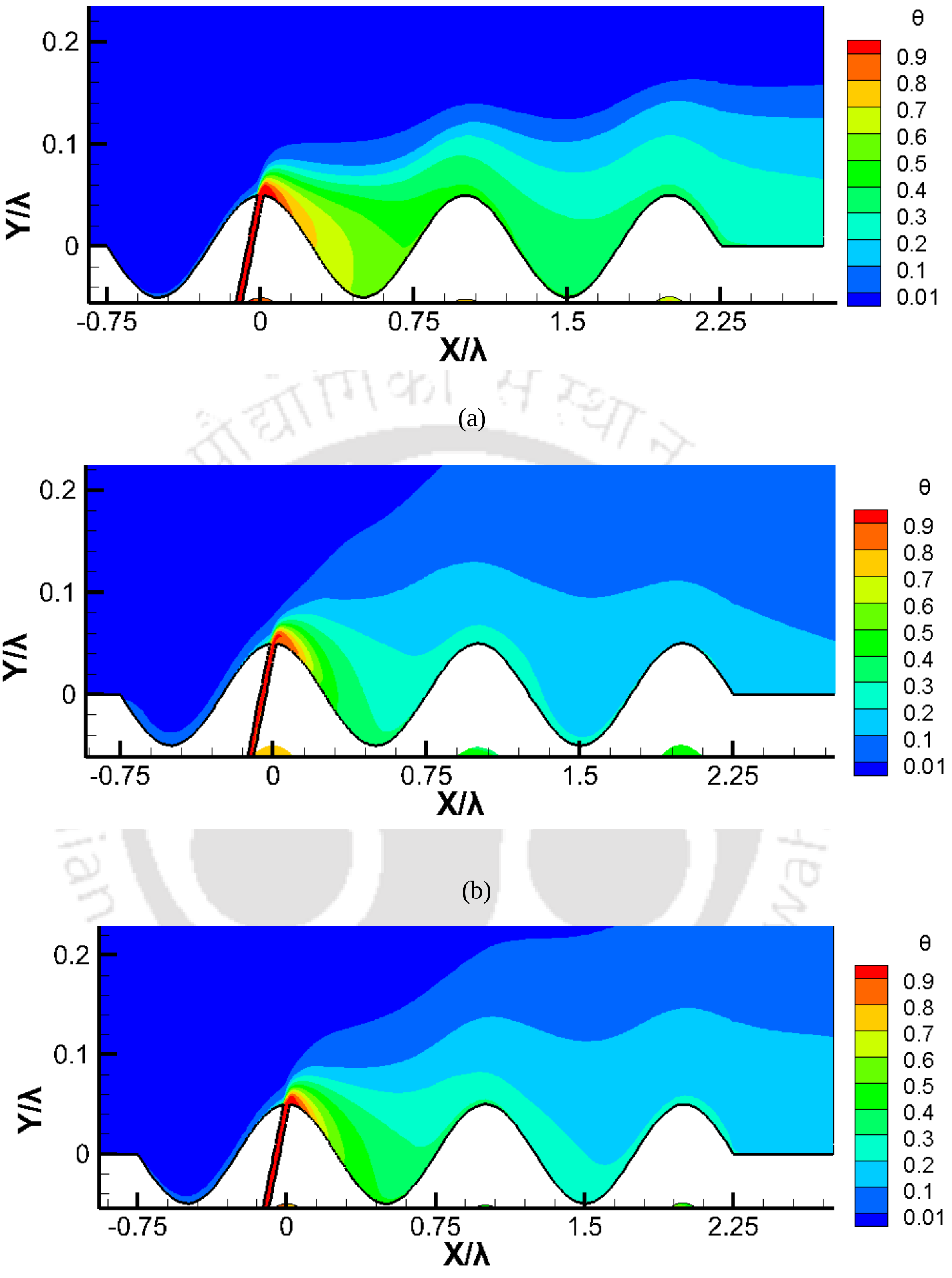

(a)

(b)

(c)

Fig.4.9: Effect of density ratio flow field and non-dimensional temperature (θ) for L_0 injection location M =1, (a) DR =1.095; (b) DR=2.5; (c) DR=4.

Apart from that, for the L_0 and L_{25} injection locations, the centreline effectiveness plot exhibits a sudden drop close to the injection location with a drop-in density ratio (DR = 4 to 1.095). However, the centreline effectiveness plots for the L_{50} and L_{75} injection locations show similar trends for all density ratio injection locations as shown in Fig.4.8 (c) to (d). From Fig.4.8 (c) it can be observed that the increase of density ratio from DR = 1.095 to 2.5 increases the centreline throughout the downstream locations, X/λ = 0.25 to 0.48. However, the further increase of density ratio from DR = 2.5 to 4, improves centreline effectiveness from X/λ = 0.5 to 0.68 and after that decreases. Figure 4.8 (d) shows nearly similar trends as compared to the L_{50} location. The centreline effectiveness increases with the increase of density ratio from DR = 1.095 to 2.5, and further increase of density ratio from DR = 2.5 to 1.095 decreases the centreline effectiveness.

4.4.7 Effect of Blowing Ratio

The impact of the blowing ratio is extensively studied to improve film cooling performance. The too-low blowing ratio causes insufficient coolant coverage, however, too high a blowing ratio causes coolant jet soot into the hot stream. Hence, blowing ratio optimization is very important. Fig.4.10 shows the effect blowing ratio on centerline film cooling effectiveness for various injection locations. The numerical simulations are carried out for wide ranges of blowing ratios from M= 0.5 to 3, at a fixed density ratio (DR = 1.095) and the centerline effectiveness is compared. Fig. 4.10 (a) clearly shows that the centerline effectiveness increases as the blowing ratio increases from M= 0.5 to 2, and thereafter further increase in blowing ratio from M= 2 to 3, causing secondary flow lift-up from the corrugated surface, and hence a small drop can be observed. Apart from that, it can be also seen that the increase in blowing ratio from M=1 to 3 causes a sudden drop in the effectiveness plot from X/λ = 0 to 0.3. Similar trends of variations can be observed for the L_{25} injection location the, increase of blowing ratio increases from M= 0.5 to 2, and thereafter further increase in blowing ratio from M= 2 to 3, causing a small drop in centerline effectiveness. Moreover, a small drop in centerline effectiveness is reported from X/λ = 0.25 to 0.3 as the blowing ratio from M=1. Fig. 4.10 (c) shows the centerline effectiveness variations for L_{50} locations, from the figure it can be observed that centerline effectiveness increases with the blowing ratio for M= 0.5 to 2, and thereafter the further increase of blowing ratio from M= 2 to 3, effectiveness drops. A similar trend of variations can be observed for L_{75}, where effectiveness improves up to blowing ratio M=2 and after that decreases (Fig.4.10 (d)).

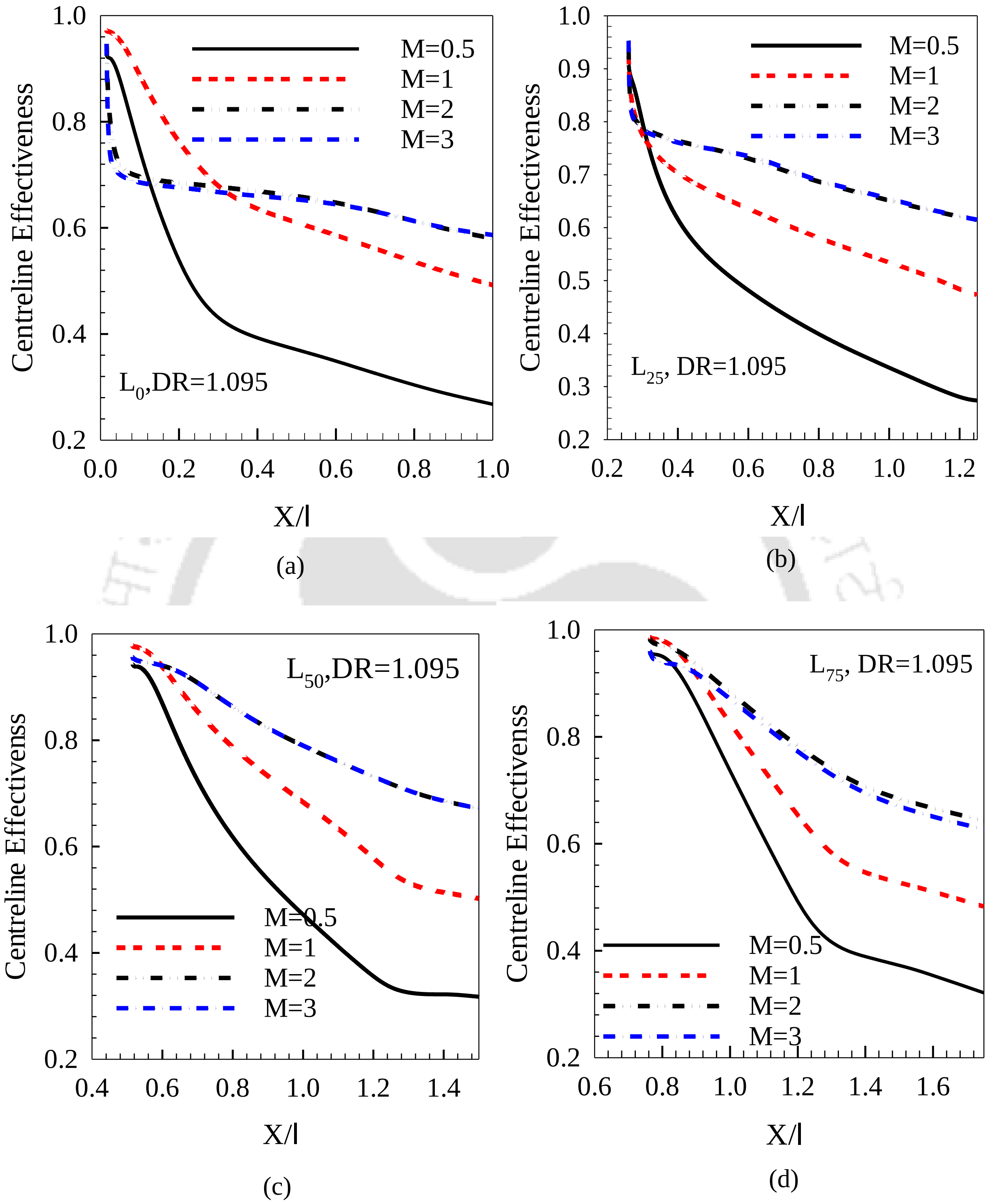

(a) (b)

(c) (d)

Fig.4.10: The Effect of blowing ratio on film cooling effectiveness (a) L_0; (b) L_{25}; (c) L_{50}; (d) L_{75}.

4.5 Conclusion

Experimental and numerical studies have been performed for various injection locations (viz. L_0, L_{25}, L_{50}, and L_{75}), and corrugation amplitude to wavelength ratio to find out the suitable injection configurations and operating parameters for film cooling applications on the corrugated surface. The numerical studies have been carried out for a wide range of parameters such as blowing ratio (M= 0.25-3), density ratio (DR= 1.095, 2.5, and 4,), (a/λ= 0.05, 0.075, and 0.1,) and pressure ratio (Pr = 1, 5, 10 and 15). Based on the present study following conclusions can be drawn:

1. The study shows that film cooling effectiveness is strongly influenced by the secondary flow injection locations. Four different locations viz. L_0, L_{25}, L_{50}, and L_{75} were considered and the study reveals that the performance of L_{50} and L_{75} injection locations is higher as compared to L_0 and L_{25} locations.
2. The increase in corrugation amplitude to the wavelength ratio (a/λ) restricts the coolant spread and with the increase of corrugation depth the film cooling effectiveness decreases. The maximum decrease is reported for L_0 injection, the amplitude to wavelength ratio increases from a/λ= 0.05 to 0.075 and a/λ= 0.05 to 0.1 reducing the centreline average effectiveness by 24% and 31.3%, respectively.
3. The parametric study indicates that the secondary flow attachment to the corrugated surface and the film cooling effectiveness is significantly influenced by the blowing ratio, with the increase in blowing ratio the centreline effectiveness increases even at a high blowing ratio.

CHAPTER 5: EXPERIMENTAL AND NUMERICAL ANALYSIS OF FILM COOLING PERFORMANCE OF A CORRUGATED SURFACE USING DOUBLE INJECTION

5.1 Introduction

The combustor liner and afterburner are the essential components of modern aero-engines, particularly those used for military fighters and bombers, mounted with afterburners on the exhaust side of the hot stream. It fulfills the additional thrust requirements during specific operations such as take-off combat, etc., by burning the additional fuels. The afterburners are designed to operate in an extremely high-temperature environment however due to continuous operation in the exhaust stream of a gas turbine, the temperature often exceeds the melting points of the metal material. The corrugated surfaces provide high structural rigidity and stiffness and hence practically used in afterburner and combustor liners of modern aero-engines and fighter aircraft. However, film cooling studies using double injection on corrugated surfaces are missing in the literature.

This chapter presents the experimental validation of the numerical model developed for film cooling application of double injection locations on film cooling application of sinusoidal corrugated surface. The experimental validation is carried out for a limited arrangement of parameters; however, the numerical study is extended for a wide range of parameters. The experimental study is performed for different double injection locations (per wavelength) viz., (L_0-L_{25}), (L_0-L_{50}), (L_0-L_{75}), (L_{25}-L_{50}), (L_{25}-L_{75}) and (L_{50}-L_{75}) on the sinusoidal corrugated surface at blowing ratio (1), fixed injection angle (45^o), and density ratio (1.095). The numerical study is conducted for a wide range of operating parameters such as blowing ratios from (0.5-2), and density ratios (1.095, 2.5, and 4). To access the effect of corrugation geometry three different amplitude to wavelength viz. 0.05, 0.075, and 0.1 are considered in the present numerical study.

5.2. Corrugated Test Plate Configuration

The test plate configuration used for double slot injection is exhaustively discussed in previous chapter 2 (section 2.3.2). The corrugated test plate used in this work has a sinusoidal profile and is generated using the Maass and Suchusman [77] equation. To ensure the film cooling protection of the corrugated surface, a secondary stream of cooled air is injected over the corrugated surface through a slot of width ($w/\lambda = 0.02$). The slot was designed following the previous works of Burn and Stollery [17]. The present study considers double slot injection locations in one wavelength. Figure 2.7 (chapter 2) shows the detailed layout of the corrugated plate and various slot locations viz. L_0, L_{25}, L_{50}, and L_{75}. The level with the slot indicates the distance from the first peak of the first corrugation. The various double slot injection considered in this study are detailed, (L_0-L_{25}), (L_0-L_{50}), (L_0-L_{75}), (L_{25}-L_{50}), (L_{25}-L_{75}), and (L_{50}-L_{75}). In the present case of double slot combinations, all the measurements are performed downstream to the first hole (i.e., From L_0 for L_0-L_{25}). The detailed experimental methods, setup, and measurement techniques have been discussed in chapter 2.

Table.5.1: Summary of experimental data collection and cases.

SN.	Cases	Double-row slot positions	Corrugated plate and slot width
1.	Case-1	(L_0-L_{25})	$a/\lambda=0.05$, $w/\lambda=0.02$
2.	Case-2	(L_0-L_{50})	$a/\lambda=0.05$, $w/\lambda=0.02$
3.	Case-3	(L_0-L_{75})	$a/\lambda=0.05$, $w/\lambda=0.02$
4.	Case-4	(L_{25}-L_{50})	$a/\lambda=0.05$, $w/\lambda=0.02$
5.	Case-5	(L_{25}-L_{75})	$a/\lambda=0.05$, $w/\lambda=0.02$
6.	Case-6	(L_{50}-L_{75})	$a/\lambda=0.05$, $w/\lambda=0.02$

5.3 Numerical Studies

5.3.1 Computational Domain

The computational domain used in the present numerical study is the two-dimensional domain. It consists of a mainstream inlet, secondary stream inlet, pressure outlet, plenum chamber, and corrugated wall. A detailed description of computational domains is presented in chapter 2 (section 2.9.3). The length and height of the domain are 4λ and 2λ where λ indicates the wavelength of the corrugated surface. The mainstream is a heated stream of air whereas the secondary stream is a relatively cold stream of air. The secondary steam of air is mixed uniformly in the plenum chamber before being supplied to the corrugated wall. In order to investigate the effect of various injection locations of double slot, various double injection combinations viz., (L_0-L_{25}), (L_0-L_{50}), (L_0-L_{75}), (L_{25}-L_{50}), (L_{25}-L_{75}) and (L_{50}-L_{75}) are considered.

5.3.2 Boundary Conditions, Operating Parameters, and Solution Methodology

The governing equations of mass momentum and energy along with the conjugate heat transfer are solved using a finite volume solver as discussed in chapter 2 (section 2.10). The detailed grid resolution and solution methodology are discussed in chapter 2 (section 2.14.3). Air is used as the working fluid for both mainstream and secondary streams, and variations of thermophysical properties are considered using temperature depended on properties. The temperature-dependent properties are discussed in chapter 2 (section 2.4).

In the present numerical study, the computational domain consists of various boundaries, the mainstream and secondary stream inlet is assigned as a velocity inlet where flow velocity, turbulence intensity, and temperature are specified. The flow outlet is treated as a pressure outlet with zero-gauge pressure. For all cases of fixed turbulence intensity of 5% is specified. The mainstream inlet and secondary stream inlet were assigned as velocity inlets, where all velocity and temperature values were specified. The numerical values of velocity and temperature correspond to the parameter sets of the various cases being computed (i.e., density ratio, blowing ratio, Reynolds number). The outlet is assigned as a pressure outlet boundary with zero-gauge pressure. The test plate is made of a low thermally conductive material with a thermal conductivity of 0.16 W/(m·K). The corrugated surface covered with a plenum, and the inner slot wall are all fluid-solid interfaces imposed with the non-slip condition. The plenum wall and top wall (as shown in Fig. 3) are assigned as no-slip adiabatic conditions.

Table.5.2: Range of operating parameters used in the present study.

S.N.	**Parameters**	**Value**
1.	Blowing ratio (M)	0.5,1,2.
2.	Density ratio (DR)	1.095,1.5 and 2.5
4.	Mainstream Reynolds Number (Re_λ)	0.95×10^5

The present study used a Finite volume solver, ANSYS FLUENT v20.0 [92] to solve governing equations of mass, momentum, and energy. The conservation equations terms are discretized with second-order accurate schemes, and the SIMPLE algorithm [93] is used for coupling of pressure and velocity. The convergence criteria for mass and momentum energy are defined as $10^{-6,}$ and 10^{-8} respectively.

5.4 Results and Discussions

5.4.1 Selection of Turbulence Model for Numerical Studies

For most of the turbulent flow applications, the Reynolds-Averaged-Navier-Stokes (RANS) equations have become a standard analysis tool, since it brings a reasonable compromise between computational accuracy and costs.

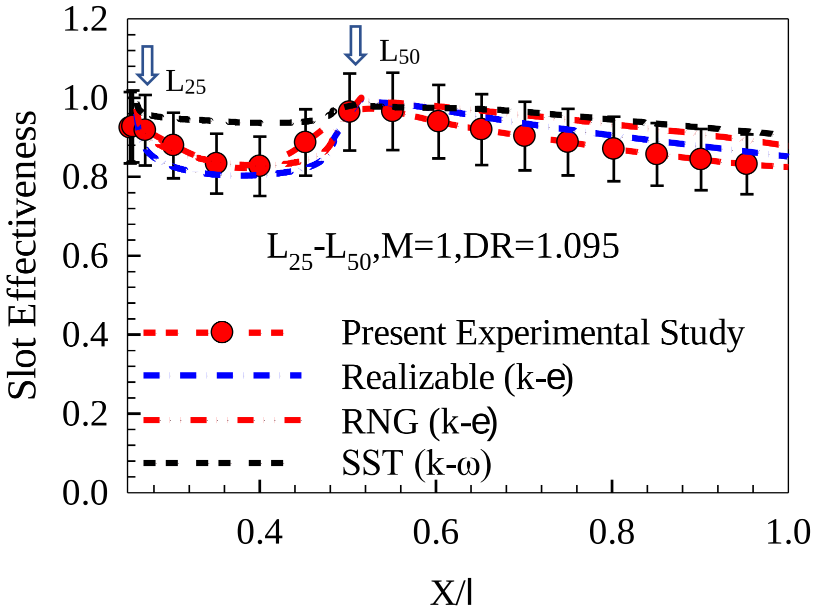

Fig.5.1: Centreline effectiveness comparison with various turbulence models.

The numerical predictions in the film cooling flow significantly depend on the turbulence modeling approach and hence the selection of a suitable turbulence model for the corrugated surfaces is very much essential. To study the capabilities of various RANS models in predicting the film cooling flow over a corrugated surface three different turbulence models viz. k-ε (RNG), k-ε (Realizable), k-ω (SST) were applied.

The numerical simulations are carried out for injection location (L_{25}-L_{50}) at blowing ratio (M=1) and density ratio (DR=1.095), and the predictions of various turbulence models are compared with experimental results, as shown in Fig.5.1. From the Fig.5.1, it can be observed that both k-ε (RNG), and k-ε (Realizable) shows close predictions as compared to k-ω (SST). The k-ε (RNG) model shows close prediction in the range of X/λ =0.25 to 0.5, and thereafter from X/λ =0.5 to 1.25 k-ε (Realizable) shows better agreement. The k-ε (RNG) and k-ε (Realizable) show maximum underpredictions of 5% and 3.9% in the range of X/λ =0.25 to 0.5 respectively. Moreover, the k-ε (RNG) and k-ε (Realizable) show maximum over predictions of 7.4% in the range of X/λ =0.5 to 1.25. Both k-ε (RNG) and k-ε (Realizable) models follow the experimental trends of variations within the uncertainty limits, however, the k-ε (Realizable) predictions are more accurate from X/λ =0.5 to 1.25, hence for further study k-ε (Realizable) is employed.

5.4.2 Comparison of Experimental and Numerical Results

To access the accuracy of the numerical model, the numerical results are compared with the present experimental results. The experimental study is performed on the corrugated surfaces for various double injection locations. These locations are labelled as (L_0-L_{25}), (L_0-L_{50}), (L_0-L_{75}), (L_{25}-L_{50}), (L_{25}-L_{75}), and (L_{50}-L_{75}), where the label with the location indicates the distance from the peak of first corrugation. The experimental study is carried out for M=1, DR =1.095, and an injection angle of 45°. The experimental results of centreline effectiveness are obtained for a distance of X/λ = 0.925 in downstream of the first injection hole (i.e., from L_0 to further downstream for the case of L_0-L_{25}. In the present numerical study, the computational domain considered is two-dimensional domain and both geometry and operating parameters are taken identical to the experimental case. Fig.5.2(a) presents the comparison of centreline effectiveness for injection location (L_0-L_{25}). From the Figure, it can be observed that the numerical model shows overprediction from X/λ = 0 to 0.15 and thereafter underprediction from X/λ = 0.15 to1. The maximum overprediction and underprediction are recorded as 9.4% and 8.3% respectively. For the injection location (L_0-L_{50}), the numerical result exhibits mix trend of prediction between L_0 and L_{50}, i.e., overprediction followed by underprediction from X/λ = 0 to 0.2 and X/λ = 0.2 to 0.5 respectively, as shown in Fig.5.2 (b). Thereafter, from X/λ = 0.5 to 1 small overprediction is observed. The maximum overprediction and underprediction are 12.2% and 18% respectively. A similar trend of variation can be observed for the injection location (L_0-L_{75}), as shown in Fig. 5.2 (c). Figure 5.2. (c) clearly shows that numerical results follow the experimental trends with a maximum over-prediction of 10% in the range of X/λ = 0 to 0.2, and a maximum underprediction of 12% in the range of X/λ = 0.2 to 0.75. Thereafter, from X/λ = 0.75 to 1 follows the experimental trends. Fig.5.2 (d) shows the comparison of injection location (L_{25}-L_{50}) with experimental results. From the figure, it can be observed that the numerical results exhibit similar trends as experimental results with a maximum underprediction and overprediction of 7.4% and 3.8% respectively. Interestingly, the injection location (L_{25}-L_{75}) exhibits a different trend as compared to (L_0-L_{25}), as shown in Fig.5.2 (e). The (L_{25}-L_{75}) exhibits small under-prediction and over-predation in the upstream and downstream to the L_{75} injection respectively.

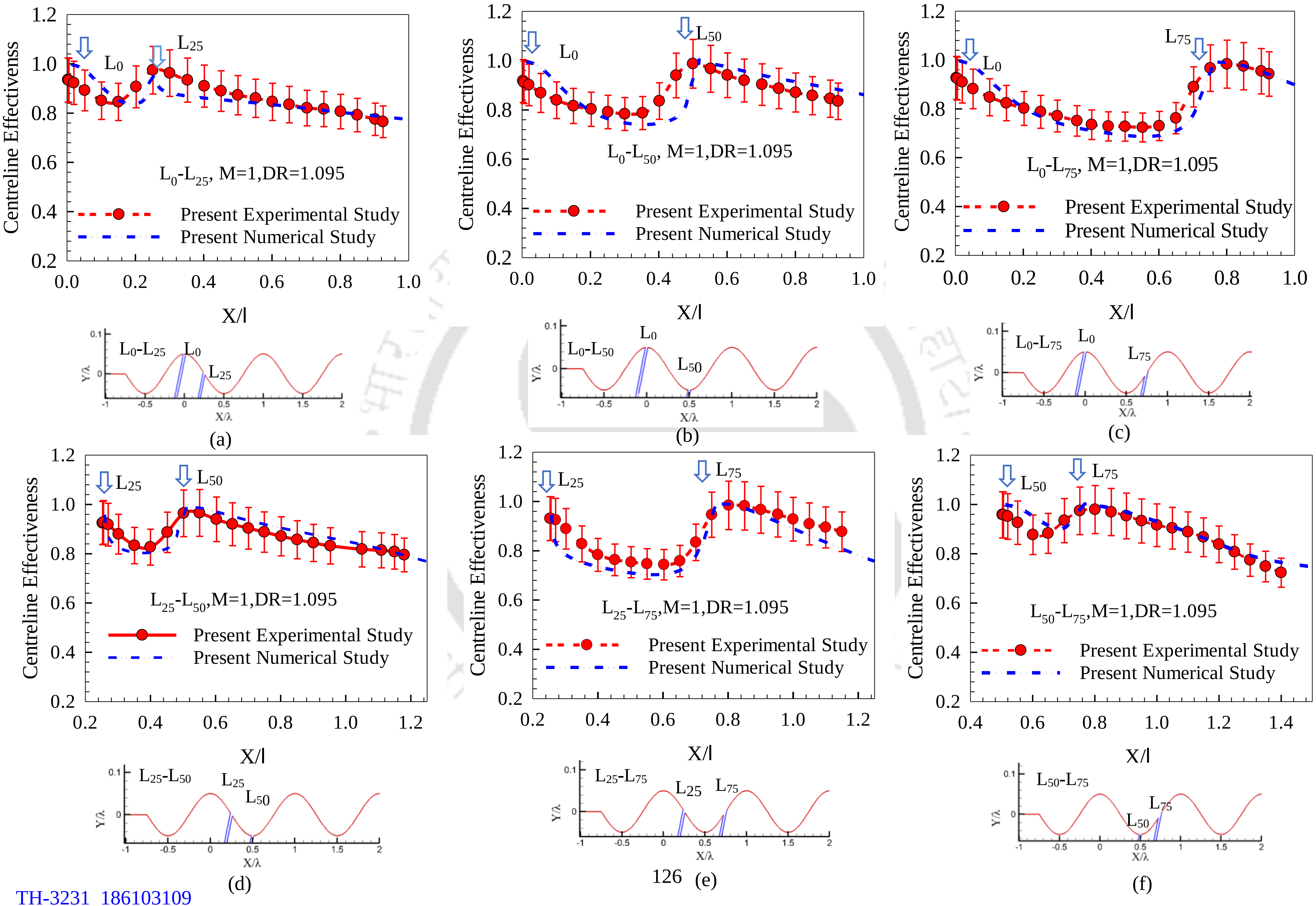

Fig.5.2: Comparison of experimental and numerical results at M=1, (a) L_0-L_{25}; (b) L_0-L_{50}; (c) L_0-L_{75}; (d) L_{25}-L_{50}; (e) L_{25}-L_{75}; (f) L_{50}-L_{75}.

Fig.5.2 (f) presents the variations of numerical results for the injection location (L_{50}-L_{75}). Fig.5.2 (f) clearly shows that the numerical results follow the experimental with a maximum overpredictions of 8% in between the L_{50}, and L_{75} locations i.e., from $X/\lambda = 0.5$ to 0.75. The results of the numerical model follow the experimental trends of variation within the uncertainty limits, and therefore the numerical model can be used in further study.

5.4.3 Effect of Secondary Stream Injection

To study the effect of secondary stream injection on velocity profile, the non-dimensional velocity of with and without secondary injection are presented in Fig.5.3 The non-dimensional velocity profile normal to the corrugated surface extracted in the mid of the double slot and compared with without secondary injection case. The numerical simulations for double slot injections are carried out for blowing ratio (M=1), Density ratio (1.095), and fixed injection angle (45^o). Fig.5.3 (a) presents the non-dimensional velocity profile at X/λ =0.1125, from the figure it can be observed that due to coolant injection through the slots, the velocity profile exhibits a steeper gradient as compared to the without injection case. Moreover, the boundary layer thickness is also reported higher as compared to the without injection case. The velocity profile at $X/\lambda = 0.125$ and $X/\lambda = 0.137$ also exhibits a similar trend as shown in Fig.5.3 (b)-(c). Moving to the other location, $X/\lambda = 0.137$ (i.e., mid of L_{25}-L_{50}) exhibit different trends in the inner shear layer and the velocity tends to retard in the core of the boundary layer. Similarly for other locations. A similar trend can be seen for other locations as shown in Fig. 5.3(e)-(f).

5.4.4 Effect of Various Injection Locations

To study the effect of injection location on film cooling performance of double slot injection film cooling on the corrugated surface, six different injection combinations are considered i.e., (L_0-L_{25}), (L_0-L_{50}), (L_0-L_{75}), (L_{25}-L_{50}), (L_{25}-L_{75}), and (L_{50}-L_{75}) per wavelength. The centreline effectiveness is compared for blowing ratios (M= 0.5, 1.2) and the amplitude to wavelength ratio ($a/\lambda = 0.05$) at fixed density ratio (DR= 1.09) and injection angle 45^o, as shown in Fig.5.4. The position of the hole is different therefore the centreline effectiveness is plotted in the downstream of the first hole for of $X/\lambda = 0$ to 1, regardless of their actual position. From Fig. 5.4, it is observed that the center effectiveness decreases in downstream of the first injection hole (i.e., L_0 in the case of (L_0-L_{25})), however secondary peak in the plot can be observed which indicates the second injection. The injection location, L_{50}-L_{75} shows a better performance range of $X/\lambda = 0$ to 0.5, and from of $X/\lambda = 0.5$ to 0.735 the injection location (L_{25}-L_{75}).

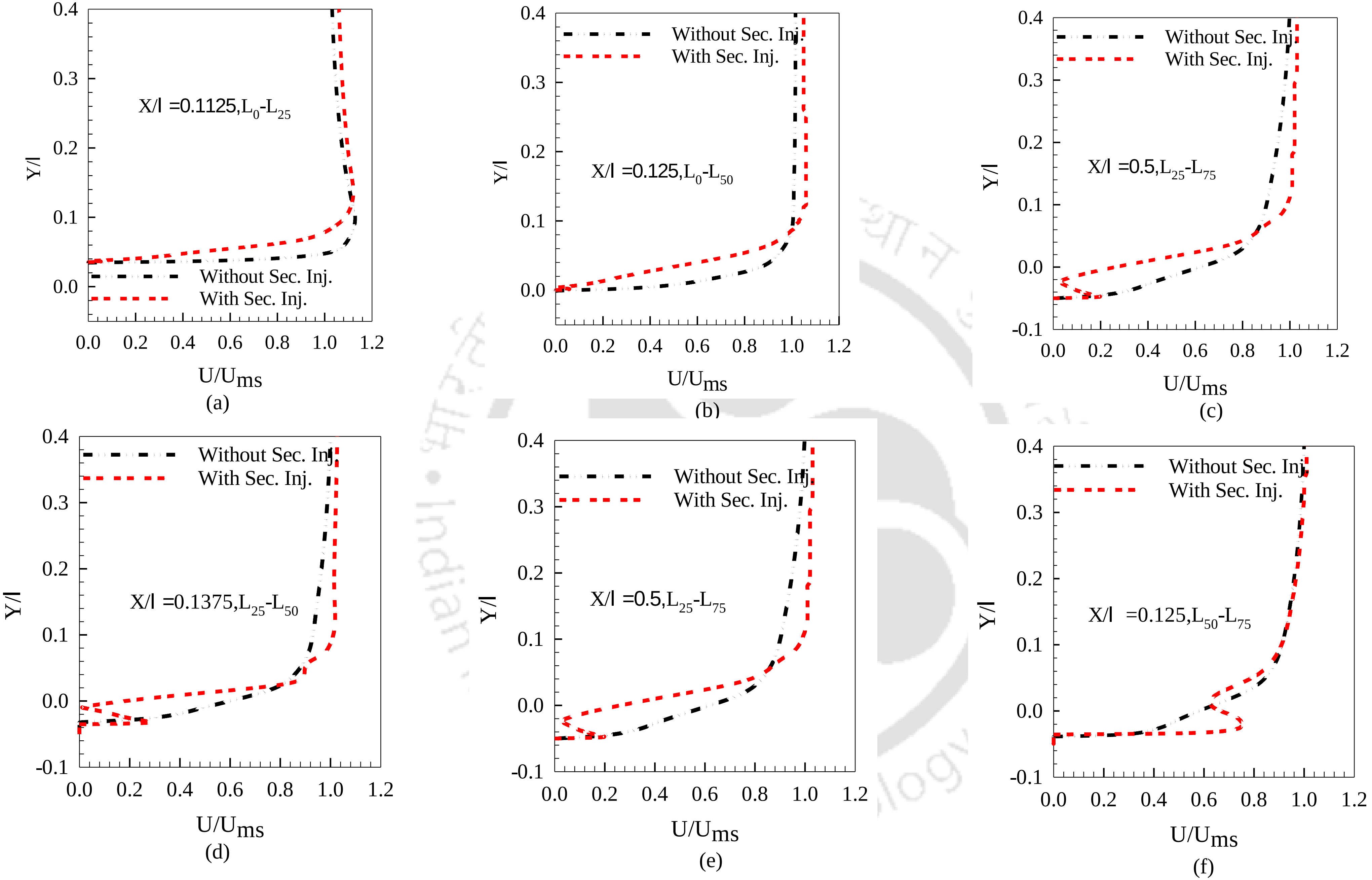

(a) (b) (c) (d) (e) (f)

Fig.5.3: Effect of secondary injection on the non-dimensional velocity (U/U$_{ms}$) profile at mid of (a) L$_0$-L$_{25}$; (b) L$_0$-L$_{50}$; (c) L$_0$-L$_{75}$; (d) L$_{25}$-L$_{50}$; (e) L$_{25}$-L$_{75}$; (f) L$_{50}$-L$_{75}$.

Moving further downstream from X/λ = 0.735 to 1, the L_0-L_{75} injection location shows improved performance. For the further increase of the blowing ratio to M=1, a similar trend can be observed, as shown in Fig. 5.4(b). Figure 5.4(b) clearly shows that the injection location, L_{50}-L_{75} performed better in the range of X/λ = 0 to 0.5, and from of X/λ = 0.5 to 0.735 the injection location (L_0-L_{50}) performance is better. Moving in further downstream from of X/λ = 0.735 to 1, the L_0-L_{75} injection location shows improved performance. Similarly, for the blowing ratio M=2 the injection location, L_{50}-L_{75} performance is a better range of X/λ = 0 to 0.5, and from X/λ = 0.5 to 0.735 the injection location (L_0-L_{50}) performance is better. Moving in further downstream from X/λ = 0.735 to 1, the L_0-L_{75} injection location shows improved performance.

To analyse the performance of various double injection cases, the centreline effectiveness average over one wavelength is plotted in Fig.5.5. The bar graph clearly shows that the performance of L_{50}-L_{75} is best among all selected locations for blowing ratio M=0.5 to 2. For the blowing ratio (M=0.5), the performance of the L_{50}-L_{75} injection location is the best among all injection locations, as shown in Fig.5.5 (a). The centreline effectiveness (wavelength average) of L_{50}-L_{75} is 18.1% higher than the L_0-L_{75} injection case. Fig.5.5 (b) shows the comparison of centreline effectiveness (wavelength average), the performance of the L_{50}-L_{75} injection location is 19% higher than the L_{25}-L_{50} case. Further increase of blowing ratio (M=2), a similar trend can be observed and film cooling effectiveness of the L_{50}-L_{75} injection location is 15% higher than the L_{25}-L_{75} case, as shown in Fig.5.5(c).

The film cooling and heat transfer characteristics of different injection locations can be well understood with the, streamline contour plots shown in Fig.5.6. Figure 5.6. shows the streamline traces for different injection locations at blowing ratio (M=1), density ratio (DR=1.095), and (a/λ =0.05). Fig. 5.6. (a) illustrates, the streamline traces for L_0-L_{25} injection locations. The streamline traces show two recirculation zones, a small recirculation zone is observed the upstream of L_{25} injection hole (i.e., X/λ = 0.1 to 0.25), and a relatively bigger zone is can be observed in the downstream of L_{25} location (i.e., X/λ = 0.25 to 0.75). Both the recirculation zones are trapped below Y/λ=0.05, and hence a sharp drop in effectiveness is reported. Fig 5.6. (b) shows the streamline contour plots for the L_0-L_{50} injection location, and a small recirculation zone can be observed between X/λ = 0.3 to 0.5. However, downstream of the L_{50} injection, the corrugation profile forms a converging region, and due to this, the recirculation zone vanishes. Therefore, the drop in effectiveness profile is relatively monotonic as compared to the upstream to the L_{50} injection location.

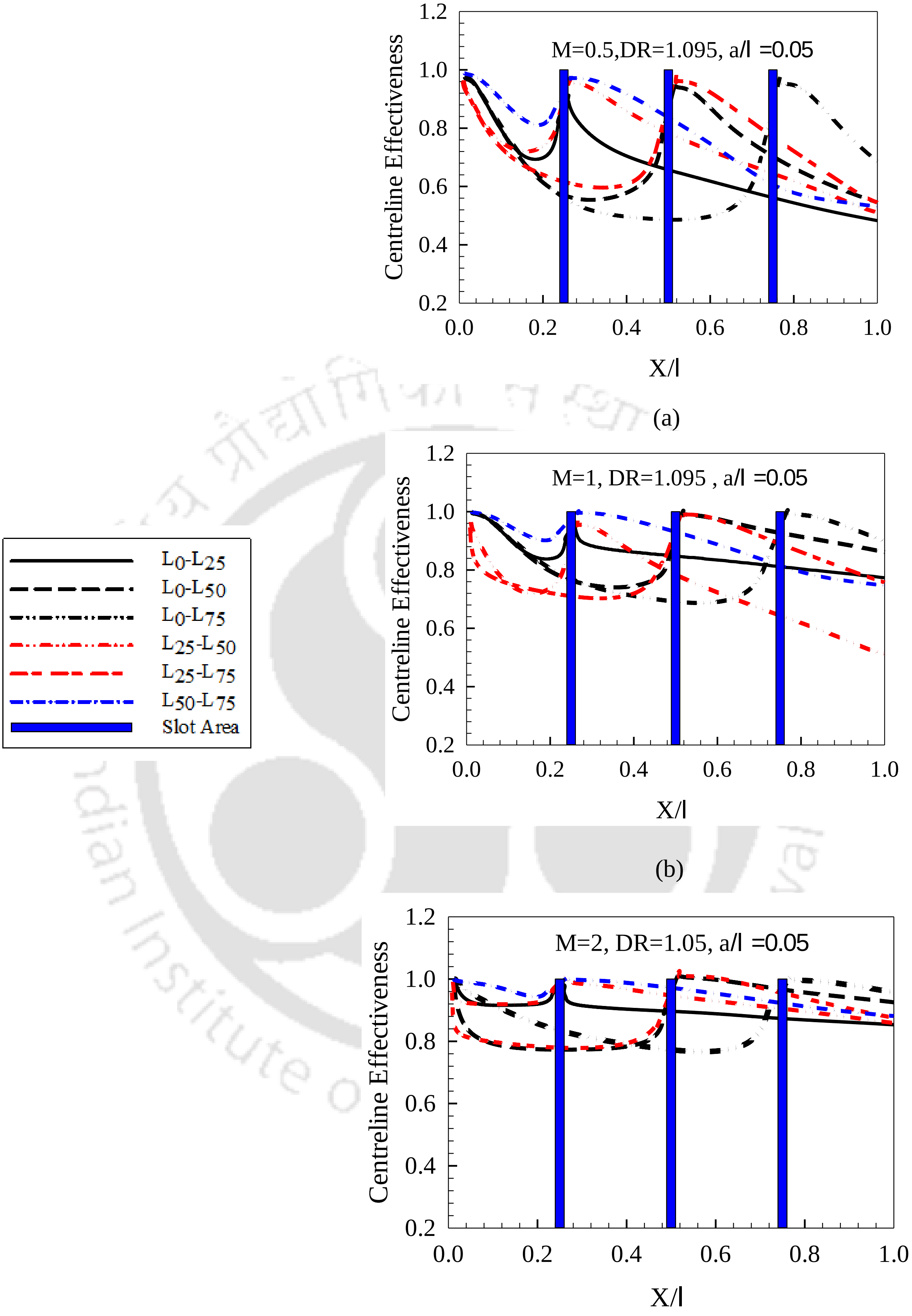

(a)

(b)

(c)

Fig.5.4: Effect of various injection locations on centreline film cooling effectiveness at (a) M=0.5; (b) M=1; (c) M=2.

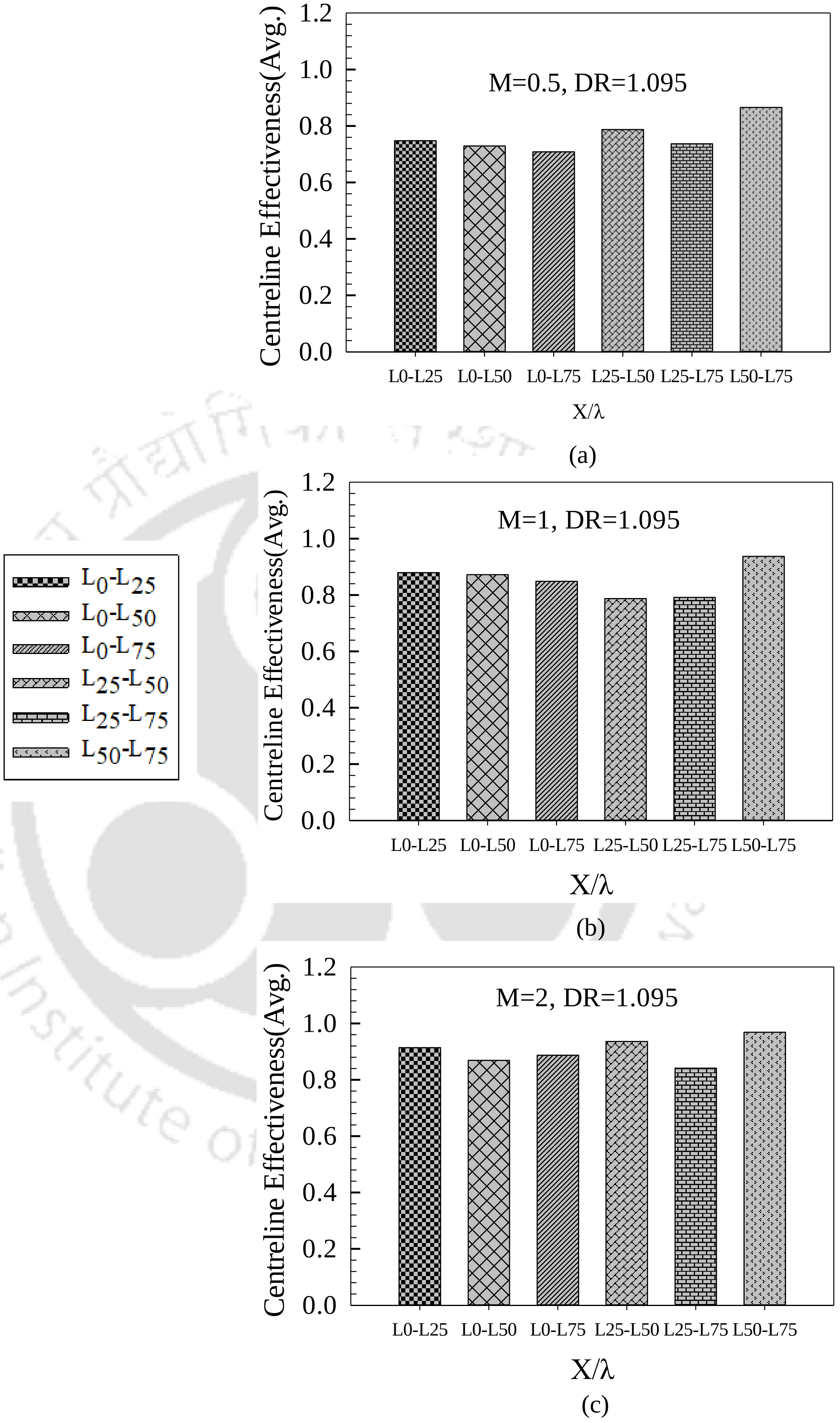

Fig.5.5: Comparison of wavelength average effectiveness of various injection locations at (a) M=0.5 (b) M=1 (c) M=2.

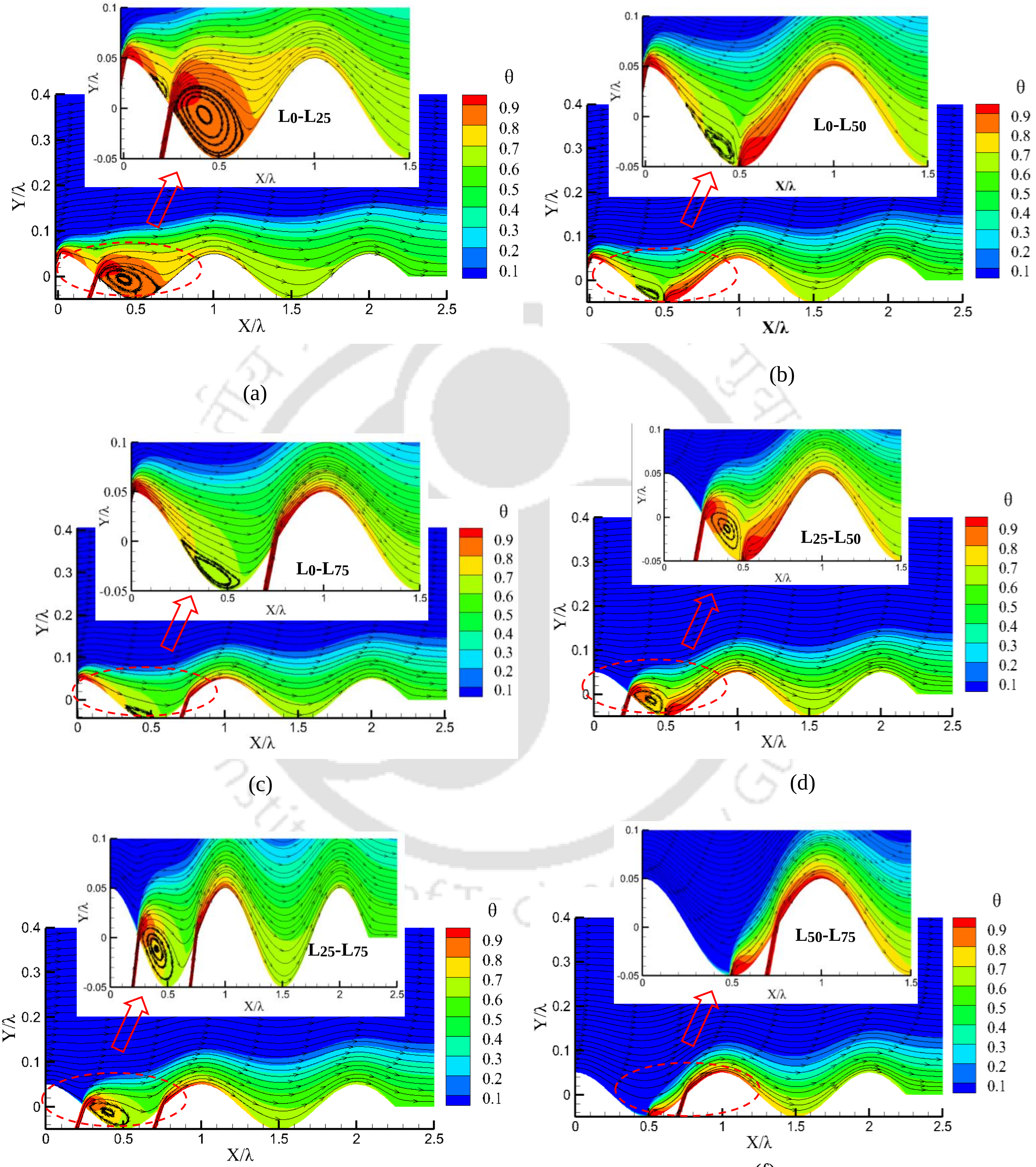

(a)

(b)

(c)

(d)

(e)

(f)

Fig.5.6: Streamline contours of various injection locations at M =1, (a) L_0-L_{25}; (b) L_0-L_{50}; (c) L_0-L_{75}; (d) L_{25}-L_{50}; (e) L_{25}-L_{75}; (f) L_{50}-L_{75}.

A similar trend to the injection location L_0-L_{50} can be observed for the L_0-L_{75} injection case, as shown in Fig. 5.6. (c), where the recirculation zone can be observed only in the direction upstream to the L_{75} injection location. Apart from that the injection locations L_{25}-L_{50} and shows L_{25}-L_{75} exhibit different trends, as shown in Fig. 5.6. (d)-(e). Fig. 5.6. (d)-(e) clearly shows the recirculation regions in the direction upstream to the L_{50} and L_{75} injection locations i.e., $X/\lambda = 0.25$ to 0.5. However, the recirculation zone vanishes in the direction upstream to the L_{75} injection locations. Moreover, the vortices are absent for the L_{50}-L_{75}, injection locations and hence improved performance can be seen.

5.4.5 Effect of Amplitude to Wavelength Ratio

The present study considers three distinct amplitude-to-wavelength ratios (a/λ), 0.05, 0.075, and 0.1, to evaluate the impact of corrugation geometry on film cooling behaviours. The numerical simulations carried out for various double injection combinations viz., (L_0-L_{25}), (L_0-L_{50}), (L_0-L_{75}), (L_{25}-L_{50}), (L_{25}-L_{75}) and (L_{50}-L_{75}) at $M=1$, injection angle 45^o and $DR = 1.095$. Figure 5.7 (a) presents the comparison plot of centreline effectiveness for the L_0-L_{25} injection location. From Fig.5.7(a) it can be observed that all the a/λ ratios have similar trends of variations, and a peak in the effectiveness can be seen near the second injection location (i.e., L_{25}). However, the increase of a/λ from 0.05 to 0.1 causes a sudden drop in effectiveness can be observed. Moving to further downstream between $X/\lambda = 0.25$ to 1, the depth of the wavy valley grows as the corrugation amplitude to wavelength increases which limits coolant spread further downstream as a result, coolant flow is constrained to a limited region, and film cooling effectiveness declines. The comparison of centreline effectiveness for the L_0-L_{50} injection case is shown in Fig.5.7 (b). Figure 5.7(b) clearly shows that an increase of a/λ from 0.05 to 0.1 causes a substantial drop in effectiveness from $X/\lambda = 0$ to 0.1, and moving to further downstream to the L_{50} the effects are insignificant. A similar trend to the L_0-L_{50} location is reported for the L_0-L_{75} case, as shown in Fig.5.7 (c). Figure 5.7(c) clearly shows that with the increase of a/λ from 0.05 to 0.075 the film cooling effectiveness drops between the two injection locations (i.e., L_0 and L_{75}), and further increase of a/λ from 0.075 to 0.1 the effects are insignificant. Apart from that the L_{25}-L_{50}, L_{25}-L_{75}, and L_{50}-L_{75} exhibit inherently different trends as compared to L_0-L_{25}, L_0-L_{50}, and L_0-L_{75} locations, as shown in Fig.5.7 (d)-(e). Figure.5.7 (d) shows the trends of variations for L_{25}-L_{50} injection location, from the figure it is observed that with the increase of amplitude to wavelength ratio a/λ from 0.05 to 0.1 the effectiveness increases between the two injection locations (i.e., between L_{25} and L_{50}, from $X/\lambda = 0.25$ to 0.50) and thereafter the effectiveness reduces (i.e., from $X/\lambda = 0.5$ to 1.25).

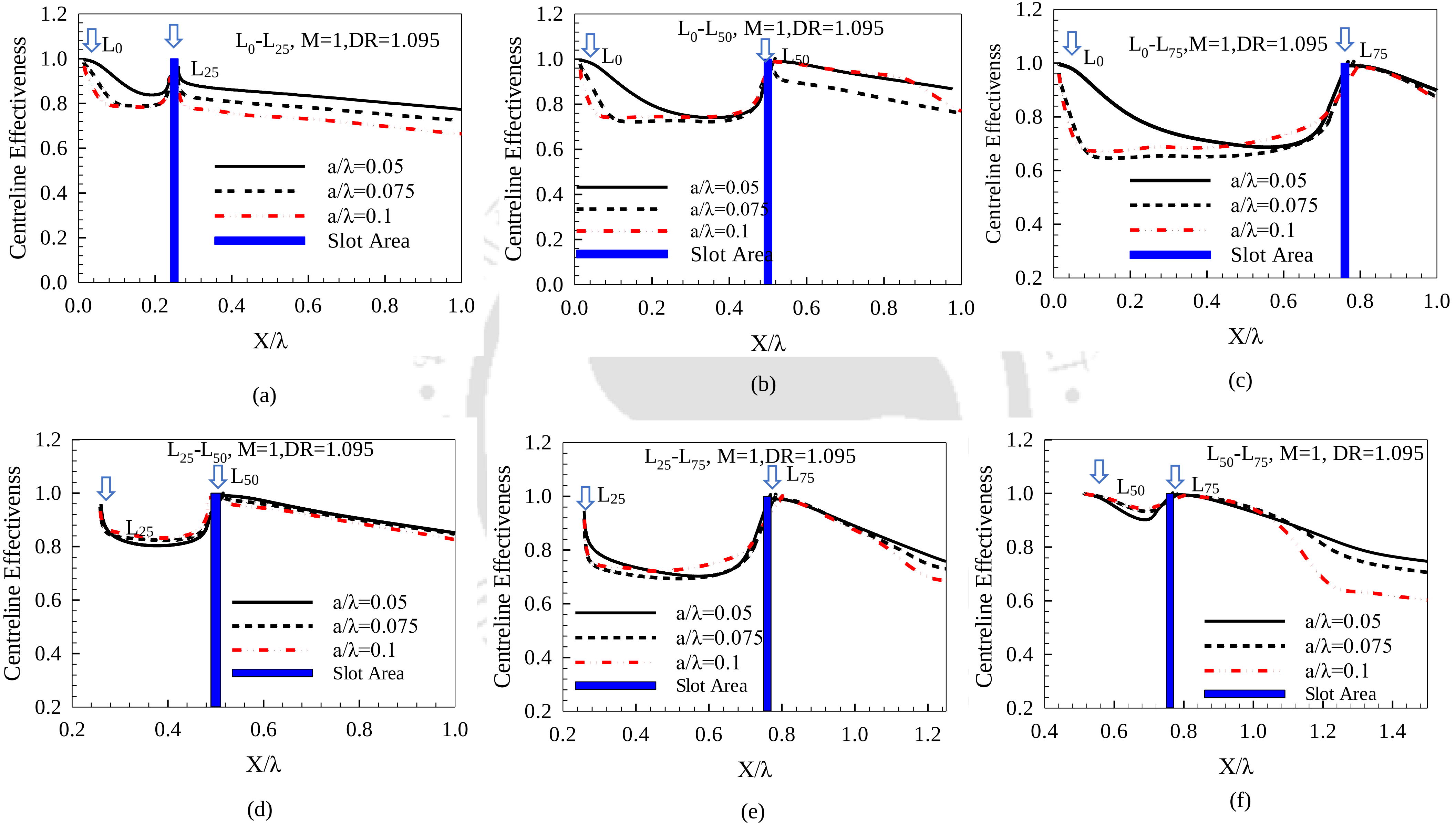

Fig.5.7: Comparison of centreline effectiveness for various amplitude to wavelength ratios at (a) L_0-L_{25} (b) L_0-L_{50} (c) L_0-L_{75} (d) L_{25}-L_{50} (e) L_{25}-L_{75} (f) L_{50}-L_{75}.

With the increase of amplitude to wavelength the coolant accumulation increases on the slant edge of corrugation in between the L_{25} and L_{50} which offer more resistance to the heat transfer and hence the effectiveness increase. A similar trend is reported for the L_{25}-L_{75} and L_{50}-L_{75}, as shown in Fig.5.7 (e)-(f), the effectiveness increases between the two injection locations and thereafter decreases.

5.4.6 Effect of Blowing Ratio

This section illustrates the effect of the blowing ratio on film cooling characteristics of double slot injection on the corrugated surface. The numerical study is performed for blowing ratio (M= 0.5, 1 and 2), at fixed density ratio (DR=1.095), injection angle (45^o), and a/λ =0.05. Fig.5.8 (a) presents the effectiveness trends for L_0-L_{25} injection location. Figure 5.8 (a) clearly shows that with the increase of M= 0.5 to 1, a significant improvement in centreline effectiveness is observed throughout downstream from X/λ = 0 to 1, and the maximum improvement is reported as 50%. However, a further increase of the blowing ratio from, M= 1 to 2 resulted in a maximum improvement of 11.75%. With the increase of blowing ratio, the mass flow rate of coolant increases and film cooling improves. Moreover, the further increase of blowing ratio causes secondary jet penetration into the mainstream and hence relatively lower impact can be observed for the increase of M=1 to 2. Fig.5.8 (b) illustrates the comparison trends of centreline effectiveness for L_0-L_{50} injection location. From Fig.5.8 (b) it is observed that, with the increase of blowing ratio from M= 0.5 to 1, centreline effectiveness increases throughout the downstream locations from X/λ = 0 to 1. The further increase of blowing ratio from M= 1 to 2, causes coolant stream lift-off from the corrugated surface, and hence a small drop in the effectiveness can be seen in the range of X/λ = 0 to 0.28. A similar trend can be observed for injection location, (L_0-L_{75}), where the centreline effectiveness increases for the increase of blowing ratio, M=0.5 to1, as shown in Fig.5.8(c). A small drop in the effectiveness can be seen in the range of X/λ = 0 to 0.12 with the further increase of blowing ratio from M= 1 to 2. Moreover, the injection locations L_{25}-L_{50} and L_{25}-L_{75} locations exhibit similar trends, as shown in Fig 5.8(d)-(e). The increase of blowing ratio M= 0.5 to 1 and M= 1 to 2 increases the centreline film cooling effectiveness, except for a narrow region near the slot where a drop can be observed. Moving to further downstream locations i.e., L_{50}-L_{75} the centreline effectiveness improves throughout the downstream location (X/λ = 0.5 to 1.5) as the blowing ratio increases from M=0.5 to 2, as shown in Fig.5.8 (f).

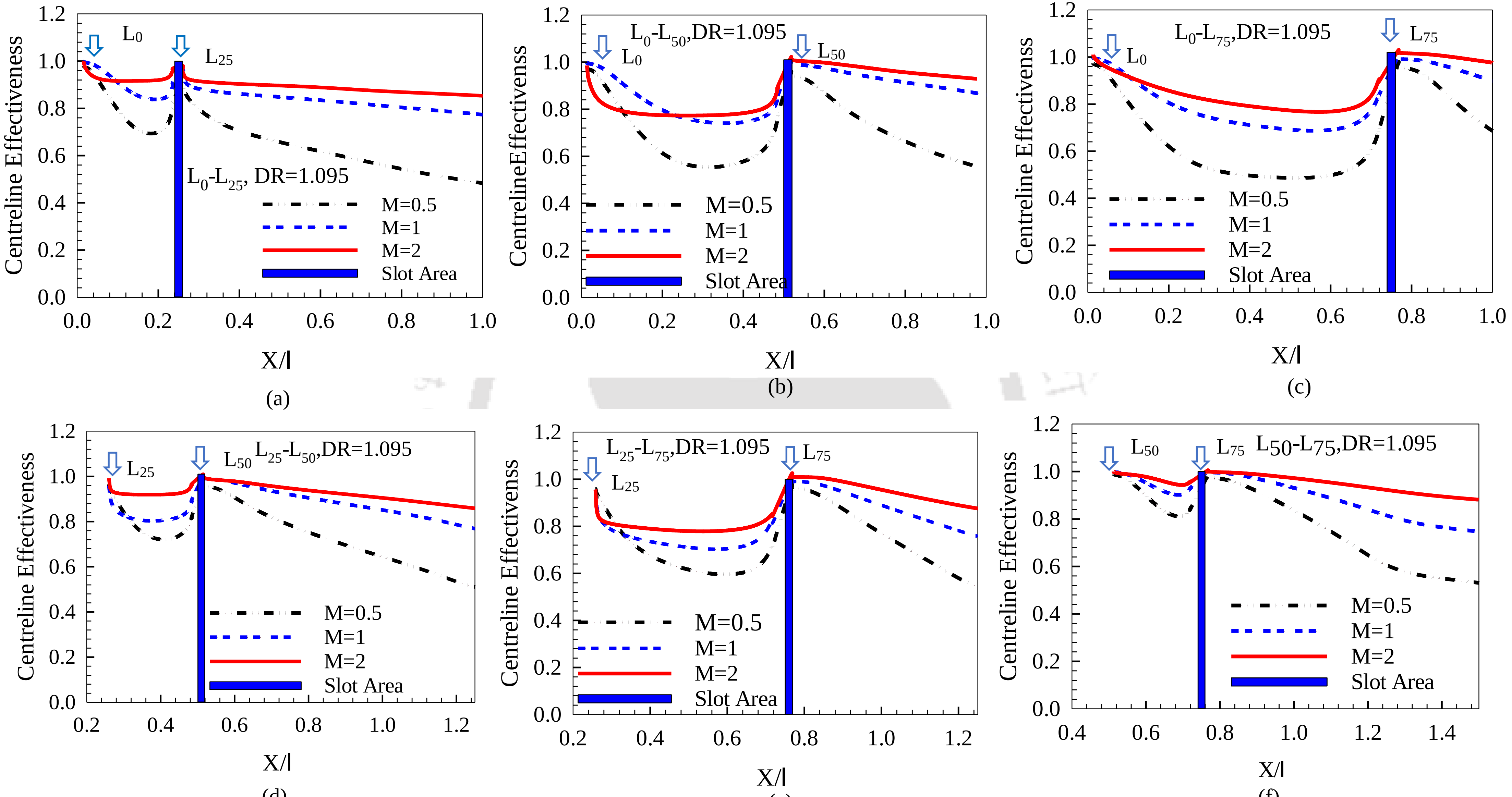

(a) (b) (c)

(d) (e) (f)

Fig.5.8: Effect of blowing ratio on centreline film cooling effectiveness of (a) L_0-L_{25}; (b) L_0-L_{50}; (c) L_0-L_{75}; (d) L_{25}-L_{50}; (e) L_{25}-L_{75}; (f) L_{50}-L_{75}.

5.4.7 Effect of Density Ratio

In order to study the effect of density ratio, on the film cooling performance of various injection locations. The centreline effectiveness is plotted as the function of the density ratio. The numerical simulations are carried out for three different density ratios viz. 1.095, 2.5, and 4 at the fixed blowing ratio, M=1, a/λ=0.05, and injection angle 45^o. The effect of the density ratio for the L_0-L_{25} injection position is shown in Fig.5.9 (a). As the density ratio increases from DR = 1.095 to 4, as seen in Fig.5.9 (a), the centreline efficacy decreases. The effect is negligible upto X/λ=0 to 0.1 and thereafter, X/λ=0.1 to 1 a significant difference can be observed. It is expected that centreline effectiveness would rise monotonically as density increases. However, for the fixed blowing ratio, an increase in density ratio leads to a reduction in the secondary mass flow rate which further reduces the cooling of the corrugated plate exposed to the plenum side. The present study considered the conjugate heat transfer through the corrugated plate exposed to the secondary flow inside the plenum chamber, and due to the reduced mass flow rate of secondary flow, a reduction in centreline effectiveness can be seen. A similar trend can be seen for L_0-L_{50}, and L_0-L_{75}, as shown in Fig.5.9 (b)-(d). From Fig.5.9 (b)-(d), it can be observed that the centreline effectiveness decreases with the increase of density ratio from DR=1.095 to 4. Apart from that, for the L_{25}-L_{50} location with the increase of density ratio from DR=1.095 to 2.5, centreline effectiveness increases in the range of X/λ=0 to 0.1 and thereafter decreases. The further increase of density ratio from DR=2.5 to 4, effectiveness decreases throughout from of X/λ=0 to1, as shown in Fig.5.9(d). A similar trend to the L_{25}-L_{50}, the effectiveness trends is reported for the L_{25}-L_{75} and L_{50}-L_{75} locations, as shown in Fig.5.9 (e)-(f).

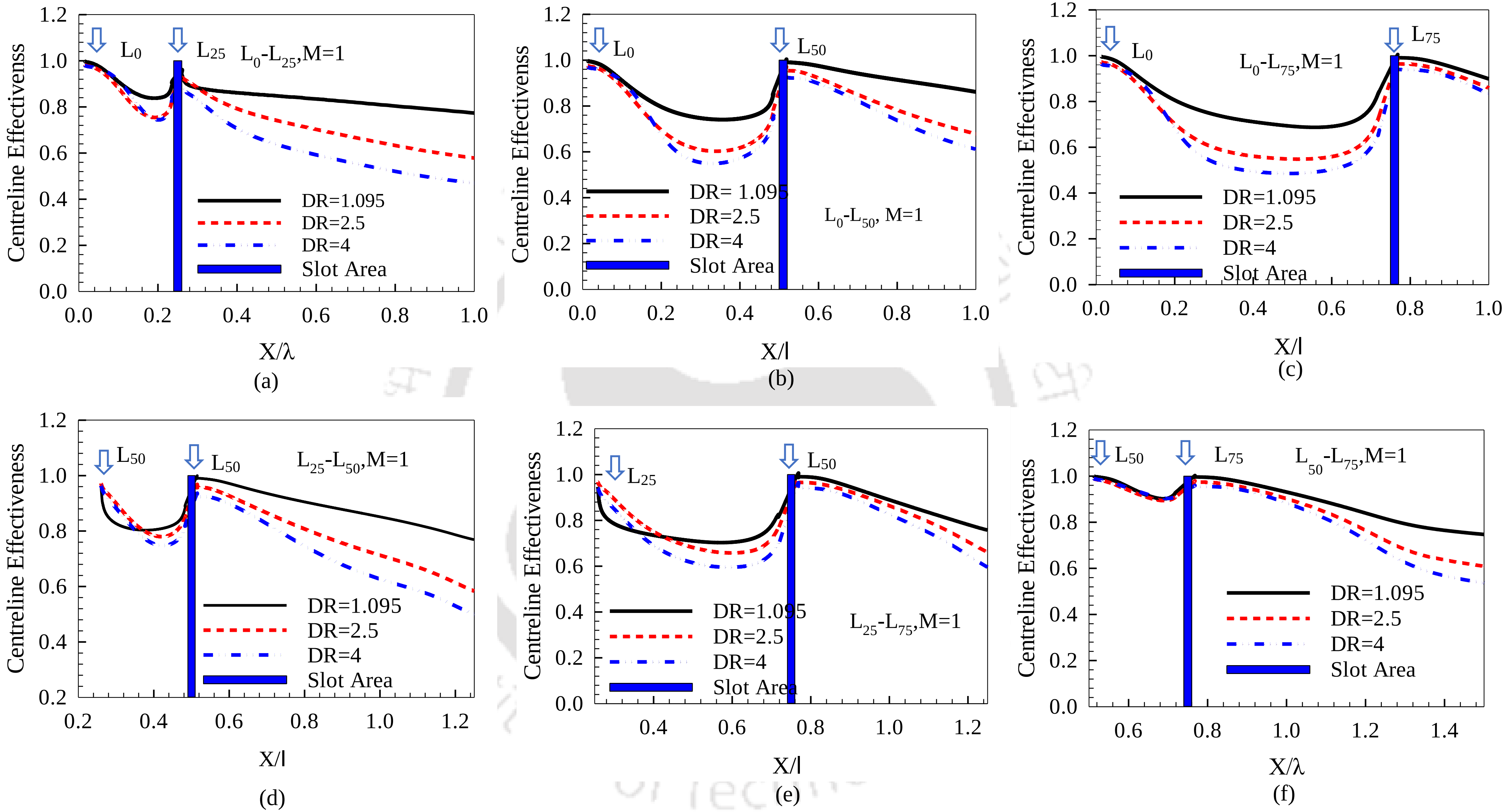

(a) (b) (c) (d) (e) (f)

Fig.5.9: Effect of density ratio on centreline film cooling effectiveness of (a) L_0-L_{25}; (b) L_0-L_{50}; (c) L_0-L_{75}; (d) L_{25}-L_{50}; (e) L_{25}-L_{75}; (f) L_{50}-L_{75}.

5.5 Conclusion

To identify the best injection configurations and operating parameters for film cooling applications on the corrugated surface, experimental and numerical studies have been conducted for a variety of double injection locations viz. injection locations and the corrugation amplitude to wavelength ratio. The numerical studies have been carried out for a wide range of parameters such as blowing ratio (M= 0.25-2), and density ratio (DR= 1.095, 2.5, and 4,) Based on the present study following conclusions can be drawn:

1. The present study demonstrates that the film cooling performance of sinusoidal corrugated surfaces strongly depends on coolant injection location. Six different injection locations viz., (L_0-L_{25}), (L_0-L_{50}), (L_0-L_{75}), (L_{25}-L_{50}), (L_{25}-L_{75}), and (L_{50}-L_{75}) were considered, and the results indicate that the film cooling performance of L_{50}-L_{75} injection is best among all selected locations. The centreline effectiveness (average over a wavelength) is reported to be 15 to 19% higher than the least-performing injection location for the blowing ratio (M= 0.5 to 2).
2. The study reveals that the increase of amplitude to wavelength ratio (a/λ) shows district impact on different injection locations. As the depth of the wavy valley grows as the corrugation amplitude to wavelength increases which limits coolant spread further downstream and restricts the coolant spread and with the increase of corrugation depth the film cooling effectiveness decreases. The impact of corrugation amplitude on the wavelength ratio is higher for L_0-L_{25}.
3. The numerical study suggests that the film cooling effectiveness of the corrugated surface strongly depends on the blowing ratio, with the increase in blowing ratio the film cooling effectiveness increases even after the blowing ratio (M=2).
4. The study suggests that the non-dimensional velocity profile is significantly influenced by the coolant injection. The non-dimensional velocity profile with coolant injection exhibits a steeper gradient for L_0-L_{25}, L_0-L_{50}, and L_0-L_{75} cases. However, for other locations such as L_{25}-L_{50}, L_{25}-L_{75}, and L_{50}-L_{75}, the velocity profile is strongly influenced in the inner shear layer.

CHAPTER 6: EXPERIMENTAL AND NUMERICAL STUDY OF THE EFFECT OF FORWARD AND REVERSE INJECTION ON FILM COOLING AND THERMAL STRESS DISTRIBUTION ON A CORRUGATED SURFACE

CHAPTER6

6.1 Introduction

The recent advancement in film cooling configuration has focused more attention on backward/reverse injection. The reverse injection over flat surfaces shows encouraging results to overcome the formation of counter-rotating vortices. The counter-rotating vortices are commonly known as kidney vortices which promote coolant lift-off and restrict the coolant spread over the surface. The reverse injection is still the infantry stage for most of the applications, such as vanes and corrugated surfaces. In practical applications, gas turbine blades, combustion chambers, and aero-engine afterburner liners are made of nickel-based super-alloy [68]. The thermal conductivity of such superalloys is high, and thus conduction heat transfer through the metal cannot be ignored. Hence, under such conditions, conjugate heat transfer analysis is more accurate. The modern aero-engine afterburner temperature as high as 2000K, and the typical values of density ratio and operating pressure is also close to 4 and 5 respectively. To ensure the safe operation of components, thermal protection is essential. Film cooling is one of the most effective techniques for the thermal management of components under the pathway of high-temperature flue gases. In the case of film cooling a coolant stream, is injected over the surface which forms a thin protection layer and a temperature gradient exit over the surface. The excessive temperature gradient exits over components and yields thermal stress. Excessive thermal stress may cause failures and structural deformation. Therefore, thermal stress analysis is essential to understanding the effective design of the cooling system.

In this chapter experimental and numerical study is focused on film cooling analysis of corrugated surfaces using forward and reverse injection. The mainstream is the hot stream of air and a secondary stream of coolants is injected through three rows of cylindrical holes. A comparative study of both forward and reverse injection is presented for the flow, and heat transfer phenomenon over the corrugated surfaces. Additionally, the temperature profile obtained from coolant injection is used to analyse the thermal stress. The experimental studies were used to validate the numerical model, and for further parametric study, the operating parameters range has been extended.

6.2 Physical Problem and Test Plate

The present work explores the effect of forward and reverse injection configurations on the flow and thermal characteristics of a sinusoidal corrugated surface. The present study uses three rows of cylindrical holes per wavelength of a corrugated test plate. The detailed positions of the holes are presented in chapter 2 (section 2.2.4). The study investigates a corrugated test plate of the sinusoidal profile, and the profile is obtained by the expression given by Maass and Suchusman [77]. The test plate is made of a low thermally conductive material with a thermal conductivity of 0.16 W/(m·K) and is placed in the mainstream flow of heated air, and the secondary stream of relatively cooled air is injected over it through the cylindrical holes of diameter ($D/\lambda = 0.06$) and lateral pitch of ($P/D = 3$). The cylindrical holes are inclined at 45^o in both forward and reverse configurations, in such a way that the axial component of the secondary flow is opposite to the mainstream in the reverse case. However, in the case of forward injection, the axial component of the secondary stream is in the same direction as the mainstream flow.

6.3 Numerical Studies

6.3.1 Computational Domain

A three-dimensional domain is used for present numerical investigations, as discussed in chapter 2 (section 2.9.4). It consists of various inlets and outlet boundaries, side walls, plenum walls, and corrugated walls. The length, width, and height of the domain are 4λ, 2λ, and 2λ where λ indicates the wavelength of the corrugation profile. The mainstream is heated air injected passing over a sinusoidal corrugated surface, and two protect it coolants are injected through three rows (R_1, R_2, and R_3) holes. The holes are placed at the uniform lateral pitch of 3D, where D is the cylindrical hole diameter. The specific positions of holes measured from the peak of the first corrugation in the direction of mainstream flow. The coolant holes are cylindrical and inclined at 45^o with the mainstream flow direction.

6.3.2 Boundary Conditions, Operating Parameters, and Solution Methodology

The governing equations of mass momentum and energy along with the conjugate heat transfer are solved using a finite volume solver as discussed in previous chapter 2. The detailed of grid resolution and solution method are also discussed in chapter 2. In the case of the present study, the air is considered as the working fluid for both mainstream and secondary streams, and density variations with temperatures are also taken into account. The density of the working fluid is calculated by using the ideal gas equations. As the temperature variations in the computational domain are significantly high, the thermophysical properties such as thermal conductivity (λ), specific heat (C_p), and viscosity (μ) are taken as temperature dependent. In the present numerical study, the computational domain consists of various boundaries, the mainstream and secondary stream inlet is assigned as a velocity inlet where flow velocity, turbulence intensity, and temperature are specified. The flow outlet is treated as a pressure outlet with zero-gauge pressure. For all cases of fixed turbulence intensity of 5% is specified. The mainstream inlet and secondary stream inlet were assigned as velocity inlets, where all velocity and temperature values were specified. The numerical values of velocity and temperature correspond to the parameter sets of the various cases being computed (i.e., density ratio, blowing ratio, Reynolds number,). The outlet is assigned as a pressure outlet boundary with zero-gauge pressure. For numerical studies, the test plate is made of Nickel-based superalloy IN738LC, the detailed physical properties are discussed in chapter 2 (section 2.11.2). The corrugated surface covered with a plenum, and the inner slot wall are all fluid-solid interfaces imposed with the non-slip condition. The plenum wall and top wall (Fig. 2.17, section 2.9.4) are assigned as no-slip adiabatic conditions.

Table.6.1: Range of operating parameters used in the present study.

S.N.	**Parameters**	**Value**
1.	Blowing ratio (M)	0.5,1,2.
2.	Density ratio (DR)	4
4.	Mainstream Reynolds Number (Re_λ)	0.36×10^5

The present study used a Finite Volume solver, ANSYS FLUENT v20.0 [92] to solve governing equations of mass, momentum, and energy. The conservation equations terms are discretized with second-order accurate schemes, and the SIMPLE algorithm [93] is used for coupling of pressure and velocity. The convergence criteria for mass and momentum energy are defined as $10^{-6,}$ and 10^{-8} respectively.

6.4 Results and Discussions

This section presents the experimental and numerical results obtained for both forward and reverse flow in terms of effectiveness distribution and flow patterns. The validation study is carried out for a limited range of parameters i.e., M=1, DR=1.08. However, the numerical study is extended for the actual operating range of the aero engine afterburner using the corrugated liner of INL738LC. The parametric study is carried out for blowing ratio (M=0.5,1 and 2) at fixed density ratio (DR=4) operating pressure (5 bar).

6.4.1 Numerical Model Validation

For the RANS-based simulations, the selection of a suitable turbulence model for corrugated surface film cooling is vital. The accurate turbulence model is chosen based on the comprehensive analysis of various two-equation turbulence models, as discussed in our previous chapters 4 and 5. This study discussed that the calculated results are highly sensitive to the turbulence models, and k-ε turbulence was found to capture the film cooling on a corrugated surface accurately. The experimental study uses a corrugated test plate of low thermal conductivity material Nylon 12. Therefore, the numerical case for validation also considers similar geometrical configurations and thermo-physical properties. The numerical simulations are carried out for injection location for both forward and reverse injection at blowing ratio (M=1) and density ratio (DR=1.08), and the predictions are compared with experimental results, as shown in Fig.6.1. The experimental results are plotted with uncertainty bar for a streamwise distance of X/λ =0 to 0.9. The detailed procedure of uncertainty calculations is given in chapter 2. The maximum uncertainty in film cooling effectiveness is reported as 10% with a 95% confidence level.

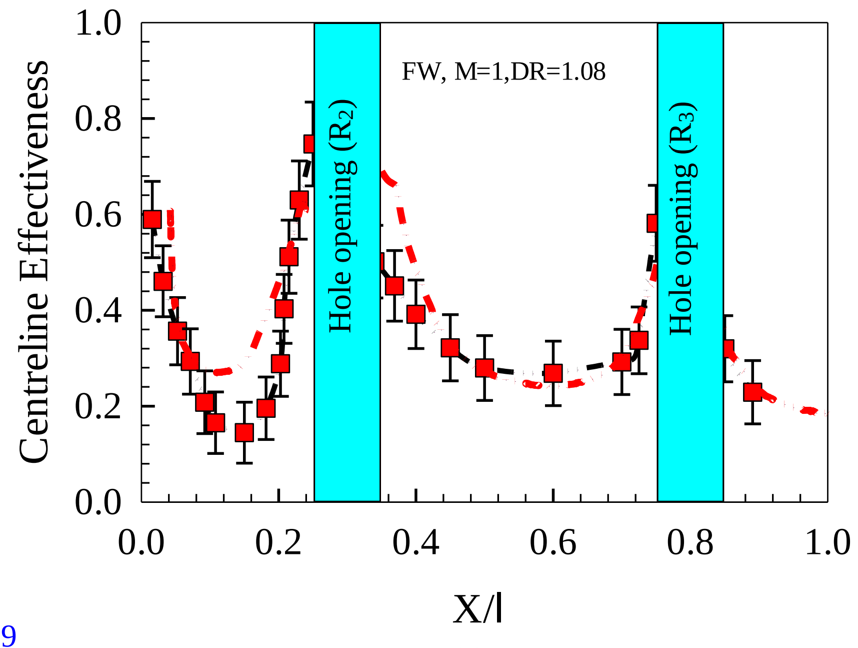

(a)

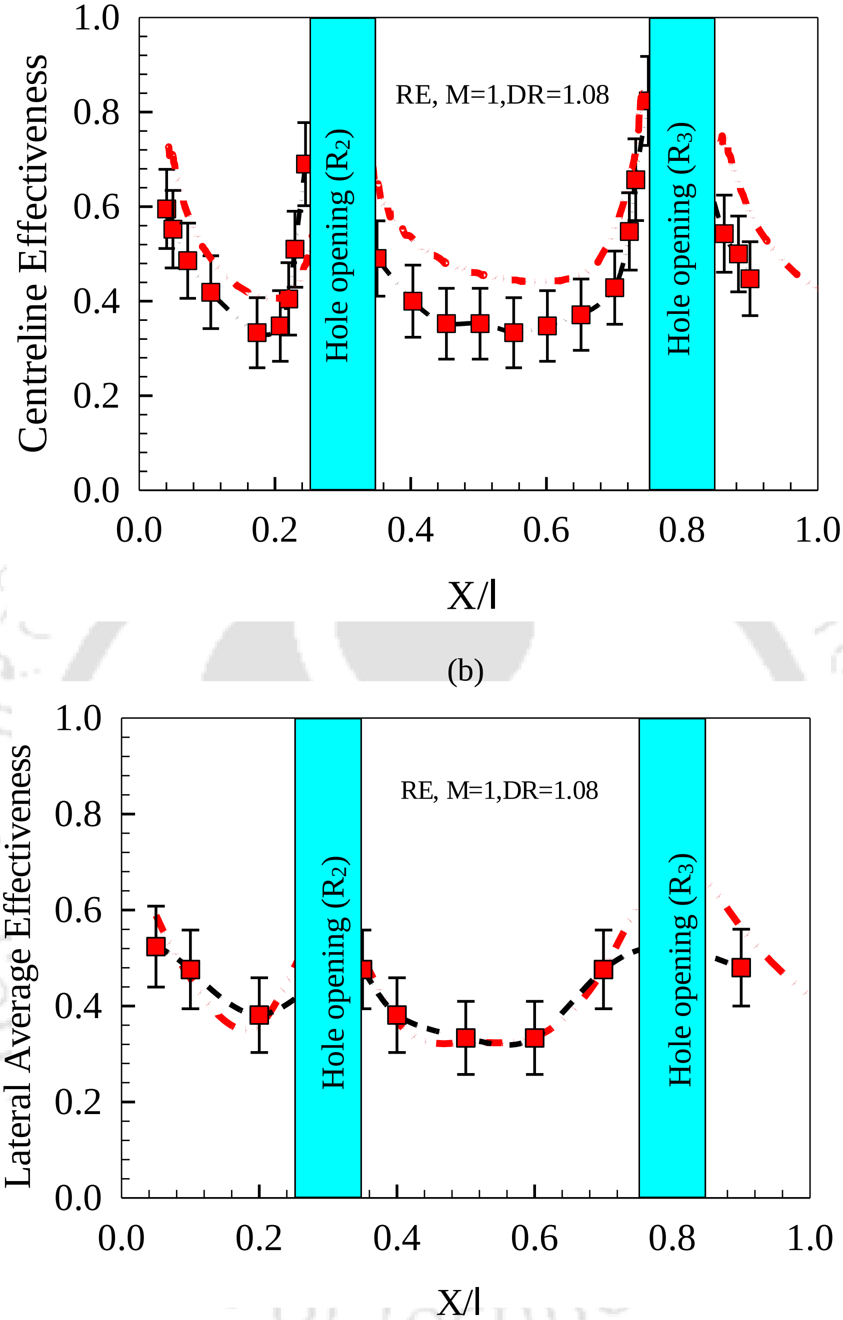

(b)

(c)

Fig.6.1: Validation of numerical model (a) centreline effectiveness (FW); (b) centreline effectiveness (RE); (c) lateral average effectiveness (RE).

The results predicted by the numerical model show a similar distribution trend for centreline effectiveness, as shown in Fig.6.1. Figure 6.1(a) clearly shows trends for forward injection, and the numerical model accurately captured the trend downstream to the second row (R_2,) however a small deviation can be seen in upstream i.e., close to X/λ =0.05 to 0.2. The maximum deviation of 26% is reported near X/λ=0.15. A similar trend is observed for reverse injection, where the numerical model follows the experimental trends with a small deviation in the range of X/λ =0.35 to 0.55, as shown in Fig. 6.1 (b). The deviations are within the experimental uncertainty limits. A better verification of the numerical model was obtained from a comparison of lateral average effectiveness. The lateral averaging is performed for ±4.5D, from the central hole (Z/D=0). Figure 6.1(c) shows the lateral average effectiveness comparison for reverse injection. From Fig.6.1 (c) it can be observed that the numerical model accurately captured the lateral spreading of coolant within uncertainty limits. The maximum deviation is 10%, at X/λ=0.9. The numerical models accurately follow the experimental trends; hence it can be employed for further investigation.

6.4.2 Centreline Effectiveness and Lateral Average Effectiveness

In this section, the film cooling effectiveness for both forward and reverse cases are compared, as shown in Fig.6.2. The centreline effectiveness is plotted along the central hole (i.e., Z/D =0). The centre of the first row of holes in the mainstream flow direction is treated as the origin, and the results are plotted to further downstream for one wavelength. From Fig.6.2 (a), it can be observed that at low blowing ratio (M=0.5), the effectiveness plot for reverse injection dominates the forward case, except the region X/λ =0 to 0.3, and X/λ = 0.48 to 0.72. The peak in effectiveness plots indicates the hole locations and the height of the peak increases in the downstream direction. The conjugate heat transfer through the test plate is taken into consideration, therefore the upstream rows are subjected to higher heat transfer from the heated mainstream. Hence the lower effectiveness peak is obtained for the hole located in the first row (i.e., R_1) and second row (i.e., R_2) compared to the third row (i.e., R_3). With the further increase of blowing ratio (M=1), the reverse injection effectiveness is better throughout downstream locations except in a narrow region X/λ = 0.16 to 0.32, as shown in Fig.6.2(b). However, for the blowing ratio (M=2), the reverse injection effectiveness is better at the downstream location, as shown in Fig.6.2(c). At a low blowing ratio, compared to forward injection the reserve injection the secondary stream flow experiences a major portion of momentum to overcome the mainstream. Hence, at a higher blowing ratio the gain in effectiveness is higher. The further increase of blowing ratio (M=2) shows significant improvement throughout downstream locations.

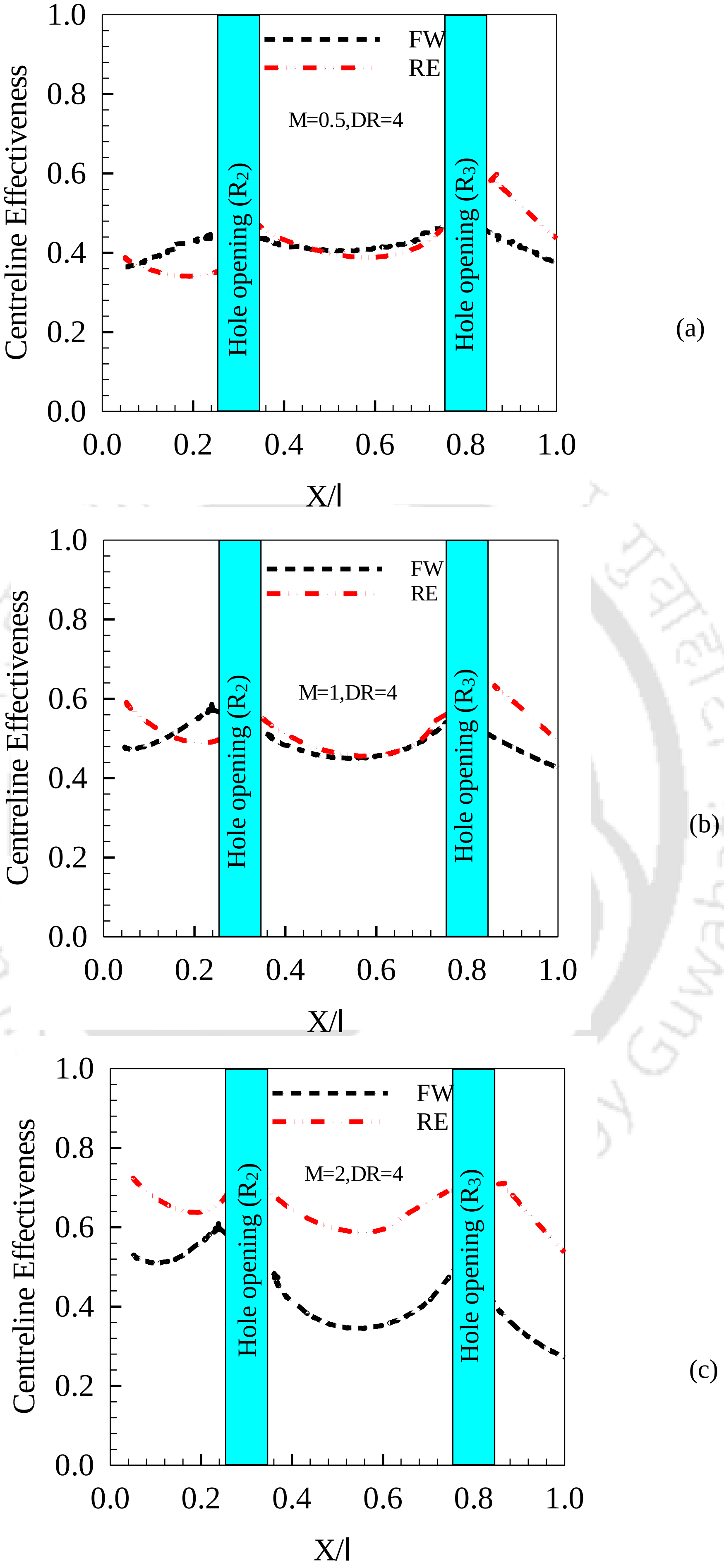

Fig.6.2: Comparison of centreline effectiveness for forward and reverse injection (a) M=0.5; (b). M=1;(c) M=2.

The film cooling performance of the hole depends on coolant coverage in both stream-wise (along mainstream and span-wise (lateral) directions. The coolant coverage in the lateral direction is evaluated in terms of lateral average effectiveness. Therefore, in the present study lateral averaging is performed for the distance ±4.5D, from the central hole. Fig.6.3(a) demonstrates the effectiveness comparison for both forward and reverse injection at blowing ratio (M=0.5). The figure clearly shows that both configurations exhibit similar trends of variations. A small drop in effectiveness plot is reported for reverse injection from $X/\lambda = 0$ to 0.36 and thereafter dominates the forward injection. A maximum improvement of 27% is reported over forward at $X/\lambda=0.86$. Moving to the higher blowing ratio M=1 (Fig.6.3 (b)), the reverse injection dominates over forward, however, exhibits similar trends as the blowing ratio (M=0.5), where the difference gain in effectiveness is higher in downstream rows.

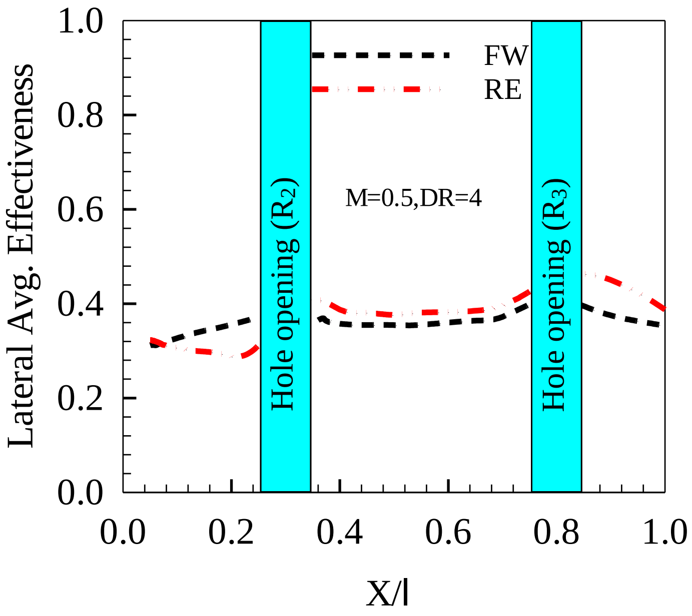

(a)

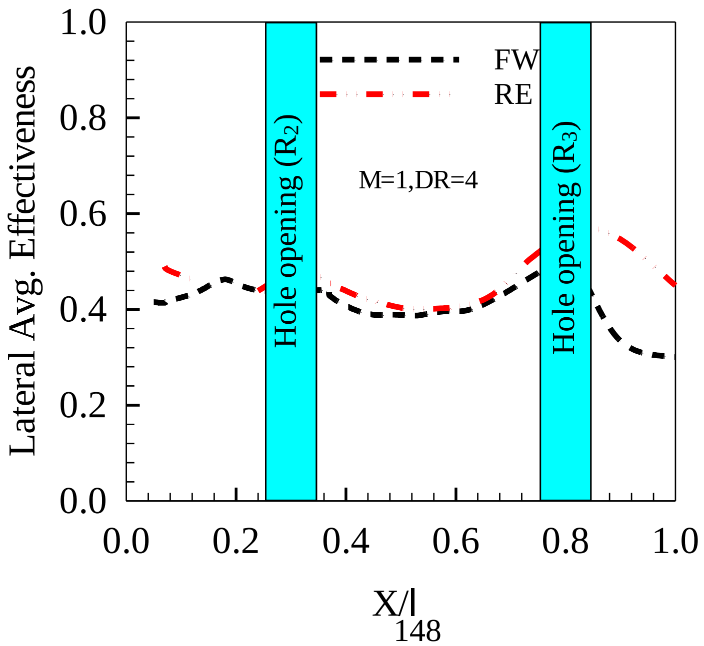

(b)

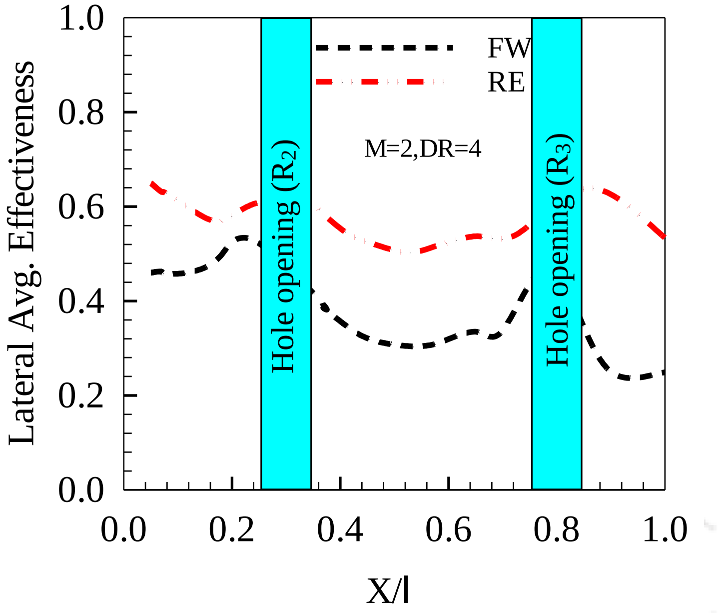

(c)

Fig.6.3: Comparison of lateral average effectiveness for forward and reverse injection (a) M=0.5; (b). M=1; (c) M=2.

The further increase of blowing ratio (M=2) shows significant improvement throughout downstream locations as shown in Fig.6.3 (c). The maximum improvement of 66.66% and 146% at $X/\lambda=0.5$ and $X/\lambda=0.88$ respectively are reported in the reverse case.

The same phenomenon can be well understood with the effectiveness contours, as shown in Fig.6.4. The coolant distribution is symmetric about the central hole (i.e., along Z/D=0). At a low blowing ratio (M=0.5) both forward and reverse injection shows similar coolant coverage. Moreover, the coolant coverage is also non-uniform along the lateral direction. With a further increase of the blowing ratio to M=1, the reverse injection shows more uniform and better coolant coverage as compared to the forward injection. The clear patch of poor coolant distribution can be seen for forward injection, in between the second and third row. For M=2, the plot clearly shows that the coolant distribution for forward injection is non-uniform and lower, however, the reverse case shows better coolant distribution. Apart from that the forward injection at the blowing ratio (M=1) shows a more uniform distribution as compared to the blowing ratio (M=2).

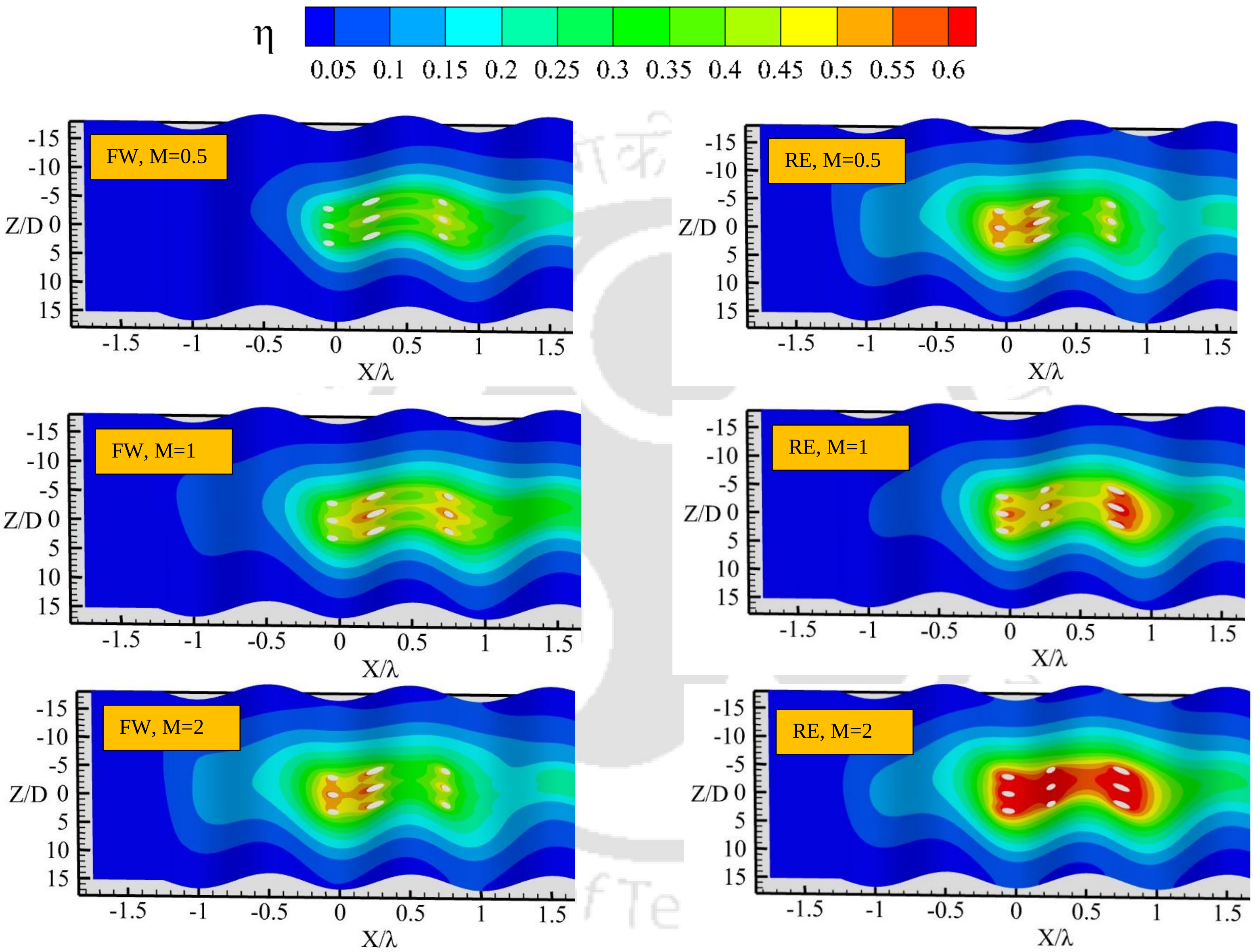

Fig.6.4: Effectiveness contours of forward (FW) and reverse (RE) injection over the corrugated surface.

Figure 6.5 and 6.6 demonstrates the secondary flow streamline injecting from coolant holes at a blowing ratio (M=1). Flow streamlines colored by non-dimensional velocity in the range of (VR=0-1) are plotted for comparison of both forward and reverse configurations. Figure 6.5 (a) and (b) clearly shows that flow issuing from a forward hole is more streamlined and skewed as compared to the novel reverse case. Moreover, the secondary flow is split into counter-rotating vortices, as shown in plane normal to mainstream Fig.6.5 (c). The streamlines of reverse injection show vortices in the corrugation plane, as shown in Fig.6.6 (a)-(c). The vortices are reported in corrugation planes improving the coolant spread in the lateral direction and therefore a better coolant coverage is evident in effectiveness contours shown in Fig.6.4.

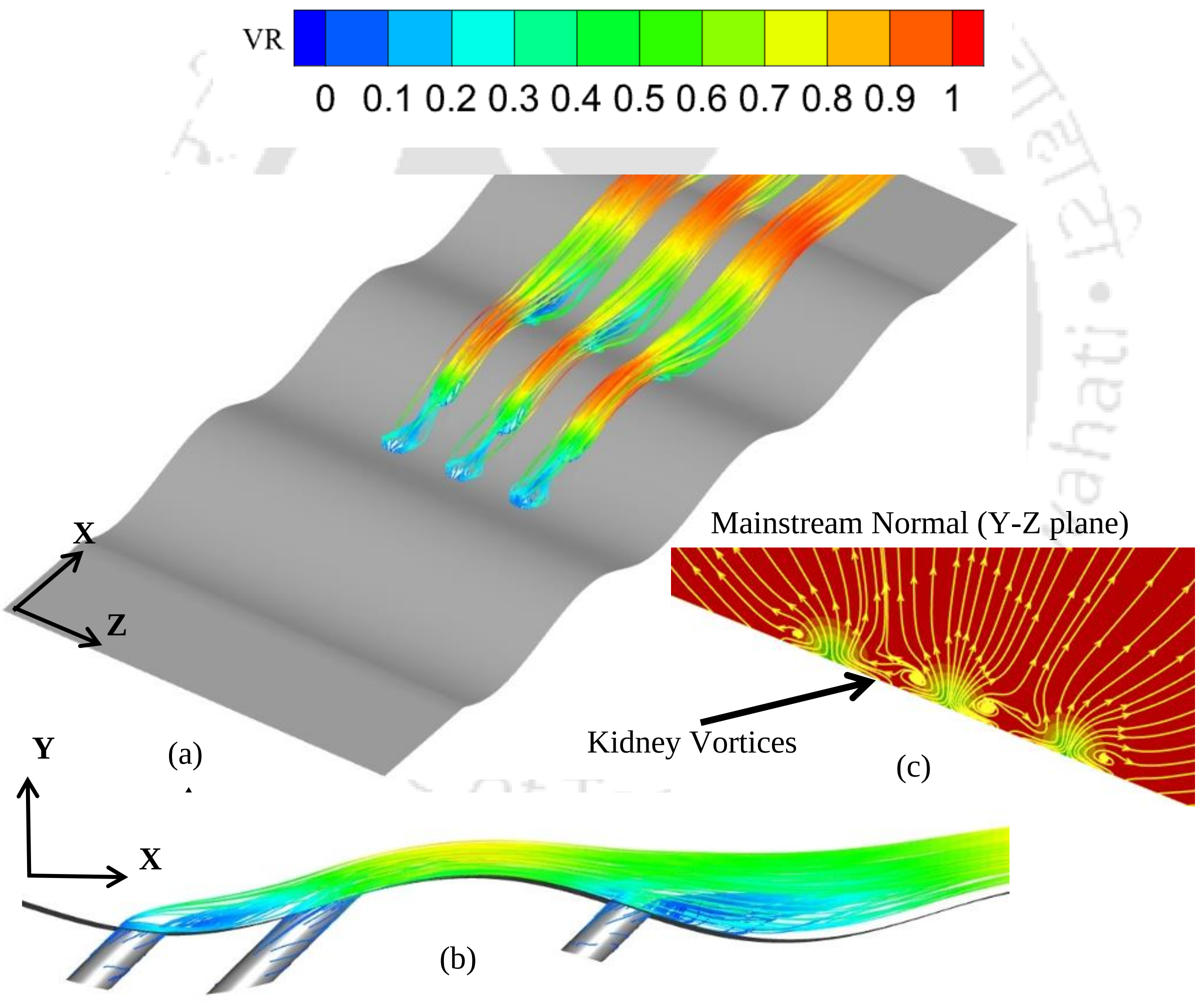

Fig.6.5: Streamline contours of secondary stream flow structure forward injection (FW) at blowing ratio (M=1) (a) corrugated plate (Z-X plane); (b) corrugated plate with cooling holes (X-Y plane); (c) normal to mainstream flow (Y-Z plane, mid plane R_2 and R_3).

Additionally, the strength of planner vortices is increasing in the downstream direction, which results in a higher gain in effectiveness particularly at the downstream location (i.e., downstream to R_3).

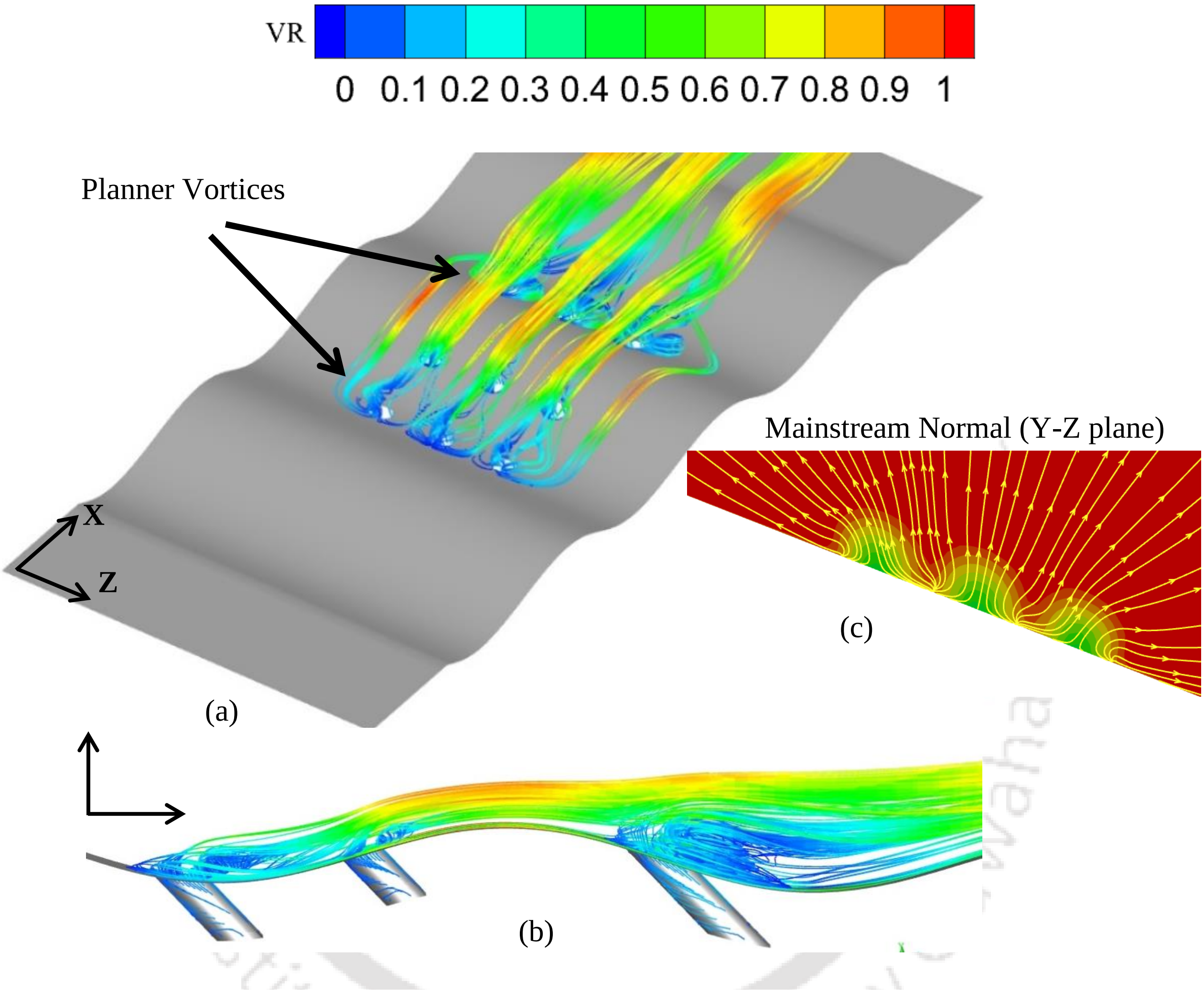

Fig.6.6: Streamline contours of secondary stream flow structure for reverse injection (RE) at blowing ratio (M=1) (a) corrugated plate (Z-X plane); (b) corrugated plate with cooling holes (X-Y plane); (c) normal to mainstream flow (Y-Z plane, mid plane R_2 and R_3).

The previous works of literature on reverse injection [51] on flat surfaces show a substantial difference in coolant coverage in a lateral direction due to both forward and reverse. For the forward injection, the coolant is mostly skewed towards the centreline and therefore the lateral spreading was less. However, the present study reveals that the coolant spread for forward injection is relatively better due to the corrugation profile, as shown in Fig.6.4. The corrugation profiles improve the coolant spread. Both forward and reveres injection shows similar trends of coolant coverage particularly at a low blowing ratio (M=0.5) and a significant difference can be seen at a high blowing ratio (M=2).

6.4.3 Local Lateral Effectiveness

The variations of local lateral effectiveness are shown in Fig. 6.7 (a)-(e). The local lateral effectiveness is plotted at two different streamwise locations, i.e., X/λ =0.15 (between R_1 and R_2) and X/λ =0.55 (between R_2 and R_3). The lateral effectiveness is plotted for lateral distances of Z/D=±4.5, (i.e., the lateral distance of ±4.5D on each side from the central hole). Figure 6.7 (a) shows the trends of variations in coolant coverage at X/λ =0.15. It can be observed that the effectiveness distribution is symmetric about the central hole (i.e., along Z/D =0) for both forward and reverse injections, and the forward case shows a relatively higher distribution. However, the effectiveness plot for reverse injection is relatively uniform as compared to reverse injection. Apart from that the case shows a peak along the holes, which is due to the skewed coolant distribution along the centreline of each hole. Moving to the further downstream location at X/λ =0.55 at M=0.5, as shown in Fig.6.7 (b), both forward and reverse cases exhibit similar trends of variations. A Similar trend can be observed at blowing ratio (M=1), and X/λ =0.15, as shown in Fig.6.7 (c). Both forward and reverse injection show similar trends of variations. Moving to the further downstream location at X/λ =0.55 at M=1, the reverse injection shows a more uniform and higher effectiveness distribution, as shown in Fig.6.7(d). Fig.6.7 (e) and (f) present the effectiveness variations at blowing ratio (M=2). Contrary to the lower blowing ratio, i.e., M=0.5 and 1, at a high blowing ratio (M=2) the reverse injection case shows more uniform and higher effectiveness. The reverse injection shows a wavy profile for both locations X/λ=0.15 and X/λ=0.55.

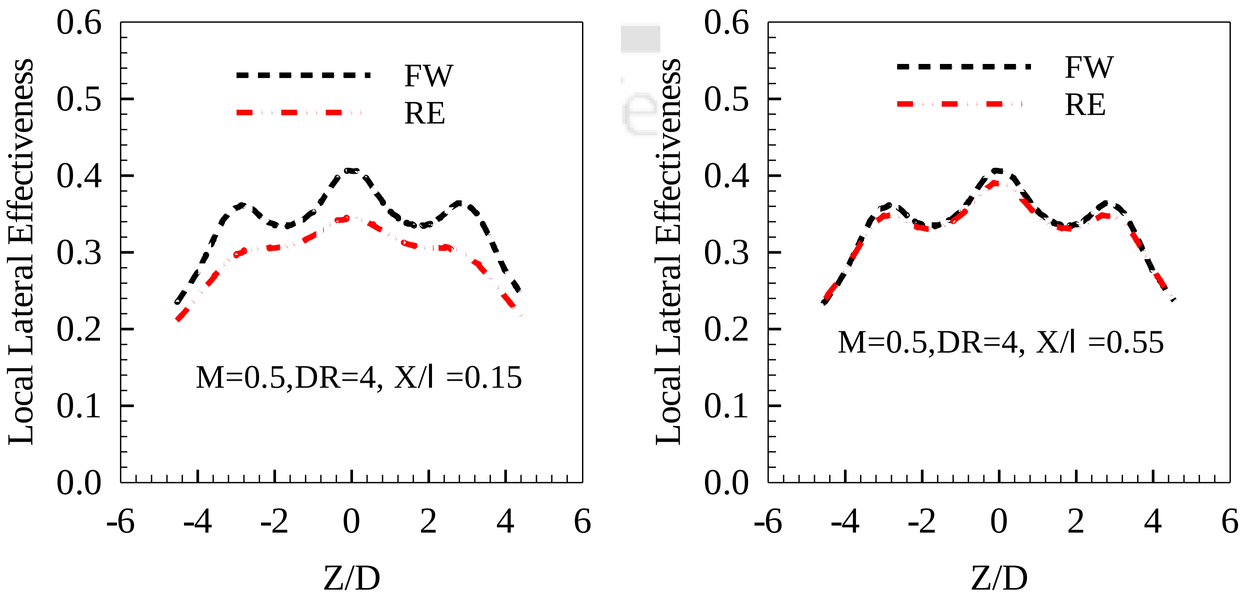

(a)

(b)

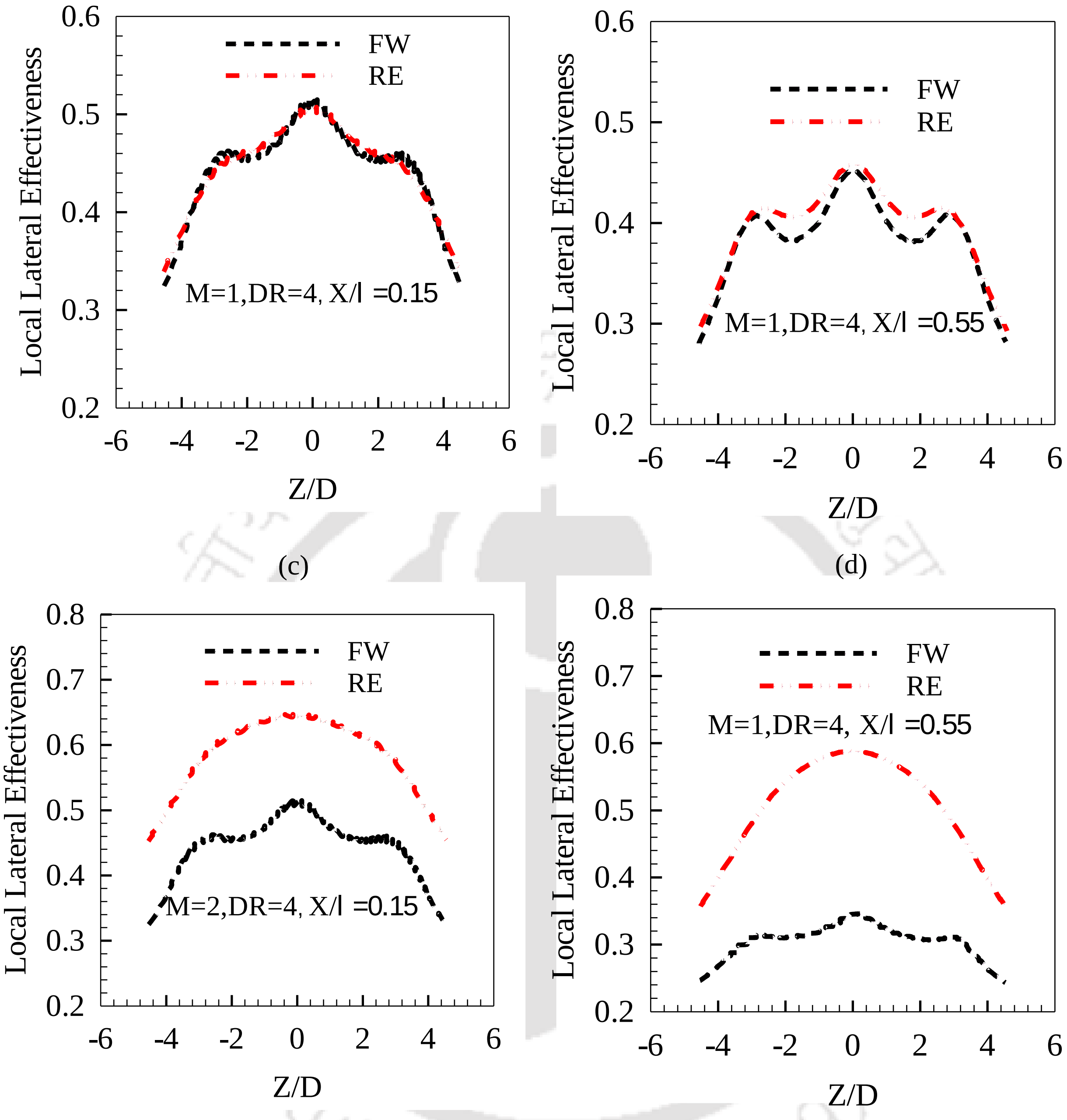

(c)

(d)

(e)

(f)

Fig.6.7: Comparison of numerically obtained local lateral effectiveness for forward and reverse cases at (a). M=0.5 (between R_1 and R_2) ;(b) M=0.5 (between R_2 and R_3); (c) M=0.5 (between R_1 and R_2); (d). M=0.5 (between R_2 and R_3); (e) M=2 (between R_1 and R_2); (f) M=2 (between R_2 and R_3).

6.4.4 Thermal Stress Analysis

In order to obtain the thermal stress distribution, finite element analysis is employed. A commercial code called ANSYS Workbench-2020 was used to conduct the thermal analysis. The present finite element analysis involves the following steps: (Step 1) create a test model using finite elements; (Step 2) define and impose the boundary conditions and the material properties; (Step 3) impose temperature profiles obtained from film cooling; and (Step 4) calculate the thermal stresses using the temperature distributions and the constraints.

Figure 6.8 illustrates the film-cooled domain considered for thermal stress analysis. Considering that the cooling holes are laterally spread with a constant pitch of 3D, a lateral distance of ±1.5D, and a streamwise distance of one wavelength are used to determine the stress. The stream-wise distance is measured from the central hole in the first row (i.e., R_1). The temperature profile obtained from the present film cooling study is imposed as the boundary condition. Figure 6.8 illustrates the finite element model and the boundary conditions on the regions near the cooling hole. Due to the presence of additional materials, symmetric boundary conditions (BCs), and BCs for uniform deformation in the X-axis direction were needed for constraints, as shown in Fig.6.8. Constraints play an important role in computation because thermal effects (resulting from temperature changes and differences) and specified constraints are the causes of the majority of stresses. Stress analysis has been done to identify the thermal damage near the typical cooling hole after these boundary conditions are imposed. It consists of unstructured cells generated using workbench. Three different grids viz. 0.6 million, 1.2 million, and 1.7 million were employed. The setup of 1.2 million was chosen for comparison, and the resulting model created a difference of less than 2% in the calculation of stress with a higher grid setup. The thermos-physical properties are taken as temperature dependent [111], as discussed in Table.6.1. The variations in poison ratio are insignificant for the substrate temperature range. Figure 6.9 demonstrate the temperature gradient for both forward and reverse injection case at a blowing ratio (M=2). The resulting temperature gradient for the forward case is higher than the revrse case particularly near cooling holes due to non-uniform cooling. The forward injection shows poor coolant coverage and uniformity as compared to the reverse injection and therefore the resulting thermal stress is higher. Figure 6.10 shows the thermal stress distribution for both forward and reverse cases based on the temperature distribution obtained through cooling and imposed boundary constrained. It can be observed that maximum von-mises stress distribution is non-uniform for both injection cases, however, differences can be identified between cooling holes R_1 and R_2. The quantitative trends of maximum von-mises stress are plotted in the bar graph, as shown in Figure 6.11. The figure clearly shows that in reverse injection with the increase of blowing ratio from 0.5 to 2, Von-mises stress monotonically decreases. Moreover 14.5 % lower equivalent von-mises stress compared to forward injection for blowing ratio (M=2).

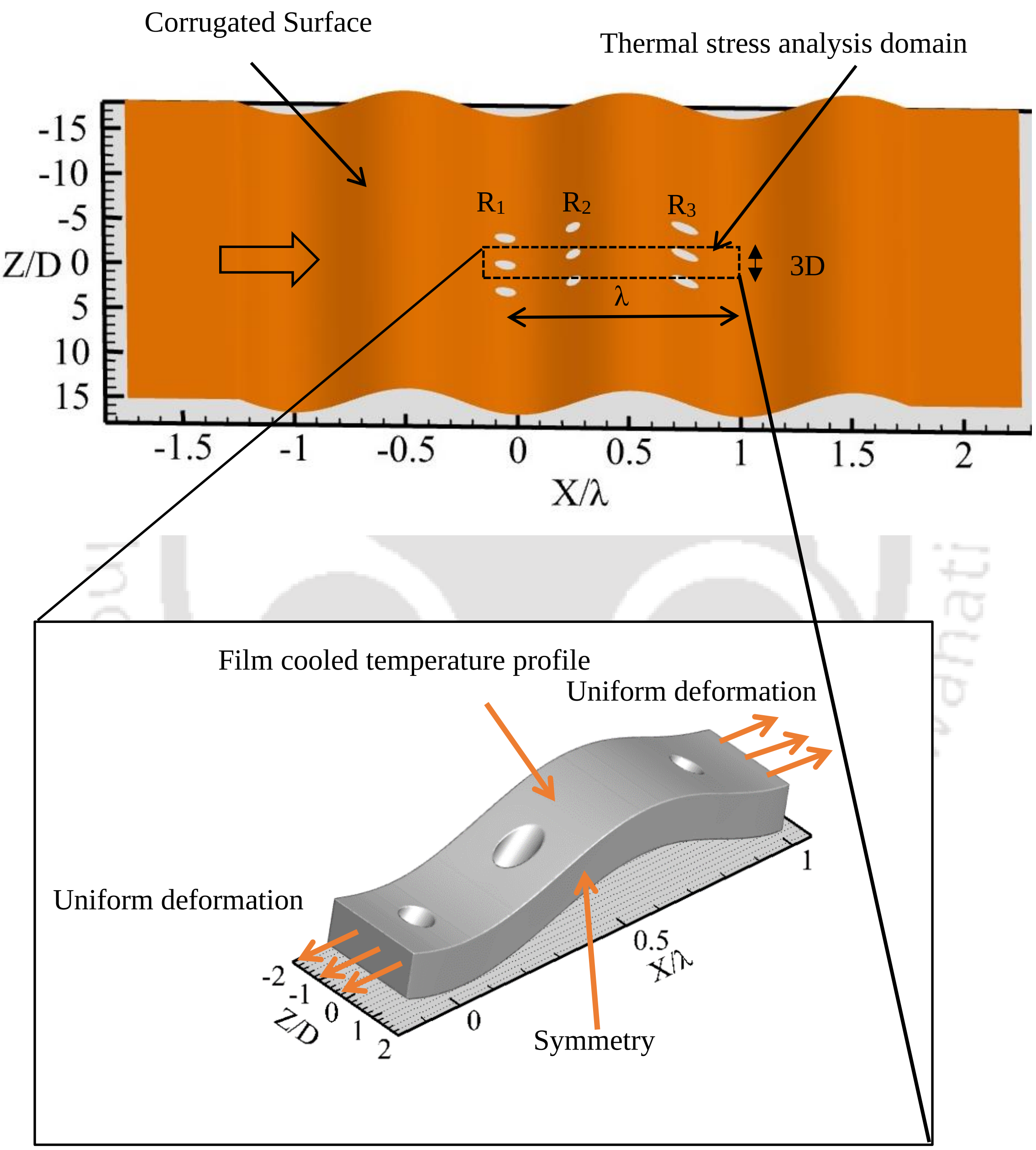

Fig.6.8: Computational domain and boundary conditions used in present thermal stress analysis.

Table.6.1 Thermophysical properties of superalloy (IN738LC) [111].

Temperature (K)	**Thermal Conductivity (W/m.K)**	**Specific Heat (J/kg.K)**	**Youngs Modulus (GPa)**	**Thermal Expansion Coefficient (µm/m-K)**
273	---	---	212	1.26E-05
373	---	449	208	1.28E-05
473	11.46	---	203	1.31E-05
573	13.3	477	196	1.35E-05
673	15.5	---	189	1.35E-05
773	16.8	504	183	1.39E-05
873	18.79	---	177.5	1.42E-05
973	20.48	545	170	1.44E-05
1073	21.8	---	165.3	1.47E-05
1173	23.64	652	151	1.52E-05
1273	25.44	---	138.7	1.54E-05
1373	27.13	---	117	1.56E-05
1773	---	740	---	---

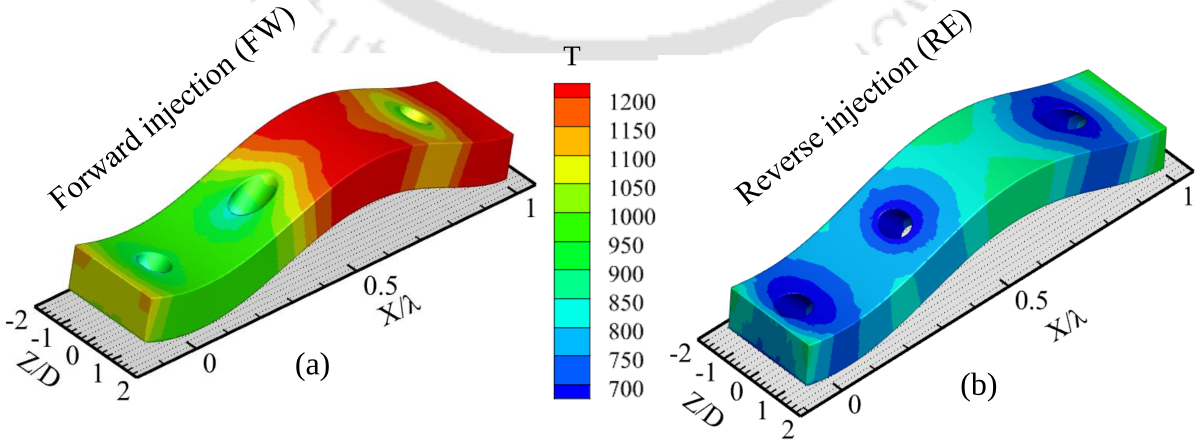

Fig.6.9: Film cooled temperature distribution for (a) FW, M=2; (b) RE, M=2.

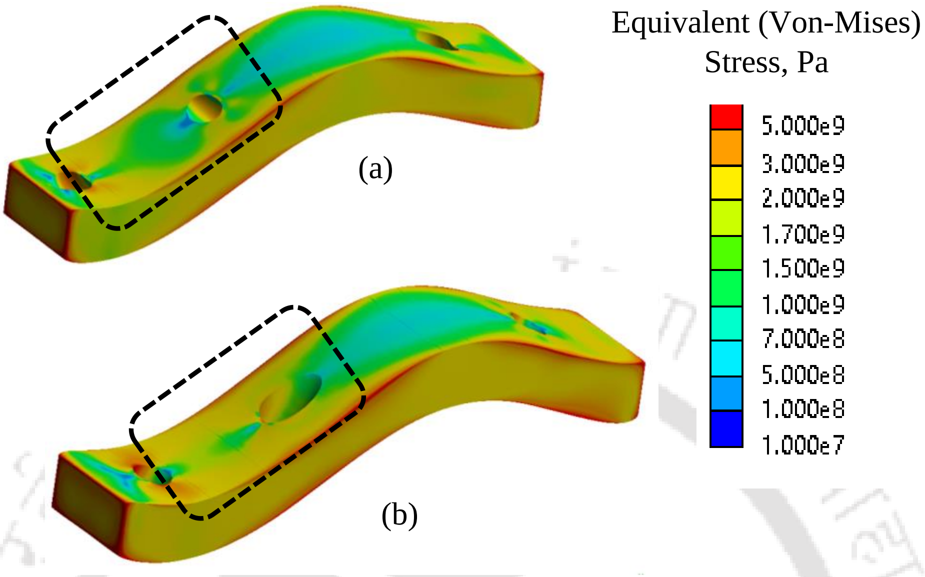

Fig.6.10: Thermal stress distribution for (a) FW, M=2; (b) RE, M=2.

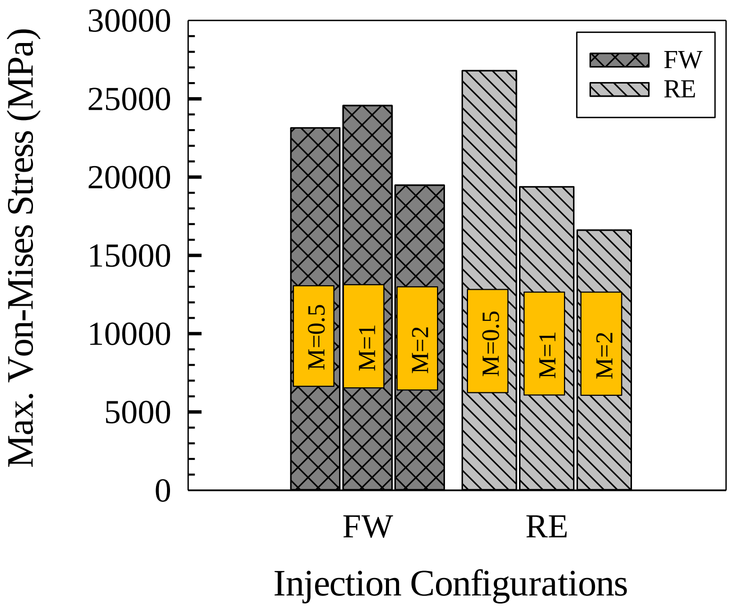

Fig.6.11: Variations of stress with blowing ratio.

6.5 Conclusion

Experimental and numerical studies have been performed for film cooling assessment of reverse injection configurations on the corrugated surface. The experiments are performed for blowing ratio (M=1) and density ratio (DR=1.08). In-house experimental data is used to verify the numerical model; however, the parametric study is extended for corrugated surfaces made up of Nickel-based super alloy (IN738LC) at blowing ratio (M=0.5,1 and 2) and density ratio (DR= 4). After detailed assessments of the results following conclusion can be drawn:

1. The present study demonstrates that the film cooling performance of sinusoidal corrugated surfaces strongly depends on injection configurations. The reverse injection shows better cooling for all investigated blowing ratios (M=0.5,1 and 2), however, a small drop can be seen near the first row at low blowing ratios i.e., M=0.5 and 1.
2. Coolant coverage in the spanwise direction is relatively uniform, for reverse injection as compared to the forward case. At low blowing ratios (M=0.5 and 1) a wavy profile is observed however at blowing ratio (M=2) reverse case shows uniform coolant spreading.
3. The thermal stress analysis indicates that reverse injection provides better thermal protection and shows 14.5 % lower equivalent von-mises stress compared to forward injection for blowing ratio (M=2).
4. The typical melting temperature of superalloy (IN738LC) lies in the range of 1200–1300^{o}C. Therefore, to ensure thermal protection, the lateral average effectiveness must be higher than 0.35. The proposed cooling configuration of three rows per wavelength successfully protects the superalloy (IN7378LC) from overheating in reverse configuration at M = 1 and 2.

CHAPTER 7: CONCLUSION AND FUTURE WORK

7.1 Conclusion

This study's primary goal is to find suitable injection configurations for film cooling applications on the corrugated surface. Corrugated surfaces are the most adopted surface configuration for afterburners of aero-engine liners, due to their effectiveness in terms of coolant attachment, high stiffness, and structural rigidity. The methodology for the present work includes experimental as well as numerical. The experimental methodology involves experimental setup design, calibration, measurement techniques, and uncertainty analysis. The mainstream is heated air whereas the secondary stream is relatively cold air, and experiments are done for a limited temperature range and used to validate the numerical model. The present work involved the development of the computational model, validation, and parametric study. The parametric study is carried out for a wide range of operating parameters using RANS and LES, turbulence models. The RANS modeling is mainly employed for corrugated surface studies; however, the flat plate film cooling flow physics is captured with the sophisticated turbulence model (i.e., LES). The appropriate RANS turbulence model is selected based on a thorough investigation of various two-equation models such as RNG k–ε, Realizable k–ε, and (SST) k–ω. The detailed objectives of the present work include (a) film cooling assessment of cylindrical and laidback fan-shaped holes with reverse injection; (b) study of the effect of various injection locations on film cooling performance of a corrugated surface; (c) study of the effect of double-row slot injection locations on the film cooling performance of a corrugated surface; (d) study of the effect of reverse injection on film cooling and thermal stress of a corrugated surface.

As a beginning of computational model development, numerical studies have been carried out on a flat plate. This study investigates the forward and reverse injection using cylindrical and shaped holes. After the detailed study and results analysis following conclusions were drawn:

(1) The film cooling performance of reverse injection is better than the forward injection, for both cylindrical and shaped holes.

(2) The formation of kidney vortices is one of the major issues in film cooling which promotes the coolant jet lift-off from the surface and lowers the film cooling performance. The vortices observed in the case of reverse cylindrical and reverse-

shaped holes are predominately in the plane of the plate and mitigate the problem of the formation of kidney vortices.

(3) The pressure drop is maximum for the reverse cylindrical hole (RCH) and minimum for the forward cylindrical hole (FCH). Moreover, the pressure drops in the case of (a reverse-shaped hole (RSH) is comparable with that of a forward-shaped hole (FSH).

The corrugated surfaces are widely used in afterburner aero-engines due to high structural rigidity and stiffness. Experimental and numerical studies have been conducted to understand the effect of various slot injection locations on film cooling performance. Mainly four injection configurations were investigated on a sinusoidal corrugated surface viz. L_0, L_{25}, L_{50}, and L_{75}, where numerical value as subscripts indicates the position of the slot from the peak of the first corrugation in the direction of mainstream flow. Based on the experimental and numerical studies following inferences have been drawn:

(1) The analysis demonstrates that the secondary flow injection locations have a significant impact on the effectiveness of film cooling. L_0, L_{25}, L_{50}, and L_{75} were the four locations that were considered into consideration, and the results showed that L_{50} and L_{75} injection locations performed better than L_0 and L_{25} locations.

(2) The parametric study reveals, that the blowing ratio has a significant impact on the secondary flow attached to the corrugated surface and film cooling.

(3) Unlike the flat surface, the corrugated surface shows better performance even at a higher blowing ratio (i.e., greater than 1). This is mainly because of secondary flow attachments with corrugated surfaces.

The film cooling study using a single slot per wavelength indicates that converging corrugation profile downstream to the slot improves coolant attachments. Therefore, for a better understanding of coolant interaction, and the effect of multiple injection locations on film cooling on a corrugated surface, experimental and numerical studies have been conducted. This study considers various double-row slot injection locations viz. (L_0-L_{25}), (L_0-L_{50}),(L_0-L_{75}),(L_{25}-L_{50}), (L_{25}-L_{75}), and (L_{50}-L_{75}). The parametric study of various injection combinations shows the following remarks:

(1) The position of coolant injection significantly impacts the film cooling performance of sinusoidally corrugated surfaces. Among six different injection locations considered viz. (L_0-L_{25}), (L_0-L_{50}), (L_0-L_{75}), (L_{25}-L_{50}), (L_{25}-L_{75}), and (L_{50}-

L_{75}) the L_{50}-L_{75} injection has the best film-cooling performance of all the cases investigated. For the blowing ratio (M= 0.5 to 2), it has been reported that the slot effectiveness (average over a wavelength) is 15 to 19% greater than the injection location with the lowest performance.

(2) The increase of amplitude to wavelength ratio (a/λ) shows a distinct impact on different injection locations. The effect of a/λ is more significant for the slot locations (L_0-L_{25}), (L_{25}-L_{50}), and (L_0-L_{75}). However, the effect is relatively lesser for (L_{25}-L_{50}), (L_{25}-L_{75}), and (L_{50}-L_{75}). As the depth of the corrugation valley, the mixing of coolant increases in the valley and limits the coolant spread, and hence performance reduces.

After identifying the suitable injection location, experimental and numerical studies have been conducted using forward and reverse injection configurations on a corrugated surface. This study includes three rows of cylindrical holes per wavelength at 45^o, and the outcome of the parametric study demonstrates the following:

(1) The present study demonstrates that the film cooling performance of sinusoidal corrugated surfaces strongly depends on injection configurations. The reverse injection shows better cooling for all investigated blowing ratios (M=0.5,1 and 2), however, a small drop can be seen near the first row at low blowing ratios i.e., M=0.5 and 1.

(2) Coolant coverage in the spanwise direction is relatively uniform, for reverse injection as compared to the forward case. At low blowing ratios (M=0.5 and 1) a wavy profile is observed however at blowing ratio (M=2) reverse case shows uniform coolant spreading.

(3) The thermal stress analysis indicates that reverse injection provides better thermal protection and shows 14.5 % lower equivalent von Mises stress compared to forward injection for blowing ratio (M=2).

7.2 Future Work Suggestions

The present study demonstrates several aspects of film cooling using various injection configurations on flat and corrugated surfaces. Based on this study the author suggests the following work to the designers of film cooling systems:

(1) The film cooling studies using reverse hole shows improved performance with both cylindrical and shaped. However, the aerodynamic analysis of the flow field is still infantry stage which needs further explorations.

(2) The experimental study is carried out for a limited temperature range, as heating of the mainstream is challenging at high speed. Therefore, further experimental facilities can be developed with an improved heating facility which can be used to validate the numerical models at a high-density ratio. Moreover, the correlation can be developed with the density ratio.

(3) The present studies on corrugated surfaces reveal that Realizable k–ε is accurately capturing the film cooling phenomenon as compared to RNG k–ε, and (SST) k–ω models. However, a better engineering solution to flow physics and heat transfer of high turbulent film cooling can be given with improved turbulence modeling approaches viz. DES, modified DES, LES, and DNS. Additionally, detailed investigations of various LES are required to assess the capability of capturing the flow physics over curved surfaces.

(4) Thermal stress is a critical parameter to evaluate the film cooling protection of a component, which is exposed to high-temperature gases. For various surface configurations, thermal stress quantification can be done to identify the merits of thermal protection.

REFERENCES

[1] L. Buduger, Fluid Dynamics and Heat Transfer of Turbomachinery, 1996. https://doi.org/10.1002/9780470172629.

[2] R.J. Goldstein, Film Cooling, Adv. Heat Transf. 7 (1971) 321–379. https://doi.org/10.1016/S0065-2717(08)70020-0.

[3] S. Ekkad, J.C. Han, A review of hole geometry and coolant density effect on film cooling, Front. Heat Mass Transf. 6 (2015). https://doi.org/10.5098/hmt.6.8.

[4] D.G. Bogard, Airfoil Film Cooling, Gas Turbine Handb. (2006) 309–321.

[5] D.I. Suslov, R. Arnold, O.J. Haidn, High Pressure Rocket Subscale Combustion Chamber, in: 48th AIAA Aerospace Sciences Meeting Including the New Horizonsorum and Aerospace Exposition, Orlando, Florida, 2010: pp. 1–10. https://doi.org/10.2514/6.2010-1150.

[6] J. Zuo, S. Zhang, J. Qin, W. Bao, N. Cui, X. Liu, Effects of cracking reaction on supersonic film cooling using gaseous hydrocarbon fuel as coolant, Appl. Therm. Eng. 171 (2020) 115134. https://doi.org/10.1016/j.applthermaleng.2020.115134.

[7] M.A. Keller, M.J. Kloker, Direct numerical simulation of foreign-gas film cooling in supersonic boundary-layer flow, AIAA J. 55 (2017) 99–111. https://doi.org/10.2514/1.J055115.

[8] S.R. Shine, S.S. Nidhi, Review on film cooling of liquid rocket engines, Propuls. Power Res. 7 (2018) 1–18. https://doi.org/10.1016/j.jppr.2018.01.004.

[9] J. Zuo, S. Zhang, J. Qin, W. Bao, N. Cui, Performance evaluation of regenerative cooling/film cooling for hydrocarbon fueled scramjet engine, Acta Astronaut. 148 (2018) 57–68. https://doi.org/10.1016/j.actaastro.2018.04.037.

[10] R.J. Goldstein, E.R.G. Eckert, J.W. Ramsey, Film cooling with injection through holes: Adiabatic wall temperatures downstream of a circular hole, J. Eng. Gas Turbines Power. 90 (1968) 384–393. https://doi.org/10.1115/1.3609223.

[11] D.G. Bogard, K.A. Thole, Gas turbine film cooling, J. Propuls. Power. 22 (2006) 249–270. https://doi.org/10.2514/1.18034.

[12] B. Sen, D.L. Schmidt, D.G. Bogard, Film cooling with compound angle holes: Heat

transfer, J. Turbomach. 118 (1996) 800–806. https://doi.org/10.1115/1.2840937.

[13] K. Wieghardt, Hot air discharge for De-Icing, AAF translation, 1946.

[14] R.A. Seban, Heat transfer and effectiveness for a turbulent boundary layer with tangential fluid injection, J. Heat Transfer. 82 (1960) 303–312. https://doi.org/10.1115/1.3679938.

[15] J.P. Hartnett, R.C. Birkebak, E.R.G. Eckert, Velocity distributions, temperature distributions, effectiveness and heat transfer for air injected through a tangential slot into a turbulent boundary layer, J. Heat Transfer. 83 (1961) 293–305. https://doi.org/10.1115/1.3682263.

[16] S.S. Papell, Effect on Gaseous Film Cooling of Coolant Injection Through Angled Slots and Normal Holes., 2008.

[17] W.K. Burns, J.L. Stollery, The influence of foreign gas injection and slot geometry on film cooling effectiveness, Int. J. Heat Mass Transf. 12 (1969) 935–951. https://doi.org/10.1016/0017-9310(69)90156-2.

[18] S. Sivasegaram, J.H. Whitelaw, Film Cooling Slots: The Importance of Lip Thickness and Injection Angle, J. Mech. Eng. Sci. 11 (1969) 22–27. https://doi.org/10.1243/jmes_jour_1969_011_005_02.

[19] T. V. Jones, Aerodynamics of slot-film cooling: Theory and experiment, J. Fluid Mech. 160 (1985) 15–27. https://doi.org/10.1017/S0022112085003366.

[20] A.D. Fitt, P. Wilmott, Slot film cooling - The effect of separation angle, Acta Mech. 103 (1994) 79–88. https://doi.org/10.1007/BF01180219.

[21] D.G. Hyams, J.H. Leylek, A detailed analysis of film cooling physics Part III: Streamwise injection with shaped holes, Proc. ASME Turbo Expo. 3 (1997). https://doi.org/10.1115/97-GT-271.

[22] R. Jia, B. Sundén, P. Miron, B. Léger, A numerical and experimental investigation of the slot film-cooling jet with various angles, J. Turbomach. 127 (2005) 635–645. https://doi.org/10.1115/1.1929821.

[23] Y.H. Zeng, W.X. Huai, Experiments on a round turbulent buoyant jet in a cross flow, Liuti Lixue Shiyan Yu Celiang/Experiments Meas. Fluid Mech. 19 (2005) 39–46.

[24] P. Chassaing, J. George, A. Claria, F. Sananes, Physical characteristics of subsonic jets in a cross-stream, J. Fluid Mech. 62 (1974) 41–64. https://doi.org/10.1017/S0022112074000577.

[25] J.F. Keffer, W.D. Baines, The round turbulent jet in a cross-wind, J. Fluid Mech. 15 (1963) 481–496. https://doi.org/10.1017/S0022112063000409.

[26] T.F. Fric, A. Roshko, Vortical Structure in the Wake of a Transverse Jet, J. Fluid Mech. 279 (1994) 1–47. https://doi.org/10.1017/S0022112094003800.

[27] J. Andreopoulos, On the structure of jets in a crossflow, J. Fluid Mech. 157 (1985) 163–197. https://doi.org/10.1017/S0022112085002348.

[28] R.M. Kelso, T.T. Lim, A.E. Perry, An experimental study of round jets in cross-flow, J. Fluid Mech. 306 (1996) 111–144. https://doi.org/10.1017/S0022112096001255.

[29] S. Acharya, M. Tyagi, A. Hoda, Flow and Heat Transfer Predictions for Film Cooling, Ann. N. Y. Acad. Sci. 934 (2006) 110–125. https://doi.org/10.1111/j.1749-6632.2001.tb05846.x.

[30] M. Tyagi, S. Acharya, Large eddy simulation of film cooling flow from an inclined cylindrical jet, J. Turbomach. 125 (2003) 734–742. https://doi.org/10.1115/1.1625397.

[31] D.R. Pedersen, E.R.G. Eckert, R.J. Goldstein, Film cooling with large density differences between the mainstream and the secondary fluid measured by the heat-mass transfer analogy, J. Heat Transfer. 99 (1977) 620–627. https://doi.org/10.1115/1.3450752.

[32] M.K. B. A. Haven , D. K. Yamagata, Anti-kidney pair of vortices in shaped holes and their influence on film cooling effectiveness, in: Present. Int. Gas Turbine Aeroengine Congr. Exhib., Orlando, Florida, USA, n.d.: pp. 1–8. https://doi.org/10.1115/97-GT-045.

[33] K. Thole, M. Gritsch, A. Schulz, S. Wittig, Flowfield measurements for film-cooling holes with expanded exits, ASME 1996 Int. Gas Turbine Aeroengine Congr. Exhib. GT 1996. 4 (1996) 327–336. https://doi.org/10.1115/96-GT-174.

[34] M. Gritsch, W. Colban, H. Schär, K. Döbbeling, Effect of hole geometry on the thermal performance of fan-shaped film cooling holes, J. Turbomach. 127 (2005) 718–725. https://doi.org/10.1115/1.2019315.

[35] C. Saumweber, A. Schulz, S. Wittig, Free-stream turbulence effects on film cooling with shaped holes, J. Turbomach. 125 (2003) 65–73. https://doi.org/10.1115/1.1515336.

[36] D. Giebert, M. Gritsch, A. Schulz, S. Wittig, Film-cooling from holes with expanded exits: A comparison of computational results with experiments, Proc. ASME Turbo Expo. 3 (1997). https://doi.org/10.1115/97-GT-163.

[37] A. Kohli, D.G. Bogard, Effects of hole shape on film cooling with large angle injection, Proc. ASME Turbo Expo. 3 (1999). https://doi.org/10.1115/99-GT-165.

[38] M. Gritsch, A. Schulz, S. Wittig, Discharge coefficient measurements of film-cooling holes with expanded exits, Proc. ASME Turbo Expo. 3 (1997). https://doi.org/10.1115/97-GT-165.

[39] C.M. Bell, H. Hamakawa, P.M. Ligrani, Film cooling from shaped holes, J. Heat Transfer. 122 (2000) 224–232. https://doi.org/10.1115/1.521484.

[40] C. Wang, F. Fan, J. Zhang, Y. Huang, H. Feng, Large eddy simulation of film cooling flow from converging slot-holes, Int. J. Therm. Sci. 126 (2018) 238–251. https://doi.org/10.1016/j.ijthermalsci.2018.01.007.

[41] L. El-Gabry, H. Xu, K. Liu, J. Chang, M. Fox, Effect of coolant injection angle on nozzle endwall film cooling: Experimental and numerical analysis in linear cascade, Proc. ASME Turbo Expo. 5C–2018 (2018) 1–11. https://doi.org/10.1115/GT2018-75877.

[42] J.E. Sargison, S.M. Guo, M.L.G. Oldfield, G.D. Lock, A.J. Rawlinson, A converging slot-hole film-cooling geometry-Part 1: Low-speed flat-plate heat transfer and loss, J. Turbomach. 124 (2002) 453–460. https://doi.org/10.1115/1.1459735.

[43] V.L. Eriksen, R.J. Goldstein, Heat Transfer and Film Cooling Following Injection Through Inclined Circular Tubes., Am. Soc. Mech. Eng. (1974) 329–334.

[44] N.. F. Lampard, D, Effectiveness Following Injection through a Row of Holes, J. Eng. Power. 102(3) (1980) 584–588. https://doi.org/https://doi.org/10.1115/1.3230306.

[45] A. Kohli, D.G. Bogard, Adiabatic effectiveness, thermal fields, and velocity fields for film cooling with large angle injection, J. Turbomach. 119(2) (1995). https://doi.org/https://doi.org/10.1115/1.2841118.

[46] C.H.N. Yuen, R.F. Martinez-Botas, Film cooling characteristics of a single round hole

at various streamwise angles in a crossflow: Part I effectiveness, Int. J. Heat Mass Transf. 46(2) (2003) 221–235.

[47] C.H.N. Yuen, R.F. Martinez-Botas, Film cooling characteristics of rows of round holes at various streamwise angles in a crossflow: Part II. Heat transfer coefficients, Int. J. Heat Mass Transf. 48 (2005) 5017–5035. https://doi.org/10.1016/j.ijheatmasstransfer.2005.05.020.

[48] K. Singh, B. Premachandran, M.R. Ravi, A numerical study on the 2D film cooling of a flat surface, Numer. Heat Transf. Part A Appl. 67 (2015) 673–695. https://doi.org/10.1080/10407782.2014.949131.

[49] S. Shetty, X. Li, G. Subbuswamy, Ht2012-58 Numerical Simulation on Gas Turbine Film Cooling of Curved Surface, in: Proc. ASME 2012 Summer Heat Transf. Conf., Rio Grande, Puerto Rico, 2012: pp. 1–8. https://doi.org/https://doi.org/10.1115/HT2012-58469.

[50] A.F. Chen, S.J. Li, J.C. Han, Film cooling for cylindrical and fan-shaped holes using pressure-sensitive paint measurement technique, J. Thermophys. Heat Transf. 29 (2015) 775–784. https://doi.org/10.2514/1.T4518.

[51] K. Singh, B. Premachandran, M.R. Ravi, Experimental and numerical studies on film cooling with reverse/backward coolant injection, Int. J. Therm. Sci. 111 (2017) 390–408. https://doi.org/10.1016/j.ijthermalsci.2016.09.027.

[52] X.C. Li, G. Subbuswamy, J. Zhou, Performance of Gas Turbine Film Cooling with Backward Injection, Energy Power Eng. 05 (2013) 132–137. https://doi.org/10.4236/epe.2013.54b025.

[53] S. Park, E.Y. Jung, S.H. Kim, H. Sohn, H. Cho, GT2015-43853, in: Proc. ASME Turbo Expo 2015 Turbine Tech. Conf. Expo., Montréal, Canada, 2017: pp. 1–9. https://doi.org/https://doi.org/10.1115/GT2015-43853.

[54] S. V. Ekkadt, J.C. Han, H. Du, Detailed film cooling measurements on a cylindrical leading edge model: Effect of free-stream turbulence and coolant density, J. Turbomach. 120(4) (1997) 799–807. https://doi.org/https://doi.org/10.1115/1.2841792.

[55] H.D. Ammari, N. Hay, D. Lampard, The effect of density ratio on the heat transfer coefficient from a film cooled flat plate, J. Turbomach. 112(3) (1990) 444–450.

https://doi.org/https://doi.org/10.1115/1.2927679.

[56] A.K. Sinha, D.G. Bogard, M.E. Crawford, Film-cooling effectiveness downstream of a single row of holes with variable density ratio, J. Turbomach. 113 (1991) 442–449. https://doi.org/10.1115/1.2927894.

[57] W. Haas, W. Rodi, B. Schönung, The influence of density difference between hot and coolant gas on film cooling by a row of holes: Predictions and experiments, J. Turbomach. 114(4) (1991) 747–755. https://doi.org/https://doi.org/10.1115/1.2928028.

[58] W.R. B. Scho¨nung, Prediction of Film Cooling by a Row of Holes With a Two-Dimensional Boundary-Layer Procedure, J. Turbomach. 109(4) (1987) 579–587.

[59] H.A. Rydhohn, An experimental investigation of the velocity and temperature fields of cold jets injected into a hot crossflow, J. Turbomach. 120(2) (1998) 320–326. https://doi.org/https://doi.org/10.1115/1.2841409.

[60] M.K. Eberly, K.A. Thole, Time-resolved film-cooling flows at high and low density ratios, J. Turbomach. 136 (2013) 1–11. https://doi.org/10.1115/1.4025574.

[61] J.R. Winka, J.B. Anderson, E.J. Boyd, D.G. Bogard, M.E. Crawford, Convex Curvature Effects on Film Cooling Adiabatic Effectiveness, J. Turbomach. 136 (2014) 1–9. https://doi.org/10.1115/1.4025691.

[62] R.E. Mayle, F.C. Kopper, M.F. Blair, D.A. Bailey, Effect of streamline curwature on film cooling, J. Eng. Gas Turbines Power. 99 (1977) 77–82. https://doi.org/10.1115/1.3446255.

[63] S.G. Schwarz, R.J. Goldstein, E.R.G. Eckert, The influence of curvature on film cooling performance, in: J. Turbomach., 1991: pp. 472–478. https://doi.org/10.1115/1.2927898.

[64] M.K. Berhe, S. V Patankar, Curvature Effects on Discrete- Hole Film Cooling, J. Turbomach. 121 (2017) 781–791. https://doi.org/https://doi.org/10.1115/1.4006329.

[65] J.D. Moore, C. Yoon, D.G. Bogard, Surface Curvature Effects on Film Cooling Performance for Shaped Holes on a Model Turbine Blade, J. Turbomach. 142 (2020) 1–9. https://doi.org/10.1115/1.4048582.

[66] K. Singh, B. Premachandran, M.R. Ravi, Numerical investigation of film cooling on a 2D corrugated surface, Numer. Heat Transf. Part A Appl. 70 (2016) 1253–1270.

https://doi.org/10.1080/10407782.2016.1230431.

[67] K. Singh, B. Premachandran, M.R. Ravi, Experimental and numerical studies on film cooling of a corrugated surface, Appl. Therm. Eng. 108 (2016) 312–329. https://doi.org/10.1016/j.applthermaleng.2016.07.093.

[68] K. Funazaki, T. Igarashi, Y. Koide, K. Shinbo, Studies on cooling air ejected over a corrugated wall: Its aerodynamic behavior and film effectiveness, Proc. ASME Turbo Expo. 3 (2001) 1–12. https://doi.org/10.1115/2001-GT-0143.

[69] K. Singh, B. Premachandran, M.R. Ravi, Effect of Thermal Barrier Coating and Gas Radiation on Film Cooling of a Corrugated Surface, J. Heat Transfer. 140 (2018) 1–5. https://doi.org/10.1115/1.4039761.

[70] L. Qu, J. Zhang, X. Tan, M. Wang, Numerical investigation on adiabatic film cooling effectiveness and heat transfer coefficient for effusion cooling over a transverse corrugated surface, Chinese J. Aeronaut. 30 (2017) 677–684. https://doi.org/10.1016/j.cja.2017.02.012.

[71] S. Yong, T. Xiao Ming, Z. Jing Zhou, W. Yan Hua, Film Cooling Experimental Study on Sinusoidal Corrugated Liner for Afterburner, Int. J. Turbo Jet-Engines. 0 (2017). https://doi.org/10.1515/tjj-2017-0014.

[72] X. Guo, W. Schröder, M. Meinke, Large-eddy simulations of film cooling flows, Comput. Fluids. 35 (2006) 587–606. https://doi.org/10.1016/j.compfluid.2005.02.007.

[73] Z. Ke, J. Wang, Conjugate heat transfer simulations of pulsed film cooling on an entire turbine vane, Appl. Therm. Eng. 109 (2016) 600–609. https://doi.org/10.1016/j.applthermaleng.2016.08.132.

[74] H. Schneider, D. von Terzi, H.J. Bauer, Large-Eddy Simulations of trailing-edge cutback film cooling at low blowing ratio, Int. J. Heat Fluid Flow. 31 (2010) 767–775. https://doi.org/10.1016/j.ijheatfluidflow.2010.06.010.

[75] A.F. Shinn, S. Pratap Vanka, Large Eddy Simulations of Film-Cooling Flows With a Micro-Ramp Vortex Generator, J. Turbomach. 135 (2012). https://doi.org/10.1115/1.4006329.

[76] P. Renze, W. Schröder, M. Meinke, Large-eddy simulation of film cooling flows with variable density jets, Flow, Turbul. Combust. 80 (2008) 119–132.

https://doi.org/10.1007/s10494-007-9080-8.

[77] C. Maass, U. Schumann, Numerical Simulation of Turbulent Flow over a Wavy Boundary, in: Fluid Mech. Its Appl., Springer, Dordrecht, 1994: pp. 287–297. https://doi.org/10.1007/978-94-011-1000-6_25.

[78] R.J. Moffat, Using uncertainty analysis in the planning of an experiment, J. Fluids Eng. Trans. ASME. 107 (1985) 173–178. https://doi.org/10.1115/1.3242452.

[79] Z. Tu, J. Mao, X. Han, Numerical study of film cooling over a flat plate with anisotropic thermal conductivity, Appl. Therm. Eng. 111 (2017) 968–980. https://doi.org/10.1016/j.applthermaleng.2016.09.170.

[80] V. Yakhot, S.A. Orszag, Renormalization group analysis of turbulence. I. Basic theory, J. Sci. Comput. 1 (1986) 3–51. https://doi.org/10.1007/BF01061452.

[81] Y. Yu, C.H. Yen, T.I.P. Shih, M.K. Chyu, S. Gogineni, Film cooling effectiveness and heat transfer coefficient distributions around diffusion shaped holes, J. Heat Transfer. 124 (2002) 820–827. https://doi.org/10.1115/1.1418367.

[82] D.C. Wilcox, Formulation of the k-ω turbulence model revisited, AIAA J. 46 (2008) 2823–2838. https://doi.org/10.2514/1.36541.

[83] J. Jiménez, The numerical computation of turbulence, Lect. Notes Turbul. Coherent Struct. Fluids, Plasmas Nonlinear Media. (2006) 281–307. https://doi.org/10.1142/9789812774071_0006.

[84] U. Schumann, Subgrid scale model for finite difference simulations of turbulent flows in plane channels and annuli, J. Comput. Phys. 18 (1975) 376–404. https://doi.org/10.1016/0021-9991(75)90093-5.

[85] H.N. Najm, P.S. Wyckoff, O.M. Knio, A Semi-implicit Numerical Scheme for Reacting Flow: I. Stiff Chemistry, J. Comput. Phys. 143 (1998) 381–402. https://doi.org/10.1006/jcph.1997.5856.

[86] A. Yoshizawa, Statistical theory for compressible turbulent shear flows, with the application to subgrid modeling., Phys. Fluids. 29 (1986) 2152–2164. https://doi.org/10.1063/1.865552.

[87] C.Y. Lee, S. Cant, Assessment of LES Subgrid-scale Models and Investigation of

Hydrodynamic Behaviour for an Axisymmetrical Bluff Body Flow, Flow, Turbul. Combust. 98 (2017) 155–176. https://doi.org/10.1007/s10494-016-9751-4.

[88] O. Penttinen, A pimpleFoam tutorial for channel flow, with respect to different LES models., Chalmers University of Technology, Sweden, 2011.

[89] K.C. Chang, K.H. Lee, Determination of mixing length in turbulent mixing layer on basis of vorticity field, Int. J. Heat Fluid Flow. 66 (2017) 121–126. https://doi.org/10.1016/j.ijheatfluidflow.2017.06.001.

[90] A. Kermanpur, N. Varahram, P. Davami, M. Rappaz, Thermal and Grain-Structure Simulation in a Land-Based Turbine Blade Directionally Solidified with the Liquid Metal Cooling Process, Metall. Mater. Trans. B. 31 (2000) 1293–1304. https://doi.org/https://doi.org/10.1007/s11663-000-0017-z.

[91] R. Prenter, M.A. Hossain, L. Agricola, A. Ameri, J.P. Bons, Experimental characterization of reverse-oriented film cooling, Proc. ASME Turbo Expo. 5C–2017 (2017) 1–14. https://doi.org/10.1115/GT2017-64731.

[92] ANSYS Fluent User Guide, 2020R1, Canonsburg, 2020.

[93] S. V. Patankar, Numerical Heat Transfer and Fluid Flow, 1st Editio, CRC Press, Boca Raton, USA, 1980. https://doi.org/https://doi.org/10.1201/9781482234213.

[94] OpenFOAM foundation, UserGuide OpenFoam, (2015) U129–U165.

[95] S. Acharya, D.H. Leedom, Large eddy simulations of discrete hole film cooling with plenum inflow orientation effects, J. Heat Transfer. 135 (2013). https://doi.org/10.1115/1.4007667.

[96] Y. Jiang, A. Murray, L. di Mare, P. Ireland, Mesh sensitivity of RANS simulations on film cooling flow, Int. J. Heat Mass Transf. 182 (2022) 121825. https://doi.org/10.1016/j.ijheatmasstransfer.2021.121825.

[97] L. Davidson, Large Eddy Simulations: How to evaluate resolution, Int. J. Heat Fluid Flow. 30 (2009) 1016–1025. https://doi.org/10.1016/j.ijheatfluidflow.2009.06.006.

[98] S.B. Pope, Ten questions concerning the large-eddy simulation of turbulent flows, New J. Phys. 6 (2004). https://doi.org/10.1088/1367-2630/6/1/035.

[99] Y. Jiang, M.L. Mao, X.G. Deng, H.Y. Liu, Numerical investigation on body-wake flow

interaction over rod-airfoil configuration, J. Fluid Mech. 779 (2015) 1–35. https://doi.org/10.1017/jfm.2015.419.

[100] N.J. Georgiadis, D.P. Rizzetta, C. Fureby, Large-eddy simulation: Current capabilities, recommended practices, and future research, AIAA J. 48 (2010) 1772–1784. https://doi.org/10.2514/1.J050232.

[101] S.V. Johnson, Perry L, Large Eddy Simulation of a Film Cooling Flow Injected From an Inclined Discrete Cylindrical Hole Into a Crossfl ow With Zero-Pressure Gradient Turbulent Boundary Layer, NASA, 2012.

[102] S. Pachpute, B. Premachandran, Experimental investigation and large eddy simulations of turbulent slot jet impingement cooling of a circular cylinder with and without a quadrilateral confinement, Appl. Therm. Eng. 144 (2018) 854–876. https://doi.org/10.1016/j.applthermaleng.2018.08.101.

[103] S. Sarkar, H. Babu, Large eddy simulation on the interactions of wake and film-cooling near a leading edge, J. Turbomach. 137 (2015) 1–11. https://doi.org/10.1115/1.4028219.

[104] Y. Jiang, M.L. Mao, X.G. Deng, H.Y. Liu, Numerical investigation on body-wake flow interaction over rod-airfoil configuration, J. Fluid Mech. 779 (2015) 1–35. https://doi.org/10.1017/jfm.2015.419.

[105] E. Sakai, T. Takahashi, H. Watanabe, Large-eddy simulation of an inclined round jet issuing into a crossflow, Int. J. Heat Mass Transf. 69 (2014) 300–311. https://doi.org/10.1016/j.ijheatmasstransfer.2013.10.027.

[106] K. Singh, M. Sharabi, R. Jefferson-Loveday, S. Ambrose, C. Eastwick, J. Cao, A. Jacobs, Modeling of Partially Wetting Liquid Film Using an Enhanced Thin Film Model for Aero-Engine Bearing Chamber Applications, J. Eng. Gas Turbines Power. 143 (2021) 1–10. https://doi.org/10.1115/1.4049663.

[107] B.A. Haven, M. Kurosaka, Kidney and anti-kidney vortices in crossflow jets, J. Fluid Mech. 352 (1997) 27–64. https://doi.org/10.1017/S0022112097007271.

[108] M. Gritsch, A. Schulz, S. Wittig, Discharge coefficient measurements of film-cooling holes with expanded exits, J. Turbomach. 120(3) (1998). https://doi.org/10.1115/97-GT-165.

[109] M. Taslim, S. Ugarte, Discharge Coefficient Measurements for Flow Through

Compound-Angle Conical Holes with Cross-Flow, Int. J. Rotating Mach. 10 (2004) 145–153. https://doi.org/10.1080/10236210490277132.

[110] C.L. Liu, J.L. Liu, H.R. Zhu, A.S. Wu, Y.H. He, Z.X. Zhou, Film cooling sensitivity of laidback fanshape holes to variations in exit configuration and mainstream turbulence intensity, Int. J. Heat Mass Transf. 89 (2015) 1141–1154. https://doi.org/10.1016/j.ijheatmasstransfer.2015.06.019.

[111] M.M. Jafari, G.A. Atefi, J. Khalesi, Advances in nonlinear stress analysis of a steam cooled gas turbine blade, Lat. Am. Appl. Res. 42 (2012) 167–175.

LIST OF PUBLICATIONS

International Journals

1. Singh, A. K., Singh, K., Singh, D., and Sahoo, N. “Large Eddy Simulations for Film Cooling Assessment of Cylindrical and Laidback Fan-Shaped Holes with Reverse Injection.” *Journal of Thermal Science and Engineering Applications*, Vol. 13, No. 3, 2021, pp. 1–16. https://doi.org/10.1115/1.4048679.
2. Singh, A. K., Singh, K., Singh, D., and Sahoo, N. “Experimental and Numerical Analysis of Film Cooling Performance of a Corrugated Surface.” *Experimental Heat Transfer*, 2022. https://doi.org/10.1080/08916152.2022.2126031.
3. Singh, A. K., Singh, K., Singh, D., and Sahoo, N. “Experimental and Numerical Study of the Effect of Double Row Slot Injection Locations on Film Cooling Performance of a Corrugated Surface.” *Experimental Heat Transfer*, 2023, pp. 1–27. https://doi.org/10.1080/08916152.2023.2204338.
4. Singh, A. K., Singh, K., Singh, D., and Sahoo, N. “Experimental and Numerical Study of the Effect of Forward and Reverse Injection on Film Cooling and Thermal Stress Distribution on a Corrugated Surface. *”Applied Thermal Engineering”*, 2023. (under review)

International Conferences

1. Singh, A. K., Singh, K., Singh, D., and Sahoo, N., “Effect of various deposition configurations on film cooling characteristics of laidback fan shape hole”. 8th International Symposium on Advances in Computational Heat Transfer – CHT-21 August 15 – 19, 2021, Rio de Janeiro, Brazil**.**
2. Singh, A. K., Singh, K., Singh, D., and Sahoo, N."Film cooling analysis of ammonia-based aviation fuels in jet engines" Indo-German International Conference on Metrology for the Development of Green Hydrogen and Renewable Fuels in India, 4-6 April 2022. Physikalisch-Technische Bundesanstalt (PTB) Bundesalle, Braunschweig, Germany.

AUTHOR’S BIOGRAPHY

Mr. Ashutosh Kumar Singh was born in 1993 in Gopalganj (Bihar), India. He completed his B.Tech in Mechanical Engineering from GZS PTU CAMPUS, Bathinda, Punjab in 2015, with Gold-Medal in academics. Subsequently, he joined the M.Tech cum Ph.D., program at the Department of Mechanical Engineering, IIT Guwahati in 2016 (under the IIT-NIT Trainee Teacher scheme of MHRD Govt’ of India). He completed his MTech from, IIT Guwahati in 2018 with a specialization in fluids and thermal engineering and joined PhD program in December 2018.